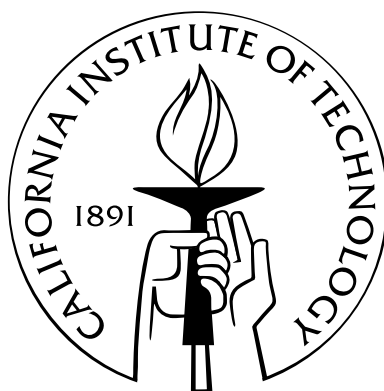


# Insights into the isoprene photochemical cascade

Thesis by  
Fabien Paulot

In Partial Fulfillment of the Requirements  
for the Degree of  
Doctor of Philosophy



California Institute of Technology  
Pasadena, California

2011  
(Defended May 23, 2011)



A mes parents, Dominique et Jean-Marie

# Acknowledgements

First and foremost, I need to thank my advisor Paul Wennberg. I had never heard of atmospheric chemistry before coming to Caltech and I recall asking him why anyone would be interested in studying the photochemistry of isoprene. He always gave me the opportunity to try my own ideas, however sketchy they were. I have greatly benefited from his ability to rapidly ask the right questions and design approaches to address them regardless of the problem. I am very grateful to John Seinfeld for his thorough guidance that helped shape and improve the studies presented in Chapters 2 and 3. In my first year at Caltech, I was fortunate to study bromine chemistry with Michael Hoffmann, Agustin Colussi and Chad Vecitis.

I am indebted to John Crounse, whose seemingly unlimited experimental expertise and scientific rigor were instrumental for much of my Ph.D. work. I have enjoyed my time in the Wennberg group with Melinda Beaver, Nathan Eddingsaas, Gretchen Keppel-Aleks, Andreas Kürten, Alan Kwan, Kathleen Spencer, Jason St. Clair and Debra Wunch. I am especially grateful to my office mate Melinda Beaver, whose patience, reality-check questions and listening qualities have been especially helpful in the last couple of months. I am also grateful to Havala Taylor Pye for her many great tips to run the GEOS-Chem model more efficiently and to Daven Henze, who greatly helped me set up and run the GEOS-Chem adjoint. More generally I am thankful to the GEOS-Chem community for developing, supporting and making available this great modeling tool. I am also grateful to Henrik Kjaergaard, whose many quantum chemical calculations made much of the work presented here possible. The third chapter owes a lot to his comments.

Over the years, I have benefited from the great support of the staff of the Geological and Planetary Science Division, in particular, Nora Oshima, Ulrika Terrones, Dian Buchness, Irma Black, Naveed Near-Ansari, Mike Blake and Scott Duncan. Their work is so efficient that it is often invisible.

I also need to thank my fellow ESE students, Scott Hersey, Tim Merlis, King-Fai Li and Xavier Levine, who helped make my first year abroad much easier than expected. I am especially grateful to Xavier, whose expertise in topics ranging from World War II tanks to classical Dutch painting, coupled with a twisted sense



of humor greatly complemented countless bike rides and hikes and sparked many laughs and improbable discussions.

I am grateful to my parents, Dominique and Jean-Marie Paulot, and my little brother, Benjamin Paulot, for their affection and unconditional support (and for the frequent emergency packages!). I would also like to acknowledge my grand-parents, Denise and Georges Bettati, and Marie-Thérèse and André Paulot, who all set wonderful examples for their grandchildren. I am immensely lucky to have you and I am definitely looking forward to seeing you more often as I move to the East Coast. This section would not be complete without thanking Xin Wang and Doris Zhang, who have made me feel at home in their family.

Finally and most importantly, I am grateful to my fiancée, Xinning Zhang. Over the years, we have gone through the few ups and the many downs of grad school, growing up together. She has been a source of much-needed balance and I am looking forward to many more years by her side.

# Abstract

Isoprene emissions are the single largest source of non-methane reduced carbon to the atmosphere. Proper simulation of the effect of its photooxidation on regional air quality and secondary organic aerosol formation requires detailed multi-generation and multi-phase photochemical mechanisms. In this work, I first demonstrate that  $\text{CF}_3\text{O}^-$  chemical ionization mass spectrometry (CIMS) is a powerful method to probe isoprene photochemical oxidation. Under high  $\text{NO}_x$ , isoprene nitrates and their photochemical products are directly observed and quantified. As isoprene nitrates are critical to the impact of isoprene photochemistry on ozone, these observations provide an important constraint on the effect of isoprene emissions on air quality in regions with large biogenic and anthropogenic emissions (e.g., Southeastern United States). The use of tandem CIMS in association with isotopically labelled hydroxy radicals is used to identify dihydroxyepoxides as major products of isoprene photooxidation in low  $\text{NO}_x$  conditions. This class of compounds may provide an important precursor for secondary organic aerosols under acidic conditions. The chemical mechanism derived from these laboratory observations is then incorporated in a chemical transport model to assess the impact of isoprene photooxidation on atmospheric chemistry. I examine how the photooxidation of isoprene impacts the budget of formic and acetic acids, two ubiquitous trace gases whose sources are poorly constrained. Comparison with observations from satellite, ground and aircraft platforms reveal a major missing source that may originate from the aging of secondary organic aerosols. Finally, the consequences of the multi-scale interplay between  $\text{NO}_x$  and isoprene photochemistry on the tropical budget of ozone are examined using forward and adjoint sensitivity simulations.

# Contents

<b>Acknowledgements</b>	<b>iv</b>
<b>Abstract</b>	<b>vi</b>
<b>1 Introduction</b>	<b>1</b>
<b>2 Isoprene photooxidation: new insights into the production of acids and organic nitrates</b>	<b>6</b>
2.1 Abstract . . . . .	7
2.2 Introduction . . . . .	7
2.3 Experiments . . . . .	8
2.3.1 Experimental setting . . . . .	8
2.3.2 Chemical ionization mass spectrometry (CIMS) . . . . .	9
2.3.3 Calibration . . . . .	10
2.4 Results . . . . .	12
2.5 Discussion . . . . .	13
2.5.1 $\delta$ -hydroxy channels . . . . .	13
2.5.1.1 Chemistry of the $\delta$ -hydroxy channels . . . . .	13
2.5.1.2 Consequences . . . . .	15
2.5.2 Organic nitrates . . . . .	17
2.5.2.1 $\delta$ -hydroxy isoprene nitrates . . . . .	17
2.5.2.2 $\beta$ -hydroxy isoprene nitrates . . . . .	18
2.5.2.3 Methacrolein and methylvinylketone hydroxynitrates . . . . .	19
2.5.3 Carboxylic acids . . . . .	20
2.5.3.1 Formic acid . . . . .	20

2.5.3.2	Acetic acid . . . . .	21
2.5.3.3	MOBA . . . . .	22
2.5.3.4	Pyruvic acid . . . . .	22
2.5.4	Atmospheric relevance . . . . .	22
2.5.4.1	Fate of organic nitrogen . . . . .	22
2.5.4.2	Carboxylic acids . . . . .	24
2.5.4.3	Development of a reduced mechanism . . . . .	25
2.6	Conclusion . . . . .	26
2.7	Acknowledgements . . . . .	26
<b>3</b>	<b>Unexpected epoxide formation in the gas-phase photooxidation of isoprene</b>	<b>45</b>
3.1	Abstract . . . . .	46
3.2	Introduction . . . . .	46
3.3	Results . . . . .	47
3.4	Atmospheric relevance . . . . .	50
3.5	Acknowledgements . . . . .	51
<b>4</b>	<b>Importance of secondary sources in the atmospheric budgets of formic and acetic acids</b>	<b>59</b>
4.1	Abstract . . . . .	60
4.2	Introduction . . . . .	60
4.3	Global budget . . . . .	61
4.3.1	Emissions . . . . .	61
4.3.1.1	Terrestrial vegetation . . . . .	61
4.3.1.2	Biomass burning and biofuel . . . . .	62
4.3.1.3	Fossil fuel . . . . .	62
4.3.1.4	Agricultural emissions . . . . .	63
4.3.1.5	Soil . . . . .	63
4.3.2	Photochemical sources of formic and acetic acids . . . . .	64
4.3.2.1	Terrestrial biogenic precursors . . . . .	64
4.3.2.2	Marine precursors . . . . .	66
4.3.2.3	Anthropogenic/biomass burning precursors . . . . .	66
4.3.3	Sources not treated . . . . .	66

4.3.4	Sinks . . . . .	67
4.3.4.1	Photochemical . . . . .	67
4.3.4.2	Dry deposition . . . . .	67
4.3.4.3	Wet deposition . . . . .	68
4.3.4.4	Dust . . . . .	68
4.3.5	Simulated distribution . . . . .	69
4.3.5.1	Formic acid . . . . .	69
4.3.5.2	Acetic acid . . . . .	71
4.4	Comparison with observations . . . . .	71
4.4.1	FTS measurements . . . . .	72
4.4.1.1	Ground-based total column . . . . .	72
4.4.1.2	ACE-FTS . . . . .	75
4.4.2	Aircraft measurements by mass spectrometry . . . . .	76
4.4.3	Summary of model-measurement comparisons . . . . .	77
4.5	Sensitivity study . . . . .	78
4.5.1	Biomass burning injection height . . . . .	78
4.5.2	Secondary source of FA and AA and organic aerosol aging . . . . .	80
4.5.3	Upper tropospheric budget of FA . . . . .	82
4.6	Conclusions . . . . .	84
4.7	Acknowledgements . . . . .	85
<b>5</b>	<b>Impact of the isoprene photochemical cascade on tropical ozone</b>	<b>102</b>
5.1	Introduction . . . . .	102
5.2	Model description . . . . .	105
5.2.1	Representation of isoprene nitrate chemistry . . . . .	106
5.2.2	Simulations . . . . .	107
5.2.2.1	Forward simulations . . . . .	108
5.2.2.2	Adjoint simulations . . . . .	108
5.3	Results . . . . .	109
5.3.1	Isoprene photochemical cascade . . . . .	109
5.3.1.1	Reference simulation . . . . .	109

5.3.1.2	Sensitivity to the treatment of isoprene nitrates . . . . .	110
5.3.2	Impact of the $\text{NO}_x$ and $\text{O}_x$ budget . . . . .	111
5.4	Discussion . . . . .	112
5.4.1	$\text{NO}_x$ removal efficiency controls the impact of isoprene nitrates over tropical continental regions . . . . .	112
5.4.2	$\text{NO}_x$ removal efficiency in the continental boundary layer influences the impact of isoprene over remote regions through deep convection . . . . .	114
5.4.3	Isoprene nitrates as $\text{NO}_x$ reservoirs and spatial scales coupling . . . . .	117
5.4.4	Can we separate the effect of chemistry, emissions and dynamics on the tropical $\text{O}_x$ budget using experimental observationsh? . . . . .	118
5.5	Conclusion . . . . .	119
<b>6</b>	<b>Conclusion and future work</b>	<b>139</b>
<b>A</b>	<b>Isoprene photooxidation: new insights into the production of acids and organic nitrates</b>	<b>141</b>
A.1	Photooxidation mechanism . . . . .	141
A.1.1	VOC chemistry . . . . .	141
A.1.1.1	OH . . . . .	141
A.1.1.2	Ozone . . . . .	142
A.1.1.3	$\text{NO}_3$ . . . . .	142
A.1.2	Peroxyradical chemistry . . . . .	142
A.1.2.1	NO . . . . .	142
A.1.2.2	$\text{NO}_2$ . . . . .	143
A.1.2.3	$\text{NO}_3$ . . . . .	143
A.1.2.4	$\text{HO}_2$ and peroxy radicals . . . . .	144
A.1.3	Photolysis . . . . .	144
A.1.4	Fate of the alkoxy radicals . . . . .	145
A.1.5	Skill of the model . . . . .	146
A.2	Calibration . . . . .	147
A.2.1	Definitions . . . . .	147
A.2.2	Dipoles and polarizabilities computed by quantum mechanics . . . . .	148
A.3	Uncertainty . . . . .	149

A.3.1	Initial branching ratio uncertainty . . . . .	149
A.3.2	Quantum mechanics . . . . .	151
A.3.3	Inorganic chemistry uncertainties . . . . .	151
<b>B</b>	<b>Unexpected epoxide formation in the gas-phase photooxidation of isoprene</b>	<b>158</b>
B.1	Chemical Ionization Mass Spectrometry . . . . .	158
B.1.1	Overview . . . . .	158
B.1.2	Negative ion mode . . . . .	160
B.1.3	Positive ion mode . . . . .	160
B.1.4	Negative ion MSMS mode . . . . .	161
B.2	Theoretical method: formation of $\beta$ and $\delta$ -IEPOX . . . . .	162
B.3	Possible interferences from isomers of IEPOX . . . . .	164
B.4	Additional mechanisms . . . . .	165
B.4.1	Addition of OH on isoprene second double bond . . . . .	165
B.4.2	Fate of IEPOX . . . . .	165
B.5	Kinetic mechanism . . . . .	168
B.6	GEOS-Chem . . . . .	169
B.7	Field measurements . . . . .	170
B.7.1	TC4 . . . . .	170
B.7.2	ARCTAS . . . . .	170
<b>C</b>	<b>Importance of secondary sources in the atmospheric budgets of formic and acetic acids</b>	<b>191</b>
C.1	Yield of formic and acetic acids from the oxidation of glycolaldehyde and hydroxyacetone by OH . . . . .	191
C.2	Retrieval of FA by ground FTS . . . . .	192
C.2.1	Method . . . . .	192
C.2.2	Error analysis . . . . .	193
C.2.2.1	Error in the spectroscopy . . . . .	193
C.2.2.2	Error in FA profile . . . . .	193
<b>D</b>	<b>Impact of the isoprene photochemical cascade on tropical ozone</b>	<b>210</b>
D.1	Rate constant adjoint . . . . .	210





# List of Tables

2.1	Signals monitored by Chemical Ionization Mass Spectrometry. $\mathcal{C}$ denotes a cluster [R 2.2] and $\mathcal{T}$ a transfer [R 2.1]. Uncertain identifications (see text) are highlighted by a $\star$ . . . . .	42
2.2	Suggested modifications of isoprene condensed photooxidation mechanism under high $\text{NO}_x$ conditions. (2,1), (3,4), E(1,4) and E(4,1) branches are not treated. Formation of organic nitrates is limited to isoprene, MVK and MACR peroxy radicals. The reaction of the isoprene nitrates with respect to ozone, as well as the fate of 3-MF, are not tackled by this mechanism (see text). MGLYX denotes methylglyoxal and HC4, a generic four-carbon VOC. . . . .	44
4.1	Biomass burning emission factors for FA and AA (in g per kg of dry matter, Yokelson (personal communication) and Akagi et al. (2010)). Emission factors from Andreae and Merlet (2001) are indicated in parentheses. . . . .	98
4.2	Soil emissions of formic and acetic acids at $T_{\text{soil}} = 30^\circ\text{C}$ in $\text{nmol}/(\text{m}^2 \text{ s})$ for different land types	99
4.3	Modeled global budget of atmospheric formic and acetic acids (2004–2008 average). Previous estimates are indicated in parentheses. . . . .	100
4.4	The increase in the median measured (m) FA and AA in polluted air observed during INTEX-B/IMPEX reflects the importance of secondary sources in the budget of FA and AA. These sources are missing from the model (M). $\alpha$ is the slope of the linear fit: $\text{AA} = \alpha\text{FA} + \beta$ following York's method (York et al., 2004) for the measurement (ordinary least square for the model). Characterization of the air masses follows the approach of Dunlea et al. (2009). .	101
5.1	Isoprene nitrate photochemical mechanism . . . . .	138
A.1	Skill of the model. $\Delta t = t_{\text{max}}^{\text{model}}/t_{\text{max}}^{\text{data}} - 1$ and $\Delta c = c_{\text{max}}^{\text{model}}/c_{\text{max}}^{\text{data}} - 1$ . . . . .	147

A.2	Weighted average dipoles ( $\bar{\mu}$ ) and polarizabilities ( $\alpha$ ). Experimental determinations are indicated in parenthesis when available. $k_X$ , is the weighted average of the collision rates calculated for conformers with an abundance greater than 5%. $k_{\text{HNO}_3} = 1.92 \times 10^{-9} \text{ cm}^3 \text{ molec}^{-1} \text{ s}^{-1}$ . $\sigma$ is the weighted standard deviation of the distribution of thermal collision rate constants, i.e., it indicates the sensitivity of the calibration to the calculated distribution of conformers. . . . .	157
B.1	Initial conditions (in ppbv) . . . . .	182
B.2	Theoretical weighted average dipole moments ( $\mu$ ) and polarizabilities ( $\alpha$ ) for conformers with abundance greater than 1%. <i>Cis</i> and <i>trans</i> refer to the position of the CH <sub>2</sub> OH group with respect to the plane of the oxirane. . . . .	183
B.3	Comparison of the experimental and theoretical calibration for three representative compounds	184
B.4	Calculated relative energies (kcal/mol) of the stationary points in the $\beta$ 4- ISOPOOH to $\beta$ -IEPOX (reaction (3.2a) and Fig. 3.5) . . . . .	185
B.5	Calculated relative energies (kcal/mol) of the stationary points in the $\beta$ 4- ISOPOOH to $\beta$ -IEPOX (reaction (3.2a) and Fig. 3.5). All single point energies on the B3LYP/cc-pVTZ optimized geometries . . . . .	186
B.6	Calculated relative energies (kcal/mol) of the stationary points in the $\delta$ 4- ISOPOOH to $\delta$ -IEPOX (reaction (3.2b) and Fig. B.3) . . . . .	187
B.7	Calculated relative energies (kcal/mol) of the stationary points in the $\beta$ 1- ISOPOOH to $\beta$ -IEPOX (reaction (3.2a) analog and Fig. B.4) . . . . .	188
B.8	Isomers of IEPOX previously observed in the aerosol phase . . . . .	189
B.9	Low NO <sub>x</sub> mechanism for the photooxidation of isoprene . . . . .	190
C.1	Windows used to retrieve FA . . . . .	194
C.2	Regional and global burden for FA (in %) . . . . .	207
C.3	Regional and global burden for AA (in %) . . . . .	208
C.4	Photochemical sources of FA and AA implemented in the GEOS-Chem chemical mechanisms. HC5: hydroxymethylbutenal (from isoprene), ISOP: isoprene, IEPOX: dihydroxyepoxide from isoprene photooxidation, $\delta$ – ISOPN: organic nitrates from isoprene (1,4 and 4,1 additions), MACR: methacrolein, MBO: methylbutenol, MONX: lumped monoterpenes, MVK: methylvinylketone, PRPE: propene + $\geq 4\text{C}$ alkene . . . . .	209

D.1	Notations . . . . .	218
-----	---------------------	-----

# List of Figures

2.1	Summary of the most prevalent first steps of isoprene photooxidation under high $\text{NO}_x$ conditions. Abbreviations: i: $\delta 1$ isomerization Reaction [R A.8] ; h: OH+VOC (abstraction or addition) $\star$ denotes the location of the reaction ; o: $\text{R} + \text{O}_2 \longrightarrow \text{RO}_2$ , O: Reaction [R A.7] ; D: Dibble mechanism (cf. 2.5.1.2) ; n: $\text{RO}_2 + \text{NO}$ - Reaction [R A.1] ; d: decomposition – reaction [R A.6] ; k: keto-enol tautomerism (possibly due to heterogeneous enol/ketone conversion). Blue circles: detected and correctly captured by the model. Red squares: Insufficient data/model discrepancy. . . . .	27
2.2	Signal recorded at $m/z=185$ (black circles) and modeled $\text{HC5}=\text{HC5 Z}(1,4)+\text{HC5 Z}(4,1) + \text{HC5 E}(4,1)$ (monitored as a cluster). . . . .	28
2.3	Signal recorded at $m/z=145$ (black circles) compared with modeled GLYC profile. The contribution of acetic acid cluster has been removed using acetic acid transfer at $m/z=79$ . Colored bars indicate the instantaneous modeled contributions of the different sources of GLYC. . . .	29
2.4	Signal recorded at $m/z=217$ (black circles) and modeled $\text{DHMOB}=\text{DHMOB}(1, 4) + \text{DHMOB}(4, 1)$ (monitored as a cluster) . . . . .	30
2.5	Sum of the signals recorded at $m/z=133$ and $m/z=199$ (black circles) compared with $\text{MOBA}=\text{MOBA Z}(1,4)+\text{MOBA Z}(4,1)$ ( $m/z=133$ (transfer)+199 (cluster)) and MHP (cluster at $m/z=133$ ) . . .	31
2.6	Signal recorded at $m/z=175$ (black circles) compared to modeled DHPN (measured as a cluster)	32
2.7	Signal recorded at $m/z=159$ (black circles) compared with modeled HACET profile. Colored bars indicate the instantaneous modeled contributions of the different sources of HACET. MPAN source has been described by Orlando et al. (2002). . . . .	33
2.8	Decomposition pathway of the different isoprene nitrates after their reaction with OH. Reaction of ISOPN with OH, $\text{O}_2$ , and NO, also yields dihydroxy-dinitrates through reaction [R A.1]. Color code is identical to Fig. 2.1. . . . .	34

2.9	Signal recorded at $m/z=232$ (black circles) compared to modeled isoprene nitrates (ISOPN (1, 2), (1,4)E/Z, (2, 1), (4, 3), (3, 4), (4, 1)E/Z (measured as clusters)) corrected for calibration changes . . . . .	35
2.10	Signal recorded at $m/z=190$ (black circles) compared to modeled ETHLN (measured as a cluster)	36
2.11	Signal recorded at $m/z=204$ (black circles) compared to modeled PROPNN (measured as a cluster). Colored bars indicate the instantaneous modeled contributions of the different sources of PROPNN . . . . .	37
2.12	Signal recorded at $m/z=189$ (black circles) compared to modeled DHB (measured as a cluster). Colored bars indicate the instantaneous modeled contributions of the different sources of DHB.	38
2.13	Signal recorded at $m/z=234$ (black circles) compared to the modeled profile of MVKN+MVKN (m)+MACRN+MACRN (m) (measured as clusters), corrected for changing calibrations . . .	39
2.14	Signal recorded at $m/z=65$ (black circles) compared to modeled formic acid. Colored bars indicate the instantaneous modeled contributions of the different sources of formic acid. . . .	40
2.15	Signal recorded at $m/z=79$ (black circles) compared to modeled acetic acid (observed as a transfer at this mass). Colored bars indicate the instantaneous modeled contributions of the different sources of acetic acid. . . . .	41
3.1	Fate of isoprene peroxy radicals . . . . .	53
3.2	IEPOX formation mechanisms . . . . .	54
3.3	Consecutive formation of ISOPOOH and IEPOX in the photooxidation of isoprene. Following the time when the photolysis of hydrogen peroxide [initially 1.66 parts per million by volume (ppmv)] begins ( $t = 0$ ), isoprene (black dotted line) decays quickly. ISOPOOH and then IEPOX are detected as major products of the oxidation of isoprene [because they are isobaric, they both are detected at $m/z = 203$ (red), the cluster of these compounds with $\text{CF}_3\text{O}^-$ ]. Tandem mass spectroscopy provides for separation of the $m/z = 203$ signal: ISOPOOH (green) is observed as the $m/z = 63$ daughter, whereas IEPOX (blue) is observed as the $m/z = 183$ daughter. The sum of IEPOX and ISOPOOH is indicated by the dashed black line. . . . .	55

- 3.4 Formation of light and heavy ISOPOOH and IEPOX in the oxidation of isoprene using  $\text{H}^{18}\text{O}^{18}\text{OH}$  as the OH source. Formation of ISOPOOH is monitored via the daughter  $m/z = 63$  (circles) of  $m/z = 203$  (red) and  $m/z = 205$  (magenta). Formation of IEPOX is monitored via the loss of HF (squares) from  $m/z = 203$ ,  $m/z = 205$ , and  $m/z = 207$  (blue). Formation of isotopically light ISOPOOH and IEPOX reflects OH reformation. Solid lines represent the modeled mixing ratios for the different isomers. Isoprene initial concentration was 23.5 parts per billion by volume (ppbv), and  $^{18}\text{OH}$  was generated from the photolysis of  $\text{H}^{18}\text{O}^{18}\text{OH}$  (1.75 ppmv initial concentration, UV lights on at  $t = 0$ ). . . . . 56
- 3.5 Relative energies for the formation of  $\beta$ -IEPOX from  $\beta$ 4-ISOPOOH (Fig. 3.2a). The alkyl-radical resulting from the addition of OH onto the  $\beta$ 4-ISOPOOH double bond is formed with enough excess energy ( $\sim 30$  kcal/mol) that it quickly decomposes to the  $\beta$ -IEPOX + OH via the  $\beta$ 4-transition state. Energies are calculated with the CCSD(T)-F12/VDZ-F12 explicitly correlated method at the B3LYP/cc-pVTZ optimized structures (see Appendix B.2). . . . . 57
- 3.6 Simulated daily distribution of IEPOX in the planetary boundary layer during the Northern Hemisphere summer (A) and winter (B). IEPOX seasonal cycle mirrors the isoprene emissions. The mixing ratio of IEPOX is higher in the tropics than in other isoprene production regions in the northern mid-latitudes (e.g., the southeast United States). This reflects the reduction in the yield of IEPOX from isoprene due to anthropogenic emissions of NO. . . . . 58
- 4.1 Annual simulated distribution of FA and AA in the boundary layer. FA and AA maxima in the tropics reflect strong biogenic sources. . . . . 86
- 4.2 Locations of the measurement sites used in this study. Red crosses: FTS ground stations (B: Barcroft, Br: Bremen, P: Paramaribo, R: La Réunion, T: Thule, W: Wollongong). Cyan dots: ship cruises. Blue, magenta, yellow and green dots: aircraft mission flight tracks . . . . . 87
- 4.3 The observed seasonal cycle of FA total column (blue, lower panel) is well captured by the model at the Wollongong site (red, lower panel) and is consistent with a strong biogenic influence (green, upper panel). This is not the case in the high latitude site at Thule where the model underpredicts measured FA. Upper panel: modeled contribution of biogenic sources (green: emission + photochemical production) and biomass burning (black: emissions + photochemical production) to FA total column. Lower panel: modeled (red) and measured (blue) FA total column. Measurements and model are averaged over a two day time period. . . . . 88

4.4	Upper panels: same as Fig. 4.3. Lower panel: comparison between modeled and measured FA total columns. Individual total column measurements are indicated with blue dots. The 2004–2008 model range is indicated by the red shaded area and the model mean by the white dashed line. . . . .	89
4.5	Monthly FA total column measured during cruises in the Atlantic ocean in 1996, 1999, 2000, 2002, 2003 and 2005 (dots). The 2004–2008 model monthly mean range is indicated by the red shaded area. FA maximum in the tropics reflects biomass and biogenic sources. . . . .	90
4.6	Measured distribution of FA (pptv) by ACE-FTS from 2004 to 2008. Median of FA measurements is calculated in 10° latitude 50 mbar bins. Only cells with more than ten measurements are shown. . . . .	91
4.7	Comparison of the simulated FA with observations by ACE-FTS suggests an altitude-dependent error. Increasing the reaction rate of OH with FA reduces the model high-bias in the upper troposphere (C), while injection of biomass burning in the free troposphere provides little improvement in the middle troposphere while degrading FA simulation in the upper troposphere (B). Absolute difference between the model and the ACE-FTS measurement is shown in pptv with contours indicating the relative difference in % ((model-measurement)/measurement). Cells with no measurements are grayed. Panel A shows the comparison for the reference run (R1), Panel B for R2b and Panel C for R4 (see Section 4.5). The model is sampled at the location and time of the ACE-FTS measurement. . . . .	92
4.8	The correlation between CO and FA observed by ACE-FTS (blue crosses) in the free troposphere is not well-captured by the model (green, red and blue crosses), suggesting a missing secondary source. Lower panel: correlation plot between FA and CO (lower panel) for the measurements (blue) and the model: R1 (red), R2b (green), R4 (black). Upper panel: distribution of measured and modeled CO. The extent of the error bars indicate the 25 and 75 percentiles. The model is sampled at the location and time of the ACE-FTS measurement. . . . .	93
4.9	In situ measurements show strong correlation of FA and AA with the abundance of organic aerosol over the West Coast of the United States and the eastern Pacific (INTEX-B), in urban environments (MILAGRO) as well as in arctic regions (ARCPAC). . . . .	94
4.10	Comparison between measured (blue) and modeled (red) vertical AA profiles. The box (thick line) extent represents the 25% and 75% percentiles. . . . .	95

- 4.11 A diffuse source of FA from aerosol aging (dominated by biomass burning (R3)) allows the model to better reproduce the increase in FA during the biomass burning season. . . . . 96
- 4.12 Including a representation of  $\text{HCHO} + \text{HO}_2$  chemistry increases FA in the upper troposphere by nearly 50% (red) compared to the reference run (blue). Such a source (black dashed line) would further amplify the high bias of the model with respect to ACE-FTS observations. Profile of FA at -14N, 60W July 2005 . . . . . 97
- 5.1 The three continental regions considered in this study (Fig. D.2) account together for  $\sim 50\%$  of isoprene global emissions (geographical breakdown is indicated in the panels' title). Very different  $\text{NO}_x$ /isoprene regimes (black line for  $\text{NO}_x$ /isoprene and dashed black line for  $\text{NO}_x^{\text{surface}}$ /isoprene) and  $\text{NO}_x$  sources (colored regions) are experienced through the year with South America C(isoprene)/N emissions exceeding 50 for most of the year. The seasonality of the ratio of isoprene emissions to  $\text{NO}_x$  emissions is primarily controlled by biomass burning, as seasonal variations of isoprene emissions (dashed blue line, in mole of C/ha/month  $\times 1/25$ , left axis) are small. The ratio of  $\text{NO}_x$  emissions to isoprene emissions is weighted by isoprene emissions to represent the average  $\text{NO}_x$  encountered by isoprene. . . . . 121
- 5.2 Overview of the isoprene photochemical cascade (thick color bars) for the reference simulation. Branching ratios for the reference run (in percent) are indicated by bars for isoprene oxidation (A, left axis), isoprene peroxy radical fate (B, left axis), isoprene nitrate sources (C, left axis),  $\text{ING}_0$  fate (D, right axis),  $\text{ING}_1$  fate (E, right axis),  $\text{ING}_2$  fate (F, right axis). Black open circles indicate the lifetime (in hours) of isoprene (A, right axis),  $\text{ING}_0$  (D, left axis),  $\text{ING}_1$  (E, left axis) and  $\text{ING}_2$  (F, left axis), and the fractional loss of  $\text{NO}_x$  caused by isoprene nitrate chemistry,  $L_{\text{ING}_0}(\text{NO}_x)/L_{\text{T}}(\text{NO}_x)$  (C, right axis in %). The extent of the error bars represents the minimum and maximum values calculated using the different representations of isoprene nitrate chemistry (see Section 5.2). J designates the isomerization of isoprene peroxy radical (B, Peeters et al., 2009) and the photolysis of  $\text{ING}_2$  (F). . . . . 122
- 5.3 Isoprene nitrate chemistry significantly affects the budget of  $\text{NO}_x$  in the tropics. Positive numbers represent the fraction of the net chemical loss of  $\text{NO}_x$  ( $\mathcal{L}_{\text{NO}_x}$ ) accounted for by  $\mathcal{D}_{\text{ING}}$  ( $\mathcal{D}_{\text{ING}} > 0$ ), negative numbers denote the fraction of the net chemical source of  $\text{NO}_x$  accounted for by  $\mathcal{D}_{\text{ING}}$  ( $\mathcal{D}_{\text{ING}} < 0$ ). . . . . 123



- 5.4 The representation of isoprene nitrate chemistry directly impacts simulated tropical ozone, as illustrated by the normalized standard deviation in simulated total column ozone for different choices of nitrate yield ( $Y$ ),  $\text{NO}_x$  recycling ( $\alpha$ ) and ING deposition (see Section 5.2.2.1). The choice of the representation of isoprene nitrate chemistry is most important outside of the biomass burning seasons (large  $\mathcal{D}_{\text{ING}}/\mathcal{L}_{\text{NO}_x}$ ) and affects large regions of the tropics. Conversely, changes in the representation of isoprene nitrate chemistry causes little change in regions affected by biomass burning. . . . . 124
- 5.5 The correlation between  $\mathcal{D}_{\text{ING}}$  and  $\mathcal{P}_{\text{O}_x}$  on the regional scale (South America) across a large range of representations of ING chemistry suggests that the influence of ING chemistry on  $\mathcal{P}_{\text{O}_x}$  is primarily controlled by its net impact on  $\text{NO}_x$ . Upward-pointing triangles/Circles/downward-pointing triangles refer to  $Y = 5\%/10\%/15\%$ ; red/black/blue colors refer to fast/medium/slow ING deposition; empty/half filled/filled refer to  $\alpha = 0/50/100\%$ . The reference simulation is indicated by a vertical cross. . . . . 125
- 5.6 The sensitivity of  $\mathcal{P}_{\text{O}_x}$  to the representation of isoprene nitrate chemistry, inferred from the slope of  $\Delta\mathcal{P}_{\text{O}_x}/\Delta\mathcal{D}_{\text{ING}}$  in Fig. D.6, is well explained by the fraction of  $\text{NO}_x$  removed through ING chemistry ( $\mathcal{D}_{\text{ING}}/\mathcal{L}_{\text{NO}_x}$ ). Red: Africa, blue: South America, green: South East Asia . . . 126
- 5.7 The sensitivity of tropospheric ozone to changes in key reactions controlling the fate of  $\text{ING}_0$ ,  $\text{ING}_1$  and  $\text{ING}_2$  exhibits strong seasonal and regional differences. Faster oxidation of  $\text{ING}_0$  and  $\text{ING}_1$  are associated with higher ozone in particular over continental regions where  $\text{NO}_x$  is limited (e.g., South America from March to June). A faster oxidation of  $\text{ING}_2$  has an opposite effect over continents ( $\mathcal{S}_{\text{OH}+\text{ING}_2}^{\text{O}_3} > 0$ ) and over oceanic basins ( $\mathcal{S}_{\text{OH}+\text{ING}_2}^{\text{O}_3} < 0$ ). . . . . 127
- 5.8 Adjoint sensitivity of tropical ozone (solid lines) and  $\text{NO}_x$  (dashed lines) to changes in the isoprene nitrate yield (red), the isoprene nitrate recycling (blue,  $\times 5$ ), the loss rate of methane (green,  $\text{CH}_4 + \text{OH}$ ), the rate of  $\text{OH} + \text{NO}_2$  (cyan,  $\times 0.5$ ) and the decomposition of PAN (black,  $\times 2$ ). Adjoint sensitivities are summed over the entire troposphere from  $-15^\circ\text{N}$  to  $7^\circ\text{N}$ . . . . . 128
- 5.9 Adjoint sensitivity of tropical ozone (solid lines) and  $\text{NO}_x$  (dash lines) to changes in the emissions of isoprene (green), lightning  $\text{NO}_x$  (red,  $\times 0.5$ ), biomass burning  $\text{NO}_x$  (blue), soil  $\text{NO}_x$  (orange) and anthropogenic  $\text{NO}_x$  (violet). Adjoint sensitivities are summed over the entire troposphere from  $-15^\circ\text{N}$  to  $7^\circ\text{N}$ . . . . . 129

- 5.10 Adjoint sensitivity of mean tropospheric ozone over South America to isoprene emissions. Symbols denote the isoprene emission region (circle: South America, diamond: Africa, square: Southeast Asia). The symbols are color coded by the sensitivity of  $\text{NO}_x$  over South America to isoprene emissions ( $S_{E(\text{ISOP})}^{\text{NO}_x}$ ) in the March–May period (low biomass burning). Open (filled) symbols denote an absolute increase (decrease) in  $S_{E(\text{ISOP})}^{\text{NO}_x}$ . Black circled symbols denote locations where  $S_{E(\text{ISOP})}^{\text{NO}_x}$  changed signs between two time periods. . . . . 130
- 5.11 Adjoint sensitivity of tropospheric ozone (solid lines) and  $\text{NO}_x$  (dashed lines) over South America (shaded region) to changes in the emissions of isoprene (green), lightning  $\text{NO}_x$  (red,  $\times 0.5$ ), biomass burning  $\text{NO}_x$  (blue), soil  $\text{NO}_x$  (orange) and anthropogenic  $\text{NO}_x$  (violet). Adjoint sensitivities are summed over the entire troposphere from  $-15^\circ\text{N}$  to  $7^\circ\text{N}$ . . . . . 131
- 5.12 Adjoint sensitivity of tropospheric ozone (solid line) and  $\text{NO}_x$  (dashed line) over the Pacific (shaded region) to changes in the emissions of isoprene (green), lightning  $\text{NO}_x$  (red,  $\times 0.5$ ), biomass burning  $\text{NO}_x$  (blue), soil  $\text{NO}_x$  (orange) and anthropogenic  $\text{NO}_x$  (violet). Adjoint sensitivities are summed over the entire troposphere from  $-15^\circ\text{N}$  to  $7^\circ\text{N}$ . . . . . 132
- 5.13 Seasonal variations in the adjoint sensitivity of Atlantic (top row) and African (bottom row) ozone to  $\text{ING}_0 \text{NO}_x$  recycling ( $\alpha$ ) summed from the surface to 500 mbar. Contours indicate the mean ratio between the loss of isoprene peroxy radicals through reaction with  $\text{HO}_2$  and the loss of isoprene peroxy radicals through reaction with  $\text{HO}_2$  and  $\text{NO}$ . . . . . 133
- 5.14 Seasonal variations in the adjoint sensitivity of Atlantic (top row) and African (bottom row) ozone to isoprene emissions. Contours indicate the mean ratio between the loss of isoprene peroxy radicals through reaction with  $\text{HO}_2$  and the loss of isoprene peroxy radicals through reactions with  $\text{HO}_2$  and  $\text{NO}$ . . . . . 134
- 5.15 Seasonal variations in the adjoint sensitivity of Atlantic (top row) and African (bottom row) ozone to biomass burning  $\text{NO}_x$  emissions. Contours indicate the associated adjoint sensitivity of  $\text{NO}_x$  (i.e.,  $^a S_{E_{bb}(\text{NO}_x)}^{\text{NO}_x}$  for the top row and  $^A S_{E_{bb}(\text{NO}_x)}^{\text{NO}_x}$  for the bottom row). . . . . 135
- 5.16 Seasonal variations of the adjoint sensitivity of Atlantic (top row) and African (bottom row) ozone to lightning  $\text{NO}_x$  emissions. Contours indicate the associated adjoint sensitivity of  $\text{NO}_x$  over the Atlantic (A, B, C) and Africa (D, E, F) (i.e.,  $^a S_{E_{li}(\text{NO}_x)}^{\text{NO}_x}$  for the top row and  $^A S_{E_{li}(\text{NO}_x)}^{\text{NO}_x}$  for the bottom row). . . . . 136

5.17	Schematic representation of the spatial modulation of the $O_x$ budget by the isoprene photochemical cascade. The impact of isoprene photooxidation on ozone depends on its impact on $NO_x$ near isoprene emissions ( $\mathcal{D}_{ING}/\mathcal{L}_{NO_x}$ , continent). In particular, $\mathcal{D}_{ING}/\mathcal{L}_{NO_x}$ influences the amount of BVOCs injected in the free troposphere and therefore the large-scale impact of the isoprene photochemical cascade. Under high $NO_x$ , an increase in the continental $\mathcal{D}_{ING}/\mathcal{L}_{NO_x}$ (green filled arrow) results in an increase of ozone downwind of continents ( $\Delta O_3 > 0$ ) because of increased transport of nitrogen reservoirs. Conversely, under low $NO_x$ , a similar increase results in a decrease of ozone downwind of continents because of diminished export from the continents. . . . .	137
A.1	Evolution of the speciation during isoprene photooxidation. The abundance of a functional group $\Pi$ is defined as the sum of the carbons bearing $\Pi$ normalized by the total amount of carbon in the chamber, i.e., five times the initial amount of isoprene. . . . .	153
A.2	Different stages of the reaction. Regime I: alkenes chemistry, $NO_x$ -dominated. Regime II: aldehydes chemistry, $NO_x$ -dominated. Regime III: ketones and peroxides chemistry, $HO_x$ -dominated . . . . .	154
A.3	Isoprene profile monitored by GC FID compared to modeled isoprene . . . . .	155
A.4	Isoprene profile monitored by GC FID compared to modeled isoprene . . . . .	156
B.1	Schematic diagram of the Caltech Chemical Ionization Mass Spectrometer (CIMS) . . . . .	173
B.2	Following the time when the photolysis of $H_2O_2$ (initially 1 ppmv) begins ( $t = 0$ ), we observe the formation of BUTOOH and then BEPOX together detected at $m/z=189$ (black). Tandem mass spectroscopy provides for separation of the $m/z=189$ signal: BUTOOH (green) is observed as the $m/z=63$ daughter while BEPOX (blue) is observed as the $m/z=169$ daughter. The sum of the measurable daughters of $m/z=189$ (red) correctly captures the profile of the parent signal. . . . .	174
B.3	Relative energies of the B3LYP/cc-pVTZ optimized geometries for the formation of $\delta 4$ -IEPOX from $\delta 4$ -ISOPOOH . . . . .	175
B.4	Relative energies of the B3LYP/cc-pVTZ optimized geometries for the formation of $\beta$ -IEPOX from $\beta 1$ -ISOPOOH . . . . .	176
B.5	Same as Fig. 3.4 for Experiment 1 . . . . .	177
B.6	Same as Fig. 3.4 for Experiment 3 . . . . .	178

B.7	Modeled yield of IEPOX from the reaction of isoprene + OH in the planetary boundary layer. Grid cells where isoprene mixing ratio is lower than 50 pptv are not shown. . . . .	179
B.8	Flight tracks for 2008 summer ARCTAS flights on July 5th, 8th, 10th, and 12th indicating the location of data and the mixing ratio for ISOPOOH_ft and IEPOX_ft . . . . .	180
B.9	Flight tracks for 2008 summer ARCTAS flights on July 5th, 8th, 10th, and 12th with color indicating the altitude of the DC-8 aircraft . . . . .	181
C.1	Influence of the window on the retrieved FA total column at Paramaribo . . . . .	195
C.2	Influence of FA a priori vertical profile on the retrieved FA total column at Paramaribo . . . .	196
C.3	A priori vertical profiles of FA used to retrieve FA total column . . . . .	197
C.4	An example of FA retrieval at Paramaribo using GFIT using the Q window. Top panel represents the fit residuals (computed–measured spectrum). Bottom panel represents the computed spectrum (black line), measured spectrum (black crosses), as well as the contribution of the different gases in the window used to retrieve FA. The weakness of FA absorption and the strong interference of H <sub>2</sub> O in the region make the retrieval of FA challenging. For this spectrum, the retrieved FA total column is $1.02 \times 10^{16}$ molec/cm <sup>2</sup> ( $\pm 19\% \pm 2.7 \times 10^{15}$ molec/cm <sup>2</sup> ).198	198
C.5	Same as Fig. 3a for CO (Wollongong). Note the anomalously high CO at the end of 2007, reflecting intense biomass burning in the region. . . . .	199
C.6	Same as Fig. 4.4c for CO at Bremen . . . . .	200
C.7	Relationship between FA and CH <sub>2</sub> O at Barcroft ( $FA \simeq 2.3 \times CH_2O$ , $R^2 = 0.77$ ) . . . . .	201
C.8	Same as Fig. 4.4c for CH <sub>2</sub> O at Barcroft . . . . .	202
C.9	Same as Fig. 4.4c for CO at Barcroft . . . . .	203
C.10	Relationship between CO and FA total columns (molec/cm <sup>2</sup> ) measured during cruises in the Atlantic Ocean . . . . .	204
C.11	Effect of a diffuse source of FA associated with aerosol aging on FA total column over the Atlantic (scenario R3). Color code same as Fig. 4.5 . . . . .	205
C.12	Effect of a diffuse source of FA associated with aerosol aging on FA total column over Bremen. Color code same as Fig. 4.4b . . . . .	206

D.1	Schematic representation of the isoprene nitrate photochemical cascade. Red arrows designate reaction with OH/NO, green arrows designate reaction with ozone and blue arrows represent NO <sub>3</sub> chemistry. Dashed arrows represent O <sub>x</sub> release. Y is the isoprene nitrate yield (ING <sub>0</sub> ) and $\alpha$ the fraction of NO <sub>x</sub> released in ING <sub>0</sub> oxidation by OH and ozone. MVK, MACR and IALD designate major second-generation products of isoprene oxidations under high NO <sub>x</sub> conditions. . . . .	211
D.2	OMI/MLS tropospheric total column ozone (Ziemke et al., 2006) in Dobson units. The different geographical regions used in the adjoint simulations are denoted by white contours. The tropical region extends from 15°S to 7°N. Top panel: June 2006–October 2006, middle panel: November 2006–February 2007, bottom panel: March 2007–May 2007 . . . . .	212
D.3	K-means clustering analysis of the factors controlling $\mathcal{D}_{\text{ING}}$ reveals important regional and seasonal differences. During periods of large biomass burning, the influence of the recycling /production and losses of secondary nitrate ING <sub>1</sub> and ING <sub>2</sub> is reinforced relative to the isoprene nitrate yield (blue cluster), as the formation of ING <sub>0</sub> has a small effect on the budget of NO <sub>x</sub> . Conversely in regions where the ratio of isoprene to NO <sub>x</sub> is high (South America (B, C) and eastern South East Asia), a large fraction of NO <sub>x</sub> is segregated in ING <sub>0</sub> . This depresses OH and ozone formation, diminishing the fraction of ING <sub>0</sub> oxidized locally. In these regions, the impact of isoprene nitrate chemistry on the local NO <sub>x</sub> budget is primarily controlled by the yield of ING <sub>0</sub> . The long range effect of isoprene nitrate chemistry on NO <sub>y</sub> is solely controlled by ING <sub>2</sub> (orange). The analysis was restricted to regions where $\mathcal{D}_{\text{ING}}$ accounts for more than 5% of the total production/loss of NO <sub>x</sub> . . . . .	213
D.4	Isoprene contributes significantly to the loss of OH even at high altitude. The color code indicates the ratio between the loss of OH through isoprene + OH and the loss of OH by isoprene and CO. A: June 2006–October 2006, B: November 2006–February 2007, C: March 2007–May 2007 . . . . .	214
D.5	Fraction of isoprene oxidized below 800 mbar . . . . .	215
D.6	Seasonal variations of the relationship between $\mathcal{D}_{\text{ING}}$ and $P_{\text{O}_x}$ over South America (A), Africa (B) and South East Asia (C) resulting from different representation of ING chemistry. Variations in $\mathcal{D}_{\text{ING}}$ and $P_{\text{O}_x}$ are normalized to the reference simulation (Y = 10%, $\alpha$ = 50% and default deposition). The linear fit for each month is indicated by a dashed line. The color code indicates the ratio between $\mathcal{D}_{\text{ING}}$ and $\mathcal{L}_{\text{NO}_x}$ in the reference run for each month. . . . .	216

D.7	Seasonal emissions of isoprene (green), lightning NO <sub>x</sub> (red), biomass burning NO <sub>x</sub> (blue, ×0.5), anthropogenic NO <sub>x</sub> (violet), soil NO <sub>x</sub> (orange). . . . .	217
-----	---	-----

## **Chapter 1**

# **Introduction**

More than 99.9% of Earth's atmosphere is comprised of only four gases: nitrogen, oxygen, argon and water. In contrast, the remaining 0.1% exhibit an incredible diversity that is critical to Earth's habitability. For instance, the ozone layer, which provides an essential shield against UV radiation, would not be more than a few millimeters thick if it were brought to the surface. Carbon dioxide and methane are present in parts per million in the atmosphere yet their strong correlation with large climate variations on geological timescales, illustrate the importance of trace greenhouse gases for Earth's climate. Particulate matter also plays a large role on Earth's energy budget, either directly (scattering and absorption of solar radiation) or indirectly (e.g., cloud formation and lifetime), and constitutes a great source of uncertainty in the assessment of the extent and consequences of climate change.

The importance of trace atmospheric compounds is not limited to the global scale. In fact, it is the study of urban smog in Los Angeles and London, pioneered by Haagen-Smit (1952), that helped atmospheric chemistry develop into an independent science. Research on anthropogenic air pollution can be credited with important regulations that have dramatically improved air quality (e.g., reduced acid deposition (National Acid Precipitation Assessment Program), ozone and particulate matter exposure (World Health Organization, 2005) and stratospheric ozone depletion (Montreal protocol)).

In the last twenty years, improvements in measurement and modeling capabilities have revealed the importance of emissions of trace gases by the biosphere. Chameides et al. (1988) demonstrated that the failure of ozone abatement strategies in the Southeast of the United States could be traced to the interaction between large biogenic and anthropogenic emissions. More recently, Goldstein et al. (2009) showed that such interactions also promote aerosol formation in the same region, as Went (1960) had envisioned.

The biosphere emits more than  $\sim 1000$  TgC of non-methane hydrocarbons to the atmosphere every year, much more than human activities (Guenther et al., 1995). Once in the atmosphere, these biogenic volatile organic compounds (BVOC) undergo a complex suite of oxidative and phase transformations, fueled by light and moisture, until oxidation products are deposited or fully oxidized to carbon dioxide (Seinfeld and Pandis, 1998). Through these photochemical processes, the biosphere exerts an important control over the composition and chemical state of the atmosphere.

There are probably tens of thousands of BVOCs emitted to the atmosphere. However fewer than one hundred are thought to be emitted with sufficient rates to affect atmospheric chemistry (Guenther et al., 2000). Isoprene (2-methyl-1,3-butadiene) emissions alone are estimated to range from 440 to 660 TgC (Guenther et al., 2006). Isoprene is primarily emitted by broad-leaf trees ( $\sim 15\%$  of vascular plants). It is thought to increase the tolerance of leaves against high temperature episodes (heat flecks) (Sharkey and



Singsaas, 1995; Sharkey et al., 2001), consistent with the temperature dependence of isoprene biosynthesis (Harley et al., 1999; Sharkey et al., 2008) and its large emissions in the wet tropics (Guenther et al., 2006). The mechanism by which isoprene provides such thermal tolerance is not well understood but it appears to stabilize the lipid membrane of leaf cells. Isoprene also provides some protection against ozone damages (Loreto and Velikova, 2001), which is beneficial in polluted urban settings. As isoprene emissions promote ozone formation in a urban setting, Lerdau (2007) suggested that isoprene-emitting plants may outcompete non-isoprene emitting plants, raising concerns for biodiversity and air quality.

The magnitude of isoprene emissions makes it an ideal compound to investigate biosphere-atmosphere interactions as well as their sensitivities to changes induced by anthropogenic activities. As such, it has been a focus of atmospheric chemistry since its discovery in the mid 1950s by Givi Sanadze (Sanadze, 2004, and references therein). It took more than 20 years for the first isoprene degradation scheme to be proposed by Zimmerman et al. (1978). Though the proposed mechanism was not derived from experimental observations, Zimmerman et al. correctly hypothesized the formation of methylvinylketone, methacrolein and formaldehyde from the photooxidation of isoprene by OH under relatively large NO concentrations ( $\text{NO} > 50 \text{ pptv}$ ). Dimitriadis (1981), Altshuller (1983) and Chameides et al. (1988) rapidly recognized that isoprene could contribute to ozone production under these conditions, and air pollution concerns would help fuel research on the fate of isoprene under “high  $\text{NO}_x$ ” condition for the next twenty years<sup>1</sup>. The identifications of many additional photochemical products such as 3-methylfuran (Gu et al., 1985; Atkinson et al., 1989), hydroxyacetone, methylglyoxal, peroxyethacetyl nitrate, organic nitrates (Tuazon and Atkinson, 1990) has shed light on the complexity of the isoprene photochemical cascade. In the 1990s, explicit and condensed mechanisms of isoprene photooxidation were developed (Carter, 1996; Carter and Atkinson, 1996; Paulson and Seinfeld, 1992) and rapidly incorporated in the recently developed chemical transport models (Crutzen and Zimmermann, 1991; Roelofs and Lelieveld, 1995). The large differences between models that incorporate non-methane hydrocarbon chemistry and those limited to CO and methane chemistry highlighted the importance of understanding the fate of biogenic emissions for past (Mickley et al., 2001), present (Müller and Brasseur, 1995; Wang et al., 1998; Horowitz et al., 1998; Poisson et al., 2000; Roelofs and Lelieveld, 2000) and future air quality (Shallcross and Monks, 2000).

In the past decade, dramatic advances in observation capabilities have uncovered important gaps in our understanding of the isoprene photochemical cascade. The first major breakthrough was made in 2004, when Claeys et al. reported observations of methyltetrols in organic aerosols over Amazonia, suggesting that the

---

<sup>1</sup>“Trees cause more pollution than automobiles do.”—Ronald Reagan (1981)

photooxidation of isoprene could yield secondary organic aerosol formation (SOA), contrary to widespread assumptions (Altshuller, 1983). Henze and Seinfeld (2006), using laboratory observations from Kroll et al. (2005, 2006), predicted that the formation of SOA from isoprene could significantly increase the modeled global SOA burden. Surratt et al. (2006, 2007, 2008) and Ng et al. (2008) showed that oligomerization and organosulfate formation are essential processes for SOA formation from isoprene. An additional channel was proposed by Volkamer et al. (2007), who suggested that glyoxal, an important photochemical product of isoprene, may be a major SOA precursor (Fu et al., 2008). The second breakthrough came from several measurement campaigns (PROPHET, GABRIEL, SOS 99) that probed isoprene photochemistry under low- $\text{NO}_x$  conditions that had not been achieved in laboratory experiments, even though most isoprene is thought to be oxidized in this chemical regime. These campaigns identified important compounds, including isoprene hydroperoxides (Crutzen et al., 2000; Warneke et al., 2001). They also revealed large discrepancies between simulated (Houweling et al., 1998; von Kuhlmann et al., 2003b) and observed  $\text{HO}_x$  (Creasey et al., 2001; Thornton et al., 2002; Tan et al., 2001; Sillman et al., 2002; Karl et al., 2006; Ren et al., 2008; Lelieveld et al., 2008; Butler et al., 2008) in regions of high biogenic loadings. Finally, in a series of theoretical studies, Dibble (2002, 2004a,b, 2005) challenged the common belief that isoprene photochemical cascade was well-understood under high  $\text{NO}_x$  by proposing that a significant fraction of the alkoxy radicals formed under these conditions could undergo isomerizations.

This thesis is organized around the interpretation of isoprene photooxidation experiments through models of various complexities. The experiments were carried out in the Caltech atmospheric chambers and the isoprene photooxidation was monitored over several photochemical generations by chemical ionization mass spectrometry (CIMS) (Crounse et al., 2006). This soft ionization technique is sensitive to a wide spectrum of oxygenated volatile organic compounds, which offers a unique opportunity to probe new parts of the isoprene photochemical cascade. Chapter 2 focuses on the high- $\text{NO}_x$  regime, with special emphasis on the yield and fate of isoprene nitrates. This class of compounds modulates the lifetime of  $\text{NO}_x$  in the atmosphere and consequently the formation of ozone (Horowitz et al., 1998). In particular, very long-lived organic nitrates originating from the photooxidation of isoprene nitrates are identified. This class of organic nitrates is important as it could contribute to the transport of reactive nitrogen to unpolluted regions (Perring et al., 2009; Horowitz et al., 1998; Wu et al., 2007; Duce et al., 2008). I also present evidence for alkoxy radicals isomerization that are qualitatively consistent with the conclusions of Dibble (2004a,b).

Chapter 3 focuses on the oxidation of isoprene under low- $\text{NO}_x$  conditions. Using isotopically-labelled reagents, I show that isoprene hydroperoxides are efficiently converted into epoxides after reacting with OH.

This suggests that isoprene is not a catalytic sink of  $\text{HO}_x$ , as was commonly assumed in major mechanisms (Horowitz et al., 1998), and may provide an important route for SOA formation under pristine conditions (Surratt et al., 2010; Froyd et al., 2010).

Under both high and low  $\text{NO}_x$  conditions, the oxidation of isoprene yields large amounts of formic and acetic acids. Formic and acetic acids are ubiquitous in the atmosphere but their budget is poorly understood (Chebbi and Carlier, 1996). Isoprene ozonolysis is thought to be a major source of both carboxylic acids (Ito et al., 2007; von Kuhlmann et al., 2003b) but cannot account for the large yield of carboxylic acids measured in the Caltech chamber experiments. This suggests the oxidation of isoprene or its photochemical products by OH may also yield carboxylic acids. In Chapter 4, I derive a detailed budget of formic and acetic acids primary and secondary sources using the chemical transport model GEOS-Chem (Bey et al., 2001). The model performances are tested using a broad suite of measurements from ground, air and space-based platforms. The model is found to perform well in regions with very large biogenic influences, consistent with the modern isotopic signature of carboxylic acids (Glasius et al., 2000; Glasius et al., 2001), but greatly underestimates formic and acetic acids in regions impacted by anthropogenic pollution and biomass burning. As concurrent measurements of carboxylic acids and organic aerosol exhibit a strong correlation, I suggest missing sources of carboxylic acids may be related to aerosol aging.

Because of the short atmospheric lifetime of isoprene ( $\sim$  hours), most research has been devoted to unravelling the impact of its photooxidation on the local photochemistry. However, isoprene photooxidation is also known to contribute to the formation of long-lived compounds (e.g. propanone nitrate, ozone) that can impact the chemical regime of the atmosphere far from isoprene source region (Stevenson et al., 2006). In Chapter 5, forward and adjoint sensitivity simulations are used to characterize several mechanisms by which the isoprene photochemical cascade impacts photochemistry on different scales. I focus this analysis on the importance of isoprene photooxidation for the poorly understood budget of tropical ozone (Bowman et al., 2009; Zhang et al., 2010).

## Chapter 2

# Isoprene photooxidation: new insights into the production of acids and organic nitrates<sup>1</sup>

---

<sup>1</sup>Adapted with permission from Paulot, F.; Crounse, J. D.; Kjaergaard, H. G.; Kroll, J. H.; Seinfeld, J. H. & Wennberg, P. O. Isoprene photooxidation: new insights into the production of acids and organic nitrates *Atmospheric Chemistry and Physics*, 2009, 9, 1479-1501 ©2009 by the authors.

## 2.1 Abstract

We describe a nearly explicit chemical mechanism for isoprene photooxidation guided by chamber studies that include time-resolved observation of an extensive suite of volatile compounds. We provide new constraints on the chemistry of the poorly-understood isoprene  $\delta$ -hydroxy channels, which account for more than one third of the total isoprene carbon flux and a larger fraction of the nitrate yields. We show that the *cis* branch dominates the chemistry of the  $\delta$ -hydroxy channel with less than 5% of the carbon following the *trans* branch. The modelled yield of isoprene nitrates is  $12 \pm 3\%$  with a large difference between the  $\delta$  and  $\beta$  branches. The oxidation of these nitrates releases about 50% of the  $\text{NO}_x$ . Methacrolein nitrates (modelled yield  $\simeq 15 \pm 3\%$  from methacrolein) and methylvinylketone nitrates (modelled yield  $\simeq 11 \pm 3\%$  yield from methylvinylketone) are also observed. Propanone nitrate, produced with a yield of 1% from isoprene, appears to be the longest-lived nitrate formed in the total oxidation of isoprene. We find a large molar yield of formic acid and suggest a novel mechanism leading to its formation from the organic nitrates. Finally, the most important features of this mechanism are summarized in a condensed scheme appropriate for use in global chemical transport models.

## 2.2 Introduction

Isoprene (2-methyl-1,3-butadiene,  $\text{C}_5\text{H}_8$ ) is a short-lived compound ( $\tau_{1/2} = 1\text{--}2$  hours) emitted by many deciduous trees during daylight hours. Between 0.5% and 2% of the carbon fixed by isoprene emitting plants is released to the atmosphere as isoprene (Harley et al., 1999), a flux accounting for about one third of the total anthropogenic and natural volatile organic compounds (VOC) emissions (Guenther et al., 2006). Isoprene plays a crucial role in determining the oxidative chemistry of the troposphere. Ozone levels in urban as well as in rural sites are impacted by the sequestration and transport of  $\text{NO}_x$  via formation of isoprene nitrates (Horowitz et al., 1998) and various isoprene-derived peroxyacylnitrates. Moreover, field (Claeys et al., 2004) and chamber studies (Kroll et al., 2006; Surratt et al., 2006) have recently shown that compounds formed in isoprene photooxidation, such as methylglyceric acid or methylerythritol, are ubiquitous in aerosol particles and may contribute significantly to the aerosol global burden (Henze and Seinfeld, 2006; van Donkelaar et al., 2007).

In the light of the potential for significant change in isoprene emissions due to climate and land use changes (Shallcross and Monks, 2000), studies have been made to predict the impact of altered isoprene

emissions on tropospheric ozone (Sanderson et al., 2003; Wiedinmyer et al., 2006). Von Kuhlmann (2004) and Fiore et al. (2005) note, however, that quantifying this impact is difficult due to uncertainties regarding: 1) the dependence of isoprene emissions on temperature (Harley et al., 2004) and CO<sub>2</sub> concentration (Rosenstiel et al., 2003); and 2) the isoprene photooxidation scheme, especially the yields and fates of isoprene nitrates.

In this study, we use negative chemical ionization mass spectrometry (CIMS) to monitor the photooxidation of isoprene. This technique greatly expands the range of compounds that can be observed during the photooxidation of isoprene and other hydrocarbons (Ng et al., 2008). Quantitative interpretation is challenging, however, because 1) calibration standards are not available for many of the compounds identified, and 2) mass analogs (compounds having the same mass) are not differentiated. Therefore the iterative development of a detailed mechanism is used to analyze the different signals and derive branching ratios and yields for the compounds identified.

First, we briefly describe the experiment emphasizing the calibration of CIMS measurements. Next, we report and identify the largest signals monitored by CIMS. We then discuss how these signals help constrain the development of the model emphasizing the  $\delta$ -hydroxy channels, the organic nitrate yield and fate, as well as some routes to organic acids. Finally we discuss the potential implications of our findings for tropospheric chemistry and present a reduced mechanism suitable for inclusion in chemical transport model.

## 2.3 Experiments

### 2.3.1 Experimental setting

The data of the present study were collected in the 28 m<sup>3</sup> Caltech atmospheric chamber, in an experiment similar to those described by Kroll et al. (2006). Initial concentrations of isoprene, NO and H<sub>2</sub>O<sub>2</sub> were 94 ppbv, 500 ppbv and 2.1 ppmv. The photolysis of H<sub>2</sub>O<sub>2</sub> constitutes the primary source of OH in the experiment. NO was added prior to isoprene so that the chamber was initially ozone free. The initial relative humidity was less than 6% and is assumed to be constant in this study. The temperature increased by about 5 degrees in the first one hundred minutes and remained constant thereafter at 296.5K. To simplify modelling, we consider this temperature to hold during the whole experiment.

Isoprene decay was monitored using GC-FID. Ozone was measured by UV absorption (Horiba) and NO and NO<sub>2</sub> (after conversion to NO) by chemiluminescence. The size distribution and the volume concentra-

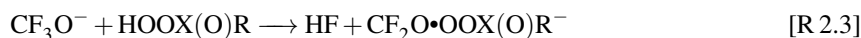
tion of secondary organic aerosol (SOA) were measured using a differential mobility analyzer (DMA, TSI 3760). Further details are available in Kroll et al. (2006).

### 2.3.2 Chemical ionization mass spectrometry (CIMS)

Gas-phase products were monitored using a novel CIMS technique (Crounse et al., 2006) with  $\text{CF}_3\text{O}^-$  as the reagent anion. Non-reactive with ozone, carbon dioxide and dioxygen (Huey et al., 1996),  $\text{CF}_3\text{O}^-$  is a versatile reagent ion suitable for the study of many oxygenated compounds. In general, two primary ionization pathways are observed:



A minor ionization pathway is observed for certain compounds:



In [R 2.3],  $\text{CF}_2\text{O}$  is incorporated into the original neutral molecule. Reaction has been observed for peroxy nitric acid (PNA) and for peroxy acetic acid (PAA). While [R 2.3] is not the major ionization pathway, in several cases it is useful for distinguishing certain mass analogs.

The dominant ionization pathway for an analyte depends mostly on the acidity (or fluoride affinity) of the neutral species (Amelynck et al., 2000; Crounse et al., 2006). Highly acidic compounds, such as nitric acid, only form the transfer product ion through reaction [R 2.1], while hydrogen peroxide and methylhydrogen peroxide (MHP) form only the cluster product ions through reaction [R 2.2]. Species with intermediate acidity (e.g., formic and acetic acids) form both the transfer and cluster products. Most of the VOC measured in this study follow reaction [R 2.2].

In this study, air was drawn from the chamber through a perfluoroalkoxy Teflon line of 1.2 m length and 0.635 cm outer diameter (OD), at a rate of 10 standard liters per minute (slm), and then sub-sampled into the CIMS flow tube using a critical orifice made of glass. The orifice constrained the flow from the chamber into the CIMS to be 145 standard cubic centimeters per minute (sccm). Upon introduction to the

CIMS flow tube, the chamber gas was diluted with 1760 sccm of UHP N<sub>2</sub> (99.999%) to a total pressure of 35 hPa, primarily to reduce the concentration of H<sub>2</sub>O<sub>2</sub> to manageable levels. The gas is expanded in a flow tube (17.8 cm, 2.54 cm OD Pyrex glass coated with a thin layer of Teflon (Fluoropel 801A, from Cytonix Corp.)) before being reacted with a transverse ion beam of the reagent anion (Fig. 1, Crounse et al., 2006).

Mass scans were conducted using a quadrupole mass spectrometer from  $m/z=18$  to  $m/z=275$  dwelling on each mass for 1s (giving a scan cycle of about  $4\frac{1}{2}$  min). The mass scans were repeated throughout the duration of the experiment (17 h). Zero scans were conducted periodically throughout the experiment by overfilling the critical orifice on the high pressure (chamber) side with UHP N<sub>2</sub>. In addition to providing instrumental backgrounds, the temporal response of the zero scans give insight into the strength of the interaction of the measured compounds with the equipment walls.

The instrumental background signals for most of the large molecular weight products produced in isoprene oxidation are very small (after the instrument has been sampling clean zero air for an extended period of time), which suggests that variations in instrumental background over the course of the experiment are not important for these signals. Compounds with a smaller molecular weight (e.g., formic and acetic acids) do have instrumental backgrounds, but the level of the instrumental background is small relative to the signal generated in the isoprene oxidation experiment (more than 10 times smaller), so ignoring instrumental background changes over the course of the experiment for these species does not introduce a substantial error.

### 2.3.3 Calibration

The concentration of a compound X, whose product ion is detected at  $m/z = p$ , is calculated through:

$$[X]_{\text{ppbv}} = \frac{\widehat{\text{Signal}(m/z = p)}}{c_X} \quad (2.1)$$

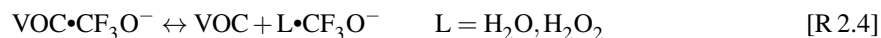
where  $\widehat{\text{Signal}(m/z=p)}$  is the normalized signal associated with X (see Appendix A.2.1) and  $c_X$  is the calibration constant for the compound X in ppbv<sup>-1</sup>.

In many cases, no standard is readily available and no experimental determination of  $c_X$  can be made. In such cases, we assume that  $c_X$  is related to the thermal capture rate ( $k_X$ ) and the binding energy of the cluster.  $k_X$  is estimated from the Langevin-Gioumoussis-Stevenson-based collision rate. We use the empirical approach developed by Su and Chesnavich (1982) to calculate  $k_X$  from the dipole moment ( $\mu_X$ ) and the polarizability ( $\alpha_X$ ) of X.



In the absence of experimental determinations of  $\mu_X$  and  $\alpha_X$ , we use quantum chemical calculations to estimate them. The lowest energy conformers of the molecules are found with the conformer searches method within the Spartan06 quantum package (Wavefunction Inc., 2006) at the B3LYP/6-31G(d) level of theory. The dipole moments and static polarizabilities are then calculated for the optimized geometries at the same level of theory. When a molecule has several low energy conformers, a thermally-weighted average of their reaction rate coefficients is used for  $k_X$  (see Appendix A.2.2 for details).

The sensitivity of the instrument to X also depends on the binding energy between X and the reagent anion as well as the nature of the reagent anion. In the presence of abundant ligands (L) such as water or hydrogen peroxide, the sensitivity of the CIMS to some VOC is modified through two different processes: 1)  $\text{CF}_3\text{O}^-\bullet\text{L}$  may react faster with X than the bare  $\text{CF}_3\text{O}^-$  anion because ligand exchange reactions can stabilize the product ion to a greater extent; 2) the cluster  $\text{CF}_3\text{O}^-\bullet\text{L}$  may be sufficiently stable leading to a lower sensitivity at higher L mixing ratio due to ligand exchange:



For example, Crounse et al. (2006) reported that the sensitivity to methylhydroperoxide (MHP) decreases with the water vapor mixing ratio due to [R 2.4].

In general large molecules featuring several functional groups (peroxide, nitrooxy, alcohol, carbonyl) exhibit only a weak dependence on the amount of water. Therefore, we neglect the binding energy effect in this study and take:

$$c_X = \frac{k_X}{k_{\text{HNO}_3}} c_{\text{HNO}_3} \quad (2.2)$$

where  $k_{\text{HNO}_3} = 1.93 \times 10^{-9} \text{ cm}^3 \text{ molec}^{-1} \text{ s}^{-1}$  is calculated using the experimental dipole and polarizability of nitric acid, and  $c_{\text{HNO}_3}$  is the sensitivity to nitric acid for typical conditions where the flow tube was operated (water vapor mixing ratio = 150 ppmv).  $\text{HNO}_3$  is used as the calibration reference because of the weak dependence of the sensitivity with water and its thorough laboratory study (Huey et al., 1996; Amelynck et al., 2000; Crounse et al., 2006).

When several compounds are observed at the same  $m/z$ , we report the signal calibrated with a reference calibration  $c_{\text{ref}}$  and the modeled concentrations of each compound  $X_i$  multiplied by  $s_{X_i} = c_{X_i}/c_{\text{ref}}$ , so that one can compare measured signal with the prediction of the mechanism. The predicted concentration of a specific compound is therefore  $[X_i]_{\text{calibrated model}}/s_{X_i}$ .

Finally, molecules such as isoprene, methacrolein (MACR), methylvinylketone (MVK) or peroxyacylni-

trate (PAN) are not observed with our measurement technique despite their relatively large dipole moment. More generally, the method is not sensitive to simple aldehydes, alcohols, and ketones, presumably due to the low binding energy of these compounds with  $\text{CF}_3\text{O}^-$ .

## 2.4 Results

After the photolysis lights are turned on, isoprene decays with a half life of  $\sim 20$  min (Fig. A.3). Several inorganic markers of the chemical evolution of the system can be monitored by CIMS (Table 2.1 and Fig. A.4). Nitrous acid (transfer at  $m/z = 66$ , cluster at  $m/z = 132$ , Fig. A.4), peaks after 50 min and has mostly disappeared after 150 min. HONO is associated with a very large concentration of NO which defines our first chemical regime ( $0 \leq t \leq 150$  min). Given the high concentration of NO, little ozone is formed and isoprene photooxidation proceeds almost entirely through OH addition. Pernitric acid (PNA, transfer at  $m/z = 98$ , cluster at  $m/z = 164$ , Fig. A.4) grows steadily, peaking at  $\sim 600$  minutes. Given the sensitivity of PNA to the ratio  $\text{HO}_2:\text{NO}_2$ , the time when PNA reaches its maximum indicates the transition from a  $\text{NO}_x$  (Regime 2:  $150 \leq t \leq 600$  min) to a  $\text{HO}_x$ -dominated chemistry (Regime 3:  $t \geq 600$  min). In this study, we focus on the  $\text{NO}_x$ -dominated chemistry, limiting our discussion to the first and second regimes. Studies of low  $\text{NO}_x$  chemistry will follow in a separate manuscript. Nitric acid (transfer at  $m/z = 82$ ) grows steadily during the experiment to reach  $\sim 430$  ppbv at the end of the experiment. We estimate dinitrogen pentoxide profile by removing the nitric acid contribution to the  $\text{NO}_3^-$  ( $m/z = 62$ ) temporal signal (Huey et al., 1996). The corrected signal exhibits a shape similar to PNA, peaking after  $\sim 500$  min at  $\sim 3$  ppbv.

In Table 2.1 and Figs. 2.2 to 2.15, we report the main signals measured by CIMS, the chemical formula of the associated compounds, as well as their most likely identification using mechanistic considerations. To our knowledge, this is the first time that the temporal evolutions of isoprene nitrates (cluster at  $m/z = 232$ , Fig. 2.9) and methacrolein/methylvinylketone nitrates (cluster at  $m/z = 234$ , Fig. 2.13) have been monitored. We also observe the formation of small carboxylic acids such as formic and acetic acid, which can be clearly identified given that they undergo both [R 2.1] and [R 2.2]. This specificity helps identify larger acidic compounds such as (Z)-2/3-methyl-4-oxobut-2-enoic acid (MOBA): the signal recorded at  $m/z = 199$  (cluster) correlates with the associated transfer at  $m/z = 133$  ( $\rho = 0.93$  for the first 400 min). This also allows differentiation of certain mass analogs, e.g., the contribution of acetic acid cluster to  $m/z = 145$  can be removed using its experimental ratio between transfer and cluster. The residual is the cluster of glycolaldehyde ( $m/z = 145$ ).

Unfortunately most mass analogs, such as isoprene nitrates ( $m/z = 232$ ) are positional isomers, and thus cannot be specifically identified using this approach, thus precluding the derivation of their concentrations. To overcome this difficulty, a detailed mechanism has been developed iteratively using the constraints of organic and inorganic signals in association with previously identified mechanisms (Appendix A.1).

## 2.5 Discussion

### 2.5.1 $\delta$ -hydroxy channels

Under chamber experimental conditions, isoprene photooxidation proceeds primarily through the addition of OH to the two double bonds (position 1, 2, 3 and 4 in Fig. 2.1). In the following we will denote the different channels by the couple (i,j), where i and j refer, respectively, to the carbon on which the OH and O<sub>2</sub> addition occurs. Besides  $\beta$ -hydroxy peroxy radicals (1,2) and (4,3), additions to positions 1 and 4 can lead, after addition of O<sub>2</sub>, to four  $\delta$ -hydroxy peroxy radicals (Sprengnether et al., 2002), referred to as Z<sub>1,4</sub>, E<sub>1,4</sub>, Z<sub>4,1</sub>, E<sub>4,1</sub>. The branching ratio between these different channels remain uncertain (cf. Section A.3.1). Here we use a combination of theoretical (Lei et al., 2000) and experimental results (Sprengnether et al., 2002; this study) as constraints:  $Y_{1,2} \simeq 41\%$ ,  $Y_{1,4} \simeq 15\%$ ,  $Y_{2,1} \simeq 2\%$ ,  $Y_{4,3} \simeq 23\%$ ,  $Y_{4,1} \simeq 14\%$ ,  $Y_{3,4} \simeq 5\%$ .

As most studies of isoprene photooxidation have focused on the main decomposition channels ((1,2) and (4,3)) yielding MACR and MVK (Paulson et al., 1992; Sprengnether et al., 2002; Karl et al., 2006), the  $\delta$ -hydroxy channels, which account for about 30% of the carbon and a large fraction of the organic nitrates, remain poorly constrained. A large number of products originating from the  $\delta$ -hydroxy channels can be monitored by CIMS, which motivates our emphasis on their chemistry.

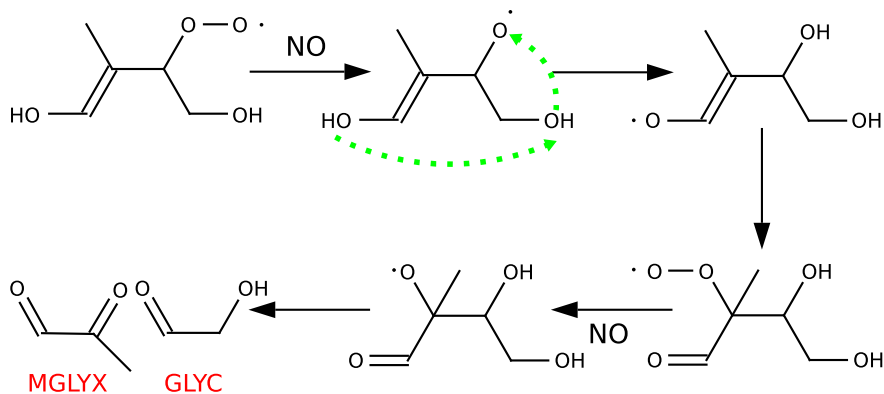
#### 2.5.1.1 Chemistry of the $\delta$ -hydroxy channels

Z<sub>1,4</sub> The reaction of the peroxy radical with NO yields an alkoxy radical which undergoes a  $\delta_1^5$  isomerization (Atkinson, 1997b; Park et al., 2004). The resulting  $\beta$ -hydroxy allyl radical can then react with O<sub>2</sub> and form a 1,4-hydroxycarbonyl, (2Z)-4-hydroxy-2-methylbut-2-enal (HC5 Z(1,4)), detected as a cluster at  $m/z = 185$  (Fig. 2.2). The detection of its <sup>13</sup>C isotope at  $m/z = 186$  supports the attribution of the signal to HC5. Formation of glycolaldehyde (GLYC cluster at  $m/z = 145$ , Fig. 2.3) and methylglyoxal (MGLYX) at this stage of the photooxidation have also been described by Dibble (2004a,b). This reaction is based on the stabilization of the alkoxy radical, reproduced below, through a double

hydrogen bond which prevents its decomposition while enhancing a double hydrogen shift involving the hydrogen of the alcohol groups.

OH can add to the HC5 Z(1,4) double bond (channels ② and ③ in Fig. 2.1), abstract the aldehydic hydrogen (channel ④) or the hydrogen  $\alpha$  to the alcohol (channel ①). Addition on position ② is expected to yield GLYC and MGLYX. The signal detected at mass  $m/z = 217$  (Fig. 2.4) suggests the existence of channel ③. In this pathway the alkoxy radical formed after addition of OH on position 3 is stabilized enough by a double hydrogen bond, so that reaction of  $O_2$  becomes competitive with unimolecular decomposition. This mechanism yields 2,4-dihydroxy-2-methyl-3-oxobutanal (DHMOB (1,4)).

The signal recorded at  $m/z = 199$  correlates well ( $\rho = 0.93$  for the first 400 min) with the one at  $m/z = 133$ . This correlation between a cluster and a transfer is usually associated with an acid functional group (see Section 2.3.2), which supports the formation of (Z)-2-methyl-4-oxobut-2-enoic acid (MOBA Z(1,4)), a five-carbon acid, from HC5 through channel ④ (Fig. 2.5).



$E_{1,4}$  The isomerization of the initial alkoxy radical can yield 2-(hydroxymethyl)prop-2-enal (HMPL) after reaction with  $O_2$ . A second isomerization would yield 4-hydroxy-3-oxobutanal (HOBL) or 4-hydroxy-3-(hydroxymethyl)but-2-enal (MHBL). The further photooxidation of HMPL and MHBL is expected to yield mainly dihydroxypropanone (DHPN), whose  $CF_3O^-$  cluster is observed at  $m/z = 175$  (Fig. 2.6), and hydroxyoxopropanal (HOPL, cluster at  $m/z = 173$  with pyruvic acid).

The reaction of OH with HOPL is expected to yield an acylperoxy radical which can further react with  $NO_2$ , yielding a PAN-like compound, 3-hydroxy-oxo-peroxyacetyl nitrate (PAN 250). This compound may be associated with the signal monitored at  $m/z = 250$ , although the identification is not certain.

Signals originating from the E branch are much smaller than those originating from its Z counterpart. This suggests a large asymmetry between the E and Z  $\delta$ -hydroxy channels.

Due to the similarity between the (4,1) and (1,4) branch, we only address the major differences.

$Z_{4,1}$  Hydroxyacetone (HACET, cluster at  $m/z = 159$ , Fig. 2.7) and glyoxal (GLYX) can be formed from the decomposition of HC5 Z(4,1) and HC5 E(4,1). Similar to the formation mechanism of DHMOB (1,4), the addition of OH to the less preferred position of HC5 Z(4,1) (and E(4,1)) is expected to yield 3,4-dihydroxy-3-methyl-2-oxobutanal, referred to as DHMOB (4,1) (Fig. 2.4).

$E_{4,1}$  The alkoxy radical configuration prevents  $\delta_1^5$  isomerization [R A.8] and slows down its decomposition [R A.6]. Therefore it is expected to react entirely with  $O_2$  [R A.7] to yield a HC5 isomer (HC5 E(4,1)).

### 2.5.1.2 Consequences

The observations of numerous compounds formed at different stages of  $\delta$ -hydroxy pathways lead to several inferences about the general mechanism:

#### Channel asymmetry

If an equal partitioning of the carbon is assumed between  $E_{1,4}$  and  $Z_{1,4}$ , as suggested by the theoretical work of Dibble (2002), the concentrations of both HOPL and DHPN are greatly overestimated while the concentrations of  $HC5=HC5\ Z(1,4)+HC5\ E(4,1)+HC5\ Z(4,1)$  and its products (DHMOB, MOBA) are underestimated. Good agreement with the observations is obtained when  $\frac{Y_{E_{1,4}}}{Y_{Z_{1,4}}} = \frac{15}{85}$ .

An additional piece of evidence suggesting that little flux of carbon occurs through  $E_{1,4}$  is the low signal recorded at  $m/z=201$ , which should include 3-methylhydroxy-4-hydroxy-butanal (MHBL) based on its structural similarity with HC5. We use  $k_{OH} = 6.13 \times 10^{-12} \text{ cm}^3 \text{ molec}^{-1} \text{ s}^{-1}$  for DHPN (25% more than the SAR estimate) and  $k_{OH} = 2.23 \times 10^{-11} \text{ cm}^3 \text{ molec}^{-1} \text{ s}^{-1}$  for HOPL in order to properly capture their measured temporal profiles (Fig. 2.6).

The asymmetry between Z/E isomers contradicts the conclusions drawn from quantum mechanical calculations (Dibble, 2002) as well as the assumption made by most kinetic models of isoprene photooxidation (Paulson and Seinfeld, 1992; Fan and Zhang, 2004). The discrepancy with quantum mechanical calculations may be related to a difference in the reaction of the *cis/trans* radical with  $O_2$ . The radicals are formed with approximately 40 kcal/mol excess energy. The minimum isomerization barrier is estimated to be about 15 kcal/mol (Dibble, 2002). Therefore, assuming a collision

stabilization of  $100 \text{ cm}^{-1} \text{ collision}^{-1}$ , the radicals undergo nearly 100 collisions (20 with  $\text{O}_2$ ) before they are cooled below the isomerization barrier. If, based on reported rate coefficients for  $\text{R}^\bullet + \text{O}_2$  (Atkinson et al., 2006), one reaction among ten is assumed to be reactive, peroxyradicals are likely to be formed before the isomers are cooled below the isomerization barrier. Therefore, the equilibrium may be shifted if the reaction of the *trans* radical with  $\text{O}_2$  is faster than the reaction of the *cis* radical. Measurements made with reduced partial pressure of  $\text{O}_2$  could test this hypothesis. The *cis* and *trans* forms can also be interconverted later in the photooxidation by the  $\delta_1^5$  isomerization. Therefore the observed discrepancy may also be attributed to the additional stability of the *cis*  $\beta$ -hydroxy allyl radical provided by the interaction between the alcohol groups.

### Evidence for Dibble's mechanism

Both HACET (Fig. 2.7) and GLYC (Fig. 2.3) exhibit a very prompt source. To our knowledge, the mechanism proposed by Dibble (2004a,b) and reproduced in Section 2.5.1.1 is the only mechanism able to yield both compounds after a single OH reaction. For GLYC, we set the branching ratio quenching:thermalization to 7:3 in good agreement with the theoretical estimate (Dibble, 2004b). The same branching ratio was applied to capture the prompt formation of HACET from the  $\text{Z}_{4,1}$  branch. Theoretical considerations do not support such a large hydroxyacetone formation (Dibble, 2004b). The hydroxyacetone rate constant with OH is set to  $k_{\text{OH}} = 5.98 \times 10^{-12} \text{ cm}^3 \text{ molec}^{-1} \text{ s}^{-1}$  (Dillon et al., 2006) and the rate constant of glycolaldehyde with OH is set to  $k_{\text{OH}} = 8 \times 10^{-12} \text{ cm}^3 \text{ molec}^{-1} \text{ s}^{-1}$  (Karunanandan et al., 2007).

### HC5 chemistry

HC5 (Fig. 2.2) exhibits a very fast decay consistent with a reaction rate coefficient with OH similar to isoprene ( $1.0\text{--}1.2 \times 10^{-10} \text{ cm}^3 \text{ molec}^{-1} \text{ s}^{-1}$ ). This estimate is consistent with the fastest rate recently derived by Baker et al. (2005) and  $\sim 80\%$  greater than the SAR estimate ( $k_{\text{OH}}^{\text{SAR}} = 6.82 \times 10^{-11} \text{ cm}^3 \text{ molec}^{-1} \text{ s}^{-1}$  or  $7.9 \times 10^{-11} \text{ cm}^3 \text{ molec}^{-1} \text{ s}^{-1}$  with the correction from Bethel et al. (2001); Papagni et al. (2001). This discrepancy can be partly explained by the effect of the alcohol group  $\alpha$  of the double bond which enhances the addition of OH (Papagni et al., 2001). The large measured yield of MOBA=MOBA Z(1,4)+MOBA Z(4,1) (Fig. 2.5) also suggests that the abstraction of the aldehydic hydrogen (channel ④) is faster than predicted, possibly related to a long distance interaction between the alcohol group and the carbonyl group (Neeb, 2000).

Experimental evidence for the formation of 3-methylfuran (3-MF) from the  $\text{Z}_{1,4}$  and  $\text{Z}_{4,1}$  branches

have been reported (Tuazon and Atkinson, 1990). However the mechanism remains unclear with evidence for both heterogeneous formation (Baker et al., 2005; Dibble, 2007; Atkinson et al., 2008) from HC5 and homogeneous formation from its parent alkoxy (Francisco-Marquez et al., 2005).

In our model, 3-MF yield is set to 4.5% based on experimental results (Atkinson et al., 1989; Paulson et al., 1992) and formed from the parent alkoxy of HC5. As a result, 37% of the alkoxyradical formed in the  $Z_{1,4}$  and  $Z_{4,1}$  branches must decompose to 3-MF in order to match the experimental yield. We can not rule out 3-MF heterogeneous formation. We note, however, that if heterogeneous processes yield 3-MF, the calculated HC5 yield would be  $\sim 20\%$  higher. Moreover, the decay rate required to match the HC5 profile would likely be faster than observed. 3-MF formation mechanism has little impact on the conclusions of this paper but has significant consequences for atmospheric chemistry. Indeed if formed through heterogeneous processes, 3-MF yield is likely to be smaller than determined in atmospheric chambers. Further work is clearly required to quantify this issue and determine the products of 3-MF photooxidation.

We note, finally, that the observation of large yields for HC5 and 3-MF are consistent with an asymmetry between the E and Z branches. If the branching ratio E:Z were close to 1:1, the fraction of peroxy radical  $Z_{1,4}$  and  $Z_{4,1}$  required to decompose to 3-MF would be 62% and the yield of HC5 only 6.1%. This is inconsistent with the yields previously reported (Baker et al., 2005).

## 2.5.2 Organic nitrates

The observation of the organic nitrates of isoprene and MVK/MACR, as well as some of the products of their photooxidation (Figs. 2.8 to 2.11), provides constraints on the isoprene nitrate yields, their lifetimes and the amount of  $\text{NO}_x$  recycled through the first stage of their photooxidation, as well as through their lifetimes.

### 2.5.2.1 $\delta$ -hydroxy isoprene nitrates

The fate of the  $\delta$ -hydroxy isoprene nitrates (1,4) and (4,1), respectively, ISOPN (1,4) and ISOPN (4,1), can be followed through their degradation products (Fig. 2.8): ethanal nitrate (ETHLN) monitored at  $m/z = 190$  (Fig. 2.10) and propanone nitrate (PROPNN) at  $m/z = 204$  (Fig. 2.11).

PROPNN features a very prompt source, which requires a fast reaction rate coefficient of ISOPN(4,1) with OH:  $k_{\text{OH}}^{\text{ISOPN}(4,1)} = 9.5 \times 10^{-11} \text{ cm}^3 \text{ molec}^{-1} \text{ s}^{-1}$ . This is  $\sim 45\%$  faster than SAR and suggests an inadequate parameterization of the effects of nitroxy groups on the reactivity of the double bond (Neeb, 2000).

No significant signal is observed at  $m/z = 230$ , confirming that the abstraction of the hydrogen in  $\alpha$  of the alcohol of ISOPN is negligible compared to addition on the double bond.

SAR suggests that ISOPN(1,4) and ISOPN(4,1) are similarly short-lived with respect to OH. This is consistent with the prompt source of ETHLN (Fig. 2.10), a product of the oxidation of ISOPN (1,4) (Fig. 2.8). The use of the primary nitrate photolysis rate (see A.1.3) and SAR rate estimate for the reaction ETHLN + OH underpredicts its decay. To match the measured profile (Fig. 2.10), we take  $k_{\text{OH}} = 1 \times 10^{-11} \text{ cm}^3 \text{ molec}^{-1} \text{ s}^{-1}$ , three times faster than the SAR estimate. If the ETHLN photolysis rate is larger than estimated ( $J \sim 4 \times 10^{-7} \text{ s}^{-1}$  using  $1\text{-C}_4\text{H}_9\text{ONO}_2$ ), the ETHLN reaction rate coefficient with OH would be commensurately slower.

$\text{NO}_x$  recycling from the (4,1) branch is  $\sim 70\%$  based on the measured ratio PROPNN: dihydroxybutanone (DHB, cluster at  $m/z = 189$ ). The reaction rate coefficient of DHB with OH is estimated to be  $1.3 \times 10^{-11} \text{ cm}^3 \text{ molec}^{-1} \text{ s}^{-1}$  or 60% of SAR (Fig. 2.12).

The yield of ETHLN is substantially overestimated if the yield of the reaction  $\text{RC}^*\text{OH} + \text{O}_2 \rightarrow \text{RCO} + \text{HO}_2$  is 100%. As will be discussed further in Section 2.5.3, we suggest that unimolecular decomposition of the  $\alpha$ -hydroxyperoxy radical from ISOPN(1,4) yields formic acid, resolving this discrepancy.

### 2.5.2.2 $\beta$ -hydroxy isoprene nitrates

To capture the decay of the  $m/z = 232$  signal requires that  $\beta$ -hydroxy isoprene nitrates (ISOPN (1,2), (2,1), (4,3) and (3,4)) be much longer-lived than  $\delta$ -hydroxy isoprene nitrates (ISOPN (1,4) and (4,1)). Unfortunately, the products of their photooxidation have multiple other sources, precluding a direct derivation of their lifetime. For instance methylvinylketone nitrate (MVKN) and methacrolein nitrate (MACRN) are also formed from MVK and MACR with similar rates. The evolution of the  $m/z = 232$  signal can be captured when the SAR chemical rates for these nitrates are reduced by 20%.

The reaction of the isoprene nitrate with ozone is included for ISOPN (1,2) and ISOPN (4,3), because their long lifetimes allow them to encounter high concentrations of ozone in the chamber (Fig. A.2). We do not observe the formation of 3 hydroxy-2-nitrooxy-2-methyl propanoic acid (no correlation between  $m/z = 184$  and  $m/z = 250$ ). Therefore, we use a simplified version of the ozonolysis products proposed by (Giacopelli et al., 2005) assuming that this reaction yields only MACRN and MVKN. These reactions contribute significantly to the total yield of MVKN and MACRN in this experiment.

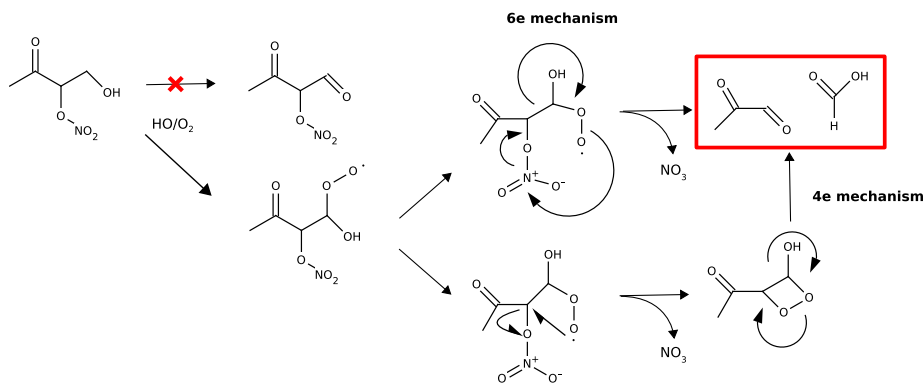


### 2.5.2.3 Methacrolein and methylvinylketone hydroxynitrates

MVKN and MACRN are monitored through their clusters with  $\text{CF}_3\text{O}^-$  at  $m/z = 234$  (Fig. 2.13).

MACRN features an aldehyde group which suggests a much faster decomposition than MVKN. This is confirmed by the profile of hydroxyacetone which does not exhibit any significant late source. As a result, the third regime of the experiment is dominated by MVKN and its reaction rate coefficient with OH can be estimated:  $k_{\text{OH}}^{\text{MVKN}} = 2.8 \times 10^{-12} \text{ cm}^3 \text{ molec}^{-1} \text{ s}^{-1}$ . The yield of MVKN can be constrained using GLYC profile since MVK is its major source:  $\alpha_{\text{MVK}} = (11 \pm 3)\%$ . Applying the same approach to MACR/MACRN/HACET is more complicated, since hydroxyacetone has many more sources than glycolaldehyde (Fig. 2.7). We find that a yield of MACRN of 15% and a reaction rate coefficient with OH of  $5 \times 10^{-11} \text{ cm}^3 \text{ molec}^{-1} \text{ s}^{-1}$  best match the peak time of  $m/z = 234$ . These values are consistent with the study of Chuong and Stevens (2004).

The abstraction of the hydrogen  $\alpha$  to the alcohol in MACRN, MVKN and MVKN (m) is expected to yield dicarbonyl nitrates. We expect CIMS to be sensitive to this class of compounds, since we are able to measure compounds featuring a carbonyl in  $\beta$  of the nitrate group, such as PROPNN or ETHLN. Since  $m/z=232$  only features early stages compounds, isoprene nitrates, there is no evidence for the formation of dicarbonyl nitrates. Recent theoretical studies (Peeters et al., 2001; Hermans et al., 2005) show that primary  $\alpha$ -hydroxy-alkylperoxy radicals can be sufficiently stabilized to undergo reactions with NO and yield formic acid. Nevertheless the photooxidation of MVKN occurs in a mostly low- $\text{NO}_x$  environment which suggests that  $\alpha$ -hydroxy-alkylperoxy radicals may undergo an intramolecular decomposition to yield a carboxylic acid and the nitrate radical. Such a reaction may involve a four-or six- $e^-$  mechanism.



Finally, the  $m/z = 234$  signal features a prompt source which can not be accounted for by MVK or MACR nor by the  $\beta$ -hydroxy isoprene nitrates, which have a similar lifetime with respect to OH. Conversely

ISOPN (1,4) is very short-lived and a MVKN (m) yield of 10–15% enables to capture this feature (Fig. 2.13).

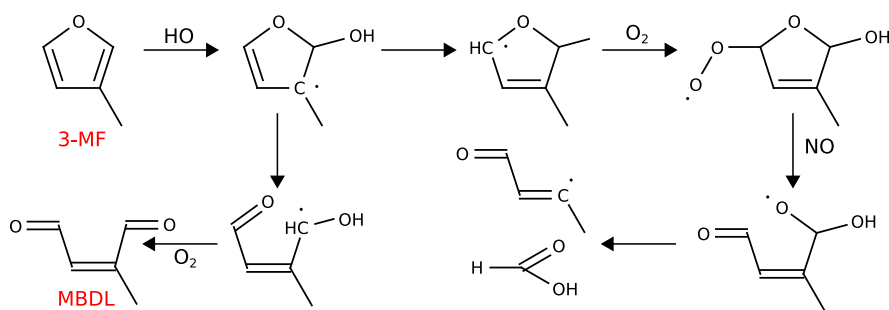
## 2.5.3 Carboxylic acids

### 2.5.3.1 Formic acid

Formic acid is detected as a cluster ( $m/z = 131$ ) and a transfer ( $m/z = 65$ ) with about equal sensitivity. At the  $\text{NO}_x$  titration ( $\sim 600$  min), a molar yield of about  $(10 \pm 3)\%$  is obtained (Fig. 2.14).

The measured profile of formic acid features the three characteristic chemical regimes of this experiment (see 2.4):

**First regime:** A very early source of formic acid is noticeable (Fig. 2.14). Several observations suggest that formic acid may be formed from an intramolecular decomposition of ISOPN (1,4) similar to the one described for MVKN earlier: 1) This source is absent from the experiments performed in the absence of  $\text{NO}_x$ , 2) the early formic acid profile correlates very well with the propanone nitrate which originates from ISOPN (4,1) decomposition, 3) ETHNL would be largely overevaluated in the absence of other decomposition channels for ISOPN (1,4). Matching the ETHNL profile (Fig. 2.10) results in a branching ratio for formic acid to ETHNL of 3:1. ISOPN(2,1) may yield acetic acid, but is not included since its contribution would be negligible. Bierbach et al. (1995) report 4-oxo-pentenal as the major product of the photooxidation of 2-methylfuran in the absence of  $\text{NO}_x$ , while formic acid accounts for about 6%. We are unaware of any study of the photooxidation of 3-MF in the presence of  $\text{NO}_x$ . Since the reaction rate coefficient of methylfuran with OH is similar to that derived for ISOPN (1,4) and (4,1), its photooxidation may contribute to the early sources of formic acid.



**Second regime:** Butkovskaya et al. (2006a,b) report a formic acid yield from the photooxidation of GLYC (HAC) of 18% (respectively, 7%). The formation of formic acid from the decomposition of

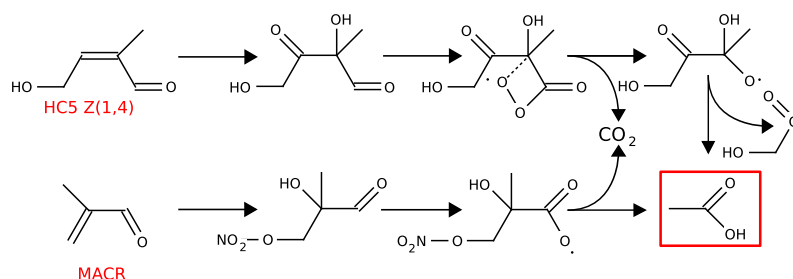
MVKN described in Section 2.5.2.3 also plays a minor role in this regime.

**Third regime (not shown):** As  $\text{NO}_x$  becomes limiting, hydroxymethyl hydroperoxide (HMHP) formation from the reaction of  $\text{CH}_2\text{OO}$  with water is enhanced. HMHP can account for most of the late formation of formic acid through its reaction with OH and its photolysis. A large additional source is missing, however, in the mechanism. Heterogeneous decomposition of HMHP (Neeb et al., 1997) and aerosol processes (Walser et al., 2007) are likely to account for this missing source. An upper limit for the strength of the aerosol source can be estimated from the decrease of the aerosol volume  $-2.5 \mu\text{m}^3/\text{cm}^3$ , which would represent a release of 2.6 ppbv  $\text{C}=\text{O}$  in the chamber, assuming a density of  $1.25 \text{ g}/\text{cm}^3$  (Kroll et al., 2006). Since the same phenomenon is observed for acetic acid (Fig. 2.15), most likely both  $\text{HO}_x$ -dominated VOC oxidation as well as organic aerosol oxidation are needed to explain the observed increase in formic and acetic acid in the third regime.

### 2.5.3.2 Acetic acid

The production of acetic acid (Fig. 2.15) occurs primarily through the oxidation of hydroxyacetone as described by (Butkovskaya et al., 2006b). Additional routes include direct formation from  $\text{CH}_3\text{CHO} + \text{OH}$  (Cameron et al., 2002) as well as  $\text{CH}_3\text{C}(\text{O})\text{OO} + \text{HO}_2$  following Reaction [R A.4].

Two additional minor routes are hypothesized: 1) decomposition of MACRN (m), 2) decomposition of DHMOB (1,4) ( $m/z = 217$ ), inspired by the mechanism proposed by Butkovskaya et al. (2006b,a). Following their analysis, we assume a 37% acetic molar yield, the remaining falling apart as  $\text{CO}_2$  and hydroxybutane-2,3-dione ( $m/z=187$ ).



### 2.5.3.3 MOBA

MOBA, the class of five-carbon acids identified at  $m/z = 183$  and  $199$  in Section 2.5.1, can react with OH and ozone under the chamber conditions. The slow decay of the signal suggests that its reactivity is dominated by ozone in the chamber and that the acid group significantly hinders the addition of OH onto the double bond. A good match is obtained by setting  $k_{\text{OH}}$  equal to  $3 \times 10^{-12} \text{ cm}^3 \text{ molec}^{-1} \text{ s}^{-1}$  ( $F_{\text{COOH}} = 0.1$  in terms of SAR) and  $k_{\text{O}_3} = 2 \times 10^{-17} \text{ cm}^3 \text{ molec}^{-1} \text{ s}^{-1}$ .

Little signal is observed at  $m/z = 93$ , which suggests no or minor formation of oxoacetic acid. This suggests that the reaction with OH does not conserve the acid group, which is likely lost as  $\text{CO}_2$ . Pyruvic acid can be expected to be a major product of MOBA ozonolysis.

### 2.5.3.4 Pyruvic acid

Pyruvic acid is a precursor for glyoxylic and oxalic acids, two carboxylic acids detected in the aerosol phase (Carlton et al., 2006). It is observed as a cluster at  $m/z = 173$  in association with HOPL, a product of DHPL photooxidation. Due to its stickiness to the walls of the flow tube, the theoretical calibration is expected to largely overestimate our sensitivity to this compound. The yield of pyruvic acid after 600 min is  $2 \pm 1\%$ .

Qualitatively, the major sources of pyruvic acid are expected to include (heterogeneous) hydrolysis of the Criegee intermediate produced in the ozonolysis of MVK and MOBA as well as the decomposition of MVKN (m) following the mechanism presented in Section 2.5.2.3.

## 2.5.4 Atmospheric relevance

### 2.5.4.1 Fate of organic nitrogen

The formation of organic nitrates, and more specifically isoprene nitrates, plays an important role in determining the amount of  $\text{NO}_x$ , and thus ozone production, in many environments.

The observation of isoprene nitrate clusters with  $\text{CF}_3\text{O}^-$ , as well as some of the products of their photooxidation, provides constraints on the isoprene nitrate yields, the amount of  $\text{NO}_x$  recycled through the first stage of their photooxidation, and their lifetimes. These three parameters are necessary to accurately assess the influence of isoprene photooxidation on atmospheric chemistry.

**Yield:** Previous estimates for the isoprene nitrate yield,  $\alpha$ , span a very large range. Chen et al. (1998) reported an overall yield of 4.4%, Chuong and Stevens (2002), 15% using an indirect method, Sprengnether

et al. (2002), 12%, and Patchen et al. (2007), 7% at 130 hPa. Using experimental yields collected for compounds similar to isoprene, Giacomelli et al. (2005) estimated the nitrate yield of the  $\beta$  and  $\delta$ -hydroxy isoprene nitrates to be respectively 5.5% for the former and 15% for the later, for an overall yield of 8.6%. Since organic nitrates sequester  $\text{NO}_x$ , such a large variation in the estimated yields has profound implications to the assessments of ozone production caused by isoprene photooxidation (von Kuhlmann et al., 2004; Fiore et al., 2005; Horowitz et al., 2007).

We report a yield of  $(11.7 \pm 3)\%$  with a large discrepancy between the yields of the nitrates originating from  $\delta$  ( $\simeq 24\%$ ) and  $\beta$ -hydroxy channels ( $\simeq 6.7\%$ ). We emphasize, however, that we derived a total yield rather than specific branching ratios so that the specific organic nitrate yields are affected by the choice of the initial  $\beta$ : $\delta$ -hydroxy channel ratio (see A.3.1). Nevertheless, the discrepancy between  $\delta$ -hydroxy channels and  $\beta$ -hydroxy channels is a reliable feature, with the  $\delta$ -hydroxy isoprene nitrates accounting for about 60% of the total isoprene nitrate yield. Giacomelli et al. (2005) suggested this behaviour previously using measurement collected for similar compounds.

**Lifetime:** The efficiency of both  $\text{NO}_x$  transport and removal through organic nitrates is related to their lifetimes. The transport of isoprene-nitrates and their alkylnitrate degradation products is of special importance since it is thought to be a major source of  $\text{NO}_x$  in rural areas (Horowitz et al., 1998). In this  $\text{NO}_x$ -limited environment, the release of  $\text{NO}_x$  through their decomposition would greatly influence  $\text{O}_3$  production. In the absence of experimental data, Giacomelli et al. (2005) estimated using Kwok’s SAR that the  $\delta$ -hydroxy isoprene nitrates should be significantly shorter-lived than the  $\beta$ -hydroxy isoprene nitrates. With the help of the propanone nitrate profile, we can experimentally confirm this discrepancy. With  $\text{OH} = 10^6 \text{ molecule cm}^{-3}$ , the photochemical lifetime with OH of the  $\delta$ -hydroxy isoprene nitrates (respectively the  $\beta$ -hydroxy isoprene nitrate) is  $\tau_{\text{OH}}^\delta = 3 \text{ h}$  ( $\tau_{\text{OH}}^\beta = 18 \text{ h}$ ). Horowitz et al. (2007) show that the deposition of isoprene nitrates is likely to be dominated by dry processes and that  $\tau_d^{\text{HNO}_3} \simeq 7 \text{ h} \leq \tau_d^{\text{ISOPN}} \leq \tau_d^{\text{PAN}} \simeq 100 \text{ h}$ . As a result, the fate of the  $\delta$ -hydroxy isoprene nitrates is likely to be dominated by their reactivity with OH and possibly  $\text{O}_3$ , similar to isoprene, while other processes such as dry deposition and reaction with  $\text{NO}_3$  must be taken into account for proper modeling of the  $\beta$ -hydroxy isoprene nitrates. Therefore, the latter are likely to have greater influence on tropospheric chemistry.

The large difference in the lifetime of the organic nitrates formed in the  $\delta$ -hydroxy and  $\beta$ -hydroxy channels may explain some of the spread in the reported yields and  $\text{NO}_x$  recyclings. Studies focusing on the very first step of isoprene photooxidation (e.g., Sprengnether et al., 2002) tend to report the highest nitrate

yield, suggesting that the short-lived  $\delta$ -hydroxy isoprene nitrates may have been underestimated in some previous experiments (see inset of Fig. 2.9). The same argument may also explain the observations of a greater variety of isoprene nitrates in laboratory experiments than in the field (Giacopelli et al., 2005).

**Recycling:** The efficiency of the  $\text{NO}_x$  sequestration depends on the fate of the isoprene nitrates and more specifically on how much  $\text{NO}_x$  is released in their subsequent photooxidation.  $\text{NO}_x$ -recycling is defined as the difference between the  $\text{NO}_x$  released by the reaction and the  $\text{NO}$  consumed. As a result, since ISOPN(2,1) oxidation does not yield any  $\text{NO}_2$ , its recycling is negative due to the formation of dinitrates, which we have observed at  $m/z = 311$  in another experiment. Horowitz et al. (2007) obtain the best agreement with the boundary layer data when 40% of the  $\text{NO}_x$  is recycled with a low nitrate yield (4%). We find a  $\text{NO}_x$  recycling of  $57\% \pm 10\%$  by the isoprene peroxy radicals consistent with the conclusion of Horowitz et al. (2007) despite our very different yields. As highlighted in the inset of Fig. 2.9, this may be related to the wrong estimation of isoprene nitrate yield due to the short lifetime of the  $\delta$ -hydroxy channels. The photooxidation of isoprene leads to the formation of other significant organic nitrates MVKN, MACRN, PROPNN ( $\simeq 1\%$ ) and ETHLN ( $\simeq 1\%$ ). All these compounds are substantially longer-lived than isoprene nitrates and therefore are more likely to influence the  $\text{NO}_x$ -balance on a larger scale (assuming a similar deposition velocity). The formation of PROPNN and MVKN appear especially important as their photochemical sinks are very slow:  $\tau_{OH}^{MVKN} \simeq 100\text{h}$  and  $\tau_{OH}^{PROPNN} > 200\text{h}$ . Therefore, they may constitute important pathways for  $\text{NO}_x$  transport, as well as significant  $\text{NO}_x$ -sinks through deposition. They also can contribute to the growing source of atmospheric nitrogen to the open ocean (Duce et al., 2008).

In contrast to ISOPN, MACRN and MVKN release most of their  $\text{NO}_x$  in the course of their decomposition, possibly through the formation of formic and pyruvic acids. These organic nitrate channels may contribute significantly to the missing source of small carboxylic acid in the free troposphere.

#### 2.5.4.2 Carboxylic acids

Small carboxylic acids are ubiquitous in the atmosphere both in the gas-phase and in the aqueous phase, playing an important role in rain acidity and cloud reactions (Chebbi and Carlier, 1996).

The photooxidation of isoprene under high  $\text{NO}_x$  produces substantial amounts of formic (yield  $\simeq (10 \pm 3)\%$  after 600 min) and acetic acids (yield  $\simeq (3 \pm 1)\%$  after 600 min). Acetic and formic acids are highly correlated after the first 150 minutes ( $\rho = 0.988$ ), since their main source, hydroxyacetone for acetic acid and glycolaldehyde for formic acid, share a similar origin and lifetimes (Figs 2.7 and 2.3). We find  $[Acetic\ Acid] =$

$$0.46 \pm 0.02 \times [\textit{Formic Acid}] - 0.02 \pm 0.01 \times [\textit{Isoprene}]_0.$$

A strong correlation between formic and acetic acids has been observed previously over Amazonia (Andreae et al., 1988) and Virginia (Talbot et al., 1995). In most large scale chemical models, these compounds originate primarily from biomass burning and to a lesser extent from ozonolysis of alkenes. Since the main source of both acids in the chamber is unlikely to result from the ozonolysis of the alkenes, our study shows that additional channels for their formation should be included. The main identified sources (hydroxyacetone, glycolaldehyde, organic nitrates) are much longer-lived than the ones currently included in global models, which may help resolve part of the discrepancy between models (Jacob and Wofsy, 1988) and atmospheric observations (Andreae et al., 1988; Talbot et al., 1990).

Finally the identification of MOBA, a five-carbon acid, could be important for aerosols, as its vapor pressure and the vapor pressures of the products of its photooxidation are expected to be low.

### 2.5.4.3 Development of a reduced mechanism

The new constraints derived in this study primarily originate from our observation of the chemistry of the  $\delta$ -hydroxy channels. In particular, we have shown that these channels account for a large fraction of the isoprene nitrates and small carboxylic acids, whose role is important on a global scale. Most of the reduced isoprene photooxidation mechanism implemented in chemical transport models, e.g., MOZART (Pfister et al., 2008), do not adequately account for the chemistry of the  $\delta$ -hydroxy channels, thus impeding proper modeling of the consequences of isoprene photooxidation on tropospheric chemistry.

The detailed chemical mechanism described in this study is too complex to be included in large scale atmospheric chemistry simulations. To aid in such investigations, we propose that a few modifications of these simplified mechanisms be implemented (Table 2.2). While adding little complexity and maintaining carbon balance, these few changes describe more accurately the formation and fate of nitrates as well as the yield of carboxylic acid. In particular, the long lifetime of PROPNN and MVKN enables transport of organic nitrates over long distances.

In our reduced mechanism, we neglect the E  $\delta$ -hydroxy channel branch ( $\simeq 5\%$  of the carbon) as well as the non-Dibble branch yielding MPDL and OBL (Fig. 2.1). We have only included the formation of organic nitrates which were directly constrained in this study (ISOPN, PROPNN, ETHNL). The yield of minor organic nitrates can be derived using the number of carbons of the parent peroxy radical, a common approach in most chemical transport models. We introduce a generic four-carbon hydrocarbon, HC4, to account for the decomposition of MOBA. This study does not constrain the fate of 3-methylfuran and the

reaction of isoprene nitrates with ozone; more theoretical and experimental work is required.

## 2.6 Conclusion

A substantial fraction of the terrestrial Northern Hemisphere is characterized by conditions in which the fate of isoprene peroxy radicals is dominated by reactions with NO. Chameides et al. (1988) demonstrated that they play a major role in the formation of ozone in urban areas. This study complements previous investigations of isoprene photooxidation mechanism by focusing on the  $\delta$ -hydroxy channels, whose chemistry is not adequately represented in chemical transport models. We focus on the large yields of small carboxylic acids and propose new constraints for the yield and the fate of organic nitrates. Both constitute outstanding uncertainties in the photooxidation of isoprene, impeding proper modeling of tropospheric chemistry on a global scale. To aid in the development of improved simulations of this chemistry, we propose simple modifications of current condensed mechanism which maintains carbon balance and accounts for the new constraints and mechanisms identified in this study (Table 2.2).

## 2.7 Acknowledgements

The authors wish to thank T. S. Dibble, D. Taraborrelli and an anonymous referee for their helpful comments on the initial manuscript. F. Paulot wishes to thank C. D. Vecitis for helpful discussions regarding chemical mechanisms. This study was supported by the National Science Foundation (NSF) under grant ATM-0432377, by the US Department of Energy under grant DE-FG02-05ER63983, by the US Environmental Protection Agency under grant RD-83374901 and by the Marsden Fund administrated by the Royal Society of New Zealand. F. Paulot is supported by the William and Sonya Davidow graduate fellowship. J. D. Crounse thanks the EPA-STAR Fellowship Program (FP916334012) for providing support. This work has not been formally reviewed by the EPA. The views expressed in this document are solely those of the authors and the EPA does not endorse any products or commercial services mentioned in this publication.



Figure 2.1: Summary of the most prevalent first steps of isoprene photooxidation under high NO<sub>x</sub> conditions. Abbreviations: i:  $\delta 1$  isomerization Reaction [R A.8] ; h: OH+VOC (abstraction or addition) \* denotes the location of the reaction ; o:  $R + O_2 \longrightarrow RO_2$  , O: Reaction [R A.7] ; D: Dibble mechanism (cf. 2.5.1.2) ; n:  $RO_2 + NO$  - Reaction [R A.1] ; d: decomposition – reaction [R A.6] ; k: keto-enol tautomerism (possibly due to heterogeneous enol/ketone conversion). Blue circles: detected and correctly captured by the model. Red squares: Insufficient data/model discrepancy.

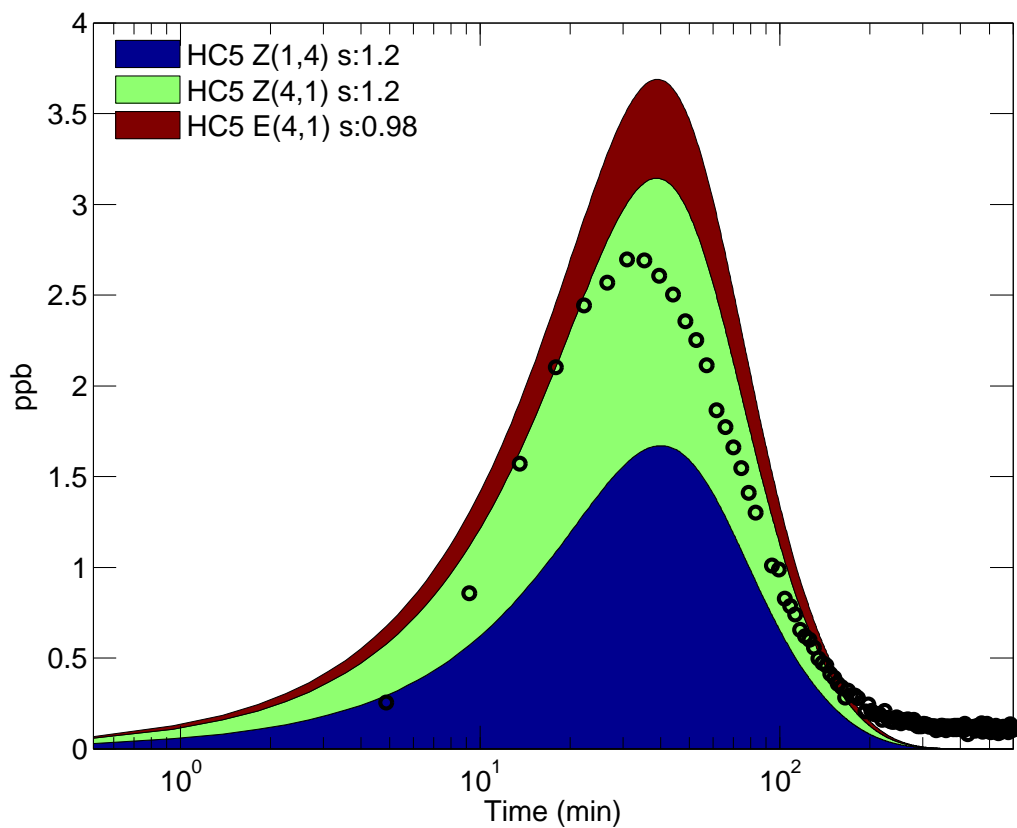


Figure 2.2: Signal recorded at  $m/z=185$  (black circles) and modeled  $\text{HC5} = \text{HC5 Z}(1,4) + \text{HC5 Z}(4,1) + \text{HC5 E}(4,1)$  (monitored as a cluster).

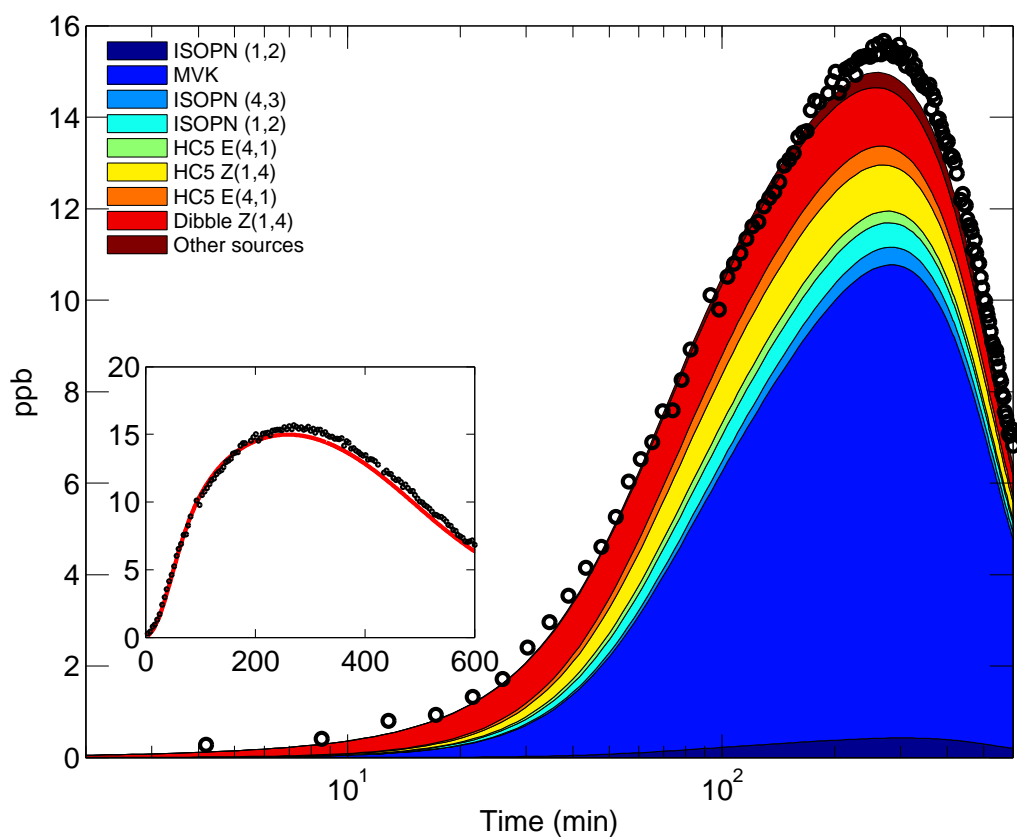


Figure 2.3: Signal recorded at  $m/z=145$  (black circles) compared with modeled GLYC profile. The contribution of acetic acid cluster has been removed using acetic acid transfer at  $m/z=79$ . Colored bars indicate the instantaneous modeled contributions of the different sources of GLYC.

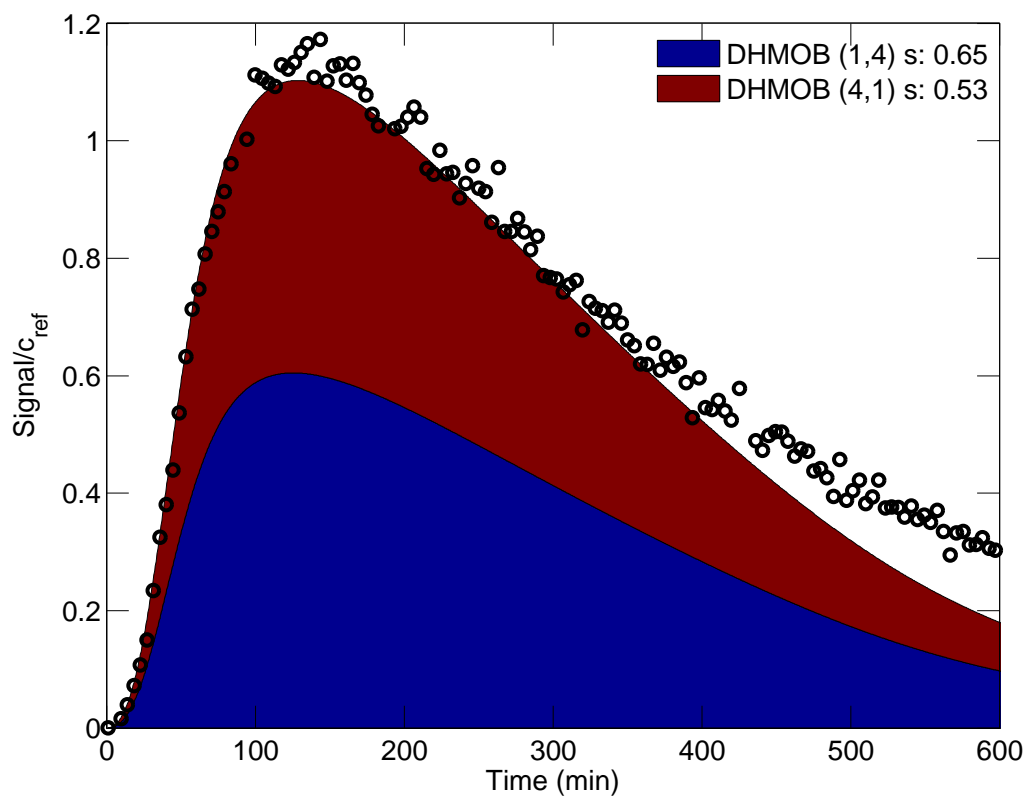


Figure 2.4: Signal recorded at  $m/z=217$  (black circles) and modeled  $\text{DHMOB} = \text{DHMOB}(1, 4) + \text{DHMOB}(4, 1)$  (monitored as a cluster)

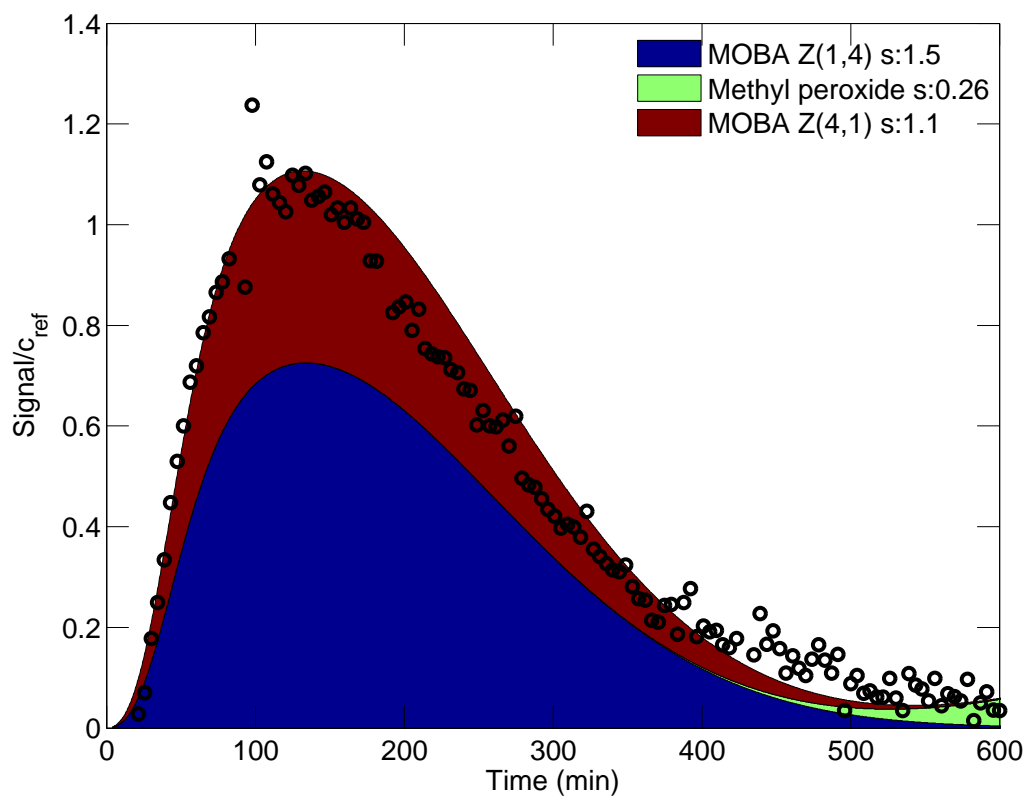


Figure 2.5: Sum of the signals recorded at  $m/z=133$  and  $m/z=199$  (black circles) compared with MOBA=MOBA Z(1,4)+MOBA Z(4,1) ( $m/z=133$  (transfer)+199 (cluster)) and MHP (cluster at  $m/z=133$ )

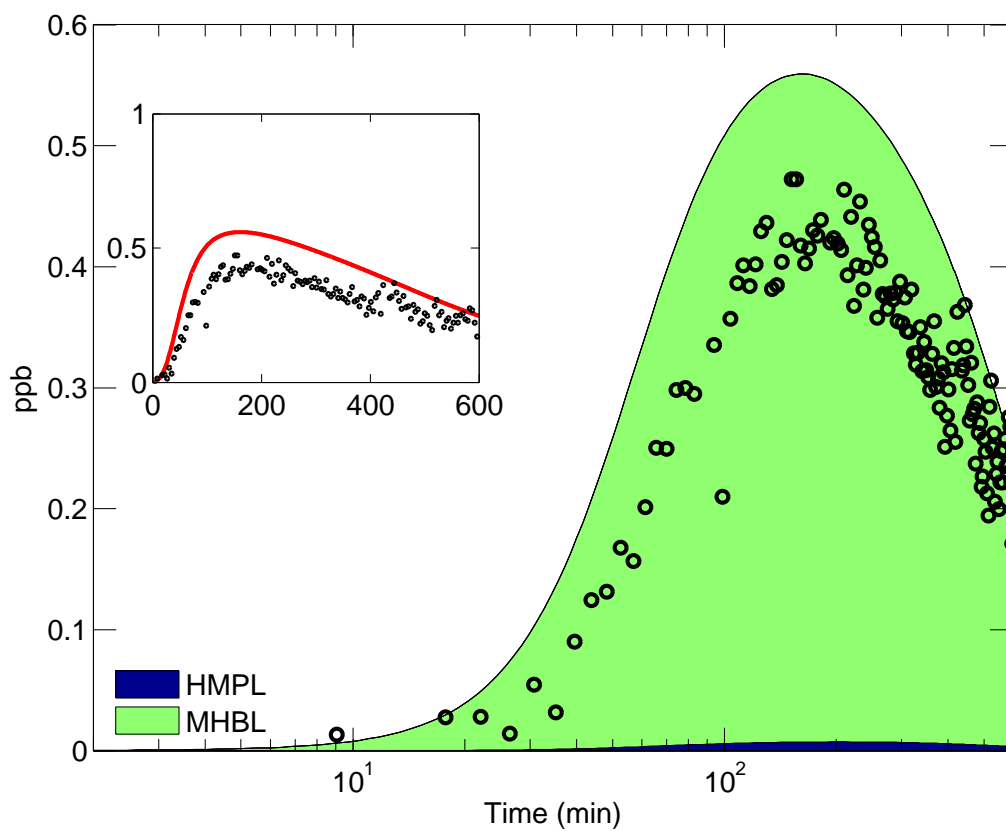


Figure 2.6: Signal recorded at  $m/z=175$  (black circles) compared to modeled DHPN (measured as a cluster)

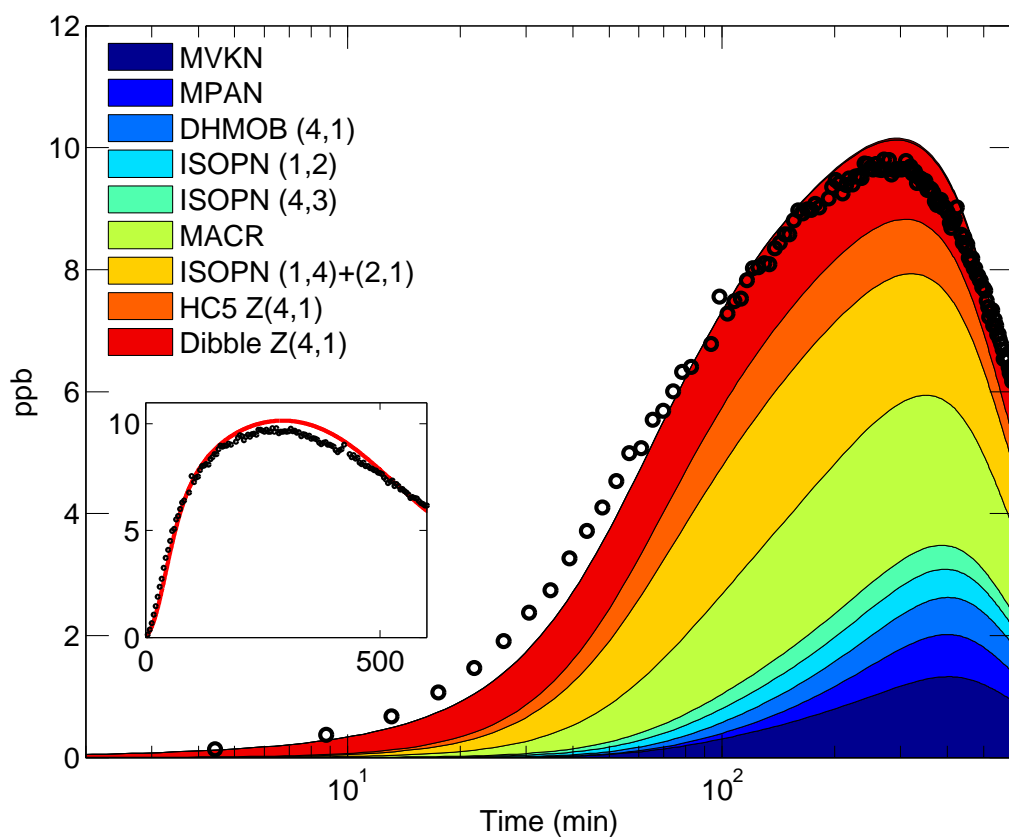


Figure 2.7: Signal recorded at  $m/z=159$  (black circles) compared with modeled HACET profile. Colored bars indicate the instantaneous modeled contributions of the different sources of HACET. MPAN source has been described by Orlando et al. (2002).

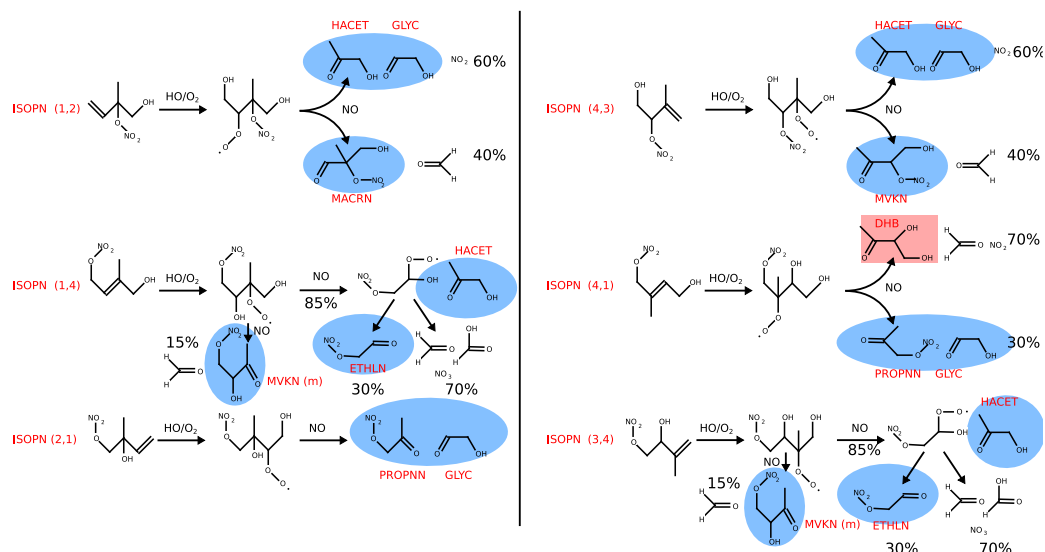


Figure 2.8: Decomposition pathway of the different isoprene nitrates after their reaction with OH. Reaction of ISOPN with OH, O<sub>2</sub>, and NO, also yields dihydroxy-dinitrates through reaction [R A.1]. Color code is identical to Fig. 2.1.



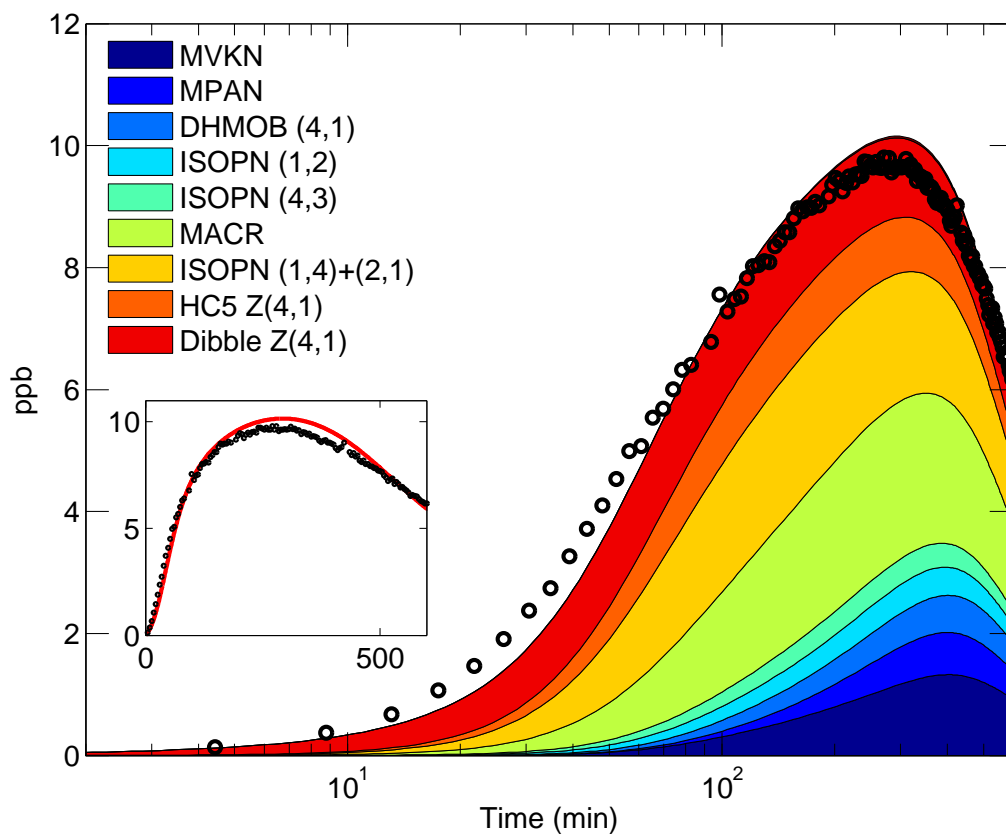


Figure 2.9: Signal recorded at  $m/z=232$  (black circles) compared to modeled isoprene nitrates (ISOPN (1, 2), (1,4)E/Z, (2, 1), (4, 3), (3, 4), (4, 1)E/Z (measured as clusters)) corrected for calibration changes

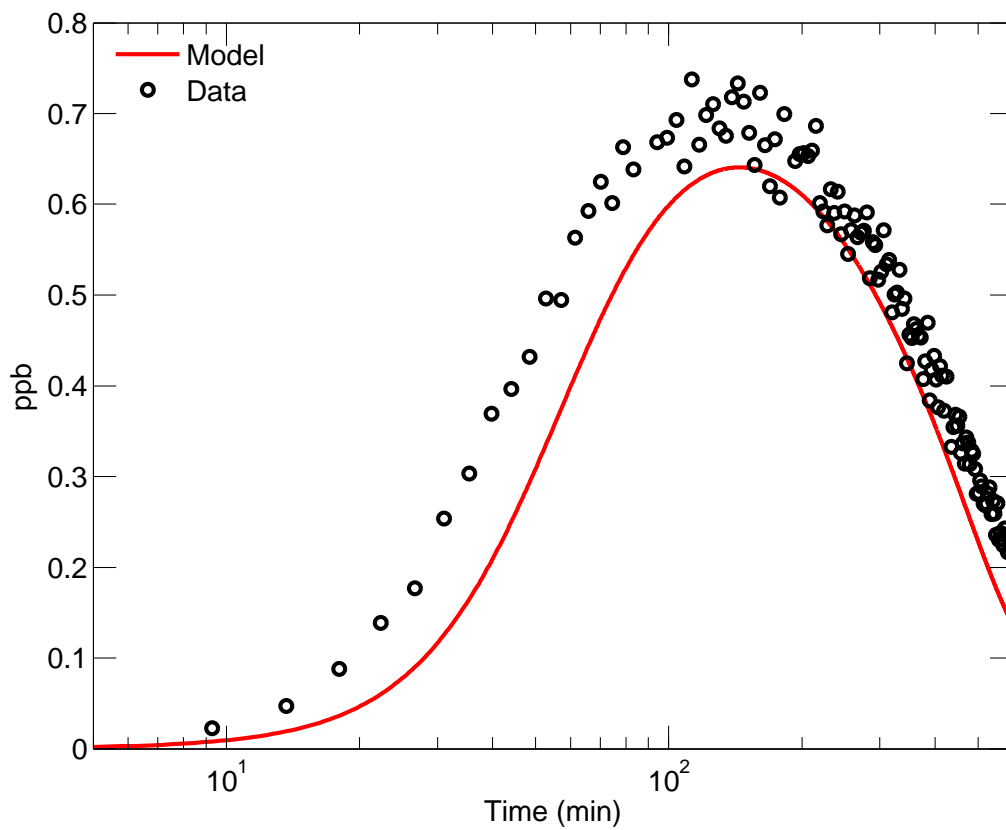


Figure 2.10: Signal recorded at  $m/z=190$  (black circles) compared to modeled ETHLN (measured as a cluster)

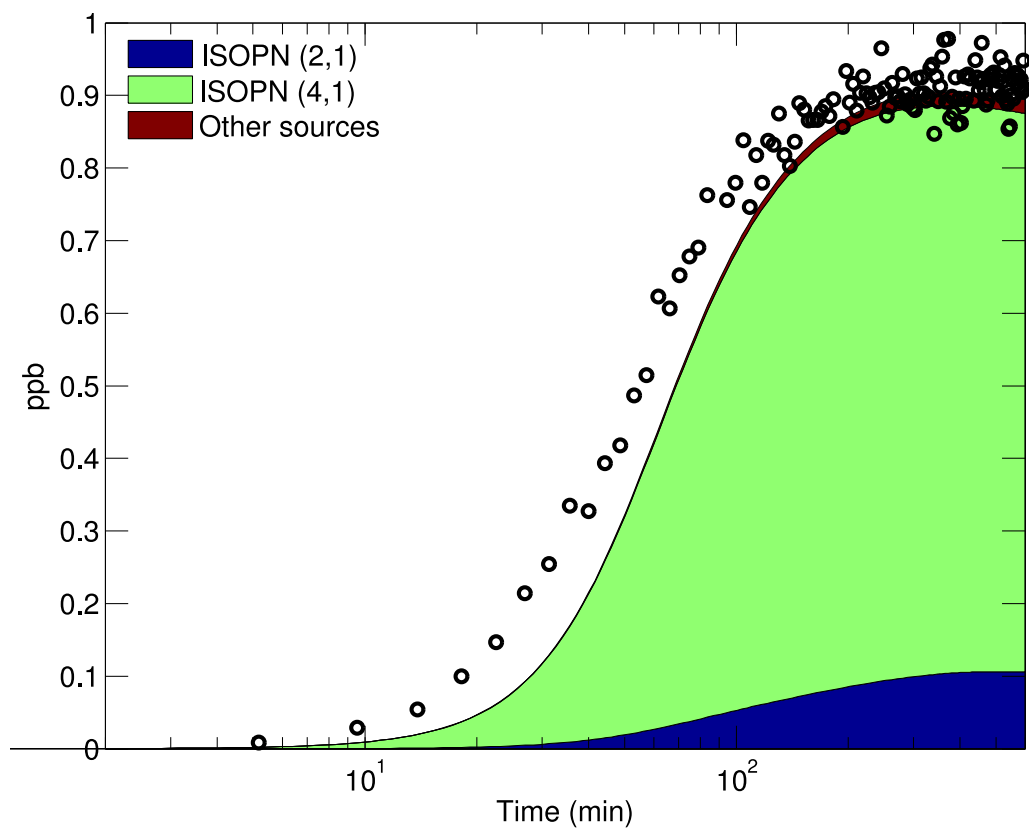


Figure 2.11: Signal recorded at  $m/z=204$  (black circles) compared to modeled PROPNN (measured as a cluster). Colored bars indicate the instantaneous modeled contributions of the different sources of PROPNN

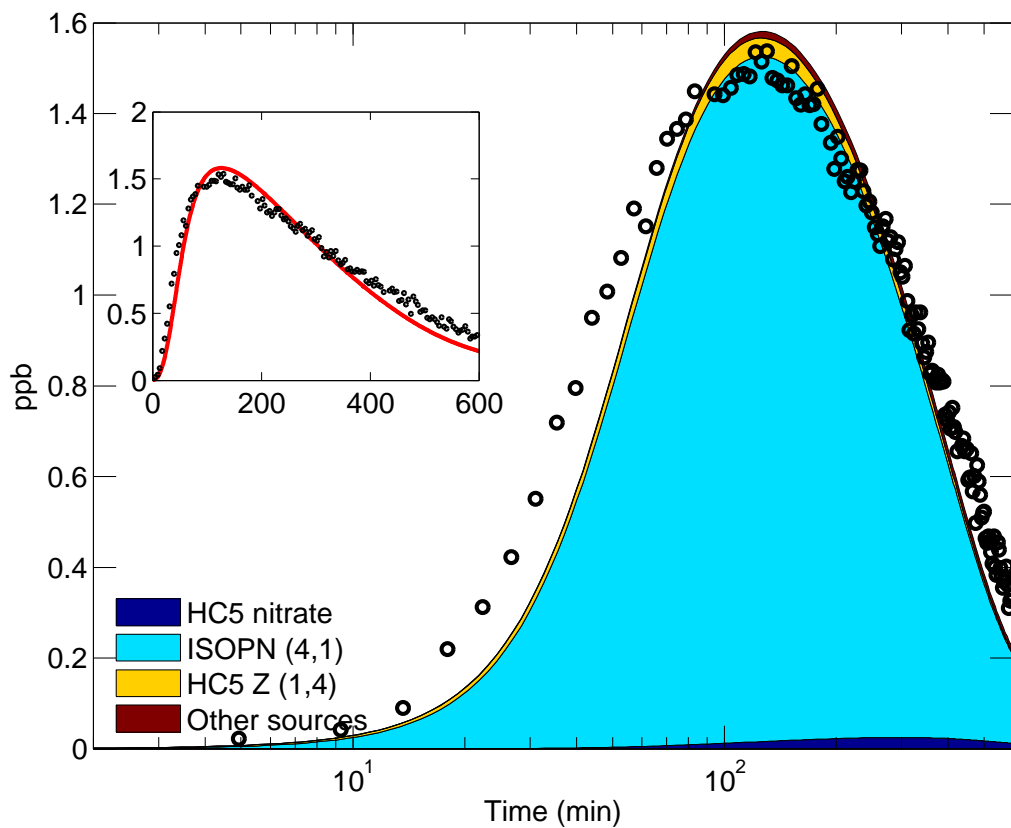


Figure 2.12: Signal recorded at  $m/z=189$  (black circles) compared to modeled DHB (measured as a cluster). Colored bars indicate the instantaneous modeled contributions of the different sources of DHB.

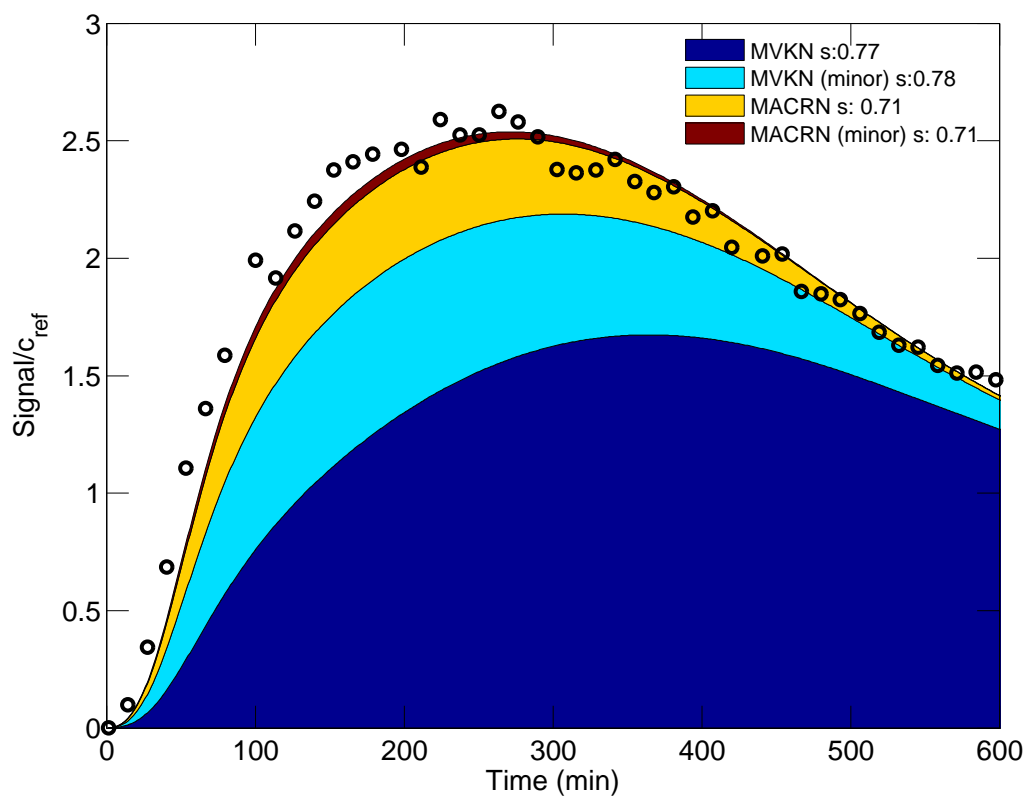


Figure 2.13: Signal recorded at  $m/z=234$  (black circles) compared to the modeled profile of MVKN+MVKN (m)+MACRN+MACRN (m) (measured as clusters), corrected for changing calibrations

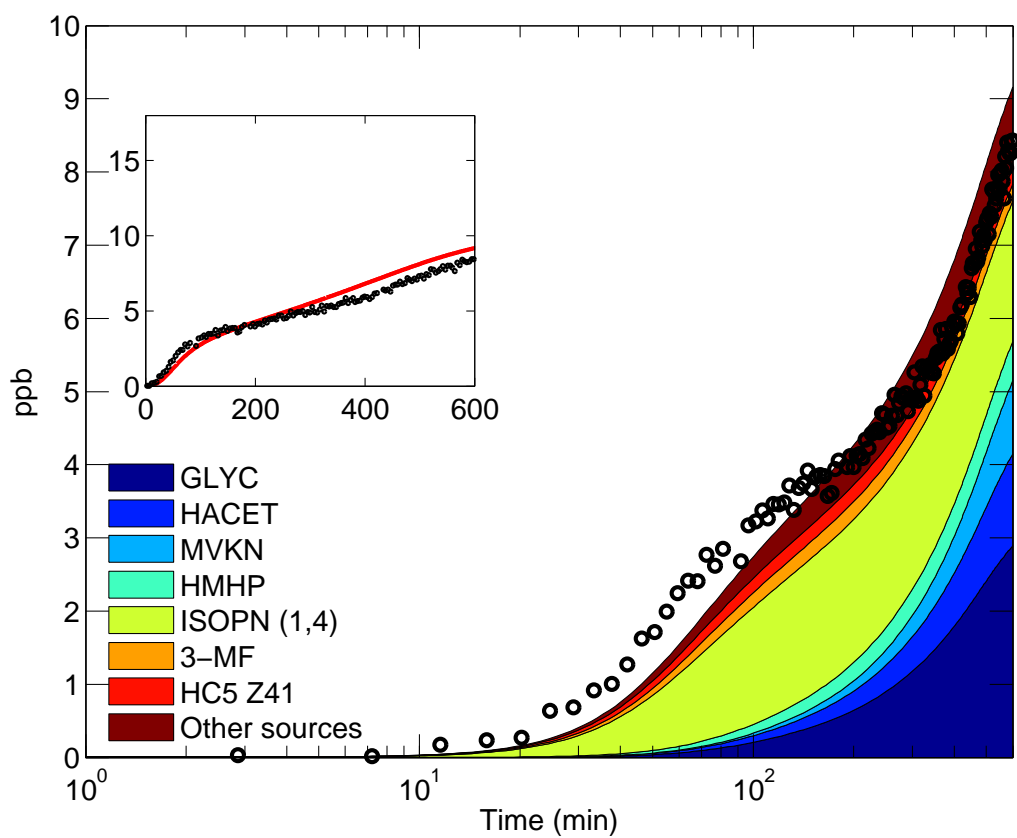


Figure 2.14: Signal recorded at  $m/z=65$  (black circles) compared to modeled formic acid. Colored bars indicate the instantaneous modeled contributions of the different sources of formic acid.

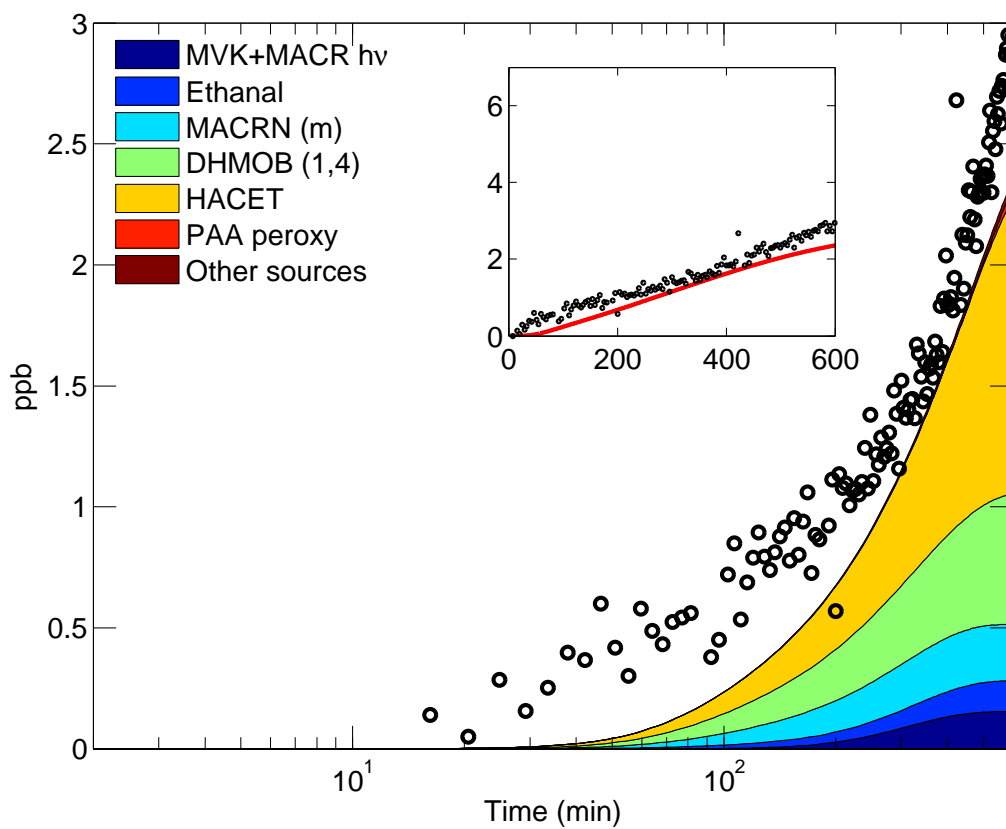


Figure 2.15: Signal recorded at  $m/z=79$  (black circles) compared to modeled acetic acid (observed as a transfer at this mass). Colored bars indicate the instantaneous modeled contributions of the different sources of acetic acid.

Table 2.1: Signals monitored by Chemical Ionization Mass Spectrometry.  $\mathcal{C}$  denotes a cluster [R 2.2] and  $\mathcal{T}$  a transfer [R 2.1]. Uncertain identifications (see text) are highlighted by a  $\star$ .

$m/z$	Nature	Attribution	Formula	CAS
<i>Organic</i>				
65	$\mathcal{T}$	Formic Acid	$\text{CH}_2\text{O}_2$	64-18-6
79	$\mathcal{T}$	Acetic Acid	$\text{C}_2\text{H}_4\text{O}_2$	64-19-7
107	$\mathcal{T}$	Pyruvic Acid $\star$	$\text{C}_3\text{H}_4\text{O}_3$	127-17-3
131	$\mathcal{C}$	Formic Acid	$\text{CH}_2\text{O}_2$	64-18-6
133	$\mathcal{C}$	MHP	$\text{CH}_4\text{O}_2$	3031-73-0
133	$\mathcal{T}$	MOBA Z(1,4)	$\text{C}_5\text{H}_6\text{O}_3$	63170-47-8
133	$\mathcal{T}$	MOBA Z(4,1)	$\text{C}_5\text{H}_6\text{O}_3$	70143-04-3
145	$\mathcal{C}$	Acetic Acid	$\text{C}_2\text{H}_4\text{O}_2$	64-19-7
145	$\mathcal{C}$	GLYC	$\text{C}_2\text{H}_6\text{O}_2$	141-46-8
159	$\mathcal{C}$	HACET	$\text{C}_3\text{H}_6\text{O}_2$	116-09-6
161	$\mathcal{C}$	PAA	$\text{C}_2\text{H}_4\text{O}_3$	116-09-6
169	$\mathcal{C}$	HMHP	$\text{CH}_4\text{O}_3$	15932-89-5
173	$\mathcal{C}$	HOPL $\star$	$\text{C}_3\text{H}_4\text{O}_3$	997-10-4
173	$\mathcal{C}$	Pyruvic Acid $\star$	$\text{C}_3\text{H}_4\text{O}_3$	127-17-3
175	$\mathcal{C}$	DHPN	$\text{C}_3\text{H}_6\text{O}_3$	96-26-4
185	$\mathcal{C}$	HC5 E(4,1)	$\text{C}_5\text{H}_8\text{O}_2$	
185	$\mathcal{C}$	HC5 Z(1,4)	$\text{C}_5\text{H}_8\text{O}_2$	519148-47-1
185	$\mathcal{C}$	HC5 Z(4,1)	$\text{C}_5\text{H}_8\text{O}_2$	519148-44-8
189	$\mathcal{C}$	DHB	$\text{C}_4\text{H}_8\text{O}_3$	57011-15-1
190	$\mathcal{C}$	ETHLN	$\text{C}_2\text{H}_3\text{NO}_4$	72673-15-5
199	$\mathcal{C}$	MOBA Z(1,4)	$\text{C}_5\text{H}_6\text{O}_3$	63170-47-8
199	$\mathcal{C}$	MOBA Z(4,1)	$\text{C}_5\text{H}_6\text{O}_3$	70143-04-3
201	$\mathcal{C}$	MHBL $\star$	$\text{C}_5\text{H}_8\text{O}_3$	
204	$\mathcal{C}$	PROPNN	$\text{C}_3\text{H}_5\text{NO}_4$	6745-71-7
217	$\mathcal{C}$	DHMOB (1,4)	$\text{C}_5\text{H}_8\text{O}_4$	
217	$\mathcal{C}$	DHMOB (4,1)	$\text{C}_5\text{H}_8\text{O}_4$	



232	$\mathcal{C}$	ISOPN (1,2)	$\text{C}_5\text{H}_9\text{NO}_4$	227607-01-4
232	$\mathcal{C}$	ISOPN (1,4) Z	$\text{C}_5\text{H}_9\text{NO}_4$	227606-97-5
232	$\mathcal{C}$	ISOPN (1,4) E	$\text{C}_5\text{H}_9\text{NO}_4$	227606-98-6
232	$\mathcal{C}$	ISOPN (2,1)	$\text{C}_5\text{H}_9\text{NO}_4$	227607-02-5
232	$\mathcal{C}$	ISOPN (3,4)	$\text{C}_5\text{H}_9\text{NO}_4$	601487-80-3
232	$\mathcal{C}$	ISOPN (4,1) Z	$\text{C}_5\text{H}_9\text{NO}_4$	227606-99-7
232	$\mathcal{C}$	ISOPN (4,1) E	$\text{C}_5\text{H}_9\text{NO}_4$	227607-00-3
232	$\mathcal{C}$	ISOPN (4,3)	$\text{C}_5\text{H}_9\text{NO}_4$	227606-96-4
234	$\mathcal{C}$	MACRN	$\text{C}_4\text{H}_7\text{NO}_5$	
234	$\mathcal{C}$	MACRN (m)	$\text{C}_4\text{H}_7\text{NO}_5$	
234	$\mathcal{C}$	MVKN	$\text{C}_4\text{H}_7\text{NO}_5$	
234	$\mathcal{C}$	MVKN (m)	$\text{C}_4\text{H}_7\text{NO}_5$	

*Inorganic*

62		$\text{NO}_3^-$ (proxy for $\text{N}_2\text{O}_5$ )	14797-55-8
66	$\mathcal{T}$	HONO	7782-77-6
82	$\mathcal{T}$	$\text{HNO}_3$	7697-37-2
98	$\mathcal{T}$	$\text{HO}_2\text{NO}_2$	26404-66-0
119	$\mathcal{C}$	$\text{H}_2\text{O}_2$	7722-84-1
132	$\mathcal{C}$	HONO	7782-77-6
148	$\mathcal{C}$	$\text{HNO}_3$	7697-37-2
164	$\mathcal{C}$	$\text{HO}_2\text{NO}_2$	26404-66-0

Table 2.2: Suggested modifications of isoprene condensed photooxidation mechanism under high  $\text{NO}_x$  conditions. (2,1), (3,4), E(1,4) and E(4,1) branches are not treated. Formation of organic nitrates is limited to isoprene, MVK and MACR peroxy radicals. The reaction of the isoprene nitrates with respect to ozone, as well as the fate of 3-MF, are not tackled by this mechanism (see text). MGLYX denotes methylglyoxal and HC4, a generic four-carbon VOC.

Reaction		$k(T=298\text{K})$ $10^{-11} \text{cm}^3 \text{molec}^{-1} \text{s}^{-1}$
ISOP + OH $\rightarrow$	ISOPO <sub>2</sub>	10
ISOPO <sub>2</sub> + NO $\rightarrow$	0.40 MVK + 0.26 MACR + 0.883 NO <sub>2</sub> + 0.07 ISOPN $\delta$ + 0.047 ISOPN $\beta$ + 0.66 HCHO 0.10 HC5 + 0.043 (3-MF) + 0.08 DIBOO + 0.803 HO <sub>2</sub>	0.81
HC5 + OH $\rightarrow$	HC5OO	11
HC5OO + NO $\rightarrow$	NO <sub>2</sub> + 0.234 (GLYC + MGLYX) + 0.216 (GLYX + HACET) + 0.29 DHMOB 0.17 MOBA + 0.09 HC4 + 0.09 CO + HO <sub>2</sub>	0.81
ISOPN $\delta$ + OH $\rightarrow$	ISOPNOO $\delta$	9.5
ISOPNOO $\delta$ + NO $\rightarrow$	0.34 DHBN + 0.15 PROPNN + 0.44 HACET + 0.07 MVKN + 0.13 ETHLN + 0.31 HCOOH + 0.31 NO <sub>3</sub> + 0.72 HCHO + 0.15 GLYC + 1.34 NO <sub>2</sub> + 0.35 HO <sub>2</sub>	0.81
ISOPN $\beta$ + OH $\rightarrow$	ISOPNOO $\beta$	1.3
ISOPNOO $\beta$ + NO $\rightarrow$	0.6 (GLYC + HACET) + 0.4 (HCHO + HO <sub>2</sub> ) + 0.26 MACRN + 0.14 MVKN + 1.6 NO <sub>2</sub>	0.81
DIBOO + NO $\rightarrow$	HO <sub>2</sub> + NO <sub>2</sub> + 0.52 (GLYC + MGLYX) + 0.48 (GLYX + HACET)	0.81
MVK + OH $\rightarrow$	MV'KOO	1.75
MV'KOO + NO $\rightarrow$	0.625 (GLYC + CH <sub>3</sub> C(O)OO) + 0.265 (MGLYX + CH <sub>2</sub> O + HO <sub>2</sub> ) + 0.11 MVKN 0.89 NO <sub>2</sub>	0.81
MVKN + OH $\rightarrow$	0.65 (HCOOH + MGLYX) + 0.35 (CH <sub>2</sub> O + CH <sub>3</sub> C(O)C(O)OH + NO <sub>3</sub>	0.56
MACR + OH $\rightarrow$	0.47 MACROO + 0.53 MCO <sub>3</sub>	2.95
MACROO + NO $\rightarrow$	0.85 (NO <sub>2</sub> + HO <sub>2</sub> ) + 0.425 (HACET + CO) + 0.425 (CH <sub>2</sub> O + MGLYX) + 0.15 MACRN	0.81
MACRN + OH $\rightarrow$	0.08 (CH <sub>3</sub> C(O)OH + CH <sub>2</sub> O + NO <sub>3</sub> ) + 0.07 (HCOOH + NO <sub>3</sub> + MGLYX) 0.85 (HACET + NO <sub>2</sub> ) + 0.93 CO <sub>2</sub>	5
MC(O)OO + NO $\rightarrow$	NO <sub>2</sub> + CO + CO <sub>2</sub> + CH <sub>2</sub> O + CH <sub>3</sub> OO	2.1
GLYC + OH $\rightarrow$	0.75 HO <sub>2</sub> + 0.25 OH + 0.13 GLYX + 0.52 CO + 0.35 CO <sub>2</sub> + 0.16 HCOOH + 0.71 CH <sub>2</sub> O	0.8
HACET + OH $\rightarrow$	0.75 MGLYX + 0.825 HO <sub>2</sub> + 0.125 HCOOH + 0.1 OH + 0.125 CH <sub>3</sub> OO + 0.20 CO <sub>2</sub> 0.05 CO + 0.125 CH <sub>3</sub> C(O)OH	0.6
ETHLN + OH $\rightarrow$	CH <sub>2</sub> O + CO <sub>2</sub> + NO <sub>2</sub>	1
DHMOB + OH $\rightarrow$	1.5 CO + 0.5 HO <sub>2</sub> + 0.5 HACET + 0.5 HC4	1
MOBA + HO $\rightarrow$	MOBAOO	0.3
MOBAOO + NO $\rightarrow$	HC4 + CO <sub>2</sub> + HO <sub>2</sub> + NO <sub>2</sub>	0.8

## **Chapter 3**

# **Unexpected epoxide formation in the gas-phase photooxidation of isoprene<sup>1</sup>**

---

<sup>1</sup>Adapted with permission from Paulot, F.; Crounse, J. D.; Kjaergaard, H. G.; Kurten, A.; St. Clair, J. M.; Seinfeld, J. H. & Wennberg, P. O. Unexpected Epoxide Formation in the Gas-Phase Photooxidation of Isoprene *Science*, 2009, 325, 730-733 ©2009 by the Authors.

### 3.1 Abstract

Emissions of nonmethane hydrocarbon compounds to the atmosphere from the biosphere exceed those from anthropogenic activity. Isoprene, a five-carbon diene, contributes more than 40% of these emissions. Once emitted to the atmosphere, isoprene is rapidly oxidized by the hydroxyl radical OH. We report here that under pristine conditions isoprene is oxidized primarily to hydroxyhydroperoxides. Further oxidation of these hydroxyhydroperoxides by OH leads efficiently to the formation of dihydroxyepoxides and OH reformation. Global simulations show an enormous flux—nearly 100 teragrams of carbon per year—of these epoxides to the atmosphere. The discovery of these highly soluble epoxides provides a missing link tying the gas-phase degradation of isoprene to the observed formation of organic aerosols.

### 3.2 Introduction

Isoprene is the largest source of non-methane hydrocarbons to the atmosphere ( $\sim 500$  Tg C/year) (Guenther et al., 2006). It is produced by deciduous plants (Harley et al., 1999) and plays a critical role in tropospheric chemistry over large regions of the globe (Fuentes et al., 2000). In many forested regions, isoprene oxidation by OH occurs far from combustion of biomass and fossil fuel, so nitric oxide (NO) concentrations are very low. Many of the details of the chemical oxidation mechanism under these conditions remain to be elucidated, hindering assessment of the consequences of changes in isoprene emissions from land use and climate variation (Guenther et al., 2006; Rosenstiel et al., 2003; Wiedinmyer et al., 2006; von Kuhlmann et al., 2004) or changes in NO emissions. In addition to the uncertainty in the gas-phase chemistry, there is no agreement on the mechanism involved in the formation of secondary organic aerosol (SOA) from isoprene oxidation (Claeys et al., 2004).

Where NO is low, isoprene photooxidation is expected to yield the hydroxyhydroperoxides, ISOPOOH =  $\beta$ -ISOPOOH +  $\delta$ -ISOPOOH (Figs 3.1a and 3.1b) (Crutzen et al., 2000; Reeves and Penkett, 2003). These series of reactions are expected to strongly depress the concentrations of OH and HO (together known as HO<sub>x</sub>) in regions with high isoprene emissions. Observed HO<sub>x</sub> levels remain, however, almost unchanged over a wide range of isoprene concentrations, inconsistent with the simulated influence of the reactions shown in Figs 3.1a and 3.1b (Thornton et al., 2002; Ren et al., 2008; Lelieveld et al., 2008). Simulations and measurements of HO<sub>x</sub> have been partly reconciled with substitution of the speculative reaction shown in Fig. 3.1c, where formation of methacrolein (MACR) and formaldehyde is accompanied by OH formation,

thus reducing the impact of isoprene on  $\text{HO}_x$  levels (Lelieveld et al., 2008).

Analogous to the reactions shown in Figs 3.1a to 3.1c, addition of OH on the other double bond yields similar hydroxyhydroperoxides ( $\beta_1$ - and  $\delta_1$ - ISOPOOH) and methylvinylketone (MVK) (see Appendix B). Both unimolecular decomposition of the peroxy radical (Peeters et al., 2009) and reaction with  $\text{HO}_2$  (Dillon and Crowley, 2008) have been proposed for the reaction shown in Fig. 3.1c. Although OH reformation (15 to 65%) has been measured for the reactions of  $\text{HO}_2$  with acylperoxy and  $\beta$ -carbonyl peroxy radicals, low OH yields (< 6%) have been reported from the reactions of  $\text{HO}_2$  with  $\beta$ -hydroxy peroxy radicals, structurally more similar to isoprene peroxy radicals (Dillon and Crowley, 2008).

### 3.3 Results

We show here that ISOPOOH is formed in large yields (> 70%) via the channels shown in Figs. 3.1a and 3.1b, with concomitant formation of MVK and MACR in much smaller yields (< 30%) via the channel shown in Fig. 3.1c.

The mechanism depicted in Fig. 3.1c yields OH, although substantially less than required to close the  $\text{HO}_x$  budget (Lelieveld et al., 2008). We show below that the oxidation of ISOPOOH by OH produces dihydroxyepoxides (IEPOX =  $\beta$ -IEPOX +  $\delta$ -IEPOX). This  $\text{HO}_x$ -neutral mechanism produces IEPOX with yields exceeding 75% (Fig. 3.2). This mechanism is likely specific to isoprene and other polyalkenes. Analogous to liquid-phase processes (Bell et al., 1950), it profoundly differs from gas-phase oxidation of simple alkenes by OH (e.g., Figs 3.1a and 3.1b), which would result in the formation of the dihydroxydihydroperoxides. Formation of these compounds is not observed in these experiments. The gas-phase formation of IEPOX in high yields provides a suitable gas-phase precursor for secondary organic aerosol from isoprene oxidation (iSOA) under low- $\text{NO}_x$  conditions (Wang et al., 2005; Surratt et al., 2006; Minerath and Elrod, 2009) and may help resolve an outstanding puzzle in atmospheric aerosol chemistry. Although epoxides have previously been speculated as a possible precursor for iSOA (Wang et al., 2005), no mechanism was known to produce them in either the gas or aerosol phase. Consistent with expectation that IEPOX can serve as a precursor to iSOA, we observe rapid and quantitative uptake of 1,4- dihydroxy-2,3-epoxybutane (BEPOX)—a compound structurally similar to IEPOX—on acidic aerosol.

We monitor isoprene photooxidation products in the Caltech environmental chamber by chemical ionization mass spectrometry (CIMS) (Crounse et al., 2006), employing a triple-quadrupole mass filter that provides tandem mass spectra (MSMS). The reagent anion,  $\text{CF}_3\text{O}^-$ , provides sensitive detection of organic

hydroperoxides by formation of ion-molecule clusters (Crounse et al., 2006). Detection of BEPOX by CIMS confirms its sensitivity to dihydroxy-epoxides (see Appendix B). In the absence of native standards for many of the compounds described here, the calibration of the instrument was inferred from molecular properties of the analyte (Paulot et al., 2009a).

Isoprene is oxidized by OH generated through the photolysis of hydrogen peroxide ( $\text{H}_2\text{O}_2$ ) in a Teflon bag filled with 800 standard liters of ultra-zero air. Known amounts of isoprene and  $\text{H}_2\text{O}_2$  are introduced into the chamber before ultraviolet (UV) lights are energized. Isoprene is quantified using gas chromatography with flame ionization detection (GC-FID) (Appendix B).

The products formed through the mechanisms shown on Figs. 3.1a, 3.1b and 3.2—ISOPOOH and IEPOX—are isobaric and measured together by CIMS as the cluster of  $\text{CF}_3\text{O}^-$  with these compounds at the mass to charge ratio ( $m/z$ ) 203 (Fig. 3.3, red curve). However, distinct daughter ions produced through collision-induced dissociation (CID) of these cluster ions allow for quantification of each compound (McLafferty, 1981). Clusters of  $\text{CF}_3\text{O}^-$  with hydroxyhydroperoxides, produced from the oxidation of simple alkenes, fragment to  $m/z = 63$ , whereas those with BEPOX exhibit loss of hydrofluoric acid (HF). The daughter  $m/z = 63$  of 203 (Fig. 3.3, green curve), associated with the fragmentation of the ISOPOOH cluster, clearly precedes the daughter  $m/z = 183$  of 203 (Fig. 3.3, blue curve), associated with IEPOX, consistent with the proposed mechanism. Clusters of  $\text{CF}_3\text{O}^-$  with other plausible isomers of IEPOX are not known to exhibit efficient loss of HF (see Appendix B). The sum of the  $m/z = 63$  and  $m/z = 183$  daughters (Fig. 3.3, black dashed line) properly captures the shape of the parent signal (Fig. 3.3, red curve).

Experiments performed with  $^{18}\text{OH}$  produced from the photolysis of  $\text{H}^{18}\text{O}^{18}\text{OH}$  provide additional evidence for the conversion of ISOPOOH to IEPOX. With  $^{18}\text{OH}$  as the primary oxidant, ISOPOOH and IEPOX are no longer isobaric: The ISOPOOH ion cluster is primarily monitored at  $m/z = 205$  (Fig. 3.4, magenta circles) corresponding to the addition of one  $^{18}\text{OH}$  on isoprene (Figs 3.1a and 3.1b), whereas IEPOX is detected at  $m/z = 207$  (Fig. 3.4, blue squares) because its formation requires addition of a second  $^{18}\text{OH}$  and simultaneous loss of  $^{16}\text{OH}$  (Figs 3.2 and 3.4). The coincidence between  $m/z = 207$  and IEPOX fingerprint (daughter  $m/z = 187$ ) suggests that  $m/z = 207$  is derived almost entirely from the dilabeled IEPOX, consistent with the proposed mechanism.

Quantum chemical calculations confirm that, after the addition of OH, ISOPOOH is connected to IEPOX by energetically favorable adiabatic pathways (Fig. 3.5 and Tables B.4 and B.5).  $\beta$ - and  $\delta$ - IEPOX lie  $\sim 50$  kcal/mol below their ISOPOOH parent with the transition state connecting the alkyl radical and IEPOX  $\sim 20$  kcal/mol below the ISOPOOH reactant. The relative energies and structures of the stationary points

along the surface are shown in Fig. 3.5 for the  $\beta$ 4-ISOPROOH to  $\beta$ -IEPOX reaction (Fig. 3.2a). The reaction paths and energetics for the analogous  $\beta$ 1-ISOPROOH to  $\beta$ -IEPOX reaction and for the  $\delta$ 4-ISOPROOH to  $\delta$ 4-IEPOX reaction (Fig. 3.2b) are similar (Figs. B.4 and B.3 and Tables B.7 and B.6).

The formation of isotopically light ISOPROOH ( $m/z = 203$ ) (Fig. 3.4, red circles) and IEPOX ( $m/z = 203$  and 205) (Fig. 3.4, red and magenta squares) in the  $^{18}\text{OH}$ -labeled experiment provides additional evidence for the reaction shown in Fig. 3.2, because  $^{16}\text{OH}$  is released through formation of IEPOX (Fig. 3.2). The  $^{16}\text{OH}$  quickly reacts with isoprene and ISOPROOH, forming the observed isotopically light compounds. The formation of light ISOPROOH ( $m/z = 203$ ) in the first hour of the experiment cannot, however, be accounted for by the IEPOX mechanism (Fig. 3.4), alone, suggesting a small but rapid  $^{16}\text{OH}$  formation, attributed to a minor channel of the reaction between isoprene peroxy radicals and  $\text{HO}_2$  (Fig. 3.1c). This is consistent with the coincident production of MVK and MACR, measured together by proton transfer mass spectrometry at  $m/z = 89$ . Very little methylbutenediol ( $< 2\%$ ) is observed, which suggests that cross-peroxy radical reactions (Ruppert and Becker, 2000) are unlikely to account for the formation of MVK and MACR. A prompt signal at  $m/z = 201$  appears consistent with the recently hypothesized formation of (2Z)-hydroperoxymethylbutenal by a 1,6 H shift. However, its yield ( $< 10\%$  of ISOPROOH) is much less than predicted theoretically (Peeters et al., 2009).

Using a kinetic model constrained by the observed yields of MVK/MACR and the ratios between light and heavy isotopes of ISOPROOH, we estimate that 12% of the isoprene peroxy radicals react with  $\text{HO}_2$  to recycle OH through the reaction shown in Fig. 3.1c. This estimate accounts for a small initial amount of  $\text{NO}_x$  present initially in the chamber (see Appendix B). The balance of the isoprene peroxy radicals reacts with  $\text{HO}_2$  to form ISOPROOH.

The lifetime of ISOPROOH with respect to OH (3 to 5 hours) is considerably shorter than IEPOX (18 to 22 hours) (calculated for  $[\text{OH}] = 10^6 \text{ radicals cm}^{-3}$ ). The formation of unlabeled hydroxyacetone as well as singly labeled hydroxyacetone and glycolaldehyde in the photooxidation of isoprene by  $^{18}\text{OH}$  suggests that the degradation of IEPOX by OH occurs primarily through hydrogen abstraction  $\alpha$  to the alcohol (see Appendix B).

In addition to the gas-phase oxidation, dihydroxyepoxides are lost to aerosol surfaces through reactive uptake. We monitor by CID-CIMS rapid and nearly quantitative uptake of BEPOX onto acidic aerosol seeds ( $\text{MgSO}_4/\text{H}_2\text{SO}_4$ ). The resulting SOA composition can be readily related to the one identified for iSOA in pristine environments. In particular, analogs of dihydroxyenols, 2-methyltetrols, alkene-triols, and associated sulfate esters are detected (see Appendix B), which suggests that IEPOX may explain their formation

in both field (Claeys et al., 2004; Surratt et al., 2008) and chamber studies (Wang et al., 2005; Surratt et al., 2007). Epoxides are also known to polymerize easily, an essential process for SOA growth (Gao et al., 2004).

### 3.4 Atmospheric relevance

The atmospheric yield of IEPOX is directly related to the relative importance of the reactions of isoprene peroxy radicals with  $\text{HO}_2$  and  $\text{NO}$ . Using the chemical transport model GEOS-CHEM (Bey et al., 2001) with an updated chemical mechanism (Table B.9), we find that globally about one-third of isoprene peroxy radicals undergo reaction with  $\text{HO}_2$ , with the remaining fraction reacting with  $\text{NO}$ . Over the Amazon, this ratio is almost inverted (Fig. B.7). Including uncertainties in isoprene emissions, we estimate that  $95 \pm 45$  Tg C/year of IEPOX, a previously unknown class of compounds, are formed each year in the atmosphere. The largest concentrations of IEPOX are localized over the southern tropics, with substantial levels predicted over Canada and the Southeast United States during Northern Hemisphere summer (Fig. 3.6).

The presence of high concentrations of ISOPOOH and IEPOX in the atmosphere are consistent with recent aircraft-borne observations of isoprene oxidation products ( $m/z = 203$ ) over southeast Columbia [NASA Tropical Composition, Cloud, and Climate Coupling (TC4) campaign] and ( $m/z = 203$  and its daughters) over Alberta and California [NASA Arctic Research of the Composition of the Troposphere from Aircraft and Satellites (ARCTAS) campaign]. Preliminary study of the data collected in the boundary layer is consistent with the concentrations of these compounds calculated with GEOS-CHEM (Fig. B.8).

The variability in the yield and fate of IEPOX is expected to translate into highly variable iSOA yields. In particular, anthropogenic activities depress for IEPOX formation as IEPOX yield drops rapidly with increasing  $\text{NO}$ . Anthropogenic emissions, however, may enhance the iSOA yield from IEPOX because its uptake on surfaces is likely dependent on the aerosol pH and sulfur content (Minerath and Elrod, 2009; Surratt et al., 2007). This may explain part of the variability of the reported SOA biogenic yields, ranging from negligible (de Gouw et al., 2005) to potentially dramatic (Tunved et al., 2006). Given the enormous flux of IEPOX, the chemistry presented here may also resolve part of the intriguing discrepancy between bottom-up (10 to 70 Tg/year) and top-down (140 to 910 Tg/year) estimates of global SOA production (Goldstein and Galbally, 2007). Nevertheless, IEPOX is expected to undergo hundreds of collisions with aerosol surfaces before reacting with  $\text{OH}$ , and its detection in the atmosphere (Fig. B.8) suggests that a complex suite of conditions likely controls its uptake to aerosols (e.g., the pH and chemical composition of aerosol). Further-



more, iSOA formation may depend on the unquantified differences in the yields and uptake characteristics of the  $\beta$ - and  $\delta$ -IEPOX. Quantitative understanding of these complex interactions is required to assess the effect of this chemistry on the overall SOA abundance and its associated impacts (e.g., cloud condensation nuclei (Kerminen et al., 2005)).

The efficient formation of dihydroxyepoxides, a previously unknown class of gas-phase compounds, addresses many of the issues currently being debated about isoprene chemistry. Because their formation is accompanied by the reformation of OH, this chemistry contributes to the remarkable stability of HO<sub>x</sub> in remote regions of the troposphere subjected to high isoprene emissions. The formation of IEPOX also provides a gas-phase precursor for the iSOA formation. Further investigation of the multiphase chemistry of IEPOX is needed to elucidate the complex interaction between emissions from the biosphere and atmospheric composition (Went, 1960; Andreae and Crutzen, 1997). In particular, the development of a proper chemical description of these interactions is essential for assessing the sensitivity of this chemistry to changes in isoprene emissions caused by environmental changes (e.g., climate change and deforestation) and to the further development of anthropogenic activities and the accompanying NO<sub>x</sub> emissions in these regions.

### 3.5 Acknowledgements

We thank X. Levine, H. O. T. Pye, and the Harvard GEOS-Chem team (Daniel J. Jacob, principal investigator) for their help in setting up the GEOS-CHEM model; A. J. Kwan, A. W. Chan, P. S. Chhabra, and N. Eddingsaas for experimental assistance; J. D. Surratt for providing the speciation of the SOA resulting from BEPOX reactive uptake; and J. Lane, I. Maxwell-Cameron, and S. Jørgensen for helpful discussions regarding the quantum calculations. F.P. was partially supported by the William and Sonya Davidow fellowship. J.D.C. thanks the EPA Science to Achieve Results (STAR) Fellowship Program (FP916334012) for providing partial support. The mass spectrometer used in this study was purchased as part of a major research instrumentation grant from the National Science Foundation (ATM-0619783). Assembly and testing of the CIMS instrument was supported by the Davidow Discovery Fund. The numerical simulations for this research were performed on Caltech's Division of Geological and Planetary Sciences Dell Cluster. This work was supported by the Office of Science (Biological and Environmental Research), U.S. Department of Energy grant DE-FG02-05ER63983, U.S. Environmental Protection Agency STAR agreement RD-833749, and the Marsden Fund administered by the Royal Society of New Zealand. The TC4 and ARCTAS campaigns were supported by NASA grants NNX07AL33G and NNX08AD29G. This work

has not been formally reviewed by the EPA. The views expressed in this document are solely those of the authors, and the EPA does not endorse any products or commercial services mentioned in this publication.

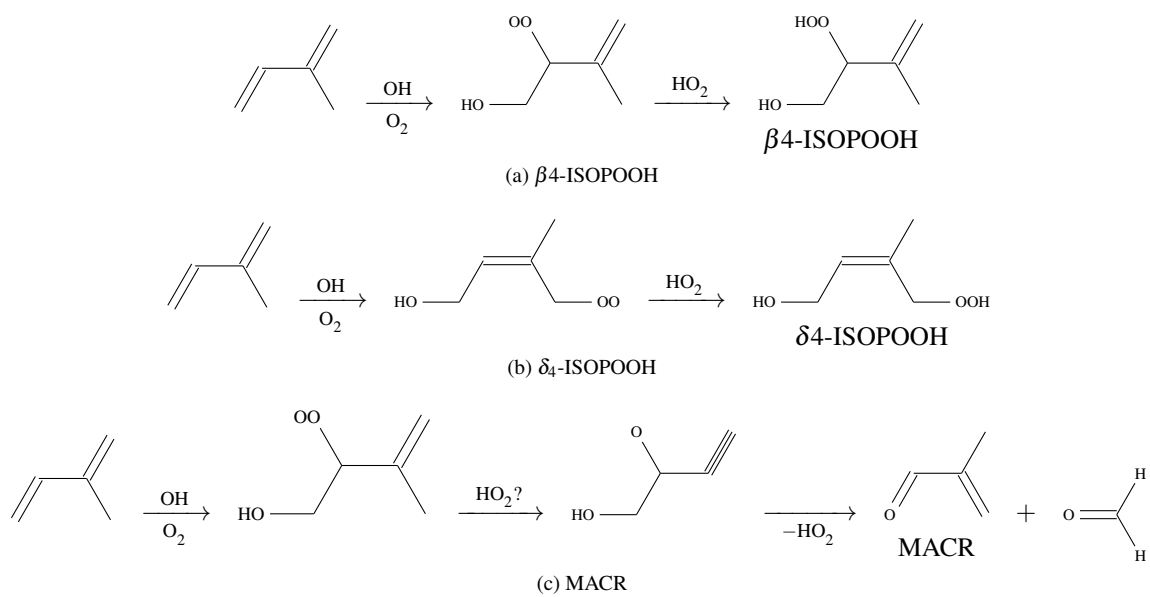


Figure 3.1: Fate of isoprene peroxy radicals

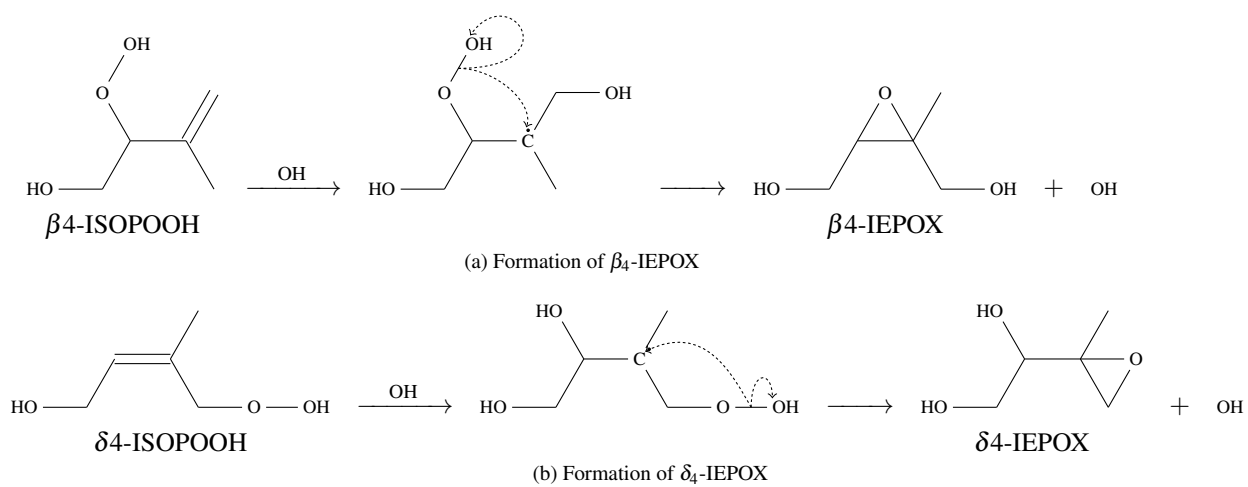


Figure 3.2: IEPOX formation mechanisms

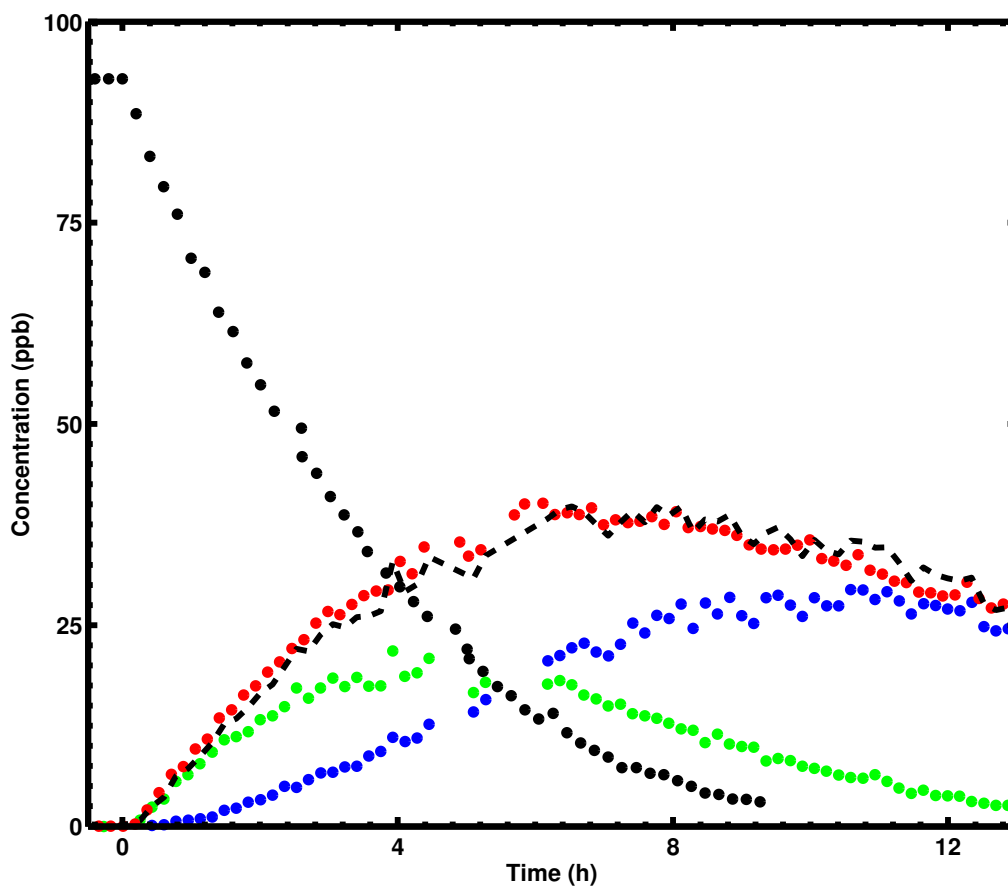


Figure 3.3: Consecutive formation of ISOPOOH and IEPOX in the photooxidation of isoprene. Following the time when the photolysis of hydrogen peroxide [initially 1.66 parts per million by volume (ppmv)] begins ( $t = 0$ ), isoprene (black dotted line) decays quickly. ISOPOOH and then IEPOX are detected as major products of the oxidation of isoprene [because they are isobaric, they both are detected at  $m/z = 203$  (red), the cluster of these compounds with  $\text{CF}_3\text{O}^-$ ]. Tandem mass spectroscopy provides for separation of the  $m/z = 203$  signal: ISOPOOH (green) is observed as the  $m/z = 63$  daughter, whereas IEPOX (blue) is observed as the  $m/z = 183$  daughter. The sum of IEPOX and ISOPOOH is indicated by the dashed black line.

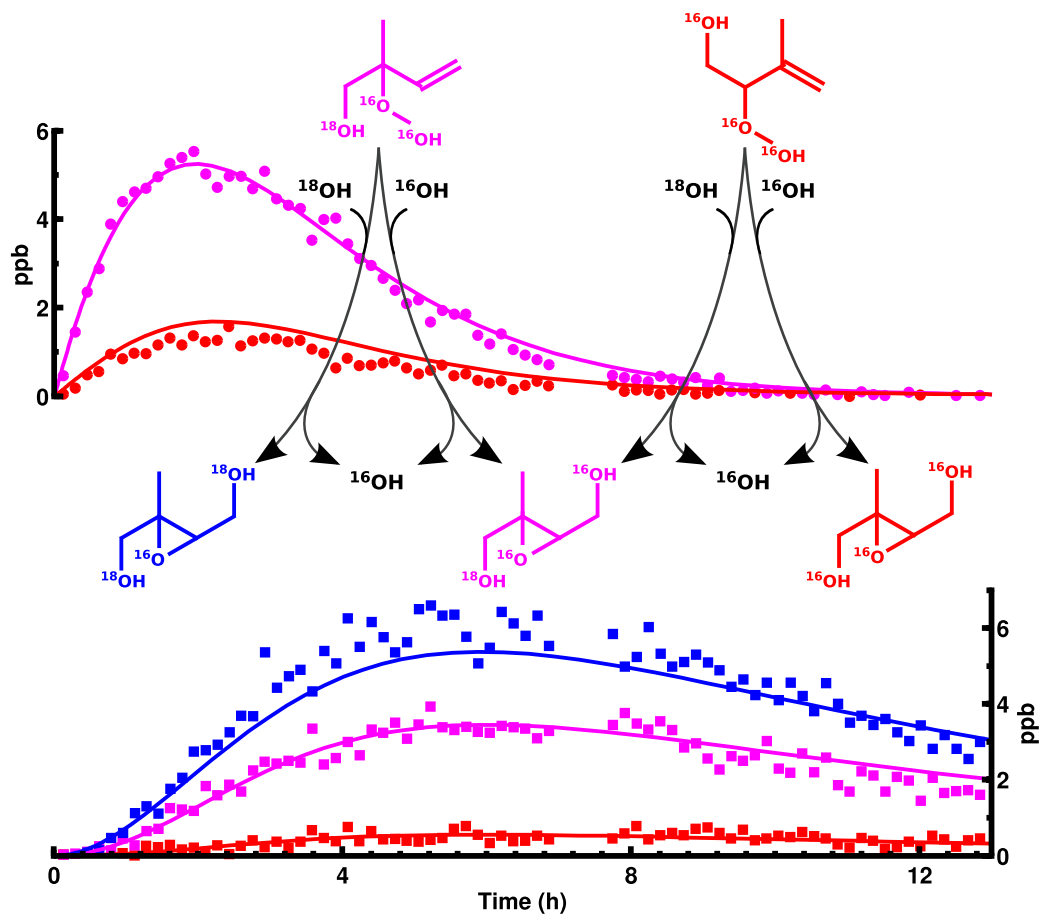


Figure 3.4: Formation of light and heavy ISOPOOH and IEPOX in the oxidation of isoprene using  $\text{H}^{18}\text{O}^{18}\text{OH}$  as the OH source. Formation of ISOPOOH is monitored via the daughter  $m/z = 63$  (circles) of  $m/z = 203$  (red) and  $m/z = 205$  (magenta). Formation of IEPOX is monitored via the loss of HF (squares) from  $m/z = 203$ ,  $m/z = 205$ , and  $m/z = 207$  (blue). Formation of isotopically light ISOPOOH and IEPOX reflects OH reformation. Solid lines represent the modeled mixing ratios for the different isomers. Isoprene initial concentration was 23.5 parts per billion by volume (ppbv), and  $^{18}\text{OH}$  was generated from the photolysis of  $\text{H}^{18}\text{O}^{18}\text{OH}$  (1.75 ppmv initial concentration, UV lights on at  $t = 0$ ).

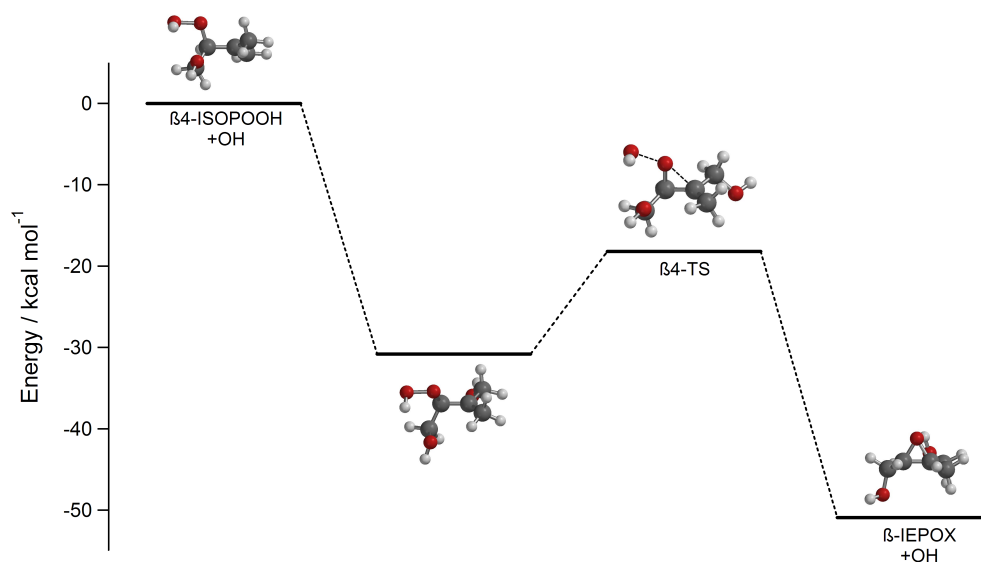


Figure 3.5: Relative energies for the formation of  $\beta$ -IEPOX from  $\beta$ 4-ISOPROOH (Fig. 3.2a). The alkylradical resulting from the addition of OH onto the  $\beta$ 4-ISOPROOH double bond is formed with enough excess energy ( $\sim 30 \text{ kcal/mol}$ ) that it quickly decomposes to the  $\beta$ -IEPOX + OH via the  $\beta$ 4-transition state. Energies are calculated with the CCSD(T)-F12/VDZ-F12 explicitly correlated method at the B3LYP/cc-pVTZ optimized structures (see Appendix B.2).

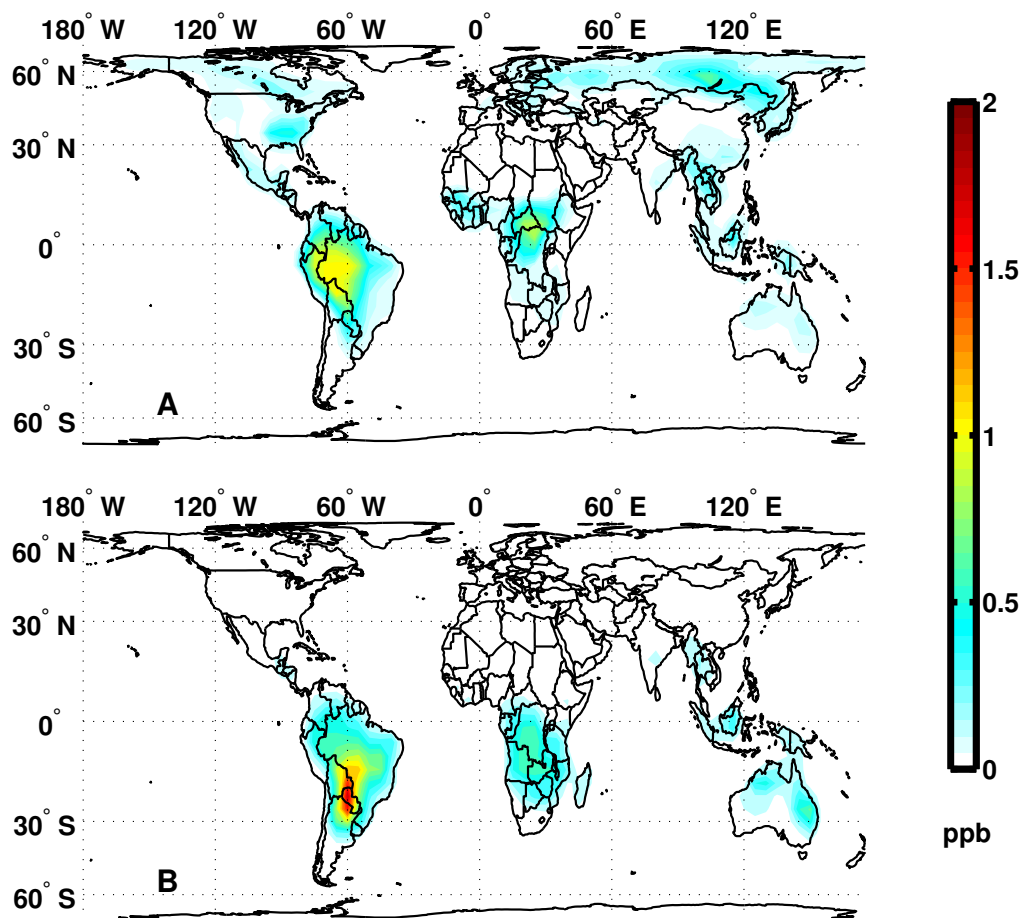


Figure 3.6: Simulated daily distribution of IEPOX in the planetary boundary layer during the Northern Hemisphere summer (A) and winter (B). IEPOX seasonal cycle mirrors the isoprene emissions. The mixing ratio of IEPOX is higher in the tropics than in other isoprene production regions in the northern mid-latitudes (e.g., the southeast United States). This reflects the reduction in the yield of IEPOX from isoprene due to anthropogenic emissions of NO.



## Chapter 4

# Importance of secondary sources in the atmospheric budgets of formic and acetic acids<sup>1</sup>

---

<sup>1</sup>Adapted with permission from Paulot, F.; Wunch, D.; Crounse, J. D.; Toon, G. C.; Millet, D. B.; DeCarlo, P. F.; Vigouroux, C.; Deutscher, N. M.; González Abad, G.; Notholt, J.; Warneke, T.; Hannigan, J. W.; Warneke, C.; de Gouw, J. A.; Dunlea, E. J.; De Mazière, M.; Griffith, D. W. T.; Bernath, P.; Jimenez, J. L. & Wennberg, P. O. Importance of secondary sources in the atmospheric budgets of formic and acetic acids *Atmos. Chem. Phys.*, 2011, 11, 1989-2013 ©2011 by the Authors.

## 4.1 Abstract

We present a detailed budget of formic and acetic acids, two of the most abundant trace gases in the atmosphere. Our bottom-up estimate of the global source of formic and acetic acids are  $\sim 1200$  and  $\sim 1400$  Gmol/yr, dominated by photochemical oxidation of biogenic volatile organic compounds, in particular isoprene. Their sinks are dominated by wet and dry deposition. We use the GEOS-Chem chemical transport model to evaluate this budget against an extensive suite of measurements from ground-, ship- and satellite-based Fourier transform spectrometers, as well as from several aircraft campaigns over North America. The model captures the seasonality of formic and acetic acids well but generally underestimates their concentration, particularly in the Northern midlatitudes. We infer that the source of both carboxylic acids may be up to 50% greater than our estimate and report evidence for a long-lived missing secondary source of carboxylic acids that may be associated with the aging of organic aerosols. Vertical profiles of formic acid in the upper troposphere support a negative temperature dependence of the reaction between formic acid and the hydroxyl radical, as suggested by several theoretical studies.

## 4.2 Introduction

Formic ( $\text{HCOOH}$ , hereafter FA) and acetic ( $\text{CH}_3\text{COOH}$ , hereafter AA) acids are among the most abundant and ubiquitous trace gases in the atmosphere. They have been detected in remote, rural, polar, marine and urban environments in the gas-phase as well as in clouds and in aerosols (Keene and Galloway, 1988; Chebbi and Carlier, 1996; Khare et al., 1999).

Sources of FA and AA include direct emissions from biomass burning, biofuel, fossil fuel, soil, vegetation, as well as secondary production from gas-phase and aqueous photochemistry (Chebbi and Carlier, 1996; Khare et al., 1999). Measurements of the isotopic composition of FA and AA have shown that they are primarily composed of modern carbon (Glasius et al., 2000; Glasius et al., 2001), consistent with major biogenic and biomass burning sources. Furthermore, most field measurements show a remarkable correlation between FA and AA, suggesting similar sources. The sources of FA and AA remain, however, very poorly understood and several investigations (Poisson et al., 2000; von Kuhlmann et al., 2003b; Ito et al., 2007) have pointed to large inconsistencies between measurements and model predictions.

Sinks of FA and AA are better understood. Both acids are relatively long-lived in the gas-phase with respect to OH photooxidation ( $\tau_{\text{FA}} \simeq 25$  days and  $\tau_{\text{AA}} \simeq 10$  days at  $T = 260\text{K}$  and  $[\text{OH}] = 10^6 \text{ molec/cm}^3$ ).

Because both gases are very soluble, their primary atmospheric sink is thought to be deposition (Chebbi and Carlier, 1996). Irreversible uptake on dust can also be an important regional sink (Falkovich et al., 2004).

Better constraints on the budget of FA and AA are important to understand patterns of rain acidity particularly in remote regions (Galloway et al., 1982). More generally, since FA and AA are major trace gases in the atmosphere and have few anthropogenic sources, the study of their budget offers a glimpse at the interaction between the biosphere and the atmosphere.

In this work, we derive a detailed inventory of FA and AA sources and sinks. We then use a chemical transport model to evaluate the resulting budget against measurements from an extensive suite of ground-, aircraft- and satellite-based measurements. Major discrepancies between the model and the measurements are investigated and several avenues for further research are discussed.

## 4.3 Global budget

We use the GEOS-Chem global 3-D chemical transport model (Bey et al., 2001) to investigate the budget of FA and AA. In the standard GEOS-Chem mechanism (v8.3), photochemical sources of AA include ozonolysis of isoprene and reaction of peroxyacyl radicals with  $\text{HO}_2$  and other peroxy radicals ( $\text{RO}_2$ ), while sinks are limited to its reaction with OH. FA is not treated explicitly.

In the following, we describe the sources and sinks of FA and AA and their implementation into the GEOS-Chem framework. In this work, the model is driven by the GEOS-5 assimilated meteorology from the NASA Goddard Earth Observing System. The horizontal resolution is degraded here to  $4^\circ \times 5^\circ$  and the vertical resolution to 47 vertical layers. The model is run from 2004 to 2008 following a one-year spin-up.

### 4.3.1 Emissions

#### 4.3.1.1 Terrestrial vegetation

Terrestrial vegetation emits both FA and AA (e.g., Kesselmeier, 2001). Emissions by trees are triggered by light and are well correlated with the transpiration rate. In contrast, crops have been reported not to emit detectable amounts of FA or AA (Kesselmeier et al., 1998). FA emissions by plants are related to the  $\text{C}_1$  pathway, ethene synthesis and photo-respiration (Kesselmeier and Staudt, 1999). The emission of AA by plants occurs as the result of the hydrolysis of acetyl-coA, a product of the degradation of fats and carbohydrates (Kesselmeier and Staudt, 1999).

We use the Model of Emissions of Gases and Aerosols from Nature (MEGAN) v2.1 (Guenther et al., 2006), implemented in GEOS-Chem as described by Millet et al. (2010), to compute biogenic emissions from each GEOS-Chem grid cell (E):

$$E = \gamma \sum_i \varepsilon_i \chi_i$$

where the sum is over the number of plant functional types with baseline emission factor,  $\varepsilon$ , and fractional coverage,  $\chi$ . For both FA and AA,  $\varepsilon$  are  $30 \mu\text{g}/(\text{m}^2.\text{h})$  for trees and shrubs and  $4.8 \mu\text{g}/(\text{m}^2.\text{h})$  for crops (Guenther et al., 2000, updated on the basis of recent measurements (A. Guenther, personal communication)). The emission activity factor,  $\gamma$ , accounts for the variability in the local environment (e.g., temperature, light, leaf area, soil moisture). In particular for FA and AA:

$$\gamma = \exp(\beta(T - 303)) \gamma_{(other)} \text{ with } \beta = 0.08 \text{ and } T \text{ in K}$$

where  $\gamma_{(other)}$  is described in Millet et al. (2010) and T is the current leaf temperature.

#### 4.3.1.2 Biomass burning and biofuel

Both FA and AA have been measured in biomass burning plumes (Goode et al., 2000; Christian et al., 2003; Yokelson et al., 2009). We estimate biomass burning emissions of FA and AA from biomass burning emissions inventory (GFEDv2 (Randerson et al., 2006)) using the emission factors (EF) summarized in Table 4.1. Emissions from biofuels are calculated in the same way using the CO emission inventory from Yevich and Logan (2003).

We note that the emission factors used in this study are generally smaller than the ones reported by Andreae and Merlet (2001) for FA but larger for AA. These changes reflect the very large variability in the reported emission factors.

#### 4.3.1.3 Fossil fuel

Emissions of FA and AA from motor vehicles were first measured by Kawamura et al. (1985). Here we estimate fossil fuel FA and AA from CO fossil fuel emissions (Duncan et al., 2007), scaled by the emission ratios derived by Talbot et al. (1988) at the Hampton Roads Bridge Tunnel (Virginia):  $2.1 \times 10^{-4}$  FA per CO and  $4.2 \times 10^{-4}$  AA per CO.

#### 4.3.1.4 Agricultural emissions

Large emissions of acetic acid are associated with intensive animal farming (from both cattle and cattle waste (Shaw et al., 2007)). Ngwabie et al. (2008) used the correlation between AA and ammonia to derive emission factors ( $2 \times 10^{-3}$  - 0.2 gC/gNH<sub>3</sub>) and a global estimate of AA emissions from cattle (4–17 Gmol/yr). Using an emission factor of 0.1 gC/gNH<sub>3</sub> and the anthropogenic emissions of ammonia (Bouwman and Hoek, 1997) located on agricultural lands, we estimate the global soil emissions of AA to be  $\sim 40$  Gmol/yr.

Ethanol, which has nearly the same molecular weight as FA, is a major emission of cattle farming. This makes it difficult to quantify the emissions of FA by proton transfer mass spectrometry (PTRMS), the most common technique for these investigations. We assume that the emissions of FA (in moles) are equal to the emissions of AA. This corresponds to 40% of the upper estimate of ethanol global emissions by Ngwabie et al. (2008).

Both FA and, to a lesser extent, AA farming emission estimates are larger than those from Ngwabie et al. (2008) and probably represent upper estimates. However, the contribution of agricultural activities to the FA and AA budget is likely to be underestimated, as one can expect FA and AA production from the photooxidation of volatile compounds emitted as a result of farming activities but not represented in the model.

#### 4.3.1.5 Soil

FA and AA production by soil bacteria is well documented, with soil concentrations ranging from 2 to 5 mol/m<sup>3</sup> (Sposito, 1989, p. 66). The few studies of FA and AA emissions (Sanhueza and Andreae, 1991; Enders et al., 1992) suggest that soil emission is an important source of acids where production from terrestrial vegetation is low.

Sanhueza and Andreae (1991) reported emissions of FA (AA) of  $\sim 0.4$  nmol/(m<sup>2</sup>s) (0.2 nmol/(m<sup>2</sup>s)) at noon over dry savanna soil. Emissions of both acids were found to be temperature dependent. Here we approximate the temperature dependence reported by Sanhueza and Andreae (1991) using an exponential law:

$$E_{FA}^{dry}(\text{savanna}) = 1.7 \times 10^{-3} \times (\exp(0.119 \times T) - 1) \quad T > 0^\circ\text{C} \quad (R^2 = 0.66)$$

$$E_{AA}^{dry}(\text{savanna}) = 2.5 \times 10^{-3} \times (\exp(0.091 \times T) - 1) \quad T > 0^\circ\text{C} \quad (R^2 = 0.50)$$

where  $T$  is the soil temperature in  $^{\circ}\text{C}$  and  $E_X$  is the emission of the acid in  $\text{nmol}/(\text{m}^2\text{s})$ . This corresponds to an average emission of  $\overline{E_{\text{FA}}} = 1.8 \times 10^{-1} \text{ nmol}/(\text{m}^2\text{s})$  and  $\overline{E_{\text{AA}}} = 8.4 \times 10^{-2} \text{ nmol}/(\text{m}^2\text{s})$  over the  $30^{\circ}\text{C}$  to  $40^{\circ}\text{C}$  temperature range.

For a similar environment and using a much larger dataset, Yienger and Levy (1995) derived  $\overline{E_{\text{NO}}} = 1.89 \times 10^{-1} \text{ nmol}/(\text{m}^2\text{s})$ . We use the soil emissions of NO from Yienger and Levy (1995) in other environments to infer the emissions of FA and AA (Table 4.2). This assumes that the ratio between the emissions of FA (AA) and NO is independent of the environment type and that the emissions of FA and AA exhibit the same temperature dependence as the one measured by Sanhueza and Andreae (1991). Field measurements are clearly needed to assess these assumptions.

Because of the weak acidity of FA ( $\text{pK}_a = 3.75$ ) and AA (4.75), their soil emissions are likely to depend on soil pH under wet conditions. We assume that the emissions listed in Table 4.2 are at  $\text{pH} = \text{pK}_a(\text{FA/AA})$  and  $30^{\circ}\text{C}$ , i.e., that they correspond to half of the maximum emissions under wet conditions. Under these assumptions, the wet emissions are thus obtained by scaling the baseline wet emission by the following factor:

$$\exp\left(-\frac{\Delta H_X}{R}\left(\frac{1}{T_{\text{soil}}} - \frac{1}{303.15}\right)\right) \times \frac{2}{1+10^{\text{pH}-\text{pK}_{aX}}} \quad \text{with } X = \{\text{FA, AA}\}$$

where the soil pH is taken from the ISRIC World Soil Information Database (<http://www.isric.org>) and  $\Delta H$  is the heat of dissolution at 298 K.

Sanhueza and Andreae (1991) also reported an increase in AA emissions after watering the soil, while FA emissions were suppressed. The AA emission increase hints at the existence of water-stressed AA-producing microorganisms, similar to denitrifying bacteria (Davidson, 1992). Here, we use the same pulsing factors for AA as the one derived by Yienger and Levy (1995) for the soil emissions of NO. AA pulsing increases AA soil emissions by  $\sim 10\%$  globally.

## 4.3.2 Photochemical sources of formic and acetic acids

### 4.3.2.1 Terrestrial biogenic precursors

The oxidation of biogenic compounds, and in particular their ozonolysis, has been suggested to be a major source of FA and AA (Jacob and Wofsy, 1988; Neeb et al., 1997).

Here we update the photochemical oxidation mechanism of isoprene, a non-methane hydrocarbon which accounts for  $\sim 30\text{--}50\%$  of biogenic emissions (Guenther et al., 2006), to include sources of FA from prod-

ucts of its photooxidation with OH: hydroxyacetone, glycolaldehyde and isoprene nitrates (Butkovskaya et al., 2006a,b; Paulot et al., 2009a, see supplementary materials). Ozonolysis of methylvinylketone (MVK) and methacrolein (MACR), two major products of isoprene photooxidation, are also known to yield FA (Aschmann et al., 1996; Grosjean et al., 1993). In contrast, isoprene photochemistry has long been thought to be an insignificant source of AA (Jacob and Wofsy, 1988). Recent experimental evidence suggests, however, that the photooxidation of hydroxyacetone produces significant amounts of AA (Butkovskaya et al., 2006b) at low temperature. Isoprene is also a significant source of peroxy acetyl radical (PA), which reacts with HO<sub>2</sub> to yield AA with a yield of 15% (Hasson et al., 2004; Dillon and Crowley, 2008).

The OH-oxidation of methylbutenol (MBO), a volatile organic compound emitted in large quantities by coniferous trees (Harley et al., 1998), also yields glycolaldehyde and hydroxymethylpropanal (HMPR), a precursor of acetone (Carrasco et al., 2006), and thus of AA via PA. MBO ozonolysis has also been shown to yield FA as well as acetone and HMPR (Carrasco et al., 2007).

The OH-oxidation of various monoterpenes has been reported to produce FA. However, the yield remains very uncertain. For instance, reported FA yields from the OH-oxidation of  $\alpha$ -pinene range from 7% (Orlando et al., 2000) to 28% (Larsen et al., 2001). Yields greater than 50% have been reported for limonene (Larsen et al., 2001). Ozonolysis of various monoterpenes also yields FA and AA (Lee et al., 2006). Monoterpenes are lumped into one species, MONX, in the GEOS-Chem chemical mechanism. We adopt a FA yield of 15.5% for the reaction of MONX with OH and a FA (AA) yield of 7.5% (8%) for its ozonolysis. The formation of carboxylic acids in the oxidation of MONX by OH has been ascribed to the reaction of stabilized  $\alpha$ -hydroxyalkyl radicals with NO (Orlando et al., 2000; Larsen et al., 2001). However, Peeters et al. (2001) calculated that this reaction is only competitive with their thermal decomposition to aldehyde + HO<sub>2</sub> under laboratory conditions (NO  $\sim$  1–10 ppmv), suggesting that the yield of FA from the first steps of MONX photooxidation is negligible (Peeters et al., 2001; Capouet et al., 2004). Conversely, the very simplified representation of MONX secondary photochemistry in GEOS-Chem may result in an underestimate of their overall FA/AA forming potential.

The OH-oxidation of acetaldehyde, whose sources include large emissions from the terrestrial and marine biosphere (Millet et al., 2010), is an important source of AA via PA+HO<sub>2</sub>. The modifications to the GEOS-Chem mechanism are summarized in Table C.4.

#### 4.3.2.2 Marine precursors

Ozonolysis of marine biogenic emissions has been suggested to provide a source of FA and AA in the marine atmosphere (Arlander et al., 1990; Sanhueza et al., 1996; Baboukas et al., 2000).

In this study, we include monthly marine emissions of isoprene, acetaldehyde, ethene and larger alkenes. Acetaldehyde marine emissions ( $\sim 1.3$  Tmol/yr) are from Millet et al. (2010) and isoprene sources are from Arnold et al. (2009) (top-down estimate: 28 Gmol/yr). Emissions of ethene (162 Gmol/yr) and larger alkenes (164 Gmol/yr) are inferred from isoprene emissions using the flux ratios observed by Broadgate et al. (1997).

#### 4.3.2.3 Anthropogenic/biomass burning precursors

In addition to fresh emissions from biomass burning or anthropogenic sources, production of FA and AA within fire plumes has been measured in many (Goode et al., 2000; Gao et al., 2003; Yokelson et al., 2003; Herndon et al., 2007), but not all instances (de Gouw et al., 2006). Here, we include formation of FA and AA from the photooxidation of acetylene (Hatakeyama et al., 1986), ethene and propene (and higher alkenes).

Anthropogenic inventories for CO are described by Bey et al. (2001) and biofuel emissions by Yevich and Logan (2003). Recent updates of these inventories are described by Millet et al. (2010). Emissions and photooxidation of acetylene, propene and ethene, which are precursors of FA and AA, were recently included or updated by Fu et al. (2008). In addition we include biomass burning emission of hydroxyacetone and glycolaldehyde (Fu et al., 2008), two precursors of FA and AA.

#### 4.3.3 Sources not treated

Graedel and Eisner (1988) estimate that emissions of FA from formicine ants could exceed motor vehicle and biomass burning emissions. The overall contribution of formicine ants to the FA budget is, however, likely to be limited (Chebbi and Carlier, 1996), but may be important in ecosystems where formicine ants are abundant (e.g., tropical forests).

Aqueous phase oxidation of formaldehyde within clouds has been proposed to be a non-negligible source of FA in remote environments (Chameides, 1984; Jacob, 1986). However Lelieveld and Crutzen (1991) argued that the very fast aqueous oxidation of FA would greatly diminish the role of cloud chemistry as a source of FA.

The source of FA and AA from enol photochemistry is not included in the model (Archibald et al., 2007). Enol are known intermediates in combustion (Taatzes et al., 2005) and could originate from keto-enol

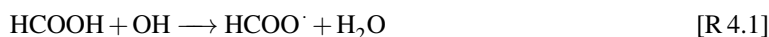


tautomerizations catalyzed by carboxylic acids (da Silva, 2010). However, the importance of these processes as a source of FA and AA is poorly known and additional experimental constraints are needed to include these processes in a global model.

### 4.3.4 Sinks

#### 4.3.4.1 Photochemical

FA reacts with OH primarily via abstraction of the acidic hydrogen with a recommended temperature independent rate of  $4.5 \times 10^{-13} \text{ cm}^3/(\text{molec.s})$  (Atkinson et al., 2006). The uncertainty of this rate coefficient is relatively large ( $\Delta \log = 0.15$  at 298 K (Atkinson et al., 2006)) because of experimental challenges (dimerization of FA). To our knowledge, this rate coefficient has not been determined below 298 K. Theoretical calculations suggest, however, that the acidic ([R 4.1]), dominant at ambient temperature, and formyl ([R 4.2]) channels have opposite temperature dependence (Galano et al., 2002; Sun and Saeys, 2008).



This results in a relatively “flat” temperature profile near 298 K where the laboratory investigations were conducted but a strong negative temperature dependence at lower temperature. This will be examined in Section 4.5.3.

In contrast, the AA reaction with OH has been studied over a much wider temperature range. The reaction follows a mechanism similar to FA (Butkovskaya et al., 2004) and exhibits a negative activation energy. The temperature dependence remains uncertain and we use the IUPAC recommendation,  $4.2 \times 10^{-14} \exp(855/T) \text{ cm}^3/(\text{molec s})$  ( $\Delta \log = 0.15$  at 298 K) (Atkinson et al., 2006), which is in excellent agreement with the two most recent determinations of this reaction rate coefficient (Butkovskaya et al., 2004; Huang et al., 2009).

#### 4.3.4.2 Dry deposition

Dry deposition of oxidants and water soluble species is computed using a resistance-in-series model based on the formulation of Wesely (1989) implemented in GEOS-Chem by Wang and Jacob (1998). The dry

deposition velocities of FA and AA depend on surface momentum and sensible heat fluxes, temperature and solar radiation, as well as the effective Henry's constant of FA and AA ( $\mathcal{H}$ ), which are calculated at a pH of 7—a reasonable assumption for most surfaces (Wesely, 1989). We use the median of the reported measurements:  $\mathcal{H}_{FA} = 5400 \text{ M/atm}$ ,  $\mathcal{H}_{AA} = 5350 \text{ M/atm}$  (Sander, 1999).

#### 4.3.4.3 Wet deposition

Wet deposition is thought to be the most important sink of FA and AA (Chebbi and Carlier, 1996). The GEOS-Chem wet deposition scheme includes scavenging of soluble tracers in convective updrafts, as well as rainout and washout of soluble tracers (Mari et al., 2000; Liu et al., 2001). We assume a rain pH of 5 and that the acids are fully retained at freezing, as with  $\text{HNO}_3$ .

We modify the GEOS-Chem deposition scheme to include the uptake of FA and AA in ice clouds. Briefly, assuming equilibrium between the ice surface concentration  $[X]_s$  (molec/cm<sup>3</sup>) and the gas-phase concentration  $[X]_g$  (molec/cm<sup>3</sup>), non-dissociative uptake and non-competitive adsorption,  $[X]_s$  can be related to the surface area of ice ( $S_{ice}$  (cm<sup>2</sup>/cm<sup>3</sup>)), the maximum number of molecules which can be adsorbed on the surface ( $N_{max}$  (molecules/cm<sup>2</sup>)) and the fractional coverage ( $\theta$ ) by:

$$[X]_s = S_{ice} \theta N_{max}$$

$\theta$  is given by the Hill-Langmuir equation:

$$\theta = \frac{\frac{K}{N_{max}} [X]_g}{1 + \frac{K}{N_{max}} [X]_g}$$

where  $K$  (cm) is a temperature-dependent partition coefficient:  $K = \alpha \times \exp(\beta/T)$  with  $\alpha_{FA} = 5.8 \times 10^{-11} \text{ cm}$ ,  $\alpha_{AA} = 1.0 \times 10^{-10} \text{ cm}$  and  $\beta_{FA} = 6500 \text{ K}$ ,  $\beta_{AA} = 6600 \text{ K}$  (Marécal et al., 2010; Crowley et al., 2010).

#### 4.3.4.4 Dust

Field measurements have identified formate and acetate on collected mineral aerosols (Lee et al., 2000; Lee et al., 2002; Russell et al., 2002; Falkovich et al., 2004). Falkovich et al. (2004) found that formate and acetate were the most abundant mono carboxylic anions in dust particles and that their uptake was facilitated at higher relative humidity (RH).

Consistent with these observations, efficient uptake of carboxylic acids on various components of dust (Usher et al., 2003) has been measured: FA on clay (montmorillonite) (Hatch et al., 2007) and  $\text{CaCO}_3$  (Al-Hosney et al., 2005); AA on  $\text{SiO}_2$ ,  $\alpha - \text{Al}_2\text{O}_3$ ,  $\alpha - \text{Fe}_2\text{O}_3$  (Carlos-Cuellar et al., 2003) and  $\text{CaCO}_3$  (Prince et al., 2008). Increased water enhances the capacity of the mineral dust to take up carboxylic acids (Al-Hosney et al., 2005; Hatch et al., 2007; Prince et al., 2008) but does not change the accommodation coefficient ( $\gamma$ ) significantly.

Surface saturation needs to be explicitly treated, as it severely reduces the efficiency of this removal mechanism (Hatch et al., 2007). Accounting for the saturation limit, Hatch et al. (2007) estimated that up to 40% of gaseous AA could be removed during a dust storm.

In GEOS-Chem, dust is carried into four different size bins. Here we use emissions from the dust entrainment and deposition (DEAD) scheme (Zender et al., 2003; Fairlie et al., 2007). From Hatch et al. (2007), we use  $\gamma_{\text{FA}} = 4 \times 10^{-4}$  and  $\gamma_{\text{AA}} = 3 \times 10^{-4}$  for  $\text{RH} < 30\%$ ;  $\gamma_{\text{FA}} = 5.4 \times 10^{-4}$  and  $\gamma_{\text{AA}} = 14 \times 10^{-4}$  for  $\text{RH} \geq 30\%$ . The dependence of surface saturation ( $S$  in  $\text{mg}(\text{acid})/\text{g}(\text{dust})$ ) on  $\text{RH}$  is approximated by fitting an exponential to Hatch et al. (2007) measurements:  $S_{\text{FA}} = 2 + 4.7 \times (1 - \exp(-8.6 \times 10^{-3} \times \text{RH}))$  and  $S_{\text{AA}} = 2 + 5.8 \times (1 - \exp(-2.6 \times 10^{-2} \times \text{RH}))$ . Heterogeneous degradation of FA (Al-Hosney et al., 2005) and AA (Prince et al., 2008) to  $\text{CO}_2$  is not represented but may further enhance the uptake of FA and AA.

### 4.3.5 Simulated distribution

#### 4.3.5.1 Formic acid

The total source of formic acid in the model is about 1200 Gmol/yr (Table 4.3). This is about twice as large as previous estimates (Ito et al., 2007; von Kuhlmann et al., 2003b). Modeled FA sources are dominated by photochemical production from the oxidation of biogenic precursors. More than a third of the FA photochemical source stems from glycolaldehyde and hydroxyacetone via the Butkovskaya's mechanism (Butkovskaya et al., 2006a,b). These sources were not included in previous estimates and account for much of the difference (Table 4.3). Other important sources include isoprene ozonolysis (14% of the photochemical production) and monoterpenes photooxidation (6%). Acetylene is the dominant non-biogenic precursor (6.5%).

Over three quarters of FA photochemical production is derived from isoprene photooxidation, many aspects of which remain uncertain. In particular, it is worth noting that the mechanism recently proposed by

Peeters et al. (2009) results in large modifications of the distribution of isoprene photooxidation products determined from chamber experiments (including hydroxyacetone and glycolaldehyde). If correct, this could significantly affect the modeled budget of FA. Nevertheless, despite our incomplete knowledge of isoprene photooxidation, its representation in the GEOS-Chem mechanism is much more explicit than for most other biogenic volatile organic compounds. This probably results in an overestimation of the importance of isoprene as a precursor for FA as the photooxidation of other biogenic volatile organic compounds, such as the different monoterpenes, is much more simplified.

Direct emissions of FA are small ( $\sim 15\%$ ) and dominated by terrestrial vegetation and biomass burning. Emissions from vehicles do not contribute significantly to the modeled FA budget, consistent with observations from de Gouw et al. (2005). Our modeled FA budget suggests, however, that more than 90% of FA is composed of modern carbon globally (Table C.2). This percentage is lower in the northern mid and high latitudes, though FA is still predicted to be largely dominated by modern sources (Table C.2), consistent with isotope studies in Europe (Glasius et al., 2001).

The enhancement in FA ( $\Delta\text{FA}$ ) in aged biomass burning plumes and its correlation with  $\Delta\text{CO}$  has frequently been used to derive emission factors from ground- or satellite-based observations (e.g., Paton-Walsh et al., 2005; Rinsland et al., 2007; González Abad et al., 2009). Our study suggests that FA is rapidly removed from the boundary layer by wet and dry deposition, so that little FA emitted or formed in the boundary layer is advected over long distances or transported into the free troposphere. Therefore  $\Delta\text{FA}$  observed in aged plumes is unlikely to represent direct emissions, as commonly assumed, but rather the production of FA from the photooxidation of biomass burning emitted precursors. Thus,  $\Delta\text{FA}$  cannot be used, in general, to derive emission factors far away from emission regions.

FA sinks are dominated by depositions. Dust is not a significant sink globally but can result in a large decrease of acids in the vicinity of large deserts.

The modeled atmospheric lifetime of FA is 3.2 days, consistent with previous estimates (Chebbi and Carlier, 1996). The lifetime of FA in the boundary layer is about 1.6 days (excluding transport to the free troposphere).

The FA atmospheric mass is highest in the tropics ( $\sim 60\%$  of the global burden, Table C.2) as a result of large biogenic and biomass burning emissions (Fig. 4.1). Modeled mixing ratios in the Northern midlatitudes are low and follow the seasonal cycle of biogenic emissions.

#### 4.3.5.2 Acetic acid

The total source of acetic acid is about 1400 Gmol/yr (Table 4.3). Emissions of AA account for about one third of AA sources. The difference with FA stems from much larger direct emissions from biomass and biofuel burning. Secondary production from anthropogenic sources or biomass burning is small. AA production has, however, been observed in biomass burning plumes. For instance, Yokelson et al. (2003) observed  $\Delta\text{AA}/\Delta\text{CO}$  increase by as much as 9% in some biomass burning plumes and noted that the secondary production of AA exceeds the measured direct emissions. This observation cannot, however, be generalized since other plumes did not exhibit production of AA (de Gouw et al., 2006; Yokelson et al., 2009, and references therein). Yokelson et al. (2009) also noted that the growth of FA and AA in the Yucatan biomass burning plumes cannot be accounted for by the photochemistry of their known precursors, pointing to unidentified high-molecular-weight precursors. The importance of these precursors as a source of FA and AA will be investigated in Section 4.5.2.

Photochemical production is dominated by the reaction of PA with  $\text{HO}_2$  (53%) and other peroxy radicals (24%), with isoprene photochemistry and acetaldehyde oxidation the primary sources of PA. Our estimates are consistent with those of von Kuhlmann et al. (2003b) and Ito et al. (2007) but much lower than the estimate by Baboukas et al. (2000). Von Kuhlmann (2003b) pointed out that this is the result of the very high branching ratio for the production of AA from  $\text{PA}+\text{HO}_2$  assumed by Baboukas et al. (2000), inconsistent with values reported in recent laboratory experiments (e.g., Dillon and Crowley, 2008).

Similar to FA, deposition is the major sink of AA. Because AA is less soluble than FA and because its oxidation by OH is faster and has a negative temperature dependence, photooxidation of AA is much more important than for FA and contributes to the significantly shorter lifetime of AA in the atmosphere: 2.3 days (1.7 days in the boundary layer). AA is predicted to primarily consist of modern carbon globally (Table C.3). The distribution follows patterns similar to FA with a stronger influence of biomass and biofuel burning.

## 4.4 Comparison with observations

In this section, we evaluate the GEOS-Chem simulation against upper tropospheric and total column measurements of FA by solar absorption spectrometry in the infrared using a Fourier transform spectrometer (FTS) as well as FA and AA aircraft measurements. The locations of ground-based stations, the ship cruises- and aircraft-based measurements are indicated in Fig. 4.2.

#### 4.4.1 FTS measurements

FA can be measured by FTS using the Q-branch of the  $\nu_6$  mode near  $1105\text{ cm}^{-1}$ . In this section, we use FA total columns retrieved by ground-based stations of the Network for the Detection of Atmospheric Composition Change (NDACC, <http://www.ndacc.org/>, Kurylo and Solomon (1990)) as well as during several cruises by the German vessel Polarstern in the Atlantic ocean (Velazco et al., 2005). We also use upper tropospheric FA profiles measured by the space-borne Atmospheric Chemistry Experiment FTS (Bernath et al., 2005). All retrievals use the revised spectroscopic parameters for FA (Vander Auwera et al., 2007) contained in the HITRAN 2008 spectral database (Rothman et al., 2009).

##### 4.4.1.1 Ground-based total column

Solar spectra in the vicinity of the  $\nu_6$  vibration have been obtained by several stations of the NDACC: Barcroft in the Inyo National Forest (California) at 3800 m; Bremen in northwestern Germany; La Réunion 700 km east of Madagascar; Paramaribo on the coast of Suriname; Thule in northwestern Greenland; and Wollongong, 100 km south of Sydney. The different measurement sites and the cruise ship tracks are depicted in Fig. 4.2. Measurement uncertainty is estimated to be  $\sim 19\%$ . The choice of the spectral microwindow used to retrieve FA could result in a systematic bias in the retrieved FA as large as  $\pm 2.7 \times 10^{15}\text{ molec/cm}^2$ . A more detailed description of the FTS retrievals can be found in the supplementary materials (Figs. C.1 to C.4 and Table C.1).

#### Photooxidation of isoprene and other biogenic emissions: a major source of FA

The FA seasonal cycle at the mid-latitude stations, Wollongong (Fig. 4.3a, see also Fig. C.5), Bremen (Fig. 4.4b, see also Fig. C.6), and Barcroft (Fig. 4.4c, see also Fig. C.7, C.8 and C.9) is consistent with a major source of FA from terrestrial biogenic emissions and their photooxidation. At Wollongong, for instance, FA and biogenic emissions peak simultaneously in January. In contrast, CO and HCN total columns generally peak around October, at the height of the biomass burning season (Fig. C.5). At Barcroft, the strong correlation between FA and  $\text{CH}_2\text{O}$  in the summer months (Fig. C.7) also suggests a large influence of biogenic emissions on the FA budget. In contrast there is no correlation between FA and HCN. This interpretation is consistent with the conclusions of Zander et al. (2010) that FA seasonal variations above the Alpine plateau are the result of natural processes.

At all sites, the model predicts large contributions of biogenic photooxidation to the FA budget. The model performs best in regions and time periods impacted by large isoprene emissions, such as in Wollon-

gong (Fig. 4.3a) and La Réunion (Fig. 4.4a). Interestingly, the model predicts a biogenic peak in FA in May at La Réunion later than the maximum in isoprene emission in Southern Africa (Otter et al., 2002). Intense precipitations from January to April over La Réunion may explain this delay by efficiently scavenging FA (leading to a minimum in the modeled FA in January). As the climate becomes drier in May, the atmospheric lifetime of FA increases resulting in higher FA total columns in spite of lower isoprene emissions. This illustrates the complicated interplay between FA sources and sinks in the tropics. The model suggests La Réunion is especially sensitive to this effect, as the modeled FA total column is dominated by transport from Madagascar and Southern Africa.

In contrast, the model greatly underestimates FA at Bremen (Fig. 4.4b) and Barcroft (Fig. 4.4c). These stations exhibit a marked biogenic signature but are located in regions with lower isoprene emissions. This likely reflects a missing biogenic precursor of FA in the model. In these regions, FA production may be promoted by seasonal biotic emissions from cattle and crop farming (Karl et al., 2009) associated with elevated ozone due to anthropogenic activities. The anthropogenic contribution to FA is predicted to be low at both sites (less than 5%), consistent with the seasonal profile of FA and previous isotope measurements in Europe (Glasius et al., 2000; Glasius et al., 2001).

We note that Barcroft data must be interpreted cautiously as the complicated topography of the region is not resolved in the model. In particular summer FA total columns show evidence for boundary layer incursions which are not captured at the coarse resolution used in this study. However, CH<sub>2</sub>O seasonality is surprisingly well-captured in the model despite a low-bias in the summer (Fig. C.8). Therefore, meteorology alone is unlikely to explain the large discrepancy between the model and the data over this site, and sources from the Central Valley (150 km to the west of Barcroft) are likely underestimated.

### **Missing biomass burning precursors**

Evidence for a large but more localized and seasonal biomass burning source of FA can be found in the Wollongong and La Réunion records (Figs. 4.3a and 4.4a). In La Réunion, FA peaks in October. This peak is also observed in CO and CH<sub>2</sub>O FTS measurements at the same location and is associated with biomass burning in Southern Africa (CO) and Madagascar (CO and CH<sub>2</sub>O) (Vigouroux et al., 2009). In Wollongong, the anomalously high FA total column measured in December 2006, the largest on the record, is also associated with biomass burning, since a) it clearly precedes the biogenic peak in FA observed in other years, b) very large bush fires burned over 1 million acres from December 2006 to January 2007 in the Victorian Alps ~ 450 km southwest of Wollongong, and c) anomalously high CO and HCN columns

are recorded during the same time period (Fig. C.5). This is consistent with the work of Paton-Walsh et al. (2005) who reported a significant correlation between aerosol optical depth and FA at the same site during bush fires from 2001 to 2003 and inferred that biomass burning could result in a strong enhancement in FA total column at this site.

The model captures the timing of the biomass burning contribution to the FA column well but underestimates FA during biomass burning periods. The coarse resolution of the model is likely to contribute to this discrepancy due to the dilution of biomass burning plumes. However, the systematic discrepancy on a multi-year average at La Réunion may also indicate missing biomass burning sources of FA.

The discrepancy for marine sites (cruise (Fig. 4.5) and Paramaribo (Fig. 4.4d)) also hints at a missing biomass burning source of FA. Air masses affected by biomass burning emissions are known to be advected aloft from Africa to South America and their impact has been measured over Paramaribo during the dry season from August to November (Peters et al., 2004; Petersen et al., 2008). High CO measured in the tropics during cruises is also well correlated with FA ( $R = 0.64$ , Fig. C.10). The lifetime of FA is, however, incompatible with a large contribution of directly emitted FA to the FA total column over Paramaribo (transport time from Africa to Paramaribo has been estimated at 10 days by Peters et al. (2004)) and suggests a missing long-lived precursor from biomass burning. Sources of FA and AA from marine emissions are also likely to be underestimated since the model predicts surface concentrations which are 2 to 5 times lower than measurements made during cruises by Arlander et al. (1990) and Baboukas et al. (2000).

### **A local source in the polar regions**

FA and AA account for a large fraction of the water-soluble organic carbon (gas + particle) over snow in polar regions (Anderson et al., 2008). Better constraints on the budget of FA and AA in these regions may help understand the large variations in FA and AA observed in the ice core record in the last 100,000 years (Legrand and De Angelis, 1996). These variations have been tentatively attributed to changes in the biosphere or biomass burning activity in boreal regions (Fuhrer and Legrand, 1997; Eichler et al., 2009).

Measured FA over Thule is about one order of magnitude lower than in Wollongong (Fig. 4.3b). The largest FA total columns are measured in the summers of 2004 and 2008. Both these periods are characterized by exceptional biomass burning in boreal regions (in North America in 2004 and in Asia in 2008) (Giglio et al., 2010), consistent with the hypothesis that FA anomalies may reflect large biomass burning events. In the absence of local sources, the modeled FA column is dominated by transport. This is reflected in the modeled vertical distribution of FA peaking in the free troposphere. The model predicts a strong



seasonal cycle with maximum during the boreal summer, corresponding to the largest biogenic and biomass burning emissions. The model underestimates FA total column by a factor of 2 to 5. This discrepancy may in part reflect insufficient biomass burning emissions (Andreae and Merlet, 2001). We also note that the model predicts very low concentrations of FA at the surface ( $\sim 10$  pptv). This is in sharp contrast with the measurements of Anderson et al. (2008) which report  $\sim 1$  ppbv of water-soluble organic carbon (primarily FA and AA) over Summit at 1.5 m above the snow. This discrepancy between model and observation in Thule may thus reflect missing local sources. Indeed, Dibb and Arsenault (2002) reported surface concentrations of FA and AA measured in the Arctic could not be sustained by transport alone but required a large source from snow photochemistry.

### Missing winter sources

Mid latitude and low altitude sites (Bremen, Wollongong) show larger relative biases between the model and the data during the winter (Figs 4.3a and 4.4b). This may point to large missing anthropogenic sources of FA (Talbot et al., 1988). Alternatively leaf decay may also contribute to the FA in the winter months (Kesselmeier et al., 1998). A missing biogenic contribution would be consistent with isotope measurements which showed that FA and AA are primarily made of modern carbon even in the winter (Glasius et al., 2001).

#### 4.4.1.2 ACE-FTS

The Atmospheric Chemistry Experiment (ACE) is a Canadian satellite that was launched by NASA on 12 August 2003. FA is measured by high spectral resolution ( $0.02 \text{ cm}^{-1}$ ) FTS operating from 2.2 to  $13.3 \mu\text{m}$ . Using solar occultation, the altitude profile of temperature, pressure and various chemical compounds, including FA, CO and  $\text{C}_2\text{H}_2$  are determined between  $85^\circ\text{N}$  and  $85^\circ\text{S}$ . Here, we are using version 3.0 of the ACE-FTS Level 2 data product.

Rinsland et al. (2006) and González Abad et al. (2009) have used the ACE-FTS spectra to retrieve mid and upper tropospheric FA. Even though most FA is located at low altitude and thus cannot be observed by ACE-FTS, these upper atmospheric profiles provide insights into the sinks, sources and transport of FA.

Fig. 4.6 shows the average distribution of FA measured by ACE-FTS from 2004 to 2008. FA is highest from  $10$  to  $50^\circ\text{S}$ , probably reflecting large biogenic sources. The Northern hemisphere exhibits lower FA mixing ratios on average. FA mixing ratios decrease rapidly with altitude and away from the source region. High mixing ratios observed at high altitudes in the Southern Hemisphere may indicate efficient transport of FA or, more likely, its precursors from the boundary layer to the free troposphere.

The model captures mid tropospheric FA in the tropics and Southern mid latitudes relatively well. It is biased low north of 40°N (Fig. 4.7), mirroring the low modeled concentration of FA in the planetary boundary layer (Fig. 4.1) and consistent with the large underestimation of FA total column over Bremen. The model is biased high south of 50°S. This region experiences among the lowest concentrations of FA and it is unclear how significant this discrepancy is.

The model greatly underestimates the measured vertical gradient of FA in the free troposphere, underestimating FA at low altitude and overestimating it at high altitude (Fig. 4.7). The correlation plot between FA and CO reveals possible reasons for this discrepancy (Fig. 4.8). The model overestimates FA at low CO (40 to 60 ppbv) which primarily reflects the high bias of the model at high altitude where most of the ACE-FTS measurements are taken. ACE HCN measurements (not shown) imply that air masses with CO mixing ratios greater than 160 ppbv are strongly influenced by fresh biomass burning emissions. This is in part captured by the model which shows a strong enhancement of FA in this regime. The largest discrepancy is found for values of CO ranging from 120 to 150 ppbv. These air masses exhibit a weak biomass burning signature and are primarily located in the lower free troposphere at high northern latitudes. These air masses may be affected by boundary layer air, carrying high mixing ratios of FA or its precursors of biogenic or anthropogenic origins. Alternatively, they may be associated with aged biomass burning, which would support the existence of long-lived biomass burning precursors of FA.

#### **4.4.2 Aircraft measurements by mass spectrometry**

From the previous section, large sources of FA appear to be missing in the Northern Hemisphere mid latitudes. Here we present data from several aircraft missions over North America to gain insights on these missing sources. We use measurements from the Intercontinental chemical transport experiment (INTEX-B/IMPEX April to May 2006 with a focus on the transport of pollution from Asia to the United States over the Pacific (Singh et al., 2009)), the Second Texas Air Quality Study (TexAQS II–August to October 2006 (Parrish et al., 2009)), the Intercontinental Transport and Chemical Transformation experiment (ITCT 2k4 campaign over the Northeastern United States (Fehsenfeld et al., 2006)) and the Aerosol, Radiation and Cloud Processes Affecting Arctic Climate study (ARCPAC 2008 over Alaska (Warneke et al., 2009)). FA and AA were measured by Chemical Ionization Mass Spectrometry during INTEX-B (Crounse et al., 2006)) and AA was measured by PTRMS during ITCT 2k4, ARCPAC 2008 and TexAQS II (de Gouw and Warneke, 2007). Even though FA was not measured during these missions, it can be expected to correlate very well with AA (e.g.,  $R = 0.9$  for INTEX-B).

The model underestimates AA and FA in all missions, consistent with total column observations in the Northern mid and high latitudes (Bremen and Thule). Missions closer to large biogenic or anthropogenic sources (ITCT 2k4 and TexAQS II) exhibit a smaller discrepancy than INTEX-B (impacted by aged Asian pollution) or ARCPAC 2008 (impacted by biomass burning). This suggests a large missing long-lived precursor of FA and AA. Consistent with this hypothesis, air masses exhibiting a strong Asian pollution signature (as defined by Dunlea et al. (2009)) exhibit a marked enhancement in FA and AA mixing ratio over other air masses sampled over the Pacific (Table 4.4). Since FA and AA emitted or formed in Asia are expected to be washed out as air is lifted out of the boundary layer, this enhancement hints at a secondary production of both acids. The correlation of FA with the organic fraction of the aerosols ( $R = 0.83$ , Fig. 4.9), which are predominantly of secondary origin (Dunlea et al., 2009) is consistent with this hypothesis. Similarly, in ARCPAC 2008, a strong correlation of AA with black carbon ( $R = 0.86$ ) and the organic content of the aerosol ( $R = 0.82$ ) hints at missing sources of AA from biomass burning.

Unrepresented precursors of FA and AA could also account for some of the discrepancy in INTEX-B (Sinreich et al., 2010). The discrepancy in the marine boundary layer for both acids is similar to the one reported by Baboukas et al. (2000) in the Atlantic ocean. Modeled marine sources of FA are a negligible fraction of FA photochemical production ( $\sim 2.5\%$ ) reflecting the low emissions of FA precursors. This is not true for AA, as acetaldehyde emissions from marine sources are large, resulting in  $\sim 8.5\%$  of AA production over the ocean. The marked maximum in FA total column in the tropics is, however, consistent with an important role of transport from the continents (Fig. 4.5).

INTEX-B measurements over the California Central Valley (Table 4.4) also confirm that cattle and/or crop farming is accompanied by very large mixing ratios of FA and AA (5 times greater than in Asian plumes and 10 times greater than in the Pacific free troposphere). In contrast with measurements taken over the Pacific, AA appears to be produced/emitted more efficiently than FA in this environment.

Comparisons between the model and the data show lower discrepancies for TexAQS II and ITCT 2k4 ( $\sim 2$ – $3\times$ , Figs. 4.10a and 4.10b). Correlations with anthropogenic markers (benzene:  $R = 0.5$  for TexAQS II,  $R = 0.75$  for ITCT 2k4 ; methoxyperoxyacetylnitrate:  $R = 0.85$  for ITCT 2k4) suggest a source of AA may be associated with anthropogenic processes.

#### 4.4.3 Summary of model-measurement comparisons

The comparisons between measurements and model results have revealed that:

1. The model captures FA concentration and seasonality in regions with large biogenic emissions (ACE-FTS in the tropics, Wollongong, La Réunion).
2. FA and AA concentrations are largely underestimated when biomass burning (ARCPAC 2008, ACE-FTS, La Réunion) or anthropogenic influences (Bremen, INTEX-B) are strong. However, even in these instances, FA and AA seasonality (Bremen) suggests that a large fraction of FA and AA is associated with emission and photooxidation of biogenic compounds.
3. The rapid decrease in FA with altitude in the upper troposphere is not captured by the model.
4. FA and AA are greatly underpredicted in polar regions and in Northern midlatitude regions impacted by anthropogenic activities.

These observations are consistent with major secondary sources of FA and AA missing in the model. In the following, we use a series of sensitivity runs to examine the criteria a secondary source of FA and AA must meet to help bridge the gap between the model and the data. The reference simulation described in this section is referred to as R1 hereafter.

## 4.5 Sensitivity study

### 4.5.1 Biomass burning injection height

As a default in GEOS-Chem, biomass burning emissions are solely released in the boundary layer. However observations have shown that major fires can inject emissions well above the boundary layer (e.g., de Gouw et al., 2006; Vigouroux et al., 2009). Several modeling studies have also shown that observations of CO and aerosols downwind of fires could be best explained when a large fraction of the fire emissions is released above the boundary layer (e.g., Turquety et al., 2007). Injection of FA/AA or their precursors outside of the boundary layer is of great importance in their budget. Indeed a fast transport of carboxylic acids out of the boundary layer increases their lifetime by reducing the dry deposition sink and results in a large increase in their net lifetime. This in turn results in enhanced transport of FA and AA on larger scales. Furthermore biomass burning has been associated with a reduction of low-level precipitation (e.g., Andreae et al., 2004) which may further increase carboxylic acid lifetime.

Several studies have associated enhancements of FA in the free troposphere to biomass burning (e.g., González Abad et al., 2009). Here we examine whether injection of biomass burning emissions outside

of the boundary layer can help bridge the gap between model and observations at high CO. We use two different scenarios. In the first one (R2a), 60% of the biomass burning is emitted in the boundary layer while 35% is emitted in the mid troposphere (from the top of boundary layer to 400 hPa) and 5% in the upper troposphere (400 hPa to 200 hPa). In the second scenario (R2b), we adopt one of the scenarios used by Turquety et al. (2007) to investigate biomass burning over North America with 40% of the biomass burning emissions in the boundary layer, 30% in the mid troposphere and 30% in the upper troposphere. Since our goal is to examine the sensitivity of free tropospheric FA to biomass burning injection height, modifications of the injection height are applied globally, an important simplification (Val Martin et al., 2010, and references therein). Furthermore we assume that EF for FA and AA are independent of the biomass burning injection height. This is another important simplification since a) the injection of biomass burning in the free troposphere strongly depends on the fire intensity, and b) EF for FA and AA exhibit some correlation with the modified combustion efficiency (MCE), an indicator of the combustion type (flaming or smoldering). Therefore, a more quantitative study of the importance of biomass burning in the FA and AA budget would require an explicit description of the relationship between MCE and EF as well as MCE and injection height.

Both scenarios lead to an enhancement of FA in the mid troposphere (by 10% for R2a (not shown) and by 35% for R2b (Fig. 4.7, panel B)). The increase is especially large at high CO, greatly reducing the discrepancy between the model and the measurements (Fig. 4.8). This is remarkable since biomass burning emissions of FA and its precursors account for a relatively small fraction of FA sources in the model. This disproportionate effect highlights the strength of boundary layer sinks of FA which greatly hinder its transport to the free troposphere. The increase in FA induced by both scenarios is, however, insufficient to bridge the gap between the model and the data in the lower troposphere. In particular, it has no effect on the modeled FA in air masses with CO mixing ratios ranging from 120 to 150 ppbv. This is not surprising if these air masses are associated with aged biomass burning, as FA sinks (photooxidation and wet deposition) are faster than for CO. In contrast, the injection of FA into the free troposphere significantly amplifies the discrepancy between the model and the measurements in the upper troposphere. The very long lifetime of FA in the upper troposphere is responsible for this strong sensitivity. In R2b, FA is increased by almost 50% in the upper troposphere compared to the reference run, resulting in large discrepancies for CO between 40 and 120 ppbv (Fig. 4.7).

These observations suggest that the distribution of FA in the free troposphere is only sensitive to biomass burning injection height for fresh biomass burning plumes. As FA is removed from the free troposphere

faster than CO, the correlation between FA and CO across the whole CO range can only be sustained if the photooxidation of long-lived unrepresented compounds (i.e., poorly soluble and reactive) produces FA. However, if such a source exists, the observed vertical gradient of FA indicates a large sink is missing from the model in the upper free troposphere.

#### 4.5.2 Secondary source of FA and AA and organic aerosol aging

The positive correlation of FA and AA with submicron organic aerosol observed in several aircraft campaigns (Fig. 4.9) hints at a possible relationship between FA and AA production and aerosol aging, i.e., processes affecting aerosol composition.

Aerosol composition is very dynamic as evidenced by the positive correlation between the oxygen to carbon ratio and the residence time of aerosols (DeCarlo et al., 2008; Capes et al., 2008). Near sources, aging is thought to be dominated by gas-phase oxidation of semivolatiles (a), while, for longer residence time, heterogeneous oxidation (b) may become important (DeCarlo et al., 2008; George et al., 2008). The combined evolution of the oxygen to carbon ratio and of the hydrogen to carbon ratio during aerosol aging was recently showed to be consistent with the formation of carboxylic groups (Heald et al., 2010). This is not inconsistent with (a), even though we are not aware of direct evidence for the formation of either FA or AA from the photooxidation of semivolatiles. In contrast, laboratory experiments provide ample evidence for the volatilization of FA and AA (b) following the photolysis of aerosols (Walser et al., 2007; Pan et al., 2009) as well as their heterogeneous oxidation by O<sub>3</sub> (Eliason et al., 2003; Park et al., 2006) and OH (Eliason et al., 2004; Molina et al., 2004; Vlasenko et al., 2008). As heterogeneous oxidation operates on relatively long time scales (> 4 days (George et al., 2008)), it could help account for observations during INTEx-B and at Paramaribo. It appears, however, to be too slow to provide a large source of FA and AA near emission centers (DeCarlo et al., 2008). These observations suggest that aerosol aging and wall reactions could result in a significant source of FA and AA in chamber experiments that was not accounted for by Paulot et al. (2009a).

Comparison between the data and the model suggests global sources of FA and AA may be underestimated by up to 50% for both acids, i.e., an additional ~2 TmolC/yr. Estimates for the global flux of carbon from the photooxidation of aerosol range from 4 to 16.5 TmolC/yr (Kwan et al., 2006), suggesting FA and AA volatilization would need to account for a very large fraction of this flux (10–50%). However this estimate does not account for the probably large dynamic exchange of matter between the gas and aerosol phases driven by semivolatile volatilization and photooxidation (Robinson et al., 2007; Kroll et al., 2009;

Jimenez et al., 2009).

Proper evaluation of the role of aerosol aging as a source of FA and AA requires detailed modeling of aerosol evolution (e.g., following the framework presented by Jimenez et al. (2009)) informed by additional laboratory measurements. This is beyond the scope of this paper. Here, we do not explicitly model secondary organic aerosol but use organic aerosol (OA) to generate a diffuse source of FA and AA associated with aerosol aging (scenario R3). In GEOS-Chem, OA represents both emitted OA (primarily from biomass burning with an important contribution of anthropogenic sources in the Northern midlatitudes) and a small and simplified secondary production from the condensation of low volatility compounds from biogenic and anthropogenic sources (Park et al., 2003). The largest global source of OA is biomass burning globally. We assume that the reaction of OH with OA produces FA and AA according to :

$$\frac{dFA}{dt} = \frac{dAA}{dt} = \left( \frac{r_p}{D_g} + \frac{4}{v\gamma} \right)^{-1} A \times OH$$

where  $r_p$  is the particle radius,  $\gamma$  the reaction probability (assumed to be 1 here),  $D_g$  the gas-phase diffusion coefficient,  $v$  the mean molecular velocity of OH and  $A$  the aerosol surface area. This reaction does not represent a physical process (OA is not lost via this reaction) but is meant to provide a diffuse source of FA and AA correlated with OA. Including this process results in an increase in the source of FA and AA by 320 Gmol/yr, about  $\sim 25\%$  ( $\sim 0.95$  TmolC/yr).

This large additional FA source greatly improves the agreement with La Réunion. The mean FA concentration increases by almost 60% in October (Fig. 4.11a). Similarly, the anomalously high FA measured in December 2006 in Wollongong is much better reproduced in the model with this hypothetical aerosol source (Fig. 4.11b). We note that it has little effect on the FA total columns for the other years, underlining the exceptional intensity of the 2006 bush fires. For both sites, a similar increase in biomass burning emissions of FA would not result in such a large improvement. This is because the lifetime of organic aerosol is longer than the lifetime of FA. This is evident in the comparison with the cruise measurements where a very large increase is observed in the tropics, reflecting the enhanced transport of FA biomass burning precursors away from their source regions (Fig. C.11). Other locations impacted by biomass burning such as Thule see large increases in FA or AA though this remains insufficient to bridge the gap between model and measurements.

In the GEOS-Chem simulations used in this study, organic aerosol sources are dominated by biomass burning. Because of the lack of a proper representation of secondary organic aerosol (SOA) in our simulation, it is not surprising the discrepancy remains very large in locations where organic aerosols are dominated

by SOA from biogenic or anthropogenic sources (e.g., Bremen (Fig. C.12), INTEX-B). Future work will focus on assessing the role of semivolatiles as a source of FA and AA. In particular, the interaction between biotic emissions (biogenic and agricultural) and anthropogenic activities need to be properly represented, as it has been shown that this interaction could result in enhanced secondary aerosol formation (de Gouw et al., 2005; Weber et al., 2007; Goldstein et al., 2009). If SOA aging is indeed a source of FA and AA, this could help explain the biogenic signature of FA and AA in polluted regions (seasonality and isotopic composition), as well as the similar magnitudes of Wollongong and Bremen FA total columns, despite very different isoprene sources.

### 4.5.3 Upper tropospheric budget of FA

The ACE-FTS comparison revealed a high bias of the model in the upper troposphere. At these altitudes, wet deposition becomes small and FA sink is dominated by the reaction of OH with FA.

To examine the sensitivity of the FA profile to the temperature dependence of its reaction with OH, we use the temperature dependence derived theoretically by Galano et al. (2002) for the acidic ( $k_1$ ) and formyl channels ( $k_2$ ) and scale it to match the experimental rate of FA + OH determined at room temperature. The resulting rate constant of FA with OH ( $k_{FA+OH}$ ) is :

$$k_{FA+OH} = k_1 + k_2 = 2.94 \times 10^{-14} \times \exp\left(\frac{786}{T}\right) + 9.85 \times 10^{-13} \times \exp\left(-\frac{1036}{T}\right)$$

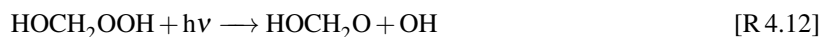
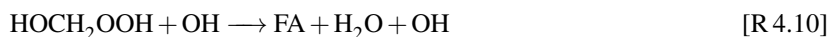
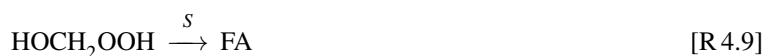
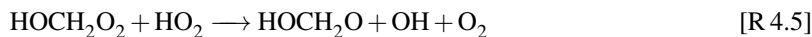
At 220 K, this predicts that the oxidation of FA is 2.3 times faster than at 298 K.

In the R4 simulation, we also include FA formation from organic aerosol (as in R3) as well as the injection of FA in the mid troposphere (as in R2a). The change in the reaction rate at cold temperature results in a dramatic decrease of FA in the upper troposphere (Fig. 4.7), because photooxidation is the dominant sink of FA in this region. This decrease is especially remarkable since mid troposphere FA is increased as a result of the injection of biomass burning in this region. This result must be interpreted cautiously as the model may underestimate  $HO_x$  in the upper troposphere, especially in the tropics (Wennberg et al., 1998). The fate of FA in the upper troposphere deserves more study since FA could provide a useful proxy to investigate biomass burning injection in the free troposphere.

The discrepancy between model and observation of FA in the upper troposphere is further amplified if



the equilibrium between  $\text{HOCH}_2\text{OO}$  and  $\text{HCHO} + \text{HO}_2$  is considered (Veyret et al., 1989).



Reaction of  $\text{HOCH}_2\text{OO}$  with  $\text{NO}$  results in  $\text{FA}$  formation. Jenkin et al. (2007) reported that [R 4.5] and [R 4.6] account for 20% and 30% of the reaction of  $\text{HOCH}_2\text{OO}$  with  $\text{HO}_2$ . The photooxidation of hydroxymethylhydroperoxide ( $\text{HOCH}_2\text{OOH}$ ) is also expected to form  $\text{FA}$  with high yield from photolysis, reaction with  $\text{OH}$  and heterogeneous decomposition (Neeb et al., 1997). Therefore we assume that the reaction of  $\text{HO}_2$  with  $\text{HOCH}_2\text{OO}$  results in  $\text{FA}$  formation with a yield of 1. As shown in Fig. 4.12,  $\text{HO}_2 + \text{HCHO}$  chemistry significantly increases  $\text{FA}$  in the upper troposphere where the lifetime of  $\text{HOCH}_2\text{OO}$  is long enough for the reaction of  $\text{HOCH}_2\text{OO}$  with  $\text{NO}$  and  $\text{HO}_2$  to compete with  $\text{HOCH}_2\text{OO}$  decomposition. As pointed out by Hermans et al. (2005), proper assesment of  $\text{HCHO} + \text{HO}_2$  importance as a sink of formaldehyde and source of  $\text{FA}$  requires very precise knowledge of the temperature dependence of [R 4.3]. Recent measurements of  $\text{HOCH}_2\text{OO} \rightarrow \text{HO}_2 + \text{CH}_2\text{O}$  by Pinceloup et al. (2003) are significantly slower than the recommended IUPAC value (Atkinson et al., 2006) used in this simulation. This suggests the source of  $\text{FA}$  from  $\text{HCHO} + \text{HO}_2$  in the free troposphere may be even larger than shown on Fig. 4.12.  $\text{FA}$  observations in the upper troposphere thus provide a much needed test of the representation of  $\text{HCHO} + \text{HO}_2$  in models.

## 4.6 Conclusions

We have derived a detailed bottom-up inventory of FA and AA in the atmosphere. Our updated source of FA is more than twice as large as previous estimates, reflecting the formation of FA from the photooxidation of isoprene and its products by OH. Both carboxylic acids are predicted to originate primarily from the photooxidation of biogenic compounds with biomass burning a significant seasonal source in many environments.

Despite these larger sources, the model remains biased low, especially in the Northern mid latitudes and in air masses affected by biomass burning. This discrepancy cannot be solely resolved by increasing biomass burning emissions of FA and AA.

We propose that a long-lived secondary source of FA and AA of order  $\sim 2$  TmolC/yr has yet to be identified. We hypothesize that the strong correlation of aerosol organic content with FA and AA hints at the possible relationship between aerosol aging and carboxylic acid production. If this relationship is demonstrated, FA and AA could prove very valuable to investigate aerosol aging, composition and sources. The simplified treatment of organic aerosols used in this study suggests that the long lifetime of OA could help account for the measured mixing ratios of carboxylic acids away from biomass burning regions. A realistic treatment of SOA (especially the missing SOA in polluted regions, including through anthropogenic-biogenic interactions), may help reduce the discrepancy in the mid latitudes where the biomass burning source of organic aerosol is limited.

The comparison between ACE-FTS mid and upper tropospheric measurements also reveals that strong enhancements in FA are consistent with injection of biomass burning emissions outside of the boundary layer (though FA is most likely associated with secondary production). FA may be used as a proxy to track biomass burning injection in the free troposphere, a very uncertain parameter in chemical transport models.

Finally even though the data set presented in this study offers the first long-term overview of the global distribution of FA, many regions of interest (in particular Africa and Asia), remain very poorly sampled. Ongoing efforts to retrieve FA from TES, IASI (Clerbaux et al., 2009; Razavi et al., 2011) or MIPAS-ENVISAT (Grutter et al., 2010) are thus particularly promising.

## 4.7 Acknowledgements

The authors thank two anonymous referees and T. Stavrakou for their constructive comments. FP is supported by a NASA Earth and Space Science fellowship. GGA is supported by the Wild Fund and the National Center for Earth Observation (NCEO). DBM acknowledges support from NASA under Grant NNX10AG65G. The National Center for Atmospheric Research is supported by the National Science Foundation. The NCAR FTS observation program at Thule (GR) is supported under contract by the National Aeronautics and Space Administration (NASA). This work is also supported by the NSF Office of Polar Programs (OPP). PFD, EJD and JLJ were supported by NASA NNX08AD39G and NOAA NA08OAR4310565. The authors wish to thank the Danish Meteorological Institute for support at the Thule site. JN acknowledges funding by the grant from the Deutsche Forschungsgemeinschaft (DFG) NO 404/14-1. NMD and DWTG acknowledge support from the Australian Department of Innovation, Industry, Science and Research, International Science Linkage under Grant CG130014. CV and MDM acknowledge the PRODEX project SECPEA and the project AGACC from the Belgian Science Policy Office (contracts SD/AT/O1A and SD/AT/O1B) for supporting the FTIR experiment at La Réunion. Part of this work was performed at the Jet Propulsion Laboratory, California Institute of Technology, under contract with NASA. The ACE mission is supported primarily by the Canadian Space Agency. Some support was also provided by the UK Natural Environment Research Council (NERC), through the National Centre for Earth Observation (NCEO). Measurements of FA and AA during the INTEx-B and Milagro missions were supported by NASA under Grant NNG06GB32B. The authors are grateful to Stephen Arnold and Dominick Spracklen for providing the marine isoprene fluxes, and to Sheryl Akagi and Robert Yokelson for providing updated biomass burning and biofuel emission factors. The numerical simulations for this research were performed on Caltech's Division of Geological and Planetary Sciences Dell cluster.

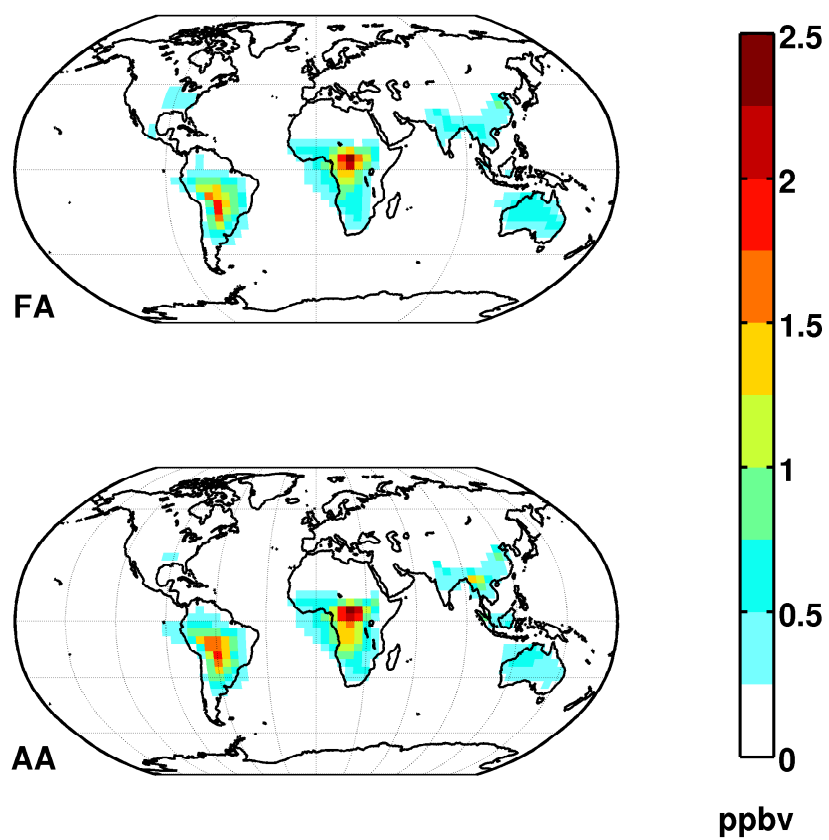


Figure 4.1: Annual simulated distribution of FA and AA in the boundary layer. FA and AA maxima in the tropics reflect strong biogenic sources.

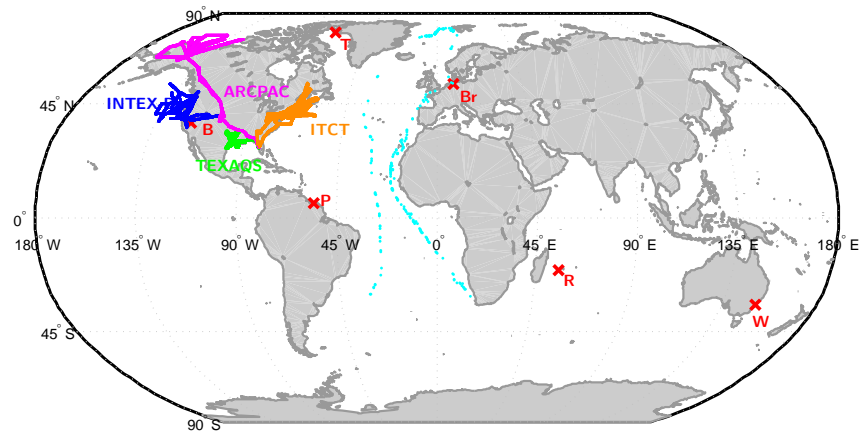


Figure 4.2: Locations of the measurement sites used in this study. Red crosses: FTS ground stations (B: Barcroft, Br: Bremen, P: Paramaribo, R: La Réunion, T: Thule, W: Wollongong). Cyan dots: ship cruises. Blue, magenta, yellow and green dots: aircraft mission flight tracks

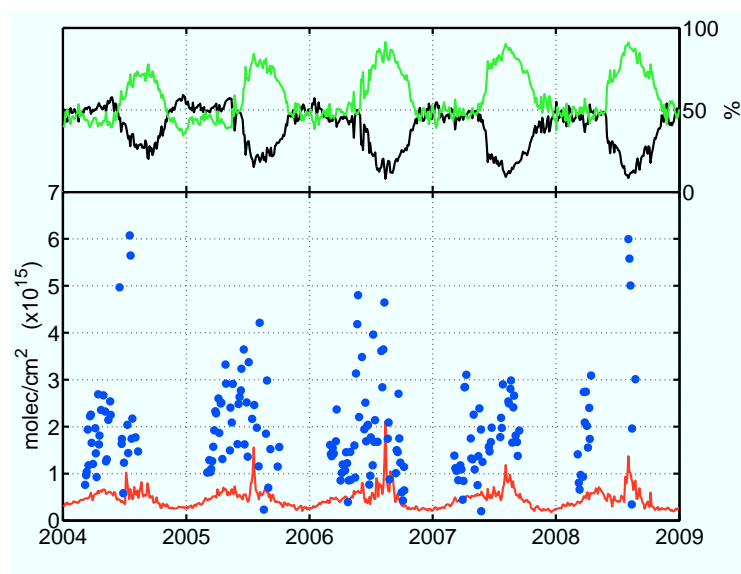
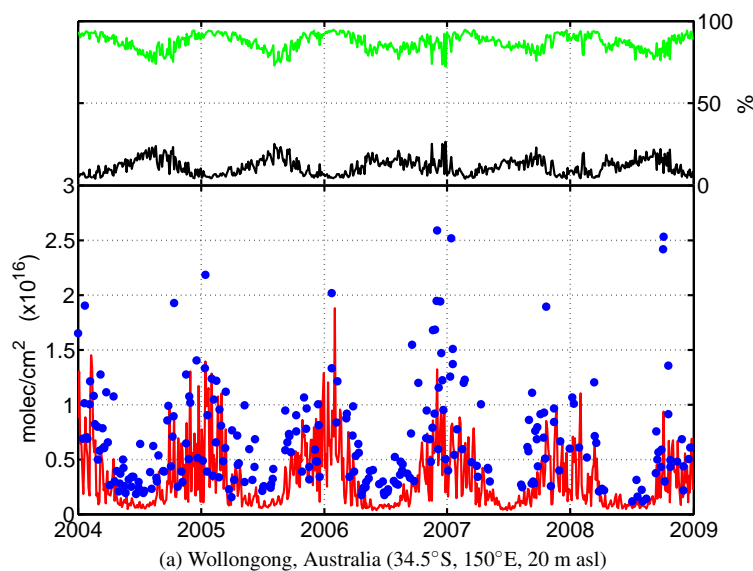
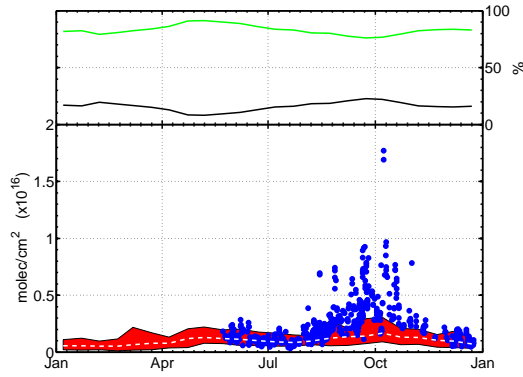
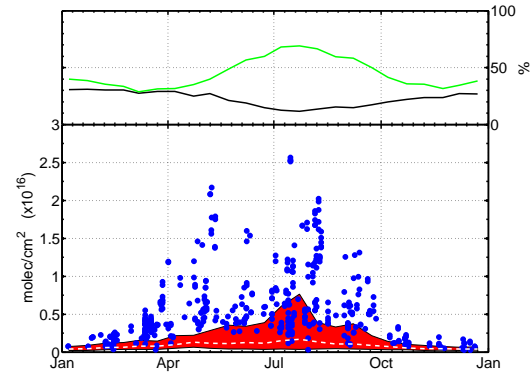


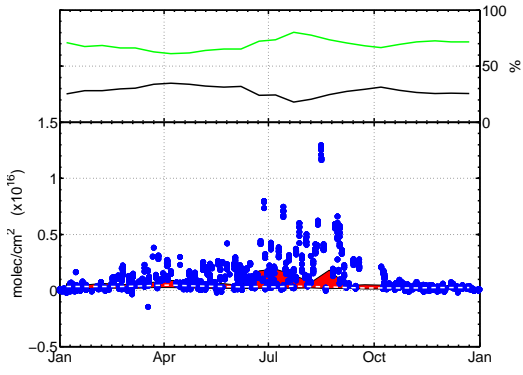
Figure 4.3: The observed seasonal cycle of FA total column (blue, lower panel) is well captured by the model at the Wollongong site (red, lower panel) and is consistent with a strong biogenic influence (green, upper panel). This is not the case in the high latitude site at Thule where the model underpredicts measured FA. Upper panel: modeled contribution of biogenic sources (green: emission + photochemical production) and biomass burning (black: emissions + photochemical production) to FA total column. Lower panel: modeled (red) and measured (blue) FA total column. Measurements and model are averaged over a two day time period.



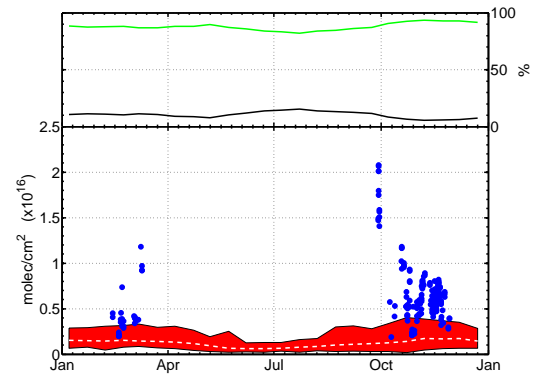
(a) La Réunion, France ( $-20.9^{\circ}\text{N}$ ,  $55.5^{\circ}\text{E}$ , 10 m asl). Measurements are from campaigns in 2004 (Aug-Oct), 2007 (May-June ; Aug-Oct) and 2009 (May-Dec).



(b) Bremen, Germany ( $53.1^{\circ}\text{N}$ ,  $8.9^{\circ}\text{E}$ , 27 m asl). Measurements are from 2002 to 2010.



(c) Barcroft, United States ( $37.6^{\circ}\text{N}$ ,  $-118.2^{\circ}\text{E}$ , 3800 m asl). Measurements are from campaigns in 1994 (Aug), 1998 (Oct-Dec), 1999 (Jan-Jul), 2000 (Oct-Dec), 2001 and 2002 (Jan-Aug).



(d) Paramaribo, Suriname ( $5.8^{\circ}\text{N}$  -  $55.2^{\circ}\text{W}$ , 23 m asl). Measurements are from campaigns in 2004/2006 (Oct-Nov), 2005/2007 (Feb-Mar ; Sep).

Figure 4.4: Upper panels: same as Fig. 4.3. Lower panel: comparison between modeled and measured FA total columns. Individual total column measurements are indicated with blue dots. The 2004–2008 model range is indicated by the red shaded area and the model mean by the white dashed line.

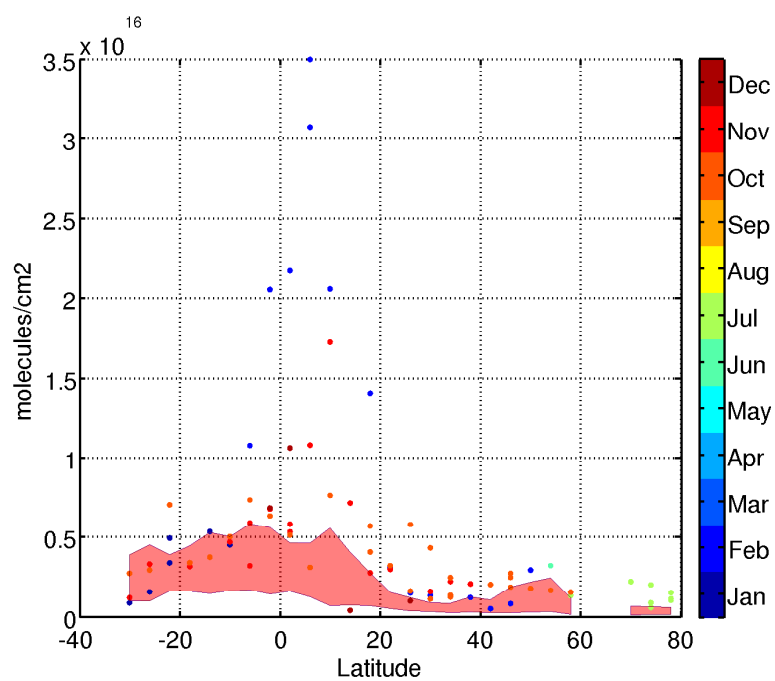


Figure 4.5: Monthly FA total column measured during cruises in the Atlantic ocean in 1996, 1999, 2000, 2002, 2003 and 2005 (dots). The 2004–2008 model monthly mean range is indicated by the red shaded area. FA maximum in the tropics reflects biomass and biogenic sources.



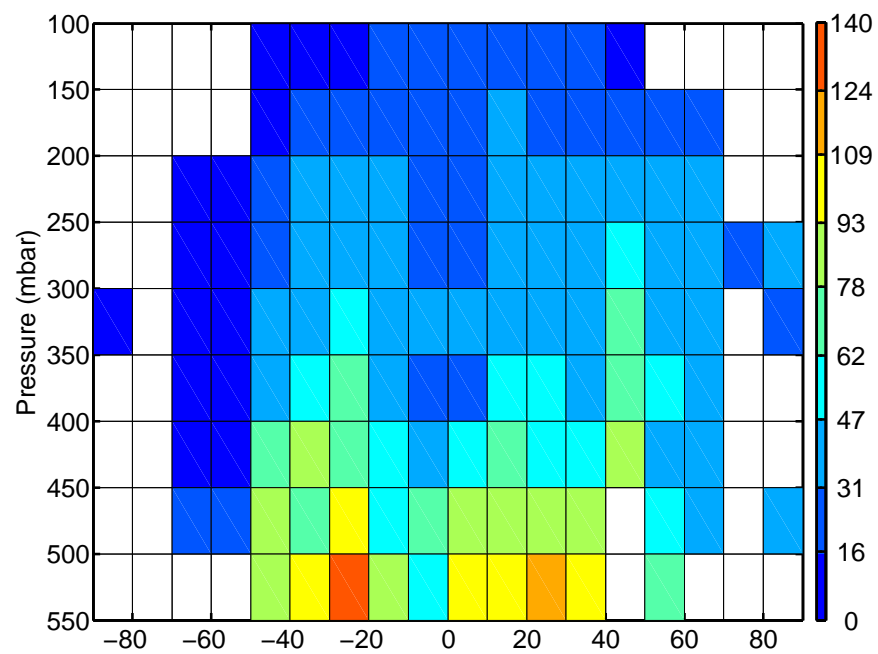


Figure 4.6: Measured distribution of FA (pptv) by ACE-FTS from 2004 to 2008. Median of FA measurements is calculated in  $10^\circ$  latitude 50 mbar bins. Only cells with more than ten measurements are shown.

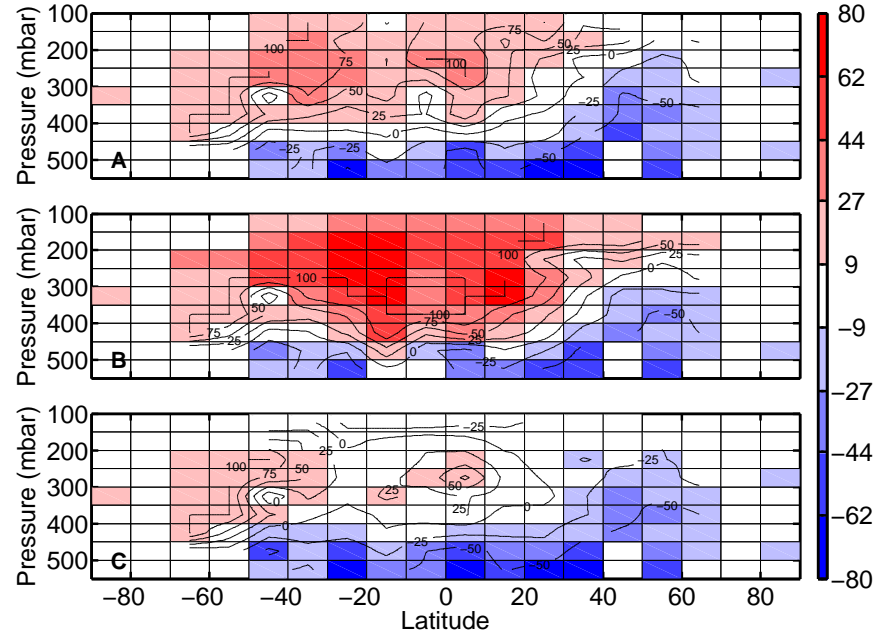


Figure 4.7: Comparison of the simulated FA with observations by ACE-FTS suggests an altitude-dependent error. Increasing the reaction rate of OH with FA reduces the model high-bias in the upper troposphere (C), while injection of biomass burning in the free troposphere provides little improvement in the middle troposphere while degrading FA simulation in the upper troposphere (B). Absolute difference between the model and the ACE-FTS measurement is shown in pptv with contours indicating the relative difference in %  $((\text{model-measurement})/\text{measurement})$ . Cells with no measurements are grayed. Panel A shows the comparison for the reference run (R1), Panel B for R2b and Panel C for R4 (see Section 4.5). The model is sampled at the location and time of the ACE-FTS measurement.

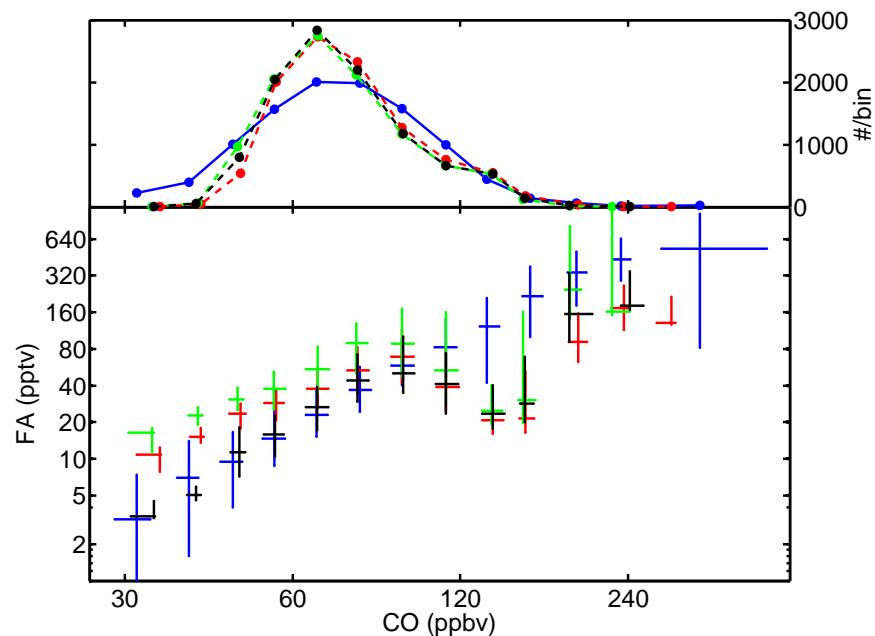


Figure 4.8: The correlation between CO and FA observed by ACE-FTS (blue crosses) in the free troposphere is not well-captured by the model (green, red and blue crosses), suggesting a missing secondary source. Lower panel: correlation plot between FA and CO (lower panel) for the measurements (blue) and the model: R1 (red), R2b (green), R4 (black). Upper panel: distribution of measured and modeled CO. The extent of the error bars indicate the 25 and 75 percentiles. The model is sampled at the location and time of the ACE-FTS measurement.

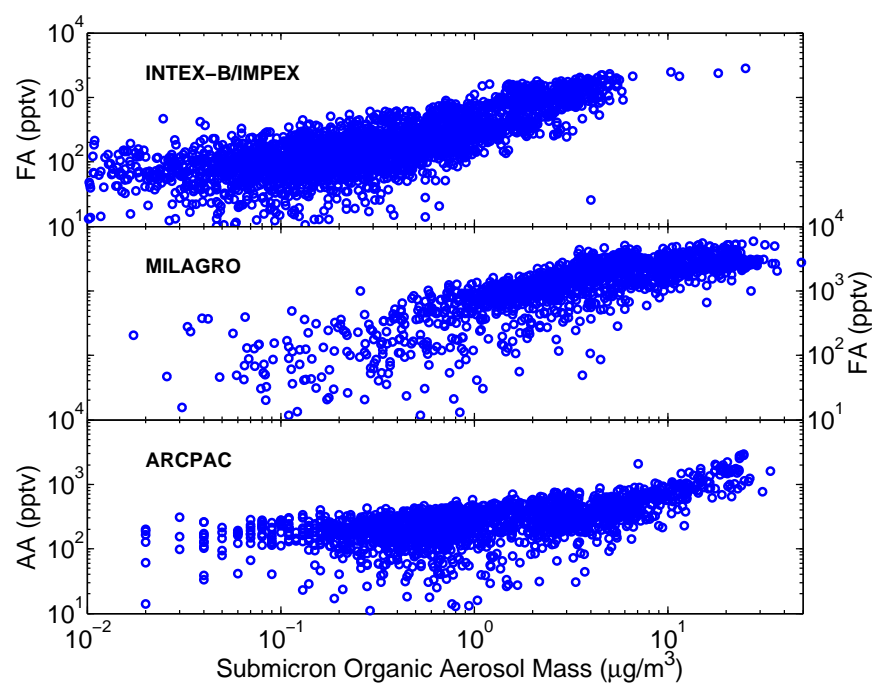


Figure 4.9: In situ measurements show strong correlation of FA and AA with the abundance of organic aerosol over the West Coast of the United States and the eastern Pacific (INTEx-B), in urban environments (MILAGRO) as well as in arctic regions (ARCPAC).

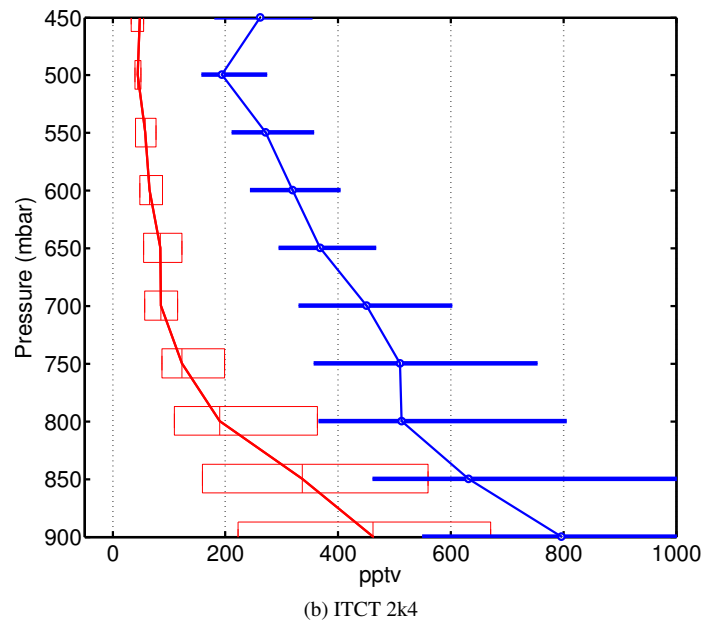
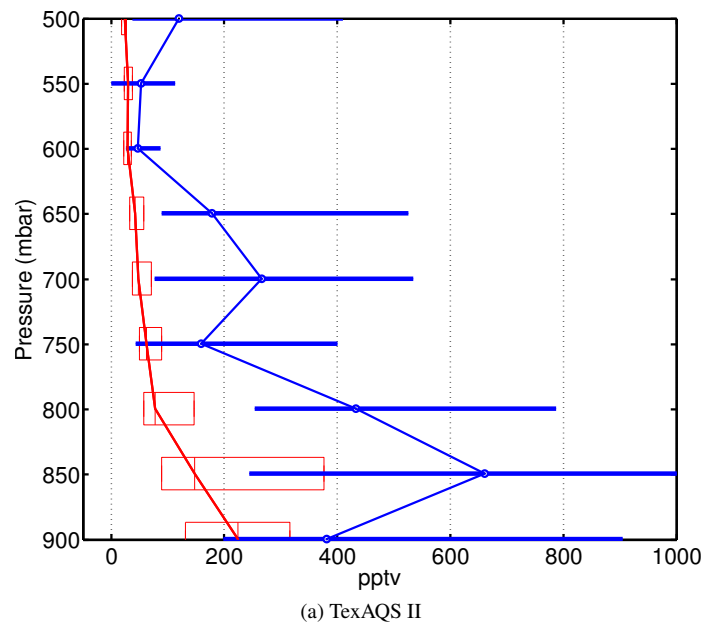
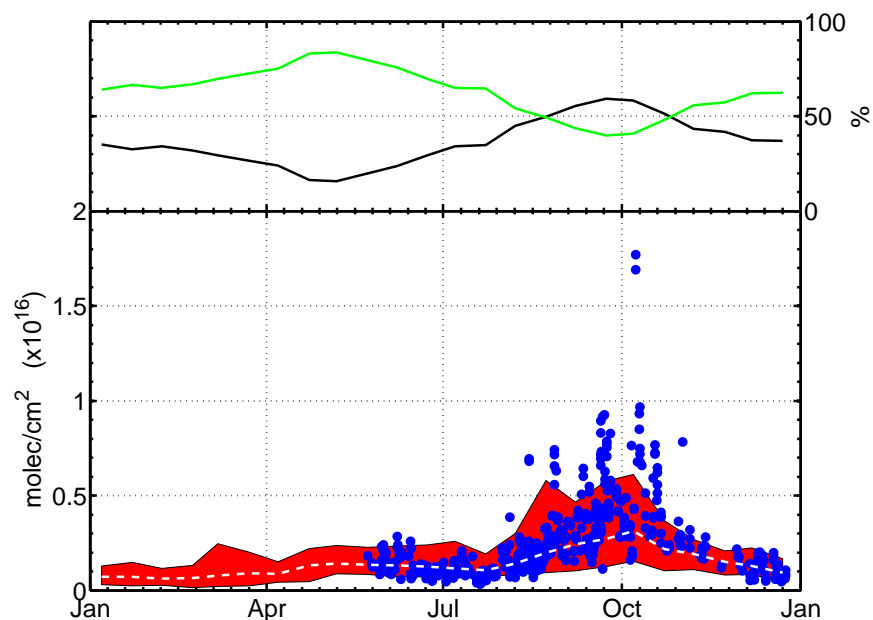
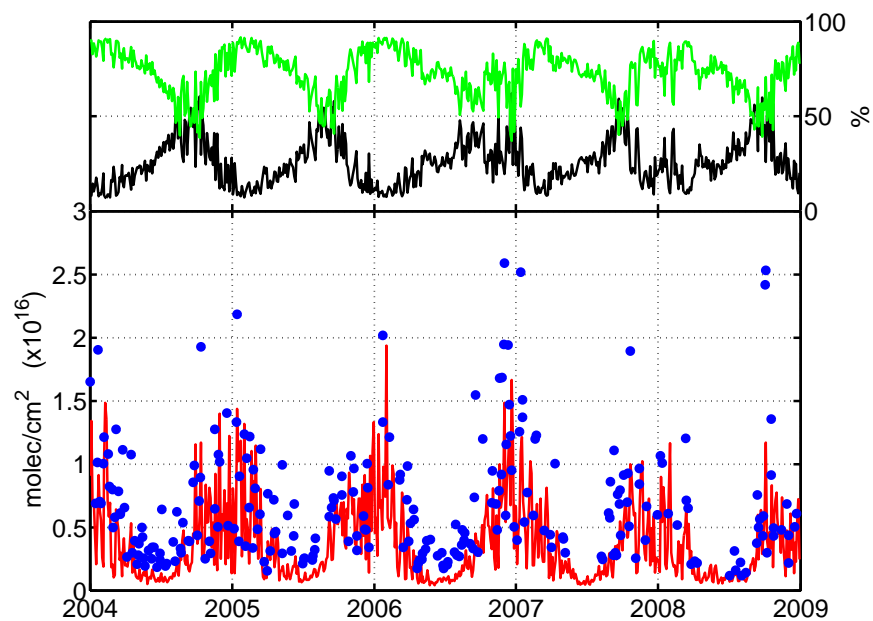


Figure 4.10: Comparison between measured (blue) and modeled (red) vertical AA profiles. The box (thick line) extent represents the 25% and 75% percentiles.



(a) La Réunion. Color code as Fig. 4.4a.



(b) Wollongong. Color code as Fig. 4.3a

Figure 4.11: A diffuse source of FA from aerosol aging (dominated by biomass burning (R3)) allows the model to better reproduce the increase in FA during the biomass burning season.

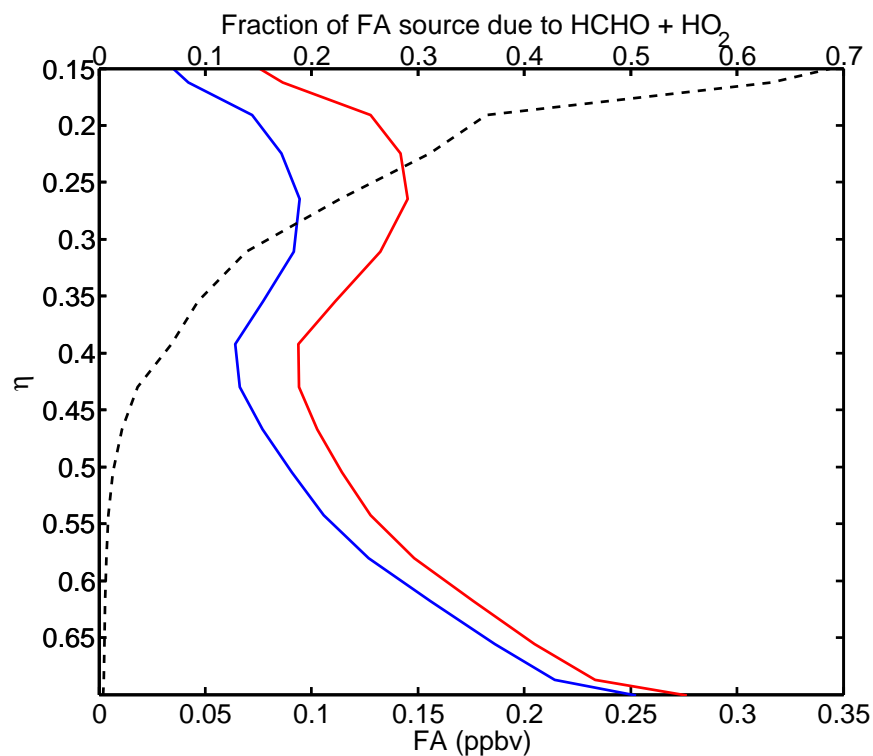


Figure 4.12: Including a representation of HCHO + HO<sub>2</sub> chemistry increases FA in the upper troposphere by nearly 50% (red) compared to the reference run (blue). Such a source (black dashed line) would further amplify the high bias of the model with respect to ACE-FTS observations. Profile of FA at -14N, 60W July 2005

Table 4.1: Biomass burning emission factors for FA and AA (in g per kg of dry matter, Yokelson (personal communication) and Akagi et al. (2010)). Emission factors from Andreae and Merlet (2001) are indicated in parentheses.

	Savanna	Tropical	Boreal	Biofuel <sup>a</sup>
FA	0.18 (0.7)	0.42 (1.1)	0.80 (2.9±2.4)	0.22 (0.13)
AA	1.58 (1.3)	3.11 (2.1)	4.05 (3.8±1.8)	4.97 (0.4-1.4)

(a): Derived from open-cooking.



Table 4.2: Soil emissions of formic and acetic acids at  $T_{soil} = 30^{\circ}\text{C}$  in  $\text{nmol}/(\text{m}^2 \text{ s})$  for different land types

Land Type <sup>a</sup>	Formic Acid		Acetic Acid	
	wet	dry	wet	dry
Agriculture (not Rice)	$1.8 \times 10^{-1}$	-	$1.1 \times 10^{-1}$	-
Agriculture (Rice)	$5.9 \times 10^{-3}$	-	$3.5 \times 10^{-3}$	-
Conifer and other deciduous	$1.47 \times 10^{-2}$	$4.9 \times 10^{-3}$	$8.8 \times 10^{-3}$	$2.9 \times 10^{-3}$
Desert	0	0	0	0
Drought deciduous	$2.9 \times 10^{-2}$	$8.9 \times 10^{-3}$	$1.8 \times 10^{-2}$	$5.4 \times 10^{-3}$
Grassland	$1.8 \times 10^{-1}$	$5.9 \times 10^{-2}$	$1.1 \times 10^{-1}$	$3.6 \times 10^{-2}$
Tropical rain forest	1.3	$1.9 \times 10^{-1}$	$7.7 \times 10^{-1}$	$1.2 \times 10^{-1}$
Tundra	$2.4 \times 10^{-2}$	$8.2 \times 10^{-3}$	$1.5 \times 10^{-2}$	$5.0 \times 10^{-3}$
Woodland	$8.3 \times 10^{-2}$	$3.2 \times 10^{-2}$	$5.0 \times 10^{-2}$	$1.9 \times 10^{-2}$
Wetland	$1.5 \times 10^{-3}$	—	$8.8 \times 10^{-4}$	-

(a) Wang et al. (1998)

Table 4.3: Modeled global budget of atmospheric formic and acetic acids (2004–2008 average). Previous estimates are indicated in parentheses.

	Formic acid ( $\tau = 3.2$ days)	Acetic acid ( $\tau = 2.3$ days)
Total Sources (Gmol/yr)	1232 (666 <sup>a</sup> , 587 <sup>b</sup> )	1424 (1550 <sup>a</sup> , 1217 <sup>b</sup> )
<u>Photochemical production</u>	1055	976
	(370 <sup>a</sup> , 370 <sup>b</sup> )	(1250 <sup>a</sup> , 700 <sup>b</sup> , 2000 <sup>c</sup> )
Biogenic	917 <sup>d</sup>	955 <sup>d</sup>
Anthropogenic	138	21
+ Biomass burning		
<u>Emissions</u>	177 (296 <sup>a</sup> , 217 <sup>b</sup> )	448 (300 <sup>a</sup> , 517 <sup>b</sup> )
Anthropogenic	3.5	7
Biofuel Burning	6.5 (25 <sup>b</sup> )	114.5 (274 <sup>b</sup> )
Biomass Burning	32.5 (174 <sup>a</sup> , 183 <sup>b</sup> )	187 (243 <sup>a</sup> , 279 <sup>b</sup> )
Cattle	39.5	39.5
	(25 – 100 <sup>f,g</sup> )	(4.2 – 16.8 <sup>f</sup> )
Soil	39	57
Terrestrial vegetation	56	43
	(122 <sup>a</sup> , 125 <sup>h</sup> , 33 – 166 <sup>i</sup> , 20 – 130 <sup>j</sup> )	(56 <sup>a</sup> , 25 <sup>h</sup> , 17 – 83 <sup>i</sup> , 10 – 33 <sup>j</sup> )
Total Sinks (Gmol/yr)	1233	1426
Photochemical	229.5	413
Dry deposition	536	522
Wet deposition	437.5	451.5
Dust	30	39.5

(a) von Kuhlmann et al. (2003b,a)

(b) Ito et al. (2007)

(c) Baboukas et al. (2000)

(d) Neglect biomass burning contribution to hydroxyacetone and glycolaldehyde

(e) Sum of biomass burning and biogenic emissions

(f) Ngwabie et al. (2008)

(g) C<sub>2</sub>H<sub>5</sub>OH + HCOOH

(h) Lathi re et al. (2006)

(i) Wiedinmyer et al. (2004)

(j) Kesselmeier et al. (1998)

Table 4.4: The increase in the median measured (m) FA and AA in polluted air observed during INTEx-B/IMPEX reflects the importance of secondary sources in the budget of FA and AA. These sources are missing from the model (M).  $\alpha$  is the slope of the linear fit:  $AA = \alpha FA + \beta$  following York’s method (York et al., 2004) for the measurement (ordinary least square for the model). Characterization of the air masses follows the approach of Dunlea et al. (2009).

	FA (pptv)		AA (pptv)		$\alpha \pm 1\sigma$ ( $R^2$ )	
	m	M	m	M	m	M
Free troposphere (Asian pollution)	296	26	193	25	$0.37 \pm 0.16$ (0.53)	0.42 (0.37)
Free troposphere (pristine + dilute Asian pollution)	108	26	86	26	$0.62 \pm 0.23$ (0.52)	0.54 (0.51)
Boundary layer (California Central Valley)	1291	81	906	62	$1.59 \pm 0.16$ (0.63)	0.40 (0.91)

## Chapter 5

# Impact of the isoprene photochemical cascade on tropical ozone

### 5.1 Introduction

The tropics play an essential role in the physical and chemical climate of Earth (Crutzen and Lelieveld, 2001). In particular, tropical tropospheric ozone plays an important role in the oxidative capacity of the atmosphere and on radiative forcing. Much work has been devoted to understanding the factors controlling its budget, in particular the impact of dynamics (Bowman et al., 2009; Nassar et al., 2009; Chandra et al., 2003; Ziemke and Chandra, 1999; Jacob et al., 1996) and of  $\text{NO}_x$  emissions from lightning (Sauvage et al., 2007b), biomass burning (Jacob et al., 1996; Chandra et al., 2002; Ziemke and Chandra, 1999; Jourdain et al., 2007) and soil (Jaeglé et al., 2004). However, recent advances in observations of tropospheric ozone have revealed that its tropical budget is not well captured by models (Bowman et al., 2009; Zhang et al., 2010).

The tropics are also characterized by very large biogenic emissions, whose photooxidation is known to modulate the ozone production efficiency, i.e., the number of molecules of ozone produced per molecule of  $\text{NO}_x$  (Liu et al., 1987). In particular the influence of the photooxidation of isoprene, a biogenic volatile organic compound (BVOC) that accounts for 30% to 50% of global BVOC emissions (Guenther et al., 1995; Guenther et al., 2006), on local photochemistry (e.g.,  $\text{HO}_x = \text{OH} + \text{HO}_2$  (Lelieveld et al., 2008) and ozone production (Chameides et al., 1988)) has motivated considerable laboratory (Ruppert and Becker, 2000; Dillon et al., 2006; Paulot et al., 2009b), field (Thornton et al., 2002; Ren et al., 2008; Lelieveld et al., 2008; Sinha et al., 2008; Warneke et al., 2001) and theoretical work (Peeters et al., 2009; Dibble,

2004a,b). Simulations including isoprene chemistry suggest that the effect of isoprene chemistry on the  $O_x = O_3 + NO_2$  budget extends to much larger scale (Roelofs and Lelieveld, 2000; von Kuhlmann et al., 2004; Pfister et al., 2008) than isoprene's short atmosphere lifetime would suggest, though the processes controlling this large-scale influence are ill-defined. This study aims to better characterize the mechanisms that control the spatial extent of the isoprene photochemical cascade, the complex suite of photochemical and physical transformations undergone by isoprene and its products, as well as its interplay with the tropical  $O_x$  and  $NO_x$  budgets.

The photooxidation of isoprene by OH produces isoprene peroxy radicals (ISOPO<sub>2</sub>), whose fate is critical to the impact of isoprene chemistry on the  $O_x$  budget:

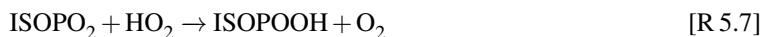


When ISOPO<sub>2</sub> react with NO, isoprene photooxidation promotes  $O_x$  formation ([R 5.2] and [R 5.4]):



Reactions [R 5.2] to [R 5.4] contribute to the formation of  $O_x$  in regions where urban centers are embedded in forested areas (e.g., Atlanta (Chameides et al., 1988)). The auto-catalytic production of  $O_x$  and  $HO_x$  is terminated by radical losses, e.g., the formation of nitric acid ( $OH + NO_2 \rightarrow HNO_3$ ) and hydrogen peroxide ( $HO_2 + HO_2 \rightarrow H_2O_2 + O_2$ ). Since the ozone production efficiency generally increases as the ratio  $NO_x/VOC$  decreases (Seinfeld and Pandis, 1998), the wet tropics that feature very high isoprene emissions and low anthropogenic emissions are extremely sensitive to increasing NO emissions (Thornton et al., 2002). For instance, ozone production in the outflow of Manaus (Brazil) is similar to that of major North American cities (Kuhn et al., 2010).

When ISOPO<sub>2</sub> react with HO<sub>2</sub>, however,  $HO_x$  is destroyed ([R 5.7]). This slows down the local photochemistry, contributing to the very low ozone levels over remote tropical forests:



Because isoprene emissions are so large, its photooxidation, i.e., the fate of isoprene peroxy radicals, can feedback on the local photochemical conditions. As discussed above, isoprene photooxidation can directly modulate  $\text{HO}_x$ . In particular, under very low  $\text{NO}_x$  conditions with high isoprene emissions, the removal of  $\text{HO}_x$  via [R 5.7] is predicted to result in very low concentrations of  $\text{HO}_x$  in the boundary layer (Houweling et al., 1998). Under these conditions, the lifetime of  $\text{ISOPO}_2$  can become long ( $\sim 60$  s) and it has been proposed that unimolecular processes could become competitive with [R 5.7] and [R 5.2], attenuating the removal of  $\text{HO}_x$  by isoprene photochemistry (Peeters et al., 2009):



Understanding low oxidative photochemical conditions is important for determining the extent of the isoprene photochemical cascade as these conditions promote the transport of isoprene and its photochemical products. In particular, the transport of biogenics to the upper troposphere through convection has been suggested as influencing the budget of ozone on the global scale as ozone and NO are much longer lived in this region of the atmosphere than at the surface (Doherty et al., 2005; Collins et al., 1999; Moxim and Levy, 2000).

The modulation of  $\text{NO}_x$  through isoprene nitrates ( $\text{ISOPONO}_2$ ), minor products of the reactions of isoprene peroxy radicals ( $\text{ISOPO}_2$ ) with nitrogen oxide NO, is another mechanism that allows the impact of isoprene photochemistry to propagate to larger scales (e.g., Wu et al., 2007; Stevenson et al., 2006; Ito et al., 2007; Horowitz et al., 1998, 2007; Fiore et al., 2005)



The formation of  $\text{ISOPONO}_2$  ([R 5.10]) modulates  $\text{O}_x$  by diminishing its local formation through  $\text{NO}_x$  sequestration. Furthermore, under high isoprene to  $\text{NO}_x$  condition, the fraction of  $\text{NO}_x$  segregated in

ISOPONO<sub>2</sub> may become important such that their formation contributes to the loss of HO<sub>x</sub>. Unlike nitric acid however, organic nitrates may not be a terminal sink of NO<sub>x</sub> but rather a reservoir (like peroxyacetylnitrate (PAN)). Depending on their lifetime and fate, they may thus contribute to the export of NO<sub>x</sub>. This depends in particular on the fraction of NO<sub>x</sub> that is returned to the atmosphere (by ISOPONO<sub>2</sub> and its nitrate-containing oxidation products R<sup>\*</sup>ONO<sub>2</sub>).



The representation of NO<sub>x</sub> recycling ([R 5.11]), segregation ([R 5.12]) and depositional loss ([R 5.13]) vary considerably across models. This is thought to contribute to differences in simulated ozone (Stevenson et al., 2006; Wu et al., 2007; Jacob and Winner, 2009; Fiore et al., 2005). For instance, in GEOS-Chem, isoprene nitrates are assumed to deposit readily, such that they behave like a terminal sink for NO<sub>x</sub> much like boundary layer nitric acid (Chen et al., 1998; Bey et al., 2001; Fiore et al., 2005). In MOZART (Horowitz et al., 2007), isoprene nitrates are short-lived and a large fraction is oxidized by ozone and OH to yield second-generation organic nitrates that are solely deposited.

In this study, we first use forward simulations to assess how the representation of isoprene nitrate photochemistry affects simulated tropical ozone. We then use adjoint simulations to examine the multiscale impact of the isoprene photochemical cascade on the tropical O<sub>x</sub> budget. Comparisons with the effect of biomass burning and lightning NO<sub>x</sub> emissions are also presented.

## 5.2 Model description

We use the GEOS-Chem global 3-D chemical transport model (Bey et al., 2001) (v8.3.2), driven by the GEOS-5 assimilated meteorology from the NASA Goddard Earth Observing System. In our simulations, the horizontal resolution is degraded to 4° × 5° and the vertical resolution to 47 vertical layers. The results reported here correspond to the period spanning June 2006 to May 2007 after a one and a half year spin-up.

Isoprene emissions are calculated using MEGANv2.1 (Guenther et al., 2006) as described by Millet et al. (2010). In the adjoint simulations, the emissions of isoprene are calculated with MEGANv2.0 (Millet

et al., 2008). Anthropogenic emissions of  $\text{NO}_x$  are calculated using the GEIA inventory scaled to the model run year according to fossil fuel usage (Bey et al., 2001; Benkovitz et al., 1996).  $\text{NO}_x$  is also emitted from biomass burning (from GFED2 inventory Randerson et al., 2006), soil (Yienger and Levy, 1995) and lightning (Price et al., 1997; Sauvage et al., 2007a). Dry deposition is calculated using a resistance-in-series model (Wesely, 1989; Wang et al., 1998). Wet deposition is calculated following the approach presented by Mari et al. (2000) and Jacob et al. (2000).

### 5.2.1 Representation of isoprene nitrate chemistry

There has been considerable laboratory research to determine the yield of isoprene nitrates ( $\sim 8 \pm 4\%$  (Chen et al., 1998; Sprengnether et al., 2002; Paulot et al., 2009a; Lockwood et al., 2010)). Laboratory (Paulot et al., 2009a; Lockwood et al., 2010) and field observations (Grossenbacher et al., 2001, 2004; Giacomelli et al., 2005; Perring et al., 2009) suggest isoprene nitrates have a very short atmospheric lifetime. However, there is much uncertainty regarding the relative importance of deposition and photochemical sinks (by OH and ozone). Ito et al. (2007) and Perring et al. (2009) estimated that the fate of isoprene nitrates is dominated by photochemical losses while Horowitz et al. (2007) and Giacomelli et al. (2005) concluded that deposition was their primary sink.

If the isoprene nitrates are primarily lost through photooxidation, assessing the impact of their photooxidation on the budget of reactive nitrogen and ozone must include proper representation of their photochemical products (Grossenbacher et al., 2001), about which very little is known. Paulot et al. (2009a) reported the formation of propanone nitrate and ethanal nitrate from ISOPNO<sub>2</sub> oxidation by OH and inferred that the ratio of [R 5.11] to [R 5.12] is  $\sim 1$ . Similarly, Giacomelli et al. (2005) proposed a suite of possible ozonolysis products. The formation of long-lived organic nitrates (e.g., propanone nitrate (Zhu et al., 1991; Paulot et al., 2009a; Sander, 1999)) is significant as they may contribute to the long-range transport of  $\text{NO}_x$  and the unexplained burden of organic nitrates in the free troposphere (Perring et al., 2009; Horowitz et al., 2007). There are also large uncertainties on the yield and fate of organic nitrates formed at night from isoprene +  $\text{NO}_3$  chemistry (Horowitz et al., 2007; Brown et al., 2009).

To evaluate the importance of these uncertainties on the  $\text{O}_x$ , isoprene nitrate photochemistry is represented here using three surrogates:  $\text{ING}_0$ ,  $\text{ING}_1$  and  $\text{ING}_2$  (Table 5.1, Fig. D.1).  $\text{ING}_0$  represents first-generation nitrates formed from isoprene photooxidation during day and nighttime.  $\text{ING}_0$  retains its double bond, such that it is rapidly oxidized by OH ( $k(298 \text{ K}) = 4.6 \times 10^{-11} \text{ cm}^3 \text{ molec}^{-1} \text{ s}^{-1}$ ) and ozone ( $k(298 \text{ K}) = 9.5 \times 10^{-17} \text{ cm}^3 \text{ molec}^{-1} \text{ s}^{-1}$ ), consistent with laboratory observations (Paulot et al., 2009a;



Lockwood et al., 2010). For simplicity, the oxidation of  $\text{ING}_0$  by OH and ozone is assumed to yield the same products.  $\text{ING}_1$  and  $\text{ING}_2$  are both second-generation organic nitrates.  $\text{ING}_1$  represents nitrates from methacrolein (MACR), methylvinylketone (MVK) and other hydroxycarbonyls formed from isoprene photooxidation (e.g., HC5 (Paulot et al., 2009a) and  $\text{ING}_0$  (Paulot et al., 2009a)).  $\text{ING}_1$  is assumed to react rapidly with OH ( $k_{\text{OH}}(298 \text{ K}) = 8 \times 10^{-12} \text{ cm}^3 \text{ molec}^{-1} \text{ s}^{-1}$ ), since it represents compounds that generally feature an aldehyde group. Lacking a double bond,  $\text{ING}_1$  does not react with ozone.  $\text{ING}_0$  photooxidation also yields  $\text{ING}_2$ . This species represents the formation of long-lived nitrates and its oxidation by OH ( $k_{\text{OH}} = 4.0 \times 10^{-13} \text{ cm}^3 \text{ molec}^{-1} \text{ s}^{-1}$  (Zhu et al., 1991)) and photolysis (Jenkin et al., 1997; Roberts and Fajner, 1989) are derived from propanone nitrate. Wet and dry deposition of  $\text{ING}_0$ ,  $\text{ING}_1$  and  $\text{ING}_2$  are treated as terminal losses of  $\text{NO}_x$ . In the following, we will use the notation  $\text{ING}$  to denote  $\text{ING}_0 + \text{ING}_1 + \text{ING}_2$ .

### 5.2.2 Simulations

Most isoprene emissions are thought to be located in the tropics (Guenther et al., 2006) though these estimates have large uncertainties as (a) bottom-up estimates are derived from ground studies that are too sparse to capture the diversity of plants in the rain forest, and (b) top-down estimates using satellite measurements of formaldehyde (Palmer et al., 2003; Barkley et al., 2008) rely on chemical mechanisms that poorly represent the photochemistry under low  $\text{NO}_x$  conditions (chemical mechanisms cannot reproduce  $\text{HO}_x$  observations in tropical atmosphere (e.g., Lelieveld et al., 2008)). In particular, the yield of formaldehyde from isoprene oxidation under low  $\text{NO}_x$  is ill-defined.

Here we focus on the regions located between  $15^\circ\text{S}$  and  $7^\circ\text{N}$  (Fig. D.2) where  $\sim 50\%$  of the global terrestrial isoprene emissions are located (Fig. 5.1). The ratio between emitted isoprene (on a C basis) and  $\text{NO}_x$  exhibits a strong seasonality that, in contrast to the mid latitudes, is not driven by isoprene, but rather, by  $\text{NO}_x$  emissions from biomass burning (Fig. 5.1). This ratio spans a very wide range from less than 10 in the peak biomass burning season in Africa and Southeast to more than 100 outside the biomass burning season in South America. In the following, we take advantage of the diversity of chemical regimes resulting from the very broad range of  $\text{NO}_x$ -to-isoprene ratios to examine how the impact of isoprene photooxidation on  $\text{O}_x$  is affected by local photochemical conditions.

### 5.2.2.1 Forward simulations

27 simulations were carried out to assess the effect of different representations of isoprene nitrates photochemistry by adjusting the yield of isoprene nitrates ( $Y = 0.05, 0.10, 0.15$ ), the recycling of  $\text{NO}_x$  from  $\text{ING}_0$  reaction with ozone and OH ( $\alpha = 0, 0.5, 1$ ), and the wet and dry deposition of  $\text{ING}_0$ ,  $\text{ING}_1$  and  $\text{ING}_2$ . The deposition of INGs is modified by adjusting their associated Henry's constants. In the base case, Henry's constants are taken from Ito et al. (2007) for  $\text{ING}_0$  and  $\text{ING}_1$  ( $H = 1.7 \times 10^4 \text{ M/atm}$ ) and from Sander (1999) for  $\text{ING}_2$  ( $H = 10^3 \text{ M/atm}$ ). In the slow deposition case, INGs ( $\text{ING}_0$ ,  $\text{ING}_1$  and  $\text{ING}_2$ ) are deposited like PAN ( $H = 3.6 \text{ M/atm}$ , no wet deposition) while in the fast deposition case, they are assumed to behave like nitric acid ( $H = 1 \times 10^{14} \text{ M/atm}$ ).

### 5.2.2.2 Adjoint simulations

ING photochemistry can affect ozone production in two different ways: (a) their formation depletes  $\text{NO}_x$ , diminishing local ozone production and the concentration of OH, and (b) their photooxidation releases  $\text{NO}_x$ , which, conversely, promotes local photochemistry and ozone formation. If ING lifetime is short, (a) and (b) largely compensate each other and the regional effect of ING is reduced, whereas if ING lifetime is long, their formation and transport will modulate the photochemistry of ozone precursors in both local and remote regions, though potentially in different ways. Because of the long lifetime of ozone, it is difficult to ascribe changes in ozone to (a), (b) or the transport of ozone using forward simulations.

Adjoint modeling allows the efficient calculation of the sensitivity of a cost function  $\mathcal{J}$  to many parameters (Giering and Kaminski, 1998). This approach is thus especially useful to evaluate the relative importance of mechanisms (a) and (b). Adjoint capabilities were added to the GEOS-Chem model by Henze et al. (2007). The adjoint of the chemistry is generated by the Kinetic PreProcessor (KPP, Damian et al. (2002); Sandu and Sander (2006)). To date, the adjoint of GEOS-Chem has been primarily used in inversion problems to improve emissions inventories (Henze et al., 2009; Kopacz et al., 2010). Here we also use it to constrain the sensitivity of ozone and  $\text{NO}_x$  to various photochemical processes controlling the isoprene photochemical cascade. This capability was incorporated into KPP by (Henze et al. (2007) and Appendix D.1). The cost function  $\mathcal{J}$  is defined as the mean tropospheric ozone or  $\text{NO}_x$  mixing ratio (in ppbv). We consider three time periods: June 2006 to October 2006 (high biomass burning in all tropical continental regions, Fig. 5.1); November 2006 to February 2007 (high biomass burning in Northern Africa, low biomass burning over South America and Southeast Asia); March 2007 to May 2007 (low biomass burning for all

tropical regions); and six geographical regions (Fig. D.2) that are isolated from pollution from Northern midlatitudes. In the following, we use the notation  ${}_{R_2}^{R_1}\mathcal{S}_B^A$  to denote the normalized sensitivity of  $A$  over region  $R_1$  to  $B$  over region  $R_2$ , i.e.,  $\frac{B|_{R_2}}{\mathcal{J}} \frac{\partial \mathcal{J}}{\partial B|_{R_2}}$  where  $\mathcal{J} = \bar{A}|_{R_1}$  and  $\overline{(\cdot)}$  designates the tropospheric mean. The acronyms used for  $R_1$  and  $R_2$  are listed in Table D.1. For instance,  ${}_A^a\mathcal{S}_{OH+ING_0}^{O_3}$  refers to the normalized sensitivity of Atlantic ozone to the rate of oxidation of  $ING_0$  by OH over Africa. We will sometimes omit  $R_2$  ( ${}^{R_1}\mathcal{S}_B^A$ ) to refer to the spatial changes in the sensitivity of  $A$  over  $R_1$  to  $B$  over the region of interest.

## 5.3 Results

### 5.3.1 Isoprene photochemical cascade

#### 5.3.1.1 Reference simulation

The oxidation of isoprene in the reference simulation ( $Y = 10\%$ ,  $\alpha = 50\%$ ,  $H_{ING_0} = H_{ING_1} = 1.7 \times 10^4$  M/atm,  $H_{ING_2} = 1.0 \times 10^3$  M/atm) is dominated by OH in every region ( $\sim 85\%$  globally, Fig. 5.2). The lifetime of isoprene can exceed six hours over South America, because of very low OH. This long lifetime results in the efficient transport of isoprene to the free troposphere through convection, such that it accounts for a significant fraction of the OH reactivity (Figs. D.4 and D.5). In the tropics, isoprene peroxy radicals react primarily with  $HO_2$  ( $\sim 50\%$ ). Reaction with NO and isomerization (Peeters et al., 2009, Crounse et al. (in preparation)) accounts for 35% and 10% of isoprene peroxy radical fate, respectively.

The uncertainty regarding the fate of isoprene peroxy radicals is large and has profound implications for simulations of tropospheric chemistry. In particular their fate depends critically on:

1. The rate of  $RO_2 + HO_2$ . GEOS-Chem and MOZART assume that the rate of  $RO_2 + HO_2$  is independent of  $R$  (for  $n(C) > 2$ ) (Horowitz et al., 1998, 2007) with  $k_{HO_2}^I = 7.4 \times 10^{-13} \exp(700/T)$ . Here we use the expression of Saunders et al. (2003) derived from multiple kinetic studies  $k_{HO_2}^{II} = 2.91 \times 10^{-13} \exp(1300/T) (1 - \exp(-0.245n))$ , in good agreement with the rate measured by Boyd et al. (2003) for isoprene. For isoprene at 298 K,  $k_{HO_2}^{II}/k_{HO_2}^I \sim 2$ .
2. The isoprene emission inventory. Compared with MEGAN, the GEIA emissions inventory (Guenther et al., 1995) is characterized by higher isoprene emissions in the northern mid-latitudes, which favor the reaction of isoprene peroxy radicals with NO. Using the GEIA inventory and  $k_{HO_2}^I$ , Paulot et al. (2009b) found the fate of isoprene peroxy radicals to be dominated by their reaction with NO.

3. The isomerization rate of isoprene peroxy radicals. Here we use the experimental rate from Crounse et al. (2011, in preparation)  $k_{isom}^I = 1.99 \times 10^8 \exp(-7510/T)$  that is significantly slower than the theoretical rate derived by Peeters et al. (2009). The global importance of the isomerization is thus much lower than previous estimates (e.g., Peeters and Muller (2010)).

The fate of isoprene peroxy radicals has important consequences regarding the yield of its second- and third-generation products. In the reference simulation, we find that IEPOX, the epoxide formed from the oxidation of isoprene hydroxyhydroperoxide (ISOPOOH) has a yield of  $\sim 33\%$ , significantly larger than that simulated by Paulot et al. (2009b) using  $k_{HO_2}^I$ , the GEIA emission inventory and neglecting isomerization. The chemical representation of the isoprene photochemical cascade also affects the use of the formaldehyde total column to estimate isoprene emissions in tropical regions as the yield of formaldehyde from the photooxidation of HPALD and ISOPOOH, which together account for  $\sim 65\%$ – $70\%$  of isoprene photooxidation, is not known (Palmer et al., 2003; Barkley et al., 2008).

In the reference simulation,  $ING_0$  sources are dominated by OH/NO chemistry. As noted by Horowitz et al. (2007) and Brown et al. (2009), however, nocturnal formation of organic nitrates (from  $NO_3$  chemistry) can be a significant source of reactive organic nitrates.  $ING_0$  fate is dominated by photooxidation, consistent with the conclusion from Ito et al. (2007). The mean photochemical lifetime of  $ING_0$  is shorter than isoprene primarily because the formation of  $ING_0$  is favored by higher concentrations of NO, which promote higher OH and ozone. Photochemical sinks of  $ING_0$  are dominated by ozone. This reflects both the short atmospheric lifetime of  $ING_0$  with respect to ozone (Lockwood et al., 2010) and the importance of nocturnal sources of  $ING_0$  when OH oxidation is negligible. Because of its short atmospheric lifetime, the impact of  $ING_0$  on the transport of reactive nitrogen to the upper troposphere and to oceanic basins is very limited, suggesting the fraction of  $NO_x$  recycled from  $ING_0$  photooxidation, as well as the fate of  $ING_1$  and  $ING_2$ , are essential for assessing the regional effect of ING photochemistry (Fig. D.3).

### 5.3.1.2 Sensitivity to the treatment of isoprene nitrates

Modifying the treatment of isoprene nitrate chemistry has little impact on the relative importance of the the oxidation channels of isoprene, because variation in ozone and OH mixing ratios are well correlated. However the lifetime of isoprene is strongly impacted by the representation of isoprene nitrate chemistry with variations exceeding  $\sim \pm 20\%$  across the different simulations. The largest changes are found over South America, where NO is very low.

The branching between night and day formation of  $\text{ING}_0$  is strongly impacted by the assumed yield of isoprene nitrates. For an organic nitrate yield of 5% from OH/NO chemistry,  $\text{NO}_3$  chemistry becomes the primary source of  $\text{ING}_0$  consistent with the conclusions from Horowitz et al. (2007). Even when  $\text{ING}_0$  is assumed to deposit as fast as nitric acid, its fate remains dominated by photooxidation reflecting its short photochemical lifetime. Because of their slower photooxidative sinks,  $\text{ING}_1$  and  $\text{ING}_2$  are much more sensitive to deposition. Better constraints on the relative importance of photochemical and depositional sinks are especially critical for  $\text{ING}_2$  since it is the primary  $\text{NO}_x$  carrier to oceanic basins. From this analysis, it is clear that the treatment of  $\text{ING}_0$  as a terminal sink of  $\text{NO}_x$  (e.g., the assumption that they readily deposit) in the GEOS-Chem standard simulations cannot be reconciled with laboratory data presented by Lockwood et al. (2010) and Paulot et al. (2009a).

### 5.3.2 Impact of the $\text{NO}_x$ and $\text{O}_x$ budget

The net removal of  $\text{NO}_x$  by isoprene nitrate chemistry can be expressed as

$$\mathcal{D}_{\text{ING}} = \mathcal{P}_{\text{ING}_0} + \mathcal{P}_{\text{ING}_1}^* - \mathcal{L}_{\text{ING}_1} - \mathcal{L}_{\text{ING}_2} - \alpha \times \mathcal{L}_{\text{ING}_0} \quad (5.1)$$

where  $\mathcal{P}_{\text{ING}_0}$  and  $\mathcal{P}_{\text{ING}_1}^*$  are the photochemical sources of  $\text{ING}_0$  and  $\text{ING}_1$  (excluding the source from  $\text{ING}_0$ );  $\mathcal{L}_{\text{ING}_0}$ ,  $\mathcal{L}_{\text{ING}_1}$  and  $\mathcal{L}_{\text{ING}_2}$  are the photochemical losses of  $\text{ING}_0$ ,  $\text{ING}_1$  and  $\text{ING}_2$ . Fig. 5.3 shows that over regions with high isoprene and low  $\text{NO}_x$  emissions,  $\mathcal{D}_{\text{ING}}$  can account for up to 75% of  $\text{NO}_x$  loss ( $\mathcal{L}_{\text{NO}_x}$ ). On a regional scale, however, a large fraction of the  $\text{NO}_x$  segregated in isoprene nitrates is cycled back to the atmosphere over continental regions (66% for Africa, 52% for South America). The transport of ING (in particular  $\text{ING}_2$ ) allows isoprene nitrate photochemistry to contribute up to 30% of  $\text{NO}_x$  production downstream from continents.

K-means clustering analysis (MacQueen, 1967) on the components of  $\mathcal{D}_{\text{ING}}$  (Fig. D.3) reveals that the impact of isoprene chemistry on the local  $\text{NO}_y$  budget is driven by the lifetime of the different isoprene nitrates more than by their production rates. Indeed if a large fraction of isoprene peroxy radicals reacts with NO, the large production of  $\text{ING}_0$  will be associated with efficient production of  $\text{O}_x$  and  $\text{HO}_x$ . Under these photochemical conditions, ING are oxidized rapidly, reducing their impact on the  $\text{NO}_x$  budget. Conversely because low  $\text{NO}_x$ /high VOC conditions are associated with low  $\text{HO}_x$  and ozone, the removal of  $\text{NO}_x$  by ING chemistry is very efficient under these conditions. This mechanism is consistent with the variation in  $\mathcal{D}_{\text{ING}}$  across continents and seasons, illustrated by the contrast in  $\mathcal{D}_{\text{ING}}/\mathcal{L}_{\text{NO}_x}$  between the densely populated

island of Java and the relatively pristine island of New Guinea (Fig. 5.3). It follows that if  $\text{HO}_x$  is underestimated in our simulations, as suggested by many recent studies (e.g., Lelieveld et al. (2008); Ren et al. (2008)), the importance of ING chemistry at the regional scale will be diminished. This will be discussed in Section 5.4.4.

The representation of ING chemistry has important consequences on the modeled tropical ozone over continental regions (Fig. 5.4). Ozone is most sensitive to the representation of ING over regions where  $\mathcal{D}_{\text{ING}}$  is large (generally regions with high isoprene and low  $\text{NO}_x$  emissions). For instance, over South America, where the isoprene-to- $\text{NO}_x$  ratio is especially high,  $\mathcal{P}_{\text{O}_x}$  can vary by as much as  $\pm 20\%$  from the reference simulation as a result of changes in the representation of ING photochemistry (Fig. 5.5). Changes in ING chemistry are not limited to continental regions with high isoprene emissions. Downwind of Africa and South America, for instance, the Atlantic and Pacific basins exhibit a sensitivity to ING chemistry similar to continental regions.

## 5.4 Discussion

In this section, we first show that the regional effect of isoprene nitrate chemistry on ozone can be well understood through its modulation of the  $\text{NO}_x$  budget. We then hypothesize that the resulting modulation of  $\text{HO}_x$  contributes to the large-scale isoprene effect through convection. Finally, we focus on the influence of isoprene photooxidation on South Atlantic ozone, which combines, in a complex way,  $\text{NO}_x$  segregation and transport as well as the transport of ozone.

### 5.4.1 $\text{NO}_x$ removal efficiency controls the impact of isoprene nitrates over tropical continental regions

The sensitivity of ozone to ING photochemistry is well correlated with its effect on the net loss of  $\text{NO}_x$  (Fig. 5.5). It follows from this correlation that very different representations of the ING chemistry can have comparable effects on  $\mathcal{P}_{\text{O}_x}$  at the continental scale. This is illustrated by the similar  $\mathcal{P}_{\text{O}_x}$  simulated for  $\{Y = 15\%, \alpha = 100\%, \text{fast deposition}\}$ ,  $\{Y = 10\%, \alpha = 50\%, \text{fast deposition}\}$ ,  $\{Y = 15\%, \alpha = 50\%, \text{default deposition}\}$ . However, as the  $\text{NO}_x$  loss mechanisms (export to oceanic basins and deposition) are different in each of these representations, they result in different predictions regarding nitrogen deposition and ozone formation downwind from continents, such that the need to accurately constrain ING photochemistry is not

relaxed.

The relationship between  $\mathcal{P}_{\text{O}_x}$  and  $\mathcal{D}_{\text{ING}}$  changes regionally and seasonally (Fig. D.6). This sensitivity can be well captured by the fraction of  $\text{NO}_x$  lost through the isoprene nitrate chemistry (i.e.,  $\mathcal{D}_{\text{ING}}/\mathcal{L}_{\text{NO}_x}$ ) as shown in Fig. 5.6.

Ozone is most sensitive to isoprene nitrate chemistry outside the biomass burning seasons when isoprene impact on  $\mathcal{L}_{\text{NO}_x}$  is largest (Figs. 5.6 and D.6). Conversely, the representation of isoprene nitrate chemistry has little impact on ozone during the biomass burning period regardless of isoprene emissions. This difference can be understood through the seasonal variation of  $\mathcal{D}_{\text{ING}}/\mathcal{L}_{\text{NO}_x}$ . During the biomass burning season, large emissions of  $\text{NO}_x$ , while increasing the production of INGs, favor higher OH and ozone such that the lifetime of INGs is reduced and their effect on the ozone budget is diminished. Consistent with this mechanism, the modeled sensitivity of ozone to ING photochemical sinks (calculated using the adjoint) is positive over continental regions (Fig. 5.7, left column).  $w_{\text{OH}+\text{ING}_0}^{\text{O}_3}$  is negative, which can be attributed to the different  $\text{NO}_x$  recycling efficiency between  $\text{OH} + \text{ING}_0$  and  $\text{O}_3 + \text{ING}_0$ : in the model, reaction of  $\text{ING}_0$  with ozone results in  $\alpha$   $\text{NO}_x$  returned to the atmosphere, whereas reaction of  $\text{ING}_0$  with OH only results in  $\gamma_{\text{NO}} \times \alpha$  recycling (where  $\gamma_{\text{NO}}$  is the fraction of  $\text{ING}_0\text{O}_2$  reacting with NO, Fig. D.1), because we assume that  $\text{ING}_0\text{O}_2 + \text{HO}_2$  does not readily release  $\text{NO}_x$ . Hence,  $\text{NO}_x$  is not efficiently recycled from the oxidation of  $\text{ING}_0$  by OH under low  $\text{NO}_x$  conditions, i.e., where ozone is most sensitive to ING chemistry. This estimate depends critically on the ozonolysis mechanism of  $\text{ING}_0$  as well as the reaction of  $\text{ING}_0\text{O}_2$  with  $\text{HO}_2$ , about which very little is known (Giacopelli et al., 2005; Lockwood et al., 2010).

Overall, ozone sensitivity to the ING representation is greater over South America than Africa (Fig. 5.7), consistent with the finding that the sensitivity of continental ozone to ING photochemistry is tied to  $\mathcal{D}_{\text{ING}}/\mathcal{L}_{\text{NO}_x}$  (Fig. 5.3). The relative importance of  $w_{\text{O}_3+\text{ING}_0}^{\text{O}_3}$  and  $w_{\text{O}_3+\text{ING}_1}^{\text{O}_3}$  also exhibits seasonal variations. The sensitivity to the fate of  $\text{ING}_0$  generally peaks outside the biomass burning seasons, reflecting the importance of  $\text{ING}_0$  as an important local sink of  $\text{NO}_x$  under low  $\text{HO}_x$  conditions.

A similar approach is used to analyze how  $\text{ING}_0$  yield (Y) and recycling ( $\alpha$ ) affect mean tropical tropospheric ozone (Fig. 5.8).  $^t\mathcal{S}_Y^{\text{O}_3}$  is always negative, which suggests the decrease of  $\mathcal{P}_{\text{O}_3}$  over continental regions ( $\partial\mathcal{D}_{\text{ING}}/\partial Y < 0$ ) is not compensated by an increase in  $\mathcal{P}_{\text{O}_3}$  downwind of isoprene source regions (due to the release of  $\text{NO}_x$  by the oxidation of  $\text{ING}_0$ ,  $\text{ING}_1$  or  $\text{ING}_2$ ). Seasonal and regional variations in  $^t\mathcal{S}_Y^{\text{O}_3}$  reflect those of  $\mathcal{D}_{\text{ING}}/\mathcal{L}_{\text{NO}_x}$ . This contrast is especially apparent in Africa where  $^t_A\mathcal{S}_Y^{\text{O}_3}$  is  $\sim 5$  greater from March to May than from November to February (Fig. 5.8). Ozone is significantly less sensitive to uncertainties in the recycling (though the uncertainty in the recycling is much larger than the uncertainty

in the yield of isoprene nitrate). Interestingly,  ${}^t\mathcal{S}_\alpha^{O_3}$ , though generally positive, as would be expected from its overall impact on continental  $\mathcal{D}_{\text{ING}}$  (Fig. 5.3), becomes negative when isoprene emissions and biomass burning are collocated (Africa, panel B). This unexpected behaviour will be discussed in section 5.4.3.

The sensitivity of tropical ozone to  $Y$  and  $\alpha$  can be compared to its sensitivity to methane oxidation.  ${}^t\mathcal{S}_{\text{OH}+\text{CH}_4}^{O_3}$  is always positive and its zonal variations largely reflect the fate of the methylperoxy radicals, i.e.  $\text{NO}_x$  concentrations (Jaeglé et al., 2001; Wennberg et al., 1998).  ${}^t\mathcal{S}_{\text{OH}+\text{CH}_4}^{O_3}$  is generally larger over continents where the largest sources of  $\text{NO}_x$  are located (biomass burning for Africa, anthropogenic emissions for western Southeast Asia).  ${}^t\mathcal{S}_{\text{OH}+\text{CH}_4}^{O_3}$  is, however, minimum over South America, reflecting the low model  $\text{HO}_x$  resulting from high biogenic and low  $\text{NO}_x$  emissions.

Ozone is very sensitive to the formation rate of nitric acid ( ${}^t\mathcal{S}_{\text{OH}+\text{NO}_2}^{O_3}$ ), the primary sink of  $\text{NO}_x$  over much of the atmosphere, emphasizing the need for very accurate kinetic rate on the reaction of OH with  $\text{NO}_2$  (Möllner et al., 2010). Both  $\text{ING}_0$  and nitric acid production result in the loss of  $\text{NO}_x$  and  ${}^t\mathcal{S}_{\text{OH}+\text{NO}_2}^{O_3}$  and  ${}^t\mathcal{S}_Y^{O_3}$  are negative throughout the tropics. Nitric acid formation is most efficient when OH and  $\text{NO}_2$  are large, i.e., over large  $\text{NO}_x$  emissions (biomass burning in Africa or anthropogenic and biomass burning in Java, Fig. 5.8). Unlike nitric acid, the photochemical lifetime of  $\text{ING}_0$  is very short under these conditions and it is not an efficient sink of  $\text{NO}_x$ . However, under low  $\text{NO}_x$  conditions and high isoprene emissions,  $\text{ING}_0$  photooxidation is limited and it behaves, at least locally, as an important sink of  $\text{NO}_x$  (Fig. 5.3). It follows that  ${}^t\mathcal{S}_{\text{OH}+\text{NO}_2}^{O_3}$  and  ${}^t\mathcal{S}_Y^{O_3}$  have opposite dependence on photochemical conditions (i.e., primarily on  $\text{NO}_x$  surface emissions). This is illustrated by their seasonal variations over South America where  ${}^t\mathcal{S}_{\text{OH}+\text{NO}_2}^{O_3}$  is greater than  ${}^t\mathcal{S}_Y^{O_3}$  during the biomass burning season ( $\mathcal{D}_{\text{ING}}/\mathcal{L}_{\text{NO}_x} \ll 1$ ), but significantly lower outside the biomass burning seasons (Fig. 5.8). Seasonal variations are even greater in Africa where  ${}^t\mathcal{S}_Y^{O_3}$  is almost negligible from November to February (Fig. 5.8, panel B) when isoprene and biomass burning emissions are collocated (Fig. 5.1), but comparable to  ${}^t\mathcal{S}_{\text{OH}+\text{NO}_2}^{O_3}$  from March to May. A similar mechanism may also explain the large contrast between Java, where  ${}^t\mathcal{S}_Y^{O_3} \ll {}^t\mathcal{S}_{\text{OH}+\text{NO}_2}^{O_3}$  as a result of large anthropogenic activities, and the more pristine New Guinea where  ${}^t\mathcal{S}_Y^{O_3} \sim {}^t\mathcal{S}_{\text{OH}+\text{NO}_2}^{O_3}$ .

#### 5.4.2 $\text{NO}_x$ removal efficiency in the continental boundary layer influences the impact of isoprene over remote regions through deep convection

A similar analysis of the sensitivity of ozone to tropical emissions of isoprene (Fig. 5.9) shows that  ${}^t\mathcal{S}_{\text{E}(\text{ISOP})}^{O_3}$  is comparable to its sensitivity to  $\text{NO}_x$  emissions from biomass burning ( ${}^t\mathcal{S}_{\text{E}_{\text{bb}}(\text{NO}_x)}^{O_3}$ ) but lower than ozone



sensitivity to lightning  $\text{NO}_x$  ( $^t\mathcal{S}_{\text{E}(\text{NO}_x)}^{\text{O}_3}$ ). Unlike  $^t\mathcal{S}_{\text{E}(\text{NO}_x)}^{\text{O}_3}$  that is always positive (regardless of the source of  $\text{NO}_x$ ),  $^t\mathcal{S}_{\text{E}(\text{ISOP})}^{\text{O}_3}$  can switch sign seasonally and regionally. For instance,  $^t\mathcal{S}_{\text{E}(\text{ISOP})}^{\text{O}_3}$  is positive during the biomass burning season (Fig. 5.9, panel A) and becomes negative as biomass burning emissions decrease (Fig. 5.9, panels B and C). Similarly,  $^t\mathcal{S}_{\text{E}(\text{ISOP})}^{\text{O}_3}$  switches sign between western Southeast Asia and eastern Southeast Asia. As we will show in this section,  $^t\mathcal{S}_{\text{E}(\text{ISOP})}^{\text{O}_3}$  seasonal and regional variations reflect the competition between different interactions of the isoprene photochemical cascade with  $\text{O}_x$  at the local and global scales.

The competition between the remote and local impacts of isoprene photooxidation on  $\text{O}_x$  is directly illustrated by the large regional variability of  $^s\mathcal{S}_{\text{E}(\text{ISOP})}^{\text{O}_3}$  (Fig. 5.10).  $^s\mathcal{S}_{\text{E}(\text{ISOP})}^{\text{O}_3}$  is negative and its regional and seasonal variation can be largely explained by  $^s\mathcal{S}_{\text{E}(\text{ISOP})}^{\text{NO}_x}$ , supporting the modulation of  $\text{NO}_x$  as the primary mechanism controlling the regional influence of isoprene photooxidation on ozone. This is also consistent with the seasonal variation of  $^s\mathcal{S}_{\text{E}(\text{ISOP})}^{\text{O}_3}$  that is greatest from March to May, when  $\mathcal{D}_{\text{ING}}$  contributes most to  $\mathcal{L}_{\text{NO}_x}$ . Unlike  $^s\mathcal{S}_{\text{E}(\text{ISOP})}^{\text{O}_3}$ , the long-range impact of isoprene emissions (dominated by Africa (Fig. 5.10)) is generally positive and not associated with a local production of ozone, since  $^s\mathcal{S}_{\text{A}(\text{ISOP})}^{\text{O}_3}$  is not correlated with  $^s\mathcal{S}_{\text{A}(\text{ISOP})}^{\text{NO}_x}$  (Fig. 5.10) and small on average (Fig. 5.11).

Large-scale ozone enhancement fueled by isoprene photochemistry may impact the transport of ozone formed over continental regions, through the well-known “Atlanta” mechanism (Chameides et al., 1988), i.e., by the boundary layer oxidation of isoprene under high- $\text{NO}_x$  conditions (e.g., from November to February in Africa). The spatial impact of this mechanism is usually limited in the midlatitudes because  $\text{O}_x$  lifetime is relatively short in the boundary layer. In the tropics, however, convection may allow  $\text{O}_x$  to be rapidly transported to the free troposphere, where it can be advected over much larger spatial scales thanks to a significantly longer lifetime (Jacob et al., 1996).

The “Atlanta” mechanism does not, however, explain why  $^s\mathcal{S}_{\text{A}(\text{ISOP})}^{\text{O}_3}$  peaks outside the biomass burning seasons (Fig. 5.11). We propose that this reflects ozone production in the free troposphere driven by the transport of boundary layer isoprene and its photochemical products by convection. Observations of high concentrations of isoprene (up to  $\sim 1$  ppbv) and its photochemical products in the upper troposphere have been reported over Europe (Colomb et al., 2006; Stickler et al., 2006), Africa (Bechara et al., 2010; Murphy et al., 2010), and South America. The model exhibits a very characteristic “C”-profile for isoprene in the tropics and a significant fraction of isoprene oxidation can take place at  $P < 800$  hPa (Figs. D.4 and D.5). In these conditions, the production of ozone is extremely efficient as (a) isoprene peroxy radicals react almost entirely with  $\text{NO}$ , and (b)  $\mathcal{D}_{\text{ING}} \sim 0$  as ING fate is almost entirely driven by  $\text{NO}_x$ -neutral photochemical

reactions. The injections of reactive isoprene can have a very large impact on ozone production in particular if it is accompanied by production of  $\text{NO}_x$  (e.g., from lightning) (Collins et al., 1999; Poisson et al., 2000; Bechara et al., 2010; Jacob et al., 1996; Prather and Jacob, 1997). The formation of  $\text{NO}_x$  reservoirs in the upper troposphere (e.g., PAN) may further amplify the impact of isoprene photochemistry on  $\text{O}_x$  through the transport of  $\text{NO}_x$  to remote regions (Poisson et al., 2000). This mechanism would be consistent with the study of Aghedo et al. (2007), which reported that most of the production of ozone fueled by African emissions does not take place over the African continent.

Since ozone production in the free troposphere increases as the supply of isoprene and its photochemical products from the boundary layer increases, i.e., under low boundary layer oxidative conditions, the production of ozone in the upper troposphere is favored, somewhat paradoxically, by its destruction in the boundary layer. Since ozone is also transported to the upper troposphere, the net effect of the transport of isoprene to the upper troposphere depends on the relative strength of these processes: ozone production in the free troposphere and transport of low boundary layer ozone. Unlike Africa, where  $\text{NO}_x$  is generally high enough such that isoprene photochemistry does not significantly depress  $\mathcal{P}_{\text{O}_x}$  in the boundary layer (Fig. 5.14), the segregation of  $\text{NO}_x$  by isoprene nitrates and the destruction of  $\text{HO}_x$  in South America by [R 5.7] results in very low boundary layer  $\text{HO}_x$  and  $\text{O}_x$  (Fig. 5.11). It follows that the net effect of this mechanism should be greater for isoprene emitted over Africa than over South America, even though less isoprene is oxidized outside of the boundary layer (Fig. D.5). This is supported by  $^{\text{P}}\mathcal{S}_{\text{E}(\text{ISOP})}^{\text{O}_3}$ , which is greater outside the biomass burning seasons over Africa than over South America (Fig. 5.12). Similarly,  $^{\text{S}}\mathcal{S}_{\text{E}(\text{ISOP})}^{\text{O}_3}$  is generally negative, reflecting its impact on the removal of  $\text{NO}_x$  by ING, while  $^{\text{P}}\mathcal{S}_{\text{S}(\text{ISOP})}^{\text{O}_3}$  can be positive during the biomass burning season, when boundary layer ozone over South America is not as impacted by isoprene photochemistry. The importance of the VOC transport thus depends on the boundary layer budget of ozone, which is largely controlled by  $\mathcal{D}_{\text{ING}}$ . It follows that ING photochemistry may indirectly modulate the large-scale effect of isoprene photooxidation on the  $\text{O}_x$  budget.

The large-scale influence of isoprene can be contrasted to that of lightning and biomass burning  $\text{NO}_x$ .  $^{\text{P/S}}_{\text{A}}\mathcal{S}_{\text{E}(\text{ISOP})}^{\text{O}_3}$  is very similar to  $^{\text{P/S}}_{\text{A}}\mathcal{S}_{\text{E}_{\text{li}}(\text{NO}_x)}^{\text{O}_3}$ , though lightning appears to favor ozone formation far from its source region (unlike isoprene). The intercontinental effect of biomass burning is more limited. Similar to isoprene, it does not appear to be driven by the large-scale transport of  $\text{NO}_x$ , suggesting the lifetime of  $\text{NO}_x$  reservoirs is not sufficiently long to impact these regions.

### 5.4.3 Isoprene nitrates as $\text{NO}_x$ reservoirs and spatial scales coupling

In Sections 5.4.1 and 5.4.2, we have presented evidence that isoprene photochemistry impacts the tropical  $\text{O}_x$  budget (through the modulation of  $\text{NO}_x$  sinks at the regional scale and the production of  $\text{O}_x$  in the upper troposphere on the global scale). In this section, we focus on regions where ING photooxidation contributes significantly to the  $\text{NO}_x$  source (downwind of continents (Fig. 5.3)). The impact of this export on the  $\text{O}_x$  budget reflects the competition between lower production of ozone over continental regions (greater continental  $\mathcal{D}_{\text{ING}}$ ) and greater ozone production downwind. Despite the loss of  $\text{NO}_x$  during its export (through deposition), this competition can result in an increase in  $\text{O}_x$  downwind of continents, since the ozone production efficiency is generally greater far from  $\text{NO}_x$  sources.

This competition is illustrated by regional variations of  $^S\mathcal{S}_{\text{OH}+\text{ING}_2}^{\text{O}_3}$ .  $\text{ING}_2$  is sufficiently long-lived to contribute to the export of  $\text{NO}_x$  to oceanic basins (Fig. D.3), such that  $^S\mathcal{S}_{\text{OH}+\text{ING}_2}^{\text{O}_3}$  is negative over oceanic basins, while it is positive over Africa and Southeast Asia (Fig. 5.7).  $^S\mathcal{S}_{\text{OH}+\text{ING}_2}^{\text{O}_3}$  is negative outside the biomass burning season over South America. This is unique and probably reflects the very low oxidative conditions over this region from March to May (high  $\mathcal{D}_{\text{ING}}$ ) that limit the continental oxidation of  $\text{ING}_2$ . Unlike  $^S\mathcal{S}_{\text{OH}+\text{ING}_2}^{\text{O}_3}$ ,  $^S\mathcal{S}_{\text{OH}+\text{ING}_0}^{\text{O}_3}$  and  $^S\mathcal{S}_{\text{OH}+\text{ING}_1}^{\text{O}_3}$  are positive, even over oceanic basins. This suggests  $\text{ING}_0$  and  $\text{ING}_1$  are too short-lived to contribute to the export of  $\text{NO}_x$  from continental regions: their impact on ozone over oceanic basins is thus limited to their modulation of ozone transport from continental regions.

We now focus on the sensitivity of South Atlantic ozone to photochemical conditions over Africa. South Atlantic ozone exhibits a well-defined zonal “wave-one” pattern (Thompson et al. (2000), Bowman et al. (2009, and references therein)). Numerous studies have been devoted to the study of the different factors controlling this pattern ranging from emissions (Sauvage et al., 2007b; Edwards et al., 2006; Jacob et al., 1996) to dynamics (Wang et al., 2006). However, to our knowledge, the influence of uncertainties in chemical mechanisms on the simulation of Atlantic ozone has not been explored.

The seasonal and geographical variations of  $^A\mathcal{S}_{\alpha}^{\text{O}_3}$  illustrate how the relative impact of continental production of ozone and  $\text{NO}_x$  export on Atlantic ozone vary in response to changing photochemical conditions over Africa. When biomass burning and isoprene emissions are collocated (Fig. 5.13 B), a large fraction of isoprene peroxy radicals reacts with  $\text{NO}$ , such that  $\mathcal{D}_{\text{ING}}$  is low and ING chemistry has a minor effect on the local  $\mathcal{P}_{\text{O}_3}$  (Fig. 5.4). Thus, an increase in  $\alpha$  results in a small fractional increase in  $\mathcal{P}_{\text{O}_3}$  and its effect on Atlantic ozone is dominated by the decrease in the transport of  $\text{NO}_x$  reservoirs (i.e., in the production of ozone closer to the receptor region). From  $^t_A\mathcal{S}_{\alpha}^{\text{O}_3} < 0$  and  $^A_A\mathcal{S}_{\alpha}^{\text{O}_3} > 0$  (consistent with  $\partial\mathcal{D}_{\text{ING}}/\partial\alpha < 0$ ) from

November to February, it follows that the decrease of  $\mathcal{P}_{O_3}$  downwind of Africa as a result of increased  $NO_x$  recycling (i.e. lower transport of  $NO_x$  reservoirs) outweighs the increase of ozone over Africa during the biomass burning season and its transport to the South Atlantic. Conversely, from March to May (Fig. 5.13 C),  ${}^a_A \mathcal{S}_\alpha^{O_3}$  is positive where isoprene peroxy radicals react primarily with  $HO_2$ . The export of ozone from this region, where  $\mathcal{D}_{ING}$  is large such that  $\mathcal{P}_{O_3}$  is very sensitive to  $\alpha$ , dominates over the export of  $NO_x$ .

Comparisons between  ${}^a_A \mathcal{S}_{E(ISO)}^{O_3}$  and  ${}^A_A \mathcal{S}_{E(ISO)}^{O_3}$  confirm that the large-scale influence of isoprene photooxidation can be anti-correlated to its regional effect (see Section 5.4.2). We also find that  ${}^a_A \mathcal{S}_{E_{bb}(NO_x)}^{O_3}$  and  ${}^a_A \mathcal{S}_{E(ISO)}^{O_3}$  are of similar magnitudes (Figs. 5.14 and 5.15). This is at odds with the conclusions of Sauvage et al. (2007b) who found that the dependence of Atlantic ozone on isoprene emissions was negligible. This may be associated with the treatment of isoprene nitrates as a terminal sink of  $NO_x$  in the standard GEOS-Chem mechanism, since under these conditions changes in  $\mathcal{D}_{ING}$  as a result of different isoprene emissions are diminished. Interestingly, even though ozone is most sensitive to biomass burning on the continental scale ( ${}^A_A \mathcal{S}_{E_{bb}(NO_x)}^{O_3} > {}^A_A \mathcal{S}_{E_{li}(NO_x)}^{O_3}$ ), this effect does not propagate efficiently to larger spatial scales ( ${}^a_A \mathcal{S}_{E_{li}(NO_x)}^{O_3} > {}^a_A \mathcal{S}_{E_{bb}(NO_x)}^{O_3}$ ), which is consistent with the conclusions of Sauvage et al. (2007b). Comparisons between  ${}^{A/a}_A \mathcal{S}_{E_{li}(NO_x)}^{NO_x}$  and  ${}^{A/a}_A \mathcal{S}_{E_{bb}(NO_x)}^{NO_x}$  suggest this may stem from the different lifetimes of biomass-burning  $NO_x$  (short-lived because solely injected into the boundary layer) and lightning  $NO_x$ . Since a significant fraction of biomass-burning  $NO_x$  may be injected outside of the boundary layer (Val Martin et al., 2010), the contrast between the large-scale and regional effects of biomass-burning and lightning  $NO_x$  is likely to be overestimated in the model.

#### 5.4.4 Can we separate the effect of chemistry, emissions and dynamics on the tropical $O_x$ budget using experimental observations?

In the previous sections, we have shown that the oxidation of biogenics plays a large role in the modulation of the  $O_x$  budget and that this modulation can vary dramatically in space and time. Thus, different representations of this coupling across models are likely to contribute to some of inconsistencies between  $O_x$  simulations in the tropics (Stevenson et al., 2006).

Most studies focusing on tropical ozone have been devoted to improving  $NO_x$  emissions from lightning, biomass burning and soil to achieve better agreement with ozone measurements (Sauvage et al., 2007b; Jaeglé et al., 2004; Ziemke et al., 2009). It follows from this study, however, that the impact of changes in  $NO_x$  emissions on the  $O_x$  budget cannot be readily separated from their modulation by different repre-

sentations of the photooxidation of biogenics and transport processes (in particular deep convection (Nassar et al., 2009)). Thus, the uncertainty of  $\text{NO}_x$  emissions derived from ozone or  $\text{NO}_2$  measurements will be commensurate with errors in the representation of these processes.

Our analysis reveals, however, that the different factors investigated here exhibit different seasonal and geographical patterns that may be used to unravel their coupling. These factors would be best differentiated by using long time series (Martin et al., 2000) and measurements from multiple compounds that are impacted differently by each process (e.g., CO,  $\text{NO}_2$ , ozone, formaldehyde Bowman et al., 2009). Of particular importance are:

- the ozone contrast between land and ocean, which is amplified by biomass burning but reduced by lightning and the transport of  $\text{NO}_x$  reservoirs.
- the fraction of isoprene (or its photochemical products) oxidized in the upper troposphere (i.e., vertical profile of isoprene) that is essential to the large-scale impact of isoprene on the  $\text{O}_x$  budget. Similar information may be obtained from the vertical profile of formaldehyde. Such vertical profiles may also provide essential constraints on the photooxidative conditions in the boundary layer, which have been suggested to be dramatically underestimated by models close to large BVOC sources. Such a multi-compound approach may also be very useful to constrain isoprene emissions from satellite observations of formaldehyde total column (Palmer et al., 2003). Under low- $\text{NO}_x$  conditions, i.e., where the fate of  $\text{ISOPO}_2$  is dominated by reactions with  $\text{HO}_2$  and isomerization, it is unlikely that isoprene emissions can be directly related to formaldehyde total columns (Barkley et al., 2008). Instead, a formal inversion approach taking into account the vertical profile of formaldehyde is probably required.

## 5.5 Conclusion

The rapid economic development of the tropical regions calls for a better assessment of how anthropogenic emissions impact tropical ozone. In particular, it is essential to evaluate how anthropogenic perturbations may influence the concentration of ozone and assess the consequences of this change on food security (Van Dingenen et al., 2009; Hewitt et al., 2009), human health (World Health Organization, 2005) and radiative forcing (directly or indirectly e.g., Sitch et al., 2007).

In this work, we have shown that accurate simulation of tropical ozone must take into account the mod-

ulation of the  $O_x$  budget by the photooxidation of biogenics. In particular, the regional simulation of ozone is shown to be very sensitive to the removal and export of  $NO_x$  by isoprene nitrates. In South America and New Guinea, the high ratio of isoprene-to-  $NO_x$  emissions makes isoprene nitrates chemistry the primary sink of  $NO_x$ .

We have also shown that the impact of isoprene photooxidation on tropical ozone is not limited to the regional scale. We hypothesize that this long-range effect is the result of dynamic and photochemical processes: efficient vertical mixing (through deep convection) and low boundary layer  $HO_x$  (as a result of high biogenics and low  $NO_x$  emissions). These conditions allow a significant fraction of isoprene to be oxidized in the free troposphere, where its contribution to ozone production is amplified.

From this work, it is clear that the effect of photochemistry cannot be simply separated from emissions, even on the global scale. In particular, a better understanding of the coupling of isoprene with  $NO_x$  emissions requires a much improved representation of the isoprene photochemical cascade as a whole, since many of the large scale effects presented here result from the photochemistry of second-, third-, etc.- generation photochemical products. More work should thus be devoted to determining their nature and fate over the broad range of peroxy radical lifetimes found in the atmosphere.

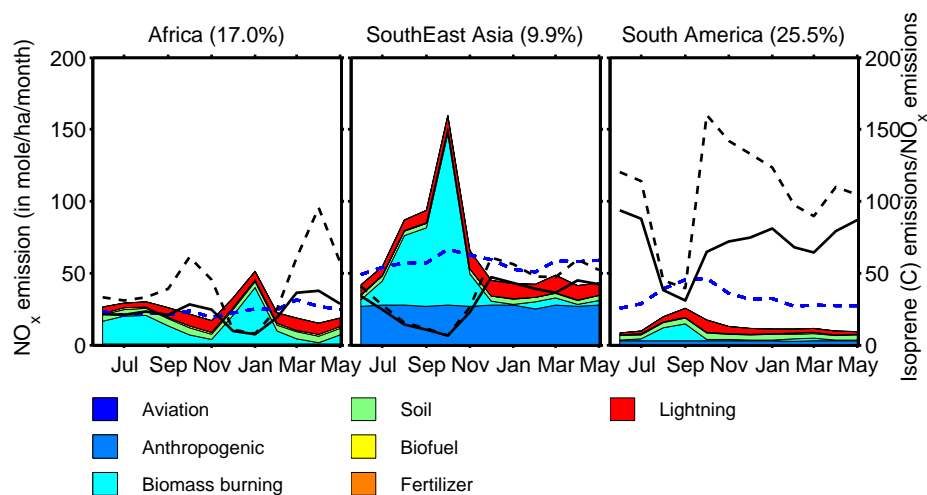


Figure 5.1: The three continental regions considered in this study (Fig. D.2) account together for  $\sim 50\%$  of isoprene global emissions (geographical breakdown is indicated in the panels' title). Very different  $\text{NO}_x$ /isoprene regimes (black line for  $\text{NO}_x$ /isoprene and dashed black line for  $\text{NO}_x^{\text{surface}}$ /isoprene) and  $\text{NO}_x$  sources (colored regions) are experienced through the year with South America C(isoprene)/N emissions exceeding 50 for most of the year. The seasonality of the ratio of isoprene emissions to  $\text{NO}_x$  emissions is primarily controlled by biomass burning, as seasonal variations of isoprene emissions (dashed blue line, in mole of C/ha/month  $\times 1/25$ , left axis) are small. The ratio of  $\text{NO}_x$  emissions to isoprene emissions is weighted by isoprene emissions to represent the average  $\text{NO}_x$  encountered by isoprene.

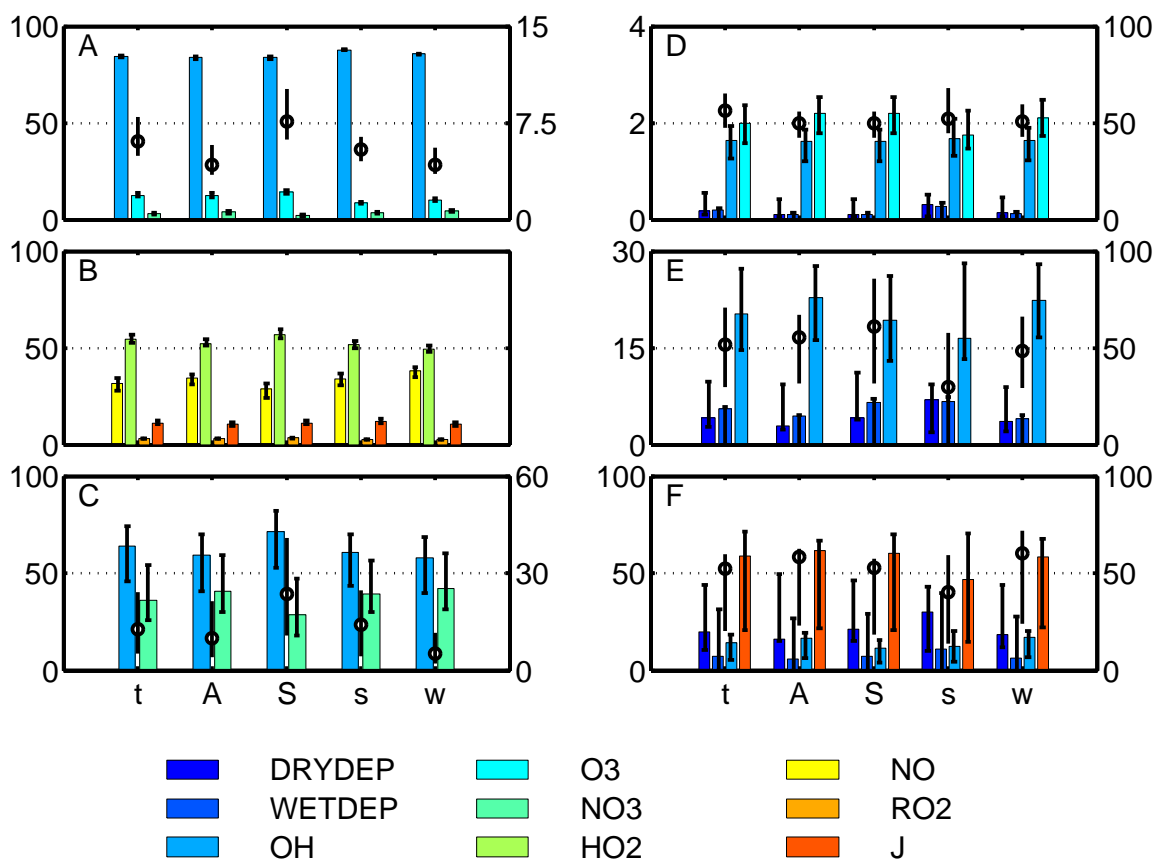


Figure 5.2: Overview of the isoprene photochemical cascade (thick color bars) for the reference simulation. Branching ratios for the reference run (in percent) are indicated by bars for isoprene oxidation (A, left axis), isoprene peroxy radical fate (B, left axis), isoprene nitrate sources (C, left axis),  $ING_0$  fate (D, right axis),  $ING_1$  fate (E, right axis),  $ING_2$  fate (F, right axis). Black open circles indicate the lifetime (in hours) of isoprene (A, right axis),  $ING_0$  (D, left axis),  $ING_1$  (E, left axis) and  $ING_2$  (F, left axis), and the fractional loss of  $NO_x$  caused by isoprene nitrate chemistry,  $L_{ING_0}(NO_x)/L_T(NO_x)$  (C, right axis in %). The extent of the error bars represents the minimum and maximum values calculated using the different representations of isoprene nitrate chemistry (see Section 5.2). J designates the isomerization of isoprene peroxy radical (B, Peeters et al., 2009) and the photolysis of  $ING_2$  (F).



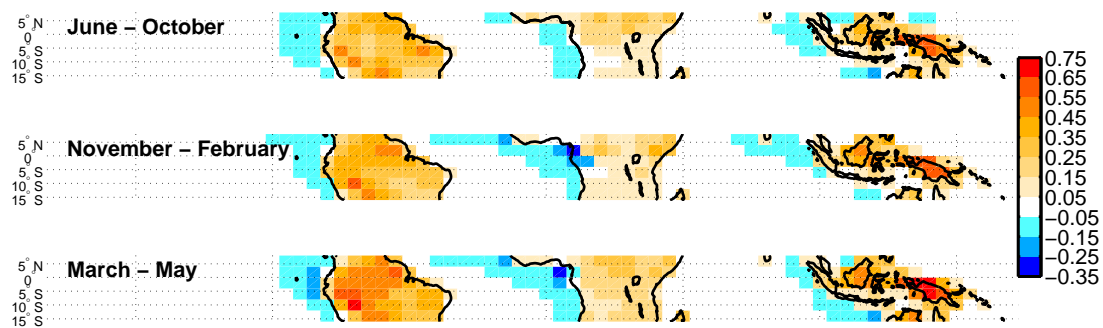


Figure 5.3: Isoprene nitrate chemistry significantly affects the budget of NO<sub>x</sub> in the tropics. Positive numbers represent the fraction of the net chemical loss of NO<sub>x</sub> ( $\mathcal{L}_{\text{NO}_x}$ ) accounted for by  $\mathcal{D}_{\text{ING}}$  ( $\mathcal{D}_{\text{ING}} > 0$ ), negative numbers denote the fraction of the net chemical source of NO<sub>x</sub> accounted for by  $\mathcal{D}_{\text{ING}}$  ( $\mathcal{D}_{\text{ING}} < 0$ ).

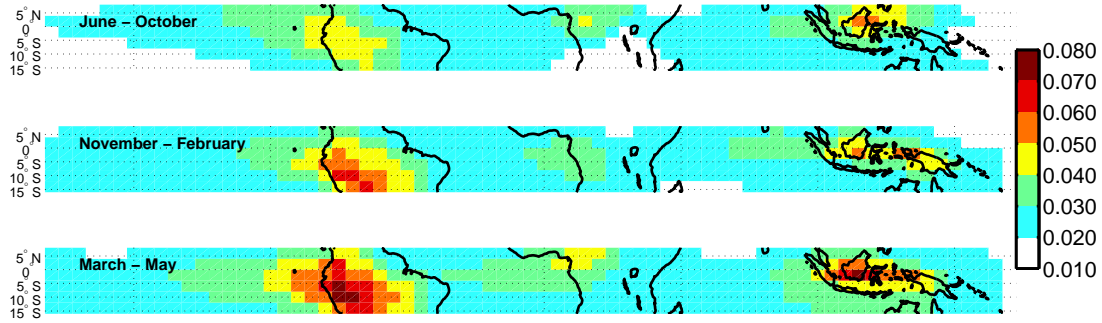


Figure 5.4: The representation of isoprene nitrate chemistry directly impacts simulated tropical ozone, as illustrated by the normalized standard deviation in simulated total column ozone for different choices of nitrate yield ( $Y$ ),  $\text{NO}_x$  recycling ( $\alpha$ ) and ING deposition (see Section 5.2.2.1). The choice of the representation of isoprene nitrate chemistry is most important outside of the biomass burning seasons (large  $\mathcal{D}_{\text{ING}}/\mathcal{L}_{\text{NO}_x}$ ) and affects large regions of the tropics. Conversely, changes in the representation of isoprene nitrate chemistry causes little change in regions affected by biomass burning.

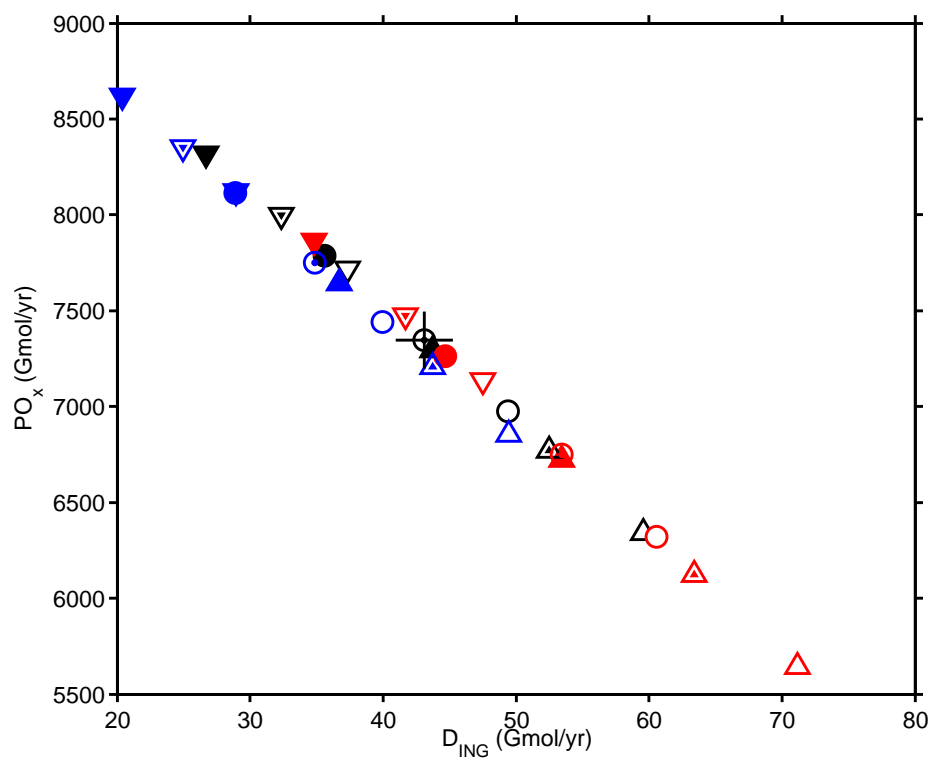


Figure 5.5: The correlation between  $\mathcal{P}_{\text{ING}}$  and  $\mathcal{P}_{\text{O}_x}$  on the regional scale (South America) across a large range of representations of ING chemistry suggests that the influence of ING chemistry on  $\mathcal{P}_{\text{O}_x}$  is primarily controlled by its net impact on  $\text{NO}_x$ . Upward-pointing triangles/Circles/downward-pointing triangles refer to  $Y = 5\%/10\%/15\%$ ; red/black/blue colors refer to fast/medium/slow ING deposition; empty/half filled/filled refer to  $\alpha = 0/50/100\%$ . The reference simulation is indicated by a vertical cross.

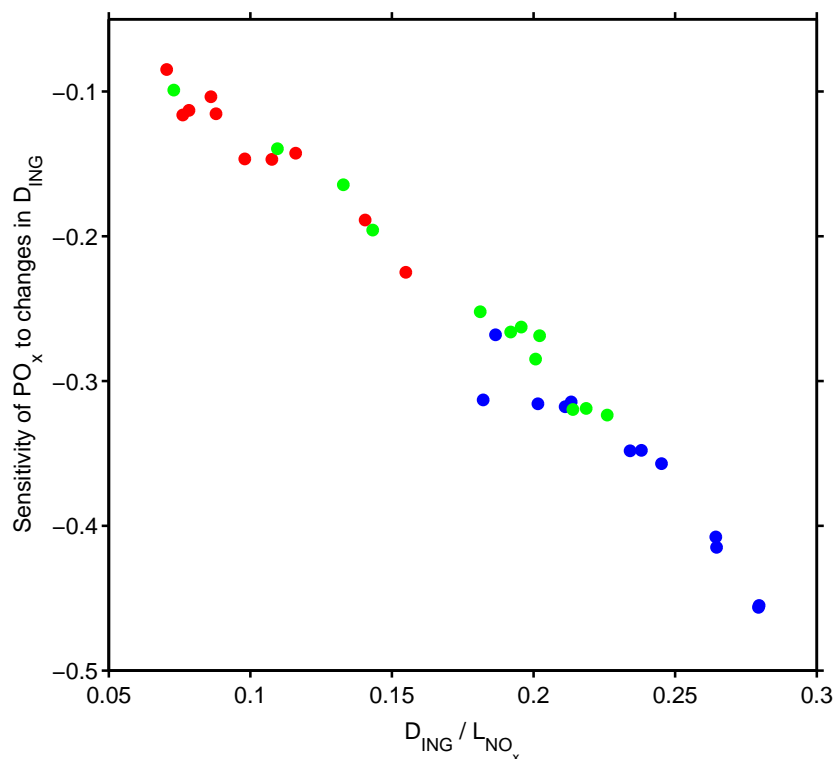


Figure 5.6: The sensitivity of  $\mathcal{P}_{\text{O}_x}$  to the representation of isoprene nitrate chemistry, inferred from the slope of  $\Delta \mathcal{P}_{\text{O}_x} / \Delta D_{\text{ING}}$  in Fig. D.6, is well explained by the fraction of  $\text{NO}_x$  removed through ING chemistry ( $D_{\text{ING}} / L_{\text{NO}_x}$ ). Red: Africa, blue: South America, green: South East Asia

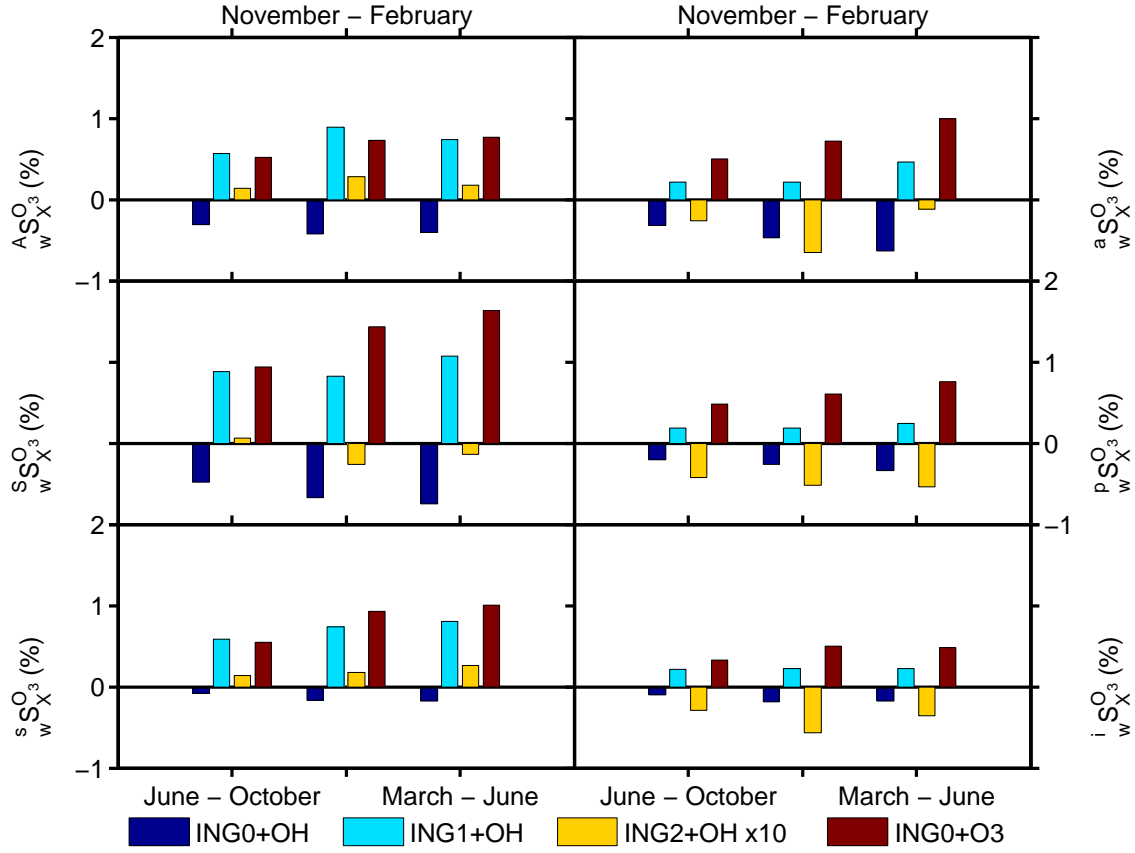


Figure 5.7: The sensitivity of tropospheric ozone to changes in key reactions controlling the fate of  $ING_0$ ,  $ING_1$  and  $ING_2$  exhibits strong seasonal and regional differences. Faster oxidation of  $ING_0$  and  $ING_1$  are associated with higher ozone in particular over continental regions where  $NO_x$  is limited (e.g., South America from March to June). A faster oxidation of  $ING_2$  has an opposite effect over continents ( $\mathcal{S}_{OH+ING_2}^{O_3} > 0$ ) and over oceanic basins ( $\mathcal{S}_{OH+ING_2}^{O_3} < 0$ ).

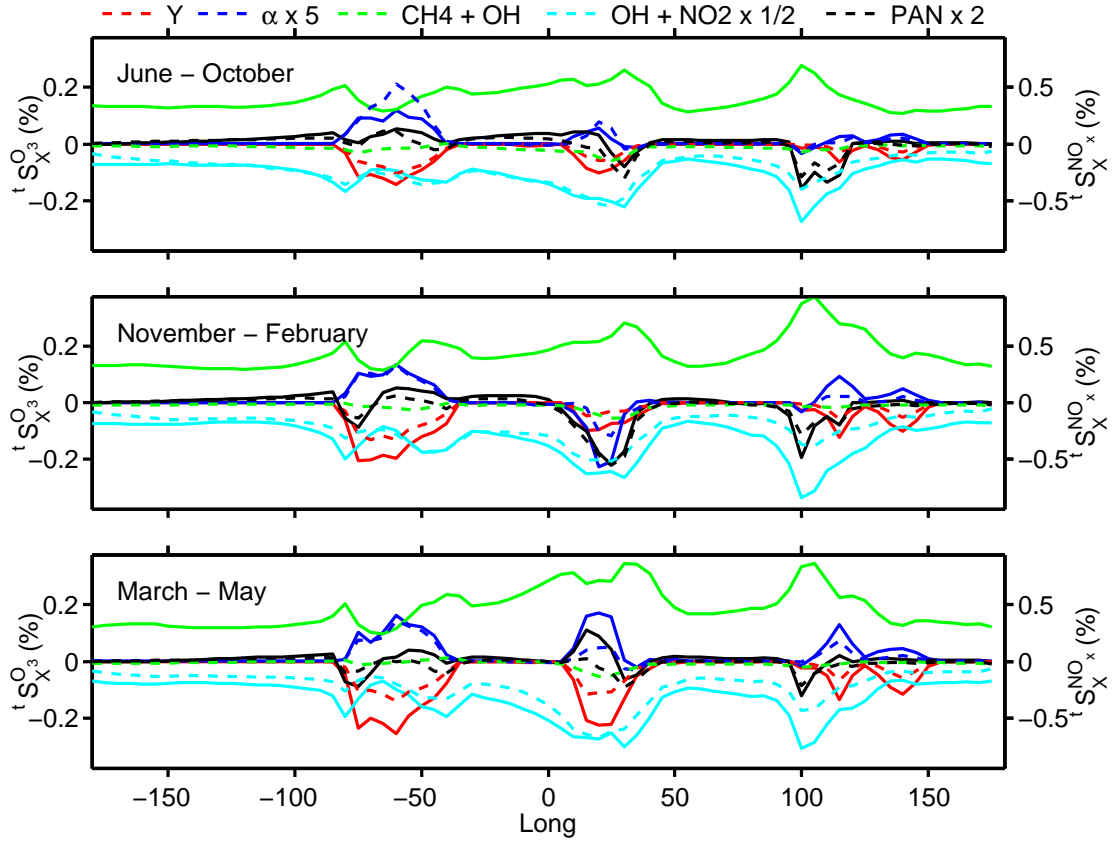


Figure 5.8: Adjoint sensitivity of tropical ozone (solid lines) and NO<sub>x</sub> (dashed lines) to changes in the isoprene nitrate yield (red), the isoprene nitrate recycling (blue,  $\times 5$ ), the loss rate of methane (green, CH<sub>4</sub> + OH), the rate of OH + NO<sub>2</sub> (cyan,  $\times 0.5$ ) and the decomposition of PAN (black,  $\times 2$ ). Adjoint sensitivities are summed over the entire troposphere from  $-15^\circ\text{N}$  to  $7^\circ\text{N}$ .

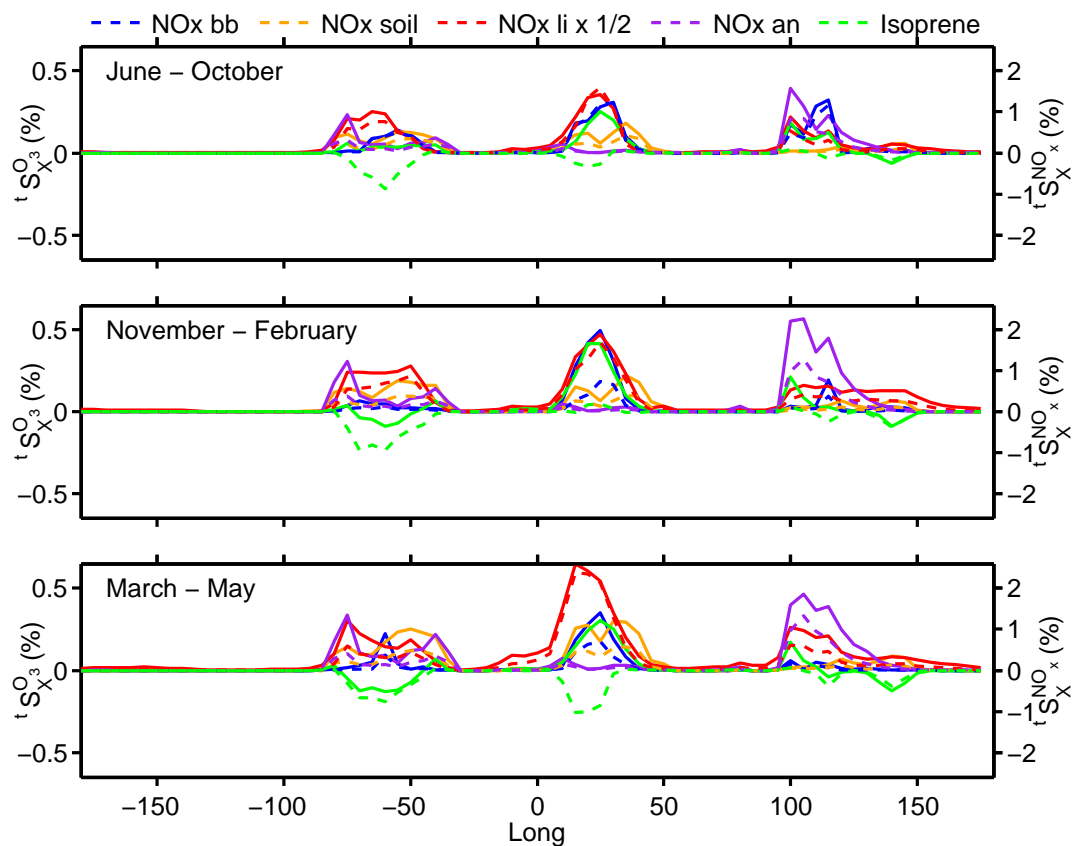


Figure 5.9: Adjoint sensitivity of tropical ozone (solid lines) and  $NO_x$  (dash lines) to changes in the emissions of isoprene (green), lightning  $NO_x$  (red,  $\times 0.5$ ), biomass burning  $NO_x$  (blue), soil  $NO_x$  (orange) and anthropogenic  $NO_x$  (violet). Adjoint sensitivities are summed over the entire troposphere from  $-15^\circ N$  to  $7^\circ N$ .

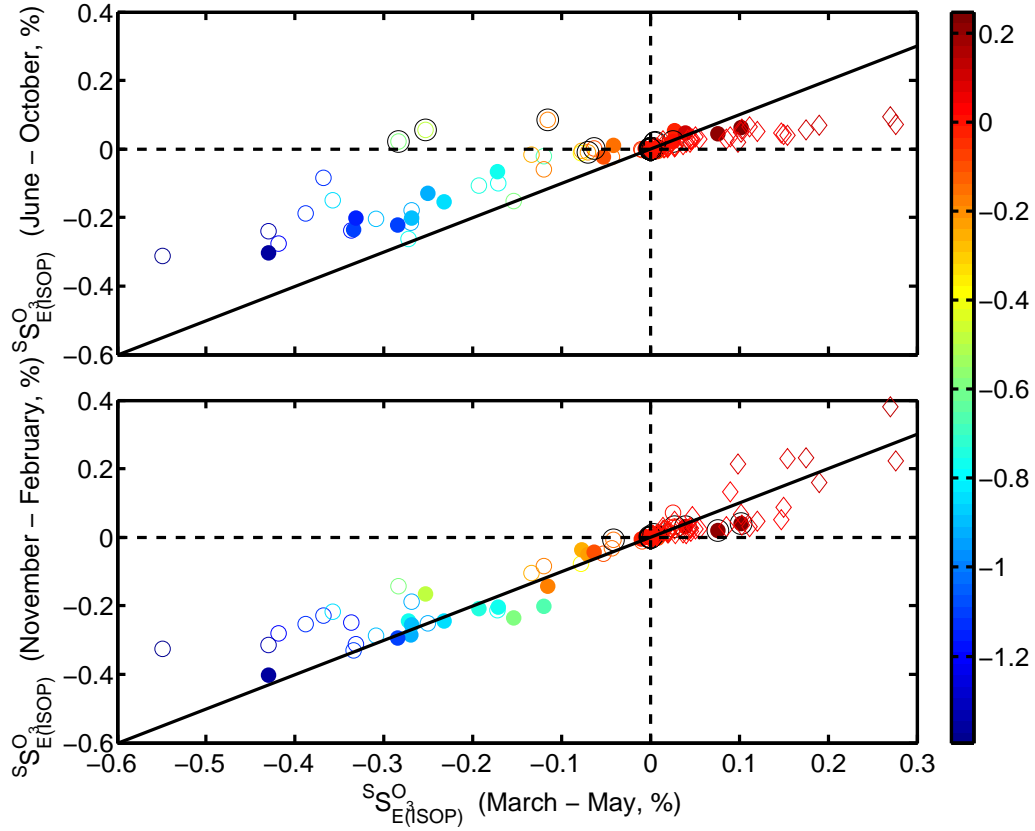


Figure 5.10: Adjoint sensitivity of mean tropospheric ozone over South America to isoprene emissions. Symbols denote the isoprene emission region (circle: South America, diamond: Africa, square: Southeast Asia). The symbols are color coded by the sensitivity of  $NO_x$  over South America to isoprene emissions ( $S_{E(ISO)}^{NO_x}$ ) in the March–May period (low biomass burning). Open (filled) symbols denote an absolute increase (decrease) in  $S_{E(ISO)}^{NO_x}$ . Black circled symbols denote locations where  $S_{E(ISO)}^{NO_x}$  changed signs between two time periods.



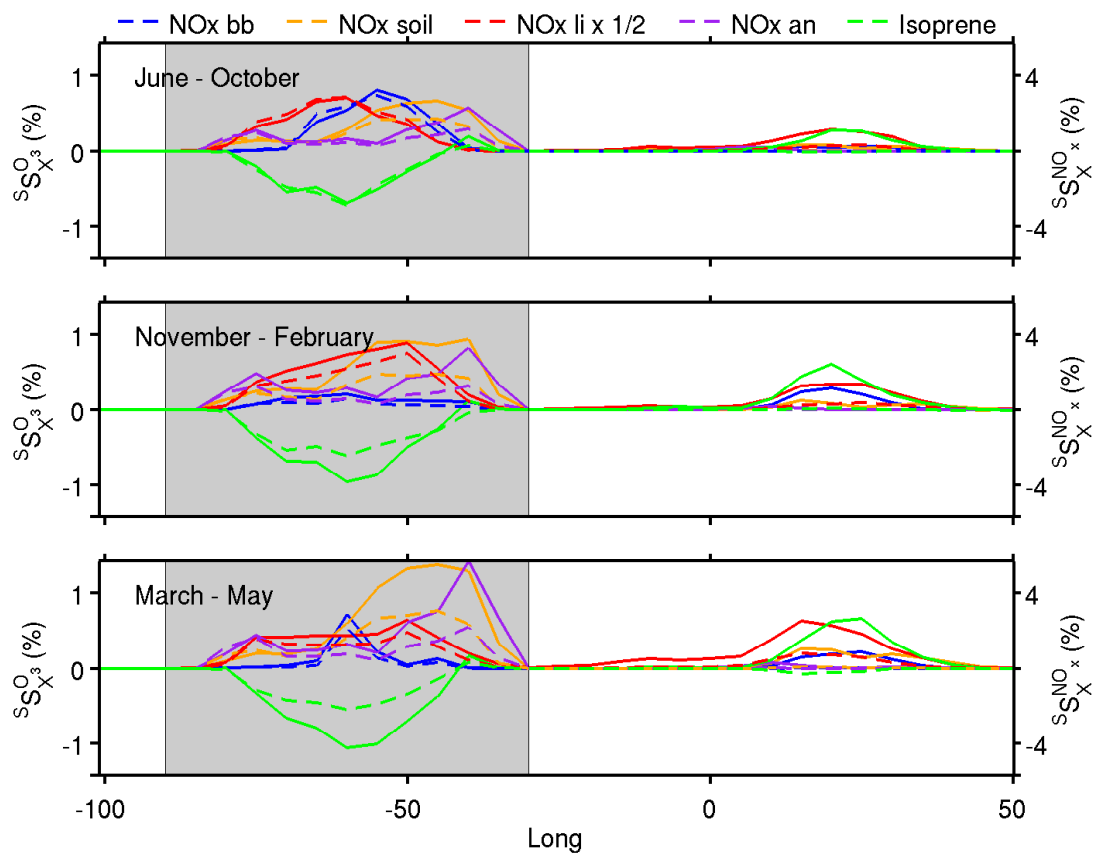


Figure 5.11: Adjoint sensitivity of tropospheric ozone (solid lines) and  $\text{NO}_x$  (dashed lines) over South America (shaded region) to changes in the emissions of isoprene (green), lightning  $\text{NO}_x$  (red,  $\times 0.5$ ), biomass burning  $\text{NO}_x$  (blue), soil  $\text{NO}_x$  (orange) and anthropogenic  $\text{NO}_x$  (violet). Adjoint sensitivities are summed over the entire troposphere from  $-15^\circ\text{N}$  to  $7^\circ\text{N}$ .

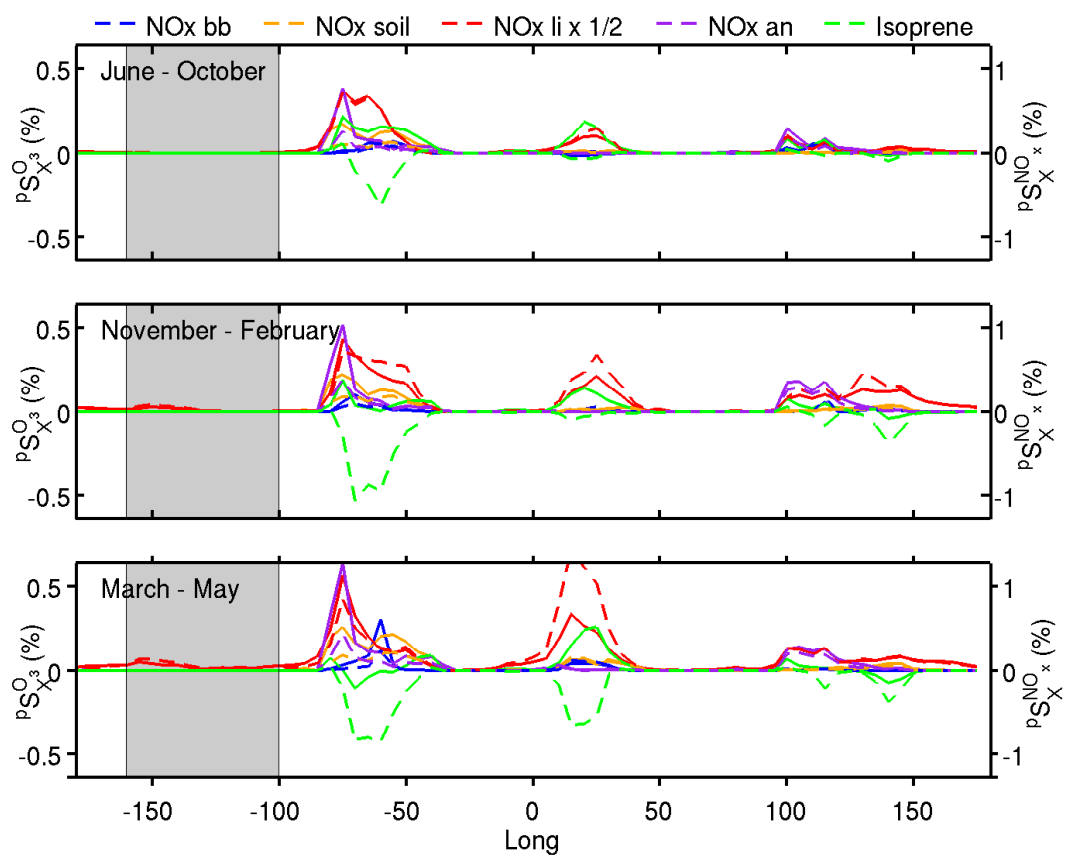


Figure 5.12: Adjoint sensitivity of tropospheric ozone (solid line) and NO<sub>x</sub> (dashed line) over the Pacific (shaded region) to changes in the emissions of isoprene (green), lightning NO<sub>x</sub> (red,  $\times 0.5$ ), biomass burning NO<sub>x</sub> (blue), soil NO<sub>x</sub> (orange) and anthropogenic NO<sub>x</sub> (violet). Adjoint sensitivities are summed over the entire troposphere from  $-15^\circ\text{N}$  to  $7^\circ\text{N}$ .

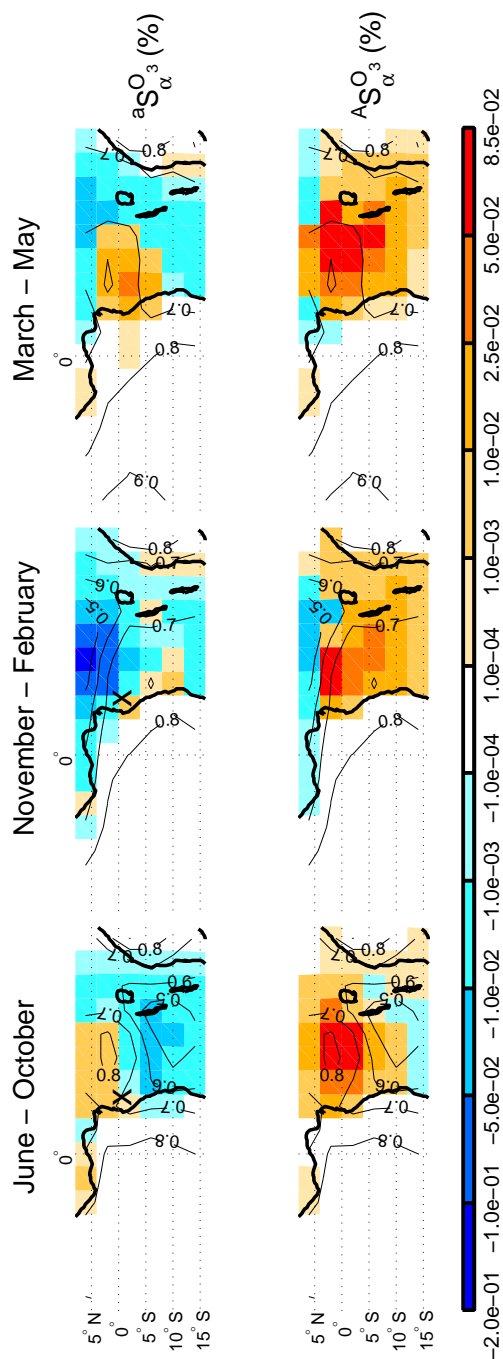


Figure 5.13: Seasonal variations in the adjoint sensitivity of Atlantic (top row) and African (bottom row) ozone to  $\text{ING}_0 \text{NO}_x$  recycling ( $\alpha$ ) summed from the surface to 500 mbar. Contours indicate the mean ratio between the loss of isoprene peroxy radicals through reaction with  $\text{HO}_2$  and the loss of isoprene peroxy radicals through reaction with  $\text{HO}_2$  and  $\text{NO}$ .

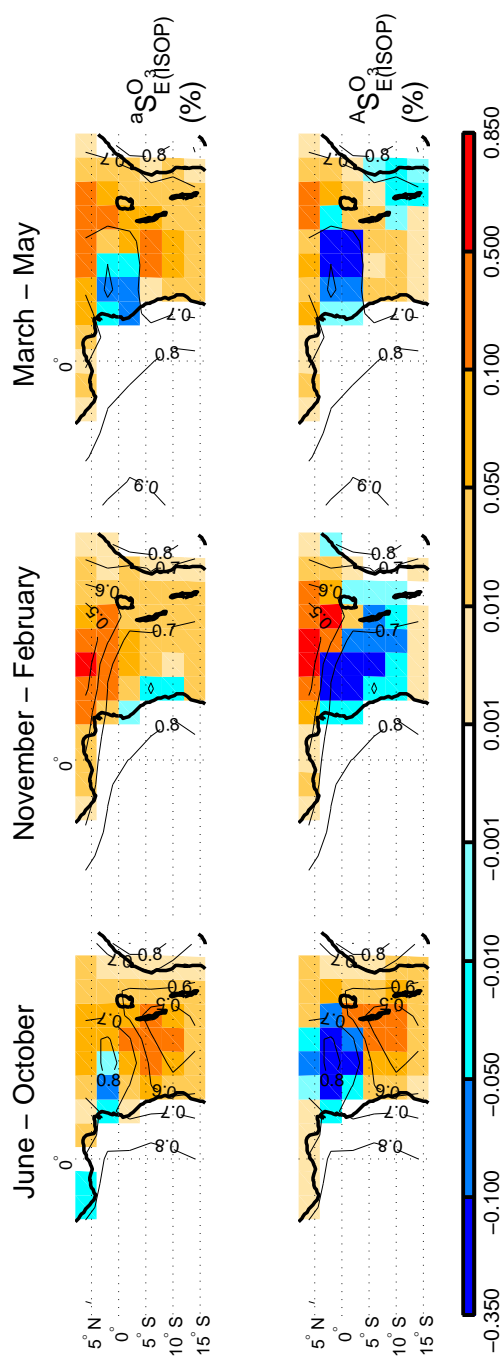


Figure 5.14: Seasonal variations in the adjoint sensitivity of Atlantic (top row) and African (bottom row) ozone to isoprene emissions. Contours indicate the mean ratio between the loss of isoprene peroxy radicals through reaction with  $\text{HO}_2$  and the loss of isoprene peroxy radicals through reactions with  $\text{HO}_2$  and  $\text{NO}$ .

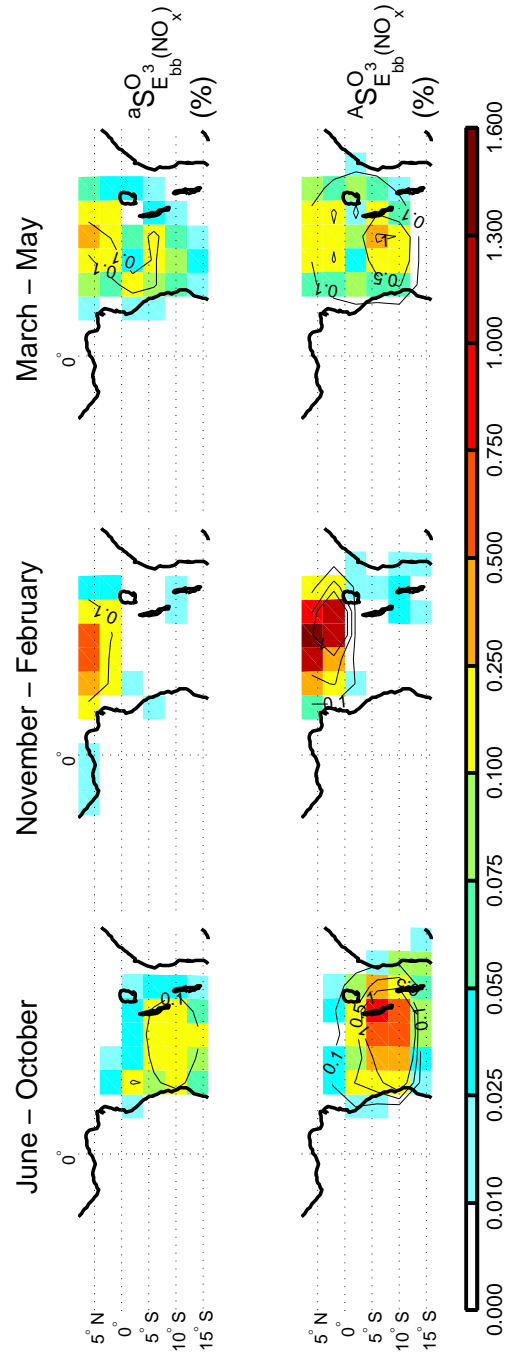


Figure 5.15: Seasonal variations in the adjoint sensitivity of Atlantic (top row) and African (bottom row) ozone to biomass burning  $\text{NO}_x$  emissions. Contours indicate the associated adjoint sensitivity of  $\text{NO}_x$  (i.e.,  $^a \mathcal{S}_{E_{bb}(\text{NO}_x)}^{\text{NO}_x}$  for the top row and  $^a \mathcal{S}_{E_{bb}(\text{NO}_x)}^{\text{NO}_x}$  for the bottom row).

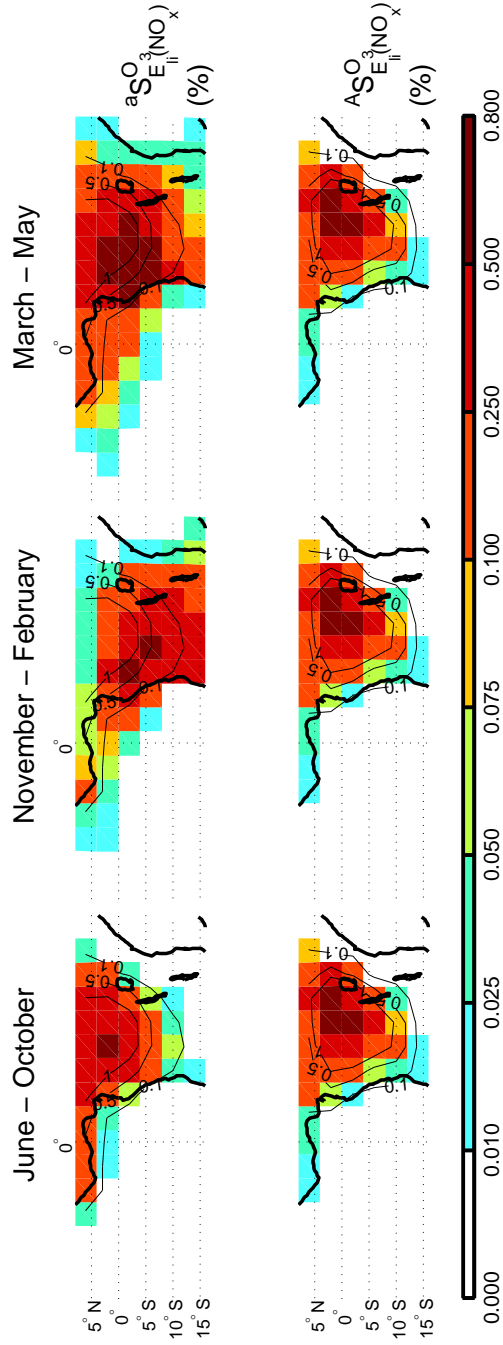


Figure 5.16: Seasonal variations of the adjoint sensitivity of Atlantic (top row) and African (bottom row) ozone to lightning  $\text{NO}_x$  emissions. Contours indicate the associated adjoint sensitivity of  $\text{NO}_x$  over the Atlantic (A, B, C) and Africa (D, E, F) (i.e.,  $^a \mathcal{S}_{E_{\text{li}}}^{\text{NO}_x}$  for the top row and  $^A \mathcal{S}_{E_{\text{li}}}^{\text{NO}_x}$  for the bottom row).

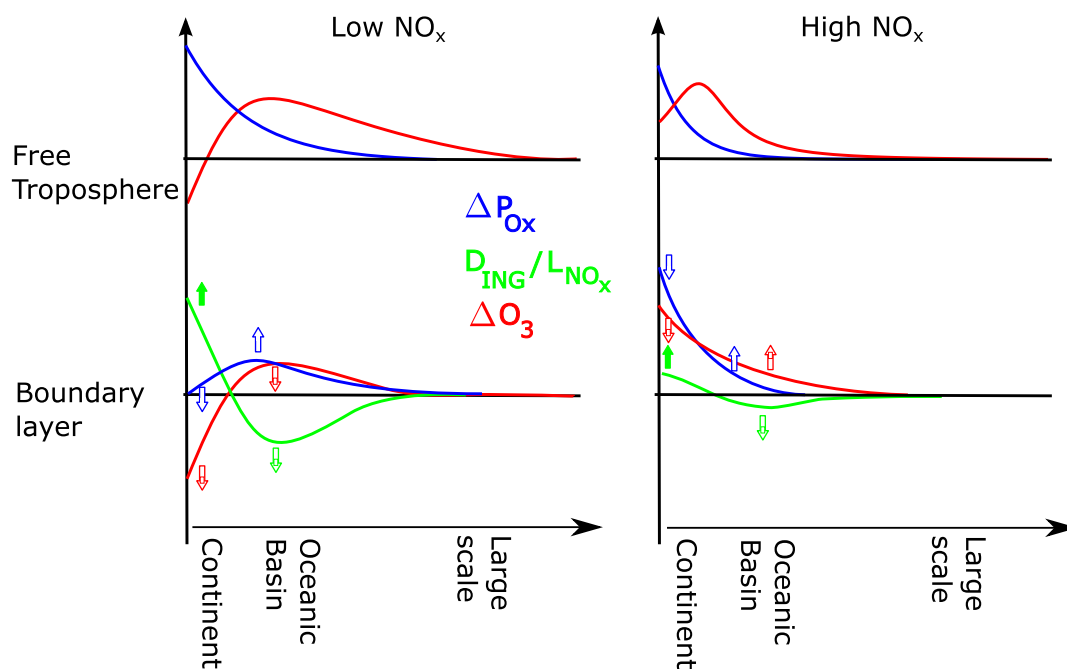


Figure 5.17: Schematic representation of the spatial modulation of the  $O_x$  budget by the isoprene photochemical cascade. The impact of isoprene photooxidation on ozone depends on its impact on  $NO_x$  near isoprene emissions ( $\mathcal{P}_{ING}/\mathcal{L}_{NO_x}$ , continent). In particular,  $\mathcal{P}_{ING}/\mathcal{L}_{NO_x}$  influences the amount of BVOCs injected in the free troposphere and therefore the large-scale impact of the isoprene photochemical cascade. Under high  $NO_x$ , an increase in the continental  $\mathcal{P}_{ING}/\mathcal{L}_{NO_x}$  (green filled arrow) results in an increase of ozone downwind of continents ( $\Delta O_3 > 0$ ) because of increased transport of nitrogen reservoirs. Conversely, under low  $NO_x$ , a similar increase results in a decrease of ozone downwind of continents because of diminished export from the continents.

Table 5.1: Isoprene nitrate photochemical mechanism

ISOP + OH	→	ISOPO <sub>2</sub>	$2.7 \times 10^{-11} \times \exp(390/T)$
ISOPO <sub>2</sub>	→	HO <sub>2</sub>	$1.99 \times 10^8 \times \exp(-7510/T)$
ISOPO <sub>2</sub> + NO	→	NO <sub>2</sub> + HO <sub>2</sub> + 0.378IALD + +0.378MVK + 0.244MACR + 0.622CH <sub>2</sub> O	$(1-Y) \times k_{\text{NO}}^b$
ISOPO <sub>2</sub> + NO	→	ING <sub>0</sub>	$Y \times k_{\text{NO}}^b$
ING <sub>0</sub> + OH	→	ING <sub>0</sub> O <sub>2</sub>	$1.28 \times 10^{-11} \times \exp(380/T)$
ING <sub>0</sub> O <sub>2</sub> + NO	→	2NO <sub>2</sub> + HO <sub>2</sub> + OVOC	$\alpha \times 2.7 \times 10^{-12} \times \exp(350/T)$
ING <sub>0</sub> O <sub>2</sub> + NO	→	0.5ING <sub>1</sub> + 0.5ING <sub>2</sub> + HO <sub>2</sub> + NO <sub>2</sub>	$(1-\alpha) \times 2.7 \times 10^{-12} \times \exp(350/T)$
ING <sub>0</sub> O <sub>2</sub> + HO <sub>2</sub>	→	NO <sub>2</sub> + HO <sub>2</sub> + OVOC	$k_{\text{HO}_2}^a$
ING <sub>0</sub> + O <sub>3</sub>	→	0.5ING <sub>1</sub> + 0.5ING <sub>2</sub> + HO <sub>2</sub>	$\alpha \times 1.09 \times 10^{-13} \times \exp(-2100/T)$
ISOP + NO <sub>3</sub>	→	INO <sub>2</sub>	$(1-\alpha) \times 1.09 \times 10^{-13} \times \exp(-2100/T)$
MVK + OH	→	MVKO <sub>2</sub>	$3.15 \times 10^{-12} \times \exp(-450/T)$
MVKO <sub>2</sub> + NO	→	NO <sub>2</sub> + 0.28HO <sub>2</sub> + OVOC	$2.6 \times 10^{-12} \times \exp(610/T)$
MVKO <sub>2</sub> + NO	→	ING <sub>1</sub>	$k_{\text{NO}}^b$
MACR + OH	→	MRO <sub>2</sub> + MAO <sub>3</sub>	$k_{\text{NO}}^b$
MRO <sub>2</sub> + NO	→	NO <sub>2</sub> + HO	$k_{\text{NO}}^b$
MRO <sub>2</sub> + NO	→	ING <sub>1</sub>	$k_{\text{NO}}^b$
INO <sub>2</sub> + NO	→	1-15NO <sub>2</sub> + 0-8HO <sub>2</sub> + 0-85ING <sub>0</sub> + 0-1MACR	$k_{\text{NO}}^b$
	→	0-15CH <sub>2</sub> O + 0-05MVK	
INO <sub>2</sub> + HO <sub>2</sub>	→	INPN	$k_{\text{HO}_2}^a$
INPN + OH	→	0-3INO <sub>2</sub> + 0-7HO <sub>2</sub> + 0-7ING <sub>0</sub>	$3.8 \times 10^{-12} \times \exp(200/T)$
IALD + OH	→	0-430IAO <sub>2</sub> + 0-570IAO <sub>3</sub>	$3.7 \times 10^{-11}$
IAO <sub>2</sub> + NO	→	OVOC + 0.920HO <sub>2</sub> + 0.920NO <sub>2</sub> + 0.080ING <sub>1</sub>	$k_{\text{NO}}^b$
INPN + OH	→	ING <sub>1</sub> + OH	$5 \times 10^{-11}$
ING <sub>1</sub> + OH	→	NO <sub>2</sub> + HO <sub>2</sub> + OVOC	$8 \times 10^{-12}$
ING <sub>2</sub> + OH	→	HO <sub>2</sub> + NO <sub>2</sub> + OVOC	$4 \times 10^{-13}$
ING <sub>2</sub>	→	NO <sub>2</sub> + PA + HO <sub>2</sub>	$J_{\text{ING}_2}$
IAO <sub>2</sub>	→	CO + MEK + OH	$k_{\text{H}}^c$
IAO <sub>3</sub>	→	PACLD + HO <sub>2</sub>	$k_{\text{H}}^c$
MRO <sub>2</sub>	→	CO + HAC + OH	$k_{\text{H}}^c$
ISOPO <sub>2</sub> + HO <sub>2</sub>	→	ISOPOOH	$k_{\text{HO}_2}^a$
ISOPOOH + OH	→	IEPOX + OH	$1.9 \times 10^{11} \times \exp(390/T)$
ISOPOOH + OH	→	0.38TRIO <sub>2</sub> + 0.613OH + 0.613IALD	$4.75 \times 10^{-12} \times \exp(200/T)$
PACLD	→		

(a)  $k_{\text{HO}_2} = 2.91 \times 10^{-13} \exp(1300/T) (1 - \exp(-0.245n))$  (Saunders et al., 2003)(b)  $k_{\text{NO}} = 2.7 \times 10^{-12} \times \exp(350/T)$ (c)  $k_{\text{H}}^c = 8.81 \times 10^9 \exp(-7510/T)$  (Crounse et al., in preparation)(d)  $J_{\text{ING}_2}$  estimated using average of cross sections from Roberts and Fajer (1989); quantum yield estimated by Jenkin et al. (1997)



## Chapter 6

# Conclusion and future work

It is somewhat disconcerting that the photochemistry of a molecule as simple as isoprene remains so uncertain, despite the many laboratory, field and theoretical studies aimed at unraveling its fate. This thesis demonstrates that CIMS, thanks to its sensitivity to many functional groups (e.g., epoxides, hydroxyhydroperoxides, hydroxyketone and aldehyde, organic and inorganic acids), can provide new insights into the isoprene photochemical cascade.

It is essential that the mechanisms derived from these chamber studies are validated against environmental data, as it remains very challenging to reproduce atmospheric conditions in the laboratory. This requires translating the observations collected in the laboratory into mechanisms that are simple enough to be included in chemical transport models. This often requires the simplification of complex photochemical steps and hypothesis regarding the nature and fate of many later-generation products. Propanone nitrate and isoprene epoxides, two products of isoprene photooxidation identified in Chapters 2 and 3, were measured during the BEARPEX campaign, which supports the relevance of some of the findings presented here to the atmosphere. I have also shown in Chapter 5 that the changes induced by different representations of the isoprene photochemical cascade can propagate to much larger scales through coupling between atmospheric chemistry and dynamics.

Because of its large emissions, isoprene is generally the only terpinoid whose photochemistry is represented in some detail in the chemical mechanisms included in global models. In the future, the isoprene photochemical cascade may be used to probe biosphere-atmosphere interactions mediated by the oxidation of biogenics and to assess how these interactions may be perturbed by human activities (Andreae, 2001). Assessing the importance of these interactions is especially important in biogenics-rich tropical regions that are currently experiencing very rapid economic development. Research may focus on:

**ozone:** At the local scale, ozone is an important pollutant and phytotoxin. Chemical transport models need to be coupled with ecosystem models to predict the consequences of human activities on ecosystem health and food security. The direct and indirect (methane oxidation, CO<sub>2</sub> uptake) effects of an increase in tropical ozone on Earth's radiative balance also need to be assessed.

**nitrogen:** A significant fraction of tropical NO<sub>x</sub> emissions interacts with isoprene photochemical products. In particular, the formation of organic nitrates and peroxyacetylnitrate modulates the transport of nitrogen, an essential nutrient, within and across biomes. It is important to constrain the spatial patterns of nitrogen depositions in the tropics as its increase may disturb fragile ecosystems and increase emissions of N<sub>2</sub>O, a potent greenhouse gas.

**aerosol:** The mechanisms underlying the formation of SOA under conditions representative of the tropical atmosphere remain elusive. The role of isoprene-derived epoxides (IEPOX) as precursors of secondary organic aerosol precursor is an important step to better understand the formation of aerosol under pristine condition and its sensitivity to anthropogenic emissions (in particular SO<sub>2</sub> emissions (Froyd et al., 2010; Surratt et al., 2010)). Much remains to be done to understand the role of SOA, in particular with respect to cloud formations that are essential for the maintenance of tropical ecosystems.

## Appendix A

# Isoprene photooxidation: new insights into the production of acids and organic nitrates

### A.1 Photooxidation mechanism

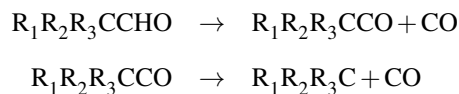
#### A.1.1 VOC chemistry

Except as noted below, we use the known rate coefficients of bimolecular and termolecular reactions as tabulated in IUPAC (Atkinson et al., 2006) and JPL (Sander, 2006) reports.

##### A.1.1.1 OH

Reactions of OH with VOC are limited to its addition on a double bond and the abstraction of the aldehydic hydrogen and the hydrogen in  $\alpha$  to an alcohol, i.e., the abstraction of hydrogens from alcohols is neglected. For the addition of OH onto double bonds, in the absence of data or previous information enabling differentiation between the two carbons, we assume that the reaction occurs only on the most favorable location based on steric considerations. A structure-activity relationship (SAR) method is used to determine unknown reaction rate coefficients (Kwok and Atkinson, 1995).

Following the studies of Orlando and Tyndall (2001) and Méreau et al. (2001), acylradicals are assumed to decompose promptly when the alkyl group features a carbonyl or an alcohol (with R secondary or tertiary) in  $\beta$  to the carbonyl:



We also assume that acylradicals featuring a nitrooxy group in  $\beta$  to the carbonyl undergo unimolecular decomposition. In all other cases, the acyl radical is assumed to add O<sub>2</sub> to yield the associated peroxy radical.

In case of resonance, the branching between the addition of O<sub>2</sub> on the carbon in  $\alpha$  of alcohol (denoted ① in Fig. 2.1) or in  $\gamma$  (②) is unknown. Addition on ① features a more stable double bond as well as a kinetically favored radical. In the mechanism, we set the branching ①:② to 65%:35%. Furthermore we note that HOPL does not exhibit any early source, suggesting that the yield of HMPL is negligible. Indeed, its formation appears unfavorable on both a thermodynamic (the double bond is less substituted) and a kinetic (formation of a secondary radical) basis. Thus, the branching ratio is set to  $Y_a^{E(1,4)} = 95\%$  and  $Y_b^{E(1,4)} = 5\%$ .

### A.1.1.2 Ozone

Ozone reacts with alkenes via the formation of a molozonide, quickly followed by its decomposition into a carbonyl and a Criegee intermediate. Assuming a generic rate constant for the reaction of alkenes with ozone,  $10^{-17} \text{ cm}^3 \text{ molec}^{-1} \text{ s}^{-1}$ , the reaction of an alkene with ozone is included if  $\tau_{OH} > \frac{\tau_{O_3}}{10}$ , where  $\tau_{OH}$  and  $\tau_{O_3}$  are the lifetimes of the alkenes with respect to OH and ozone, respectively.

Ozone reactions are included for isoprene, MACR and MVK, following IUPAC recommendations.

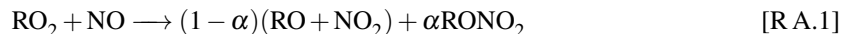
### A.1.1.3 NO<sub>3</sub>

Reactions of NO<sub>3</sub> with alkenes and aldehydes have been neglected, since  $\frac{k_{\{\text{alkenes/aldehydes}\}}^{\text{NO}_3}}{k_{\{\text{alkenes/aldehydes}\}}^{\text{HO}}} \frac{[\text{NO}_3]}{[\text{HO}]} \ll 1$  throughout the experiment.

## A.1.2 Peroxyradical chemistry

### A.1.2.1 NO

NO reacts with peroxy radicals with a rate coefficient of  $2.43 \times 10^{-12} \exp(360/T) \text{ cm}^3 \text{ molec}^{-1} \text{ s}^{-1}$  (Atkinson et al., 2006) through



The reaction rate coefficient of acyl peroxy radical with NO is set to  $6.7 \times 10^{-12} \exp(340/T) \text{ cm}^3 \text{ molec}^{-1} \text{ s}^{-1}$  based on  $\text{CH}_3\text{CH}_2\text{C}(\text{O})\text{OO}\cdot$ .

Carter's parameterization is used to compute the alkyl nitrate yield (Carter and Atkinson, 1989; Arey et al., 2001):

$$\frac{\alpha}{1 - \alpha} = \frac{Y_0^{298} [M] (T/298)^{-m_0}}{1 + \Theta} F^z \times m \quad (\text{A.1})$$

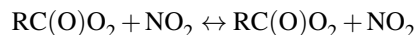
with  $z = (1 + [\log(\frac{Y_0^{298} [M] (T/298)^{-m_0}}{Y_\infty^{298} [M] (T/298)^{-m_\infty}})]^2)^{-1}$ ,  $F = 0.41$ ,  $m_0 = 0$ ,  $m_\infty = 8.0$ ,  $\beta = 1$ ,  $\Theta = \frac{Y_0^{298} [M] (T/298)^{-m_0}}{Y_\infty^{298} (T/298)^{-m_\infty}}$ ,  $\gamma = 2 \times 10^{-22} \text{ cm}^3 \text{ molecule}^{-1}$ ,  $Y_\infty^{298} = 0.43$ ,  $Y_0^{298} = \gamma e^{\beta n}$ , where  $n$  is the number of carbons in the molecule. The parameter  $m$  is set to 0.4, 1.0 and 0.3 for primary, secondary and tertiary nitrates, respectively (Arey et al., 2001).

For  $\beta$ -hydroxy peroxy radicals,  $\alpha$  is divided by two to account for the effect of the hydroxy group as highlighted by O'Brien et al. (1998).

For acylnitrates, the yield is set to the alkyl tertiary nitrate yield, providing it does not exceed 4%.

### A.1.2.2 NO<sub>2</sub>

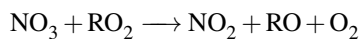
NO<sub>2</sub> reacts with peroxy acyl radicals to yield peroxyacylnitrate-like compounds, which decompose thermally or photolytically:



The rates of formation and decomposition of methyl peroxyacylnitrates (MPAN) are used for all PAN-like compounds except PAN itself. Most PAN-like compounds except PAN itself have other reactive groups (aldehyde, primary or a secondary alcohol, double bond) causing their major sink to be reaction with OH.

### A.1.2.3 NO<sub>3</sub>

NO<sub>3</sub> reacts with peroxy radicals through



The rate coefficient is set to  $2.3 \times 10^{-12} \text{ cm}^3 \text{ molec}^{-1} \text{ s}^{-1}$  independent of both the temperature and the peroxyradical.

#### A.1.2.4 HO<sub>2</sub> and peroxy radicals

HO<sub>2</sub> reacts with peroxy radicals through four different channels:



Reaction [R A.5] has only been observed for compounds such as RCH<sub>2</sub>OCH<sub>2</sub>OO and is not considered in this study. Acyl peroxides are assumed to react through Reactions [R A.2], [R A.3] and [R A.4] with a branching ratio 0.4:0.2:0.4 (Hasson et al., 2004; Jenkin et al., 2007). Acetonylperoxy radicals have also been shown to react through channels [R A.2] and [R A.4] with a branching ratio 1:2 (Hasson et al., 2004). The other alkylperoxy are assumed to react through Reaction [R A.2] only.

The reaction rate coefficient for the reaction of alkylperoxy with HO<sub>2</sub> is set to  $2.91 \times 10^{-13} \exp(1300/T) \times (1 - \exp(-0.245n_c)) \text{ cm}^3 \text{ molec}^{-1} \text{ s}^{-1}$ , where  $n_c$  is the number of carbon atoms (Saunders et al., 2003). For the acyl peroxy radicals, the reaction rate coefficient is set to  $5.2 \times 10^{-13} \exp(983/T) \text{ cm}^3 \text{ molec}^{-1} \text{ s}^{-1}$ , based on the reaction of the methylacylperoxy radical.

RO<sub>2</sub> + RO<sub>2</sub> reactions are neglected in this study. In the early stages of isoprene photooxidation the chemistry of peroxyradicals is entirely dominated by NO. At the end of the experiment, peroxy radical chemistry is dominated by HO<sub>2</sub>, which concentration is high enough so that RO<sub>2</sub> + RO<sub>2</sub> reactions can be safely neglected.

### A.1.3 Photolysis

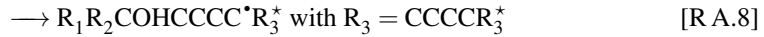
The photolysis rate of a compound i is computed via:

$$J_i = \int_{\lambda_1}^{\lambda_2} \mathcal{J}^e(\lambda) \sigma_i(\lambda) \phi_i(\lambda) d\lambda \quad (\text{A.2})$$

The effective light flux  $\mathcal{J}^e$  is computed using an experimental determination of  $J_{\text{HONO}}$  and a spectrum of the lamp output made every nanometer (LI-COR LI1800  $\lambda_1 = 300$  nm,  $\lambda_2 = 600$  nm).  $\sigma_{\text{HONO}}$  is scaled using the oscillator strength recently reported by Wall et al. (2006). This gives  $J_{\text{HOOH}} = 3.1 \times 10^{-6} \text{ s}^{-1}$ .

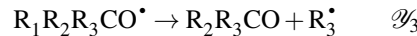
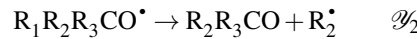
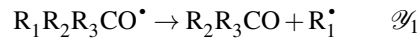
The photolysis of compounds with unknown absorption cross sections is estimated from the known photolysis rate constants of similar compounds. The photolysis of organic nitrates is assumed to yield only  $\text{RO} + \text{NO}_2$ . For primary organic nitrate, the photolysis rate is taken from  $1 - \text{C}_4\text{H}_9\text{ONO}_2$ , for secondary organic nitrates from  $2 - \text{C}_4\text{H}_9\text{ONO}_2$  and for tertiary nitrates from tertbutylnitrate (Roberts et al., 1997; Atkinson et al., 2006).

#### A.1.4 Fate of the alkoxy radicals



Since the isomerization reaction [R A.8] requires at least four carbons (Atkinson, 1997a), it occurs only in the first stages of isoprene photooxidation, when major products retain five carbons. In the case of isoprene, isomerization [R A.8] is faster than decomposition [R A.6] and reaction with  $\text{O}_2$  [R A.7]. Alkoxy radicals that cannot undergo [R A.8] are assumed to decompose through [R A.6], i.e., [R A.7] is generally neglected except for a few cases detailed in the discussion section.

Generally the decomposition of an alkoxy radical can occur through different channels, whose branching ratios ( $Y_i$ ) are estimated using their respective activation energies,  $E_{bi}$ .



with

$$\forall i \in (1, 2, 3) \quad \mathcal{Y}_i = \exp\left(\frac{E_{b1} + E_{b2} + E_{b3} - E_{bi}}{RT}\right) \quad (\text{A.3})$$

$E_b$  is calculated using the generalized structure-activity relationship developed by Peeters et al. (2004).

### A.1.5 Skill of the model

The evolution of the modelled chemical system can be examined through its instantaneous speciation (Fig. A.1). Furthermore, given that the oxidation of CO by OH is negligible in the time scale of experiment, we define the chemical speed of the system,  $\mathcal{V}$ , as  $\frac{d[\text{CO}+\text{CO}_2]}{dt}$  (Fig. A.2). Both proxies indicate that the system undergoes three different regimes:

1.  $0 < t < 150$  min

This regime is characterized by a large supply of NO, as well as very reactive compounds featuring a double bond.  $\mathcal{V}$  reaches a maximum after a few minutes at 0.7 ppv(C)/min. Ozone and PNA are very low in this regime, underlying a chemistry dominated by NO. The organic nitrate concentration reaches its maximum at the end of this regime. The reduction in OH corresponds to an increase of NO<sub>2</sub> leading to the formation of nitric acid.

2.  $150 < t < 550$  min

This regime is characterized by a very stable  $\mathcal{V}$  (0.5 ppbv(C)/min) with a chemistry dominated by aldehydes. OH recycling through HO<sub>2</sub> + NO is less efficient than in the first regime due to the abundance of ozone which favors the formation of PAN. Nevertheless, the reduction in the chemical speed due to the transition from "double bond dominated" to "aldehyde dominated" reduces OH sinks which ultimately leads to a slow increase in OH, leveling off when PNA peaks, i.e., when the NO<sub>x</sub> is titrated.

3.  $550 < t < 1000$  min

After the PNA peak, the chemistry is dominated by HO<sub>2</sub>, as evidenced by the formation of peracetic acid (PAA cluster at  $m/z = 161$ ) and methylhydroperoxide (MHP cluster  $m/z = 133$ ). Low-reactivity compounds such as ketones or long-lived nitrates dominate the chamber composition. Despite the almost constant OH, the chemical speed drops significantly to 0.1ppbv(C)/min.

These three distinct chemical regimes are consistent with the ones derived using the experimental profiles of HONO and PNA, i.e., the mechanism accurately represents the average evolution of the chemical system (Figs. A.1 and A.2).

The skill of the mechanism can be evaluated in greater detail by comparing the times when various species peak, as well as their maxima between mechanism and experiment (Table A.1). The mechanism



Table A.1: Skill of the model.  $\Delta t = t_{\max}^{\text{model}} / t_{\max}^{\text{data}} - 1$  and  $\Delta c = c_{\max}^{\text{model}} / c_{\max}^{\text{data}} - 1$ .

	HACET	GLYC	ISOPN	MVKN + MACRN	HC5
$\Delta t (\%)$	4.8	-1.4	< 1	< 1	< 1
$\Delta c_{\max} (\%)$	3.6	-4.4	2.4	-3.1	38
	ETHN	DHB	DHPN	HONO	PNA
$\Delta t (\%)$	< 1	< 1	2.1	16	-11
$\Delta c_{\max} (\%)$	-11	3.5	22	2.2	-37

generally captures correctly the peak times indicating that the chemical speed is properly modeled in the first and second regime. The error regarding the maximum intensity falls within the uncertainty of this study ( $\pm 20$ –30%). The sensitivity of the CIMS to PNA is probably overevaluated due to ligand exchange with  $\text{H}_2\text{O}_2$ . Satisfactory representation for the background chemistry species is also reached (Figs. A.3 and A.4). In particular, PNA, a very sensitive marker for the ratio of  $\text{NO}_x$  and  $\text{HO}_x$ , is well captured during the first and second regimes.

## A.2 Calibration

### A.2.1 Definitions

We define the normalized signal,  $\widehat{\text{Signal}}(m/z)$  as the absolute number of counts recorded at  $m/z$  divided by the number of counts associated with the reagent anion,  $\text{CF}_3\text{O}^-$ :

$$\widehat{\text{Signal}}(m/z) = \frac{\text{Signal}(m/z)}{\text{Signal}(\text{CF}_3\text{O}^-)} \quad (\text{A.4})$$

For the chamber experimental conditions, the reagent ion was found in several forms:  $\text{CF}_3\text{O}^-$ ,  $\text{CF}_3\text{O}^- \cdot \text{H}_2\text{O}$  and  $\text{CF}_3\text{O}^- \cdot \text{H}_2\text{O}_2$ . Due to the high count rates for the primary isotopes of the reagent ions (sum  $\sim 14$  MHz), the  $^{13}\text{C}$  isotopes were monitored instead:

$$\text{Signal}(\text{CF}_3\text{O}^-) = \sum_{m/z=86,104,120} \text{Signal}(m/z) \quad (\text{A.5})$$

As stated in Section 2.3.3, in order to get the concentration for an analyte, X, detected as a product ion with  $m/z=p$ , we divide the normalized signal for  $m/z$  by the sensitivity ( $c_X$ ) for that analyte under chamber conditions (2.1).

The above method fails when mass analog ions, i.e., different ions with the same mass-to-charge ratio, exist at the  $m/z$  of interest. The mass analog ions correspond to different analytes in the chamber, which have different reaction rate coefficients with the reagent ion. While the CIMS instrument can not separate mass analogs, the explicit model can. To compare the model results with a measured signal composed of mass analogs, we use the following:

$$\left[X_{\text{measured } m/z=a}\right]_{\text{ppbv}} = \frac{\widehat{\text{Signal}(m/z)}}{c_{\text{ref}}} \quad (\text{A.6})$$

$$\left[X_{\text{model } m/z=a}\right]_{\text{ppbv}} = \sum_{i \in \mathcal{A}} [X_i] \frac{c_{X_i}}{c_{\text{ref}}} \quad (\text{A.7})$$

where  $a$  is a  $m/z$  featuring mass analog ions,  $\mathcal{A}$  the subset of compounds yielding product ions with  $m/z=a$  and  $c_{\text{ref}} = 3.85 \times 10^{-4} \text{ pptv}^{-1}$  is taken as an approximate general calibration. Nominally,  $\text{Signal}(\text{CF}_3\text{O}^-) = 120 \text{ kcounts/s}$ , this gives  $c_{\text{ref}} = 46 \text{ counts s}^{-1} \text{ pptv}^{-1}$ , in the CIMS flow tube. Including the dilution factor (13.2), the sensitivity is  $3.5 \text{ counts s}^{-1} \text{ pptv}^{-1}$  in the chamber air.

## A.2.2 Dipoles and polarizabilities computed by quantum mechanics

The dipole moment and polarizability of a molecule depend on its charge distribution. Thus, different conformers of a molecule can have very different dipole moments. The polarizability is essentially determined by the number of electrons and so is not significantly altered by conformers.

We have calculated the dipole moment and polarizability using density functional theory. Many of the molecules of interest have a large number of structural conformers and we have calculated a conformer distribution for all molecules. To generate the initial set of conformers, we have allowed 3-fold rotation about all CC, CO, CN single bonds. This leads to, for example, 34 guess structures in the case of ISOPN Z(1,4). For each guess conformer, geometry optimization is conducted at the B3LYP/6-31G(d) level. The optimized conformers are ranked by energy, and relative population for a temperature of 298 K is determined. We have only calculated the polarizability of the lowest energy structure for each of the molecules as we found this to be relatively insensitive to structure. All calculations were performed with Spartan'06, with the default convergence criteria (Wavefunction Inc., 2006). Test calculations on a few small molecules for which the dipole moment has been measured show that the B3LYP/6-31G(d)-calculated dipole moments are in good agreement with experiment (Table A.2).

## A.3 Uncertainty

### A.3.1 Initial branching ratio uncertainty

The addition of OH onto isoprene yields eight different peroxyradicals (Fig. 2.1). The reported branching ratios vary significantly (Lei et al., 2001).

MACR and MVK are only produced through the reaction of the  $\beta$ -hydroxy alkoxy radicals with NO and by ozonolysis of isoprene (Fig. 2.1). Since the latter accounts for less than 0.5% of the total isoprene consumption in the chamber, we can use the direct determination of the yield of these products (Sprengnether et al., 2002) as a constraint.

$$(1 - \alpha_\beta)(Y_{1,2} + Y_{2,1}) = 0.44 \pm 0.06 \quad (\text{A.8})$$

$$(1 - \alpha_\beta)(Y_{4,3} + Y_{3,4}) = 0.28 \pm 0.04 \quad (\text{A.9})$$

We consider that all  $\beta$ -hydroxy peroxy radicals have the same nitrate branching ratio,  $\alpha_\beta$ , as suggested by Giacomelli et al. (2005). In this study, we assume that channels (2,1) and (3,4) yield MVK and MACR, respectively. Park et al. (2003) proposed that the radicals formed in these channels undergo a cyclization, thus reducing the yield of MVK and MACR. The yield of the nitrates which should originate from the hydrocarbons proposed by Park et al. (2003) is too small to provide conclusive experimental evidence in favor or against this mechanism. Given the small combined yield of these channels, this uncertainty remains small compared to the ones affecting the major channels.

Theoretical determinations of the branching ratio have also been made (Lee et al., 2000; Greenwald et al., 2007):

$$Y_{1,2} + Y_{1,4} = 0.56; 0.67 \quad (\text{A.10})$$

$$Y_{4,3} + Y_{4,1} = 0.29; 0.37 \quad (\text{A.11})$$

$$Y_{2,1} = 0.02 \quad (\text{A.12})$$

$$Y_{3,4} = 0.02; 0.05 \quad (\text{A.13})$$

The product of the decomposition of the isoprene nitrates formed in the (4,1) branch, dihydroxybutanone (DHB) and propanone nitrate (PROPNN), provide an additional constraint (Fig. 2.8):

$$\begin{array}{rcl}
0.01 & < (1 - \alpha_{2,1}^{dn})\gamma\alpha_{\beta}Y_{2,1} + (1 - \alpha_{4,1}^{dn})\alpha_{\delta}Y_{4,1} < & 0.034 \\
\pm 0.002 & & \pm 0.007
\end{array} \tag{A.14}$$

where  $\alpha_{\delta}$  is the nitrate yield from the  $\delta$ -hydroxy peroxy radicals,  $\gamma$  is the branching ratio of the pathway yielding propanone nitrate from ISOPN(2,1), computed using (A.3),  $\alpha_{2,1}^{dn}$  and  $\alpha_{4,1}^{dn}$ , the respective organic dinitrate branching ratios from ISOPN(2,1) and ISOPN(4,1).

The upper and lower bounds reflect the uncertainty on the identification of the  $m/z = 189$  signal. The upper bound is derived assuming all  $m/z = 189$  signal originates from the DHB yielded by ISOPN(4,1). The lower limit assumes that no DHB is formed from ISOPN but rather that the signal measured at  $m/z = 189$  results from the photooxidation of HC5 Z(1,4) (negligible based on Peeters' SAR) and ISOPN (1,4) (formation of dihydroxymethylpropanal (DHMPL) from addition of OH on the less-sterically favored carbon).

In the mechanism, we use the constraints implied by the study of Lei et al. (2000),  $Y_{MACR} = 0.26$  and  $Y_{MVK} = 0.40$ , and the upper bound of A.14. Since the use of the non-linear system formed by Eqs. (A.8) to (A.14) in order to solve for  $\alpha_{\beta}$ ,  $\alpha_{\delta}$  and  $Y_{i,j}$  does not yield a single solution, we use the branching ratios derived by Lei et al. (2001) to initialize the numerical solution of this non-linear system and obtain:  $Y_{1,2} \simeq 41\%$ ,  $Y_{1,4} \simeq 15\%$ ,  $Y_{2,1} \simeq 2\%$ ,  $Y_{4,3} \simeq 23\%$ ,  $Y_{4,1} \simeq 14\%$ ,  $Y_{3,4} \simeq 5\%$ ,  $\alpha_{\delta} \simeq 24\%$ ,  $\alpha_{\beta} \simeq 6.7\%$ . This set of parameters yields a self-consistent mechanism which captures correctly most of our observations.

The constraints implied by the theoretical study of Greenwald et al. (2007) and the experimental work of Sprengnether et al. (2002) can not be reconciled with our observations in a consistent fashion. Consider the extreme case where  $Y_{MACR} = 24\%$ ,  $Y_{4,3} + Y_{4,1} = 29\%$  and  $Y_{2,1} = 2\%$  and assume a nitrate yield of 10% for the  $\beta$ -hydroxy channels gives  $Y_{4,1} \simeq 4.7\%$ . A direct consequence of the small branching ratio for (4,1) branch is to preclude DHBN from being an important product of ISOPN(4,1). The signal measured at  $m/z=189$  would therefore mostly correspond to DHMPL formed from the photooxidation of ISOPN(1,4). There are two major inconsistencies with this hypothesis. First, due to the small carbon flux through the (4,1) branch, we are not able to capture the prompt source of hydroxyacetone attributed to Dibble mechanism. Second, DHMPL features an aldehydic group so that its lifetime with respect of OH is expected to be much shorter than DHB inconsistent with the signal recorded at  $m/z = 189$  (Fig. 2.12).

While the derivation of the specific branching ratio is affected by this major uncertainty, the determination of the overall yield of the different products identified is, on the other hand, strongly constrained by

observations and thus relatively insensitive to our choice. The asymmetry of the nitrate yields between the  $\beta$  and  $\delta$ -hydroxy channels is therefore a reliable feature. Indeed this conclusion bears a striking similarity with the estimate derived by Giacomelli et al. (2005) using a corrected Carter’s parameterization. It is also consistent with the suggestion of O’Brien et al. (1998) that hydrogen bonding in  $\beta$ -hydroxy-substituted ROONO intermediate weakens the RO–ONO bond, enhancing RO + NO<sub>2</sub> production.

### A.3.2 Quantum mechanics

In this study, we have assumed that ligand exchange has a negligible impact on CIMS sensitivity. Therefore to assess the accuracy of our calibration, we compare the calculated collision rate with the fastest experimental collision rate:

$$k_X^r = \frac{c_X^e}{c_{\text{HNO}_3}} k_{\text{HNO}_3}^r \quad (\text{A.15})$$

where  $k_{\text{HNO}_3}^r = 2.2 \times 10^{-9} \text{ cm}^3 \text{ molec}^{-1} \text{ s}^{-1}$  (Huey et al., 1996; Amelynck et al., 2000) and  $c_X^e$  is the maximum sensitivity of this technique determined experimentally by changing the water vapor mixing ratio (often found at zero water vapor mixing ratio).

The sensitivity of the CIMS to strong acids (nitric acid ( $r = \frac{k_X \cdot k_{\text{HNO}_3}^r}{k_{\text{HNO}_3} k_X^r} = 0.9$ ) or representative VOC (glycolaldehyde,  $r = 0.85$ ) appears to be correctly captured using the thermal collision rate. Furthermore in a recent study, Ng et al. (2008) monitored the oxidation of isoprene by NO<sub>3</sub> using CIMS. Using the dipoles and the polarizabilities of MNBOL (1,4)/(4,1) ((2Z)-2/3-methyl-4-(nitrooxy)but-2-ene-1-peroxol), MNBL (1,4)/(4,1) ((2Z)-3/2-methyl-4-(nitrooxy)but-2-enal) and ISOPN (4,1) (Table A.2), we infer that they account for 100% of the carbon flux, consistent with previous determination.

Conversely, the sensitivity to smaller molecules such as formic ( $r = 1.5$ ) or acetic acid ( $r = 2$ ) is largely overpredicted. If the experimental rates of Amelynck et al. (2000) are used, the agreement is much better with  $r = 1.0$  for formic acid and  $r = 1.1$  for acetic acid. The discrepancy may be explained by the smaller collisional energy used in the experiment Amelynck et al. (2000), which would result in fewer A<sup>−</sup>•HF complexes being broken.

### A.3.3 Inorganic chemistry uncertainties

In addition to uncertainties associated with the VOC chemistry, proper modeling of the background chemistry must be achieved to derive conclusions regarding the VOC chemistry. The model is especially sensitive to the following parameters:

**Nitric Acid:** The rate of  $\text{HO} + \text{NO}_2 \longrightarrow \text{HNO}_3$  is an important uncertainty regarding the background chemistry. We use the recently reported rate coefficient of  $9.16 \times 10^{-12} \text{ cm}^3 \text{ molec}^{-1} \text{ s}^{-1}$  (Okumura and Sander, 2005) which tends to reduce the rate of formation of nitric acid and conversely increases the formation rate of ozone in comparison with the previous estimates (Atkinson et al., 2006).

**N<sub>2</sub>O<sub>5</sub>:** N<sub>2</sub>O<sub>5</sub> is known to react with water on surfaces (aerosol, walls) to yield nitric acid:



The DMA measurements can be used to obtain the aerosol surface area  $\mathcal{S}$  and the collision rate,  $k_{\text{coll}} = \frac{1}{4} \sqrt{\frac{8RT}{\pi M}} \mathcal{S} = 2 \times 10^{-3} \text{ cm}^3 \text{ molec}^{-1} \text{ s}^{-1}$ . The accommodation coefficient is set to 0.05.

**Initial concentration of hydrogen peroxide:** Due to the technique used in this experiment to introduce H<sub>2</sub>O<sub>2</sub> into the chamber, its concentration is not known accurately. No calibration is available at such a high hydrogen peroxide level, so that its estimate based on CIMS measurement is uncertain: 1.9–2.3 ppm. A new injection method has been developed and should allow to reduce this uncertainty in future studies.

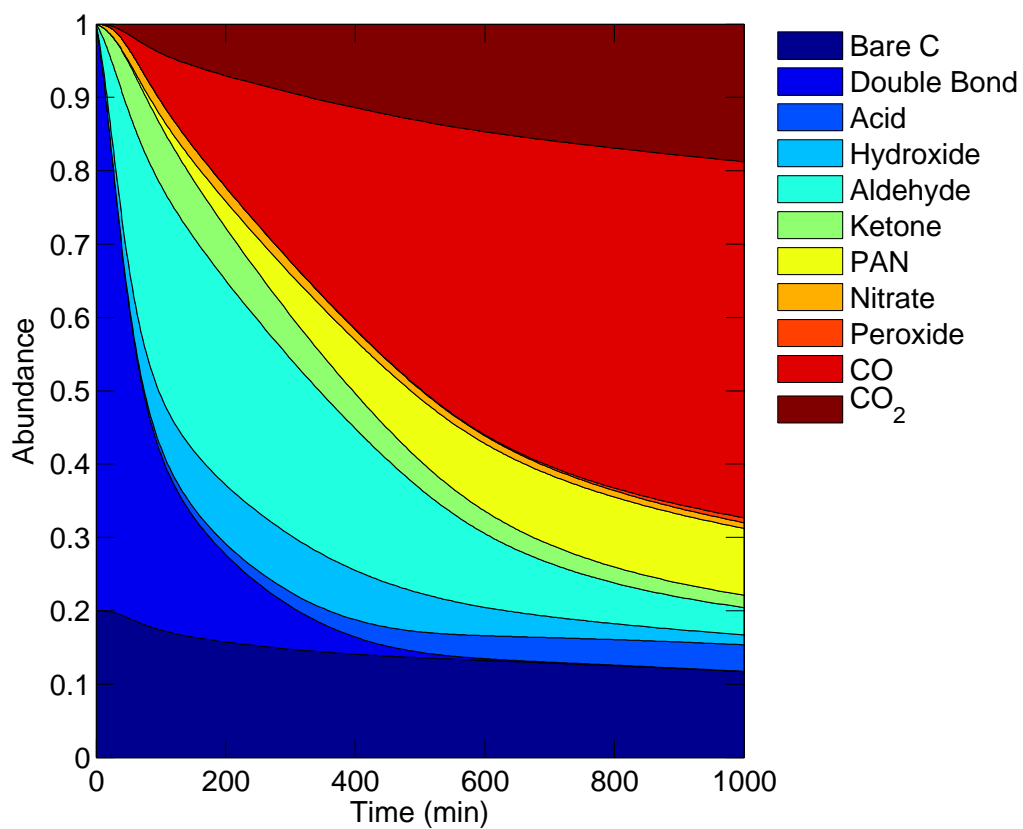


Figure A.1: Evolution of the speciation during isoprene photooxidation. The abundance of a functional group  $\Pi$  is defined as the sum of the carbons bearing  $\Pi$  normalized by the total amount of carbon in the chamber, i.e., five times the initial amount of isoprene.

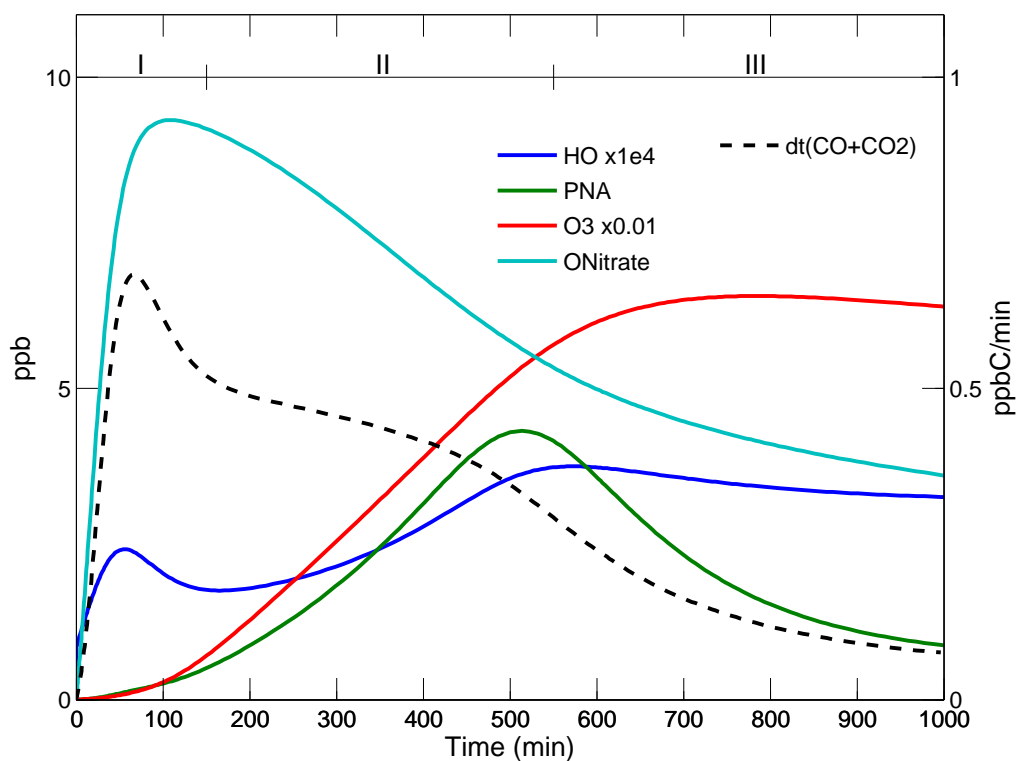


Figure A.2: Different stages of the reaction. Regime I: alkenes chemistry,  $\text{NO}_x$ -dominated. Regime II: aldehydes chemistry,  $\text{NO}_x$ -dominated. Regime III: ketones and peroxides chemistry,  $\text{HO}_x$ -dominated



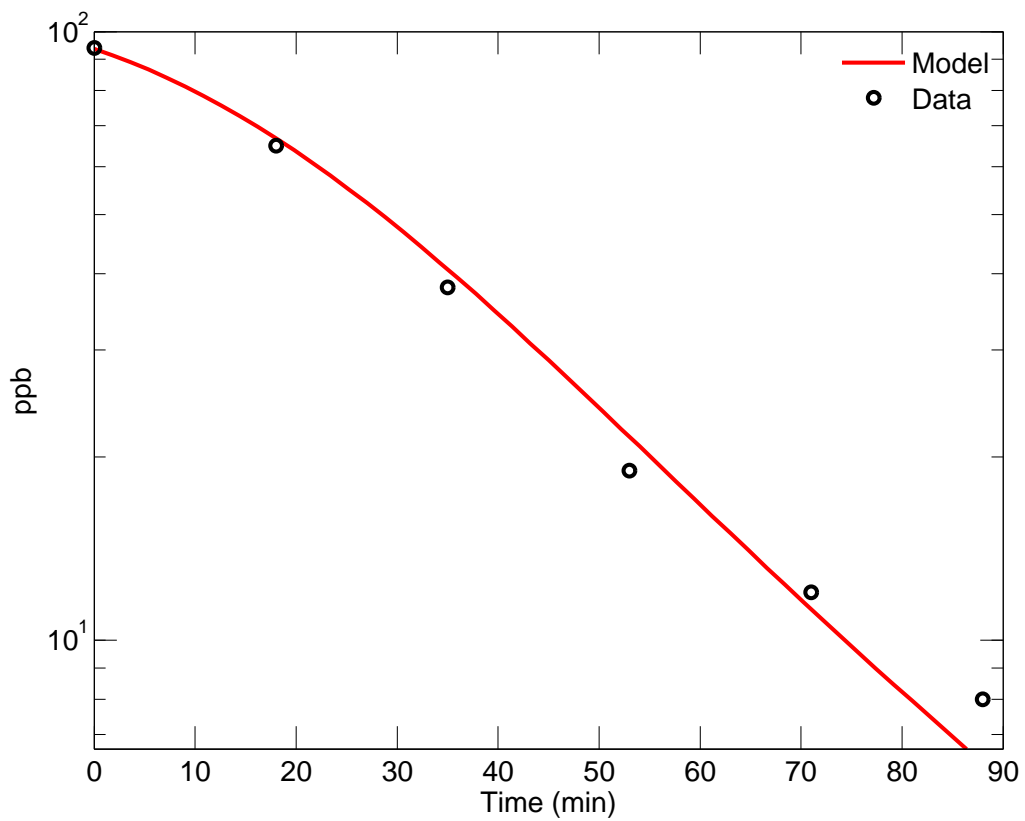


Figure A.3: Isoprene profile monitored by GC FID compared to modeled isoprene

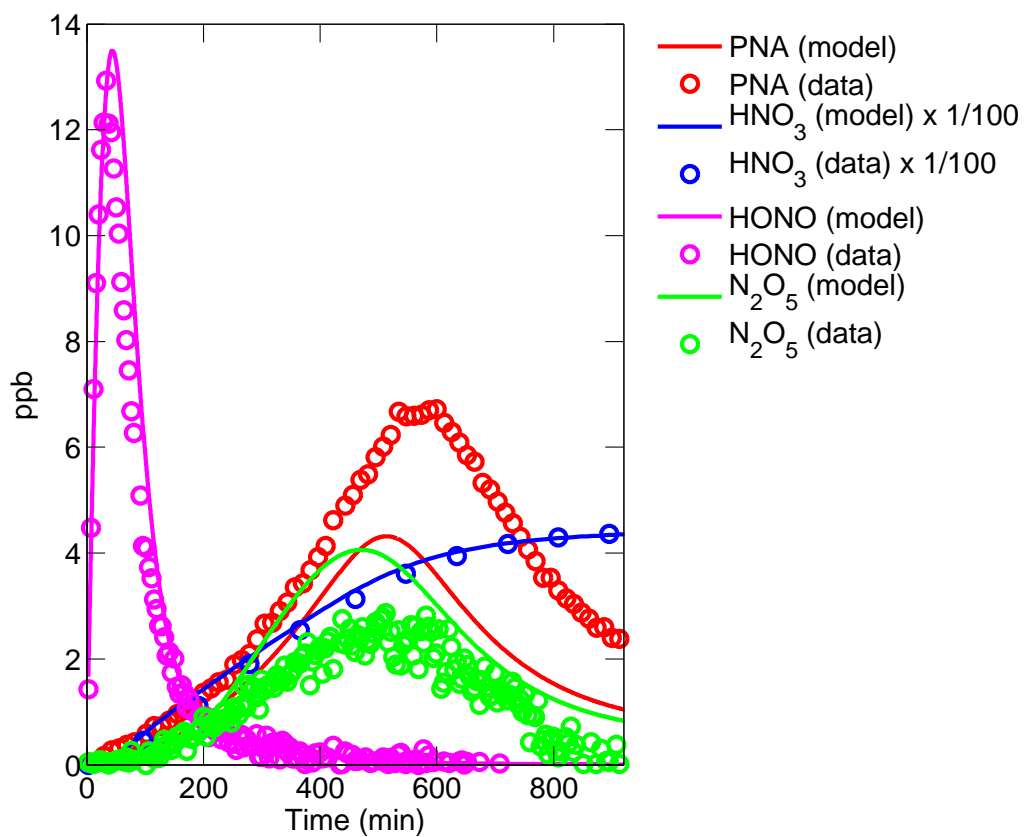


Figure A.4: Isoprene profile monitored by GC FID compared to modeled isoprene

Table A.2: Weighted average dipoles ( $\bar{\mu}$ ) and polarizabilities ( $\alpha$ ). Experimental determinations are indicated in parenthesis when available.  $k_X$ , is the weighted average of the collision rates calculated for conformers with an abundance greater than 5%.  $k_{\text{HNO}_3} = 1.92 \times 10^{-9} \text{ cm}^3 \text{ molec}^{-1} \text{ s}^{-1}$ .  $\sigma$  is the weighted standard deviation of the distribution of thermal collision rate constants, i.e., it indicates the sensitivity of the calibration to the calculated distribution of conformers.

Molecule (X)	$\bar{\mu}$ (D)	$\alpha$ ( $\text{\AA}^3$ )	$k_X/k_{\text{HNO}_3}$	$\sigma$
Acetic Acid	1.6 (1.7 $^\circ$ )	3.9 (5.1 $^*$ )	0.80 (0.84)	$\emptyset$
DHB	2.3	7.5	1.0	0.027
DHMOB14	1.5	9.3	0.79	0.26
DHMOB41	1.1	9.1	0.66	0.12
DHPN	1.5	6.0	0.74	$\emptyset$
ETHLN	2.7	6.2	1.1	0.4
Formic Acid	1.4 (1.4 $^\circ$ )	2.4 (3.3 $^\circ$ )	0.76 (0.78)	$\emptyset$
GLYC	2.3 (2.34 $^\S$ )	4.5	1.1 (1.1)	$\emptyset$
HACET	3.1 (3.1 $^\ddagger$ )	5.5	1.4 (1.4)	$0.72 \times 10^{-3}$
HC5 E(4,1)	2.8	8.9	1.2	0.22
HC5 Z(1,4)	3.5	8.7	1.5	0.14
HC5 Z(4,1)	3.7	8.9	1.5	$\emptyset$
HOPL	1.2	5.7	0.65	$1.6 \times 10^{-3}$
ISOPN (1,2)	2.5	11	1.0	0.032
ISOPN (2,1)	2.5	11	1.0	0.17
ISOPN (3,4)	2.4	11	1.0	0.11
ISOPN (4,3)	2.5	11	1.0	0.068
ISOPN (1,4)E	3.2	11	1.3	0.17
ISOPN (4,1)E	2.9	12	1.2	0.085
ISOPN (1,4)Z	3.2	11	1.3	0.028
ISOPN (4,1)Z	3.0	11	1.2	0.041
MACRN(m)	2.4	9.9	1.0	0.38
MACRN	2.0	9.8	0.87	0.045
MNBL Z(1,4)	3.6	11	1.4	0.089
MNBL Z(4,1)	3.9	12	1.5	0.12
MNBOL Z(1,4)	4.3	12	1.6	0.073
MNBOL Z(4,1)	4.2	12	1.6	0.083
MOBA Z(1,4)	4.6	9.1	1.8	0.22
MOBA Z(4,1)	3.2	9.2	1.3	$\emptyset$
MVKN(m)	2.2	9.7	0.95	0.39
MVKN	2.3	9.9	0.95	0.078
PROPNN	3.0	7.7	1.3	0.46
Propanoic Acid	1.5	5.4	0.76	0.034
Pyruvic Acid	2.4	5.5	1.0	$\emptyset$

$^\circ$ : Johnson III (2006),  $^\ddagger$ : Apponi et al. (2006),  $^*$ : Cox et al. (1971)

$^\S$ : Maryott and Buckley (1953),  $^\S$ : Marstokk and Mollendal (1973)

## Appendix B

# Unexpected epoxide formation in the gas-phase photooxidation of isoprene

### B.1 Chemical Ionization Mass Spectrometry

#### B.1.1 Overview

The Caltech Chemical Ionization Mass Spectrometer (CIMS) was originally designed for aircraft missions as a robust and lightweight instrument capable of detecting trace amounts of atmospherically-relevant substances with high selectivity and sensitivity. The reagent ion used in negative ion mode,  $\text{CF}_3\text{O}^-$ , reacts with a suite of peroxides and various other compounds, e.g.,  $\text{SO}_2$ ,  $\text{HNO}_3$  and organic acids (Huey et al., 1996; Amelynck et al., 2000; Crounse et al., 2006).

There exist two versions of the flight instrument: 1) The original version that utilizes a single quadrupole mass filter as a mass spectrometer (Crounse et al., 2006) and 2) a more recently developed instrument with the same ionization scheme but utilizing a commercial triple quadrupole mass spectrometer, thereby allowing for the differentiation of certain mass analogues using tandem MSMS. This latter instrument has been largely replicated for laboratory experiments at the Caltech environmental chamber. Additionally, this new instrument can be operated in positive ion mode similar to a classical proton transfer mass spectrometry (PTR-MS) instrument (Hansel et al., 1995). The instrument configuration allows for rapid switching between negative and positive ion chemistry. A brief general description of the CIMS follows here with a focus on the MSMS and PTR-MS capabilities, which are key features for the identification of IEPOX formation during isoprene photooxidation, and which have not been described in detail before.

The Caltech CIMS consists of a commercial triple quadrupole mass spectrometer (Varian 300-MS GC/MS, Varian, Inc.) and a custom ion source with a specially designed sample gas inlet system (Fig. B.2). During an experiment the sample air is pulled (1 slm) from the chamber through a Teflon line to the instrument. 20% of this sample flow is transferred to the CIMS instrument. The flow rate is controlled by a critical orifice made of glass which connects the sampling line with a 2.54 cm outer diameter glass flow tube coated with a thin layer of Teflon (Fluoropel 801A, Cytonix Corp.). The flow tube is operated at a constant pressure of 35 hPa. The sample flow entering the flow tube is diluted with nitrogen (ultra-high purity, 99.999 %) at a mixing ratio of 1:8.2. The exact value of the dilution flow is adjusted such that the pressure inside the flow tube is held constant at 35 hPa. With the exception of the sample flow, all gas flows are controlled by metal sealed mass flow controllers (SEC-4400, Horiba Stec) to minimize contamination.

The main modification to the Varian triple quadrupole mass spectrometer consists of the removal of the originally installed electron impact ionization source, thereby making room for a conically-shaped hexapole ion guide that efficiently transfers ions from the flow tube to the first quadrupole (Q1). The section where the hexapole is mounted is differentially pumped and only connected to the flow tube and the high-vacuum chamber by small openings.

The three linear quadrupole mass filters (Q1, Q2, and Q3) can be used in different configurations, allowing either the acquisition of single mass spectra (MS) or tandem mass spectra (MSMS). In the MSMS mode, a buffer gas, nitrogen, is added to the second quadrupole (Q2), which is partially enclosed. In Q2, the presence of several Pa of N<sub>2</sub> results in collision-induced dissociation (CID) of the ions selected in Q1. The fragments (or daughter ions) produced in Q2 are filtered by  $m/z$  in Q3 before being detected with an electron multiplier operated simultaneously in both analog and ion-counting mode. For the experiments shown here, the following modes were used: (a) Single MS (SMS)—Operating Q1 as a mass filter to select a single  $m/z$  value at a time while operating Q2 (evacuated) and Q3 in RF-only mode such that virtually all ions selected by Q1 reach the detector. In this manner, a mass spectrum can be obtained if all  $m/z$  values of interest are scanned; (b) MSMS—Operate Q1 as a mass filter to select a single  $m/z$  value for the parent ion. The pressure in the region of Q2 is increased to several Pa inducing the fragmentation of the selected ion. Fragment ions are then selected by Q3 and reach the detector. Mode (a) was conducted for both anions and cations, while mode (b) was conducted for anions only. For the experiments reported in this study, the following sequence was repeated throughout the experiments 1) negative ion SMS, 2) positive ion SMS, and 3) negative ion MSMS, with the total cycle duration being approximately 10 minutes.

### B.1.2 Negative ion mode

In negative ion mode, 400 sccm of 10 ppmv CF<sub>3</sub>OOCF<sub>3</sub> in N<sub>2</sub> passes through the ion source which contains a radioactive material (<sup>210</sup>Po foil, NRD, Inc.). The foil containing the <sup>210</sup>Po is housed in a stainless steel holder and emits particles which by ionizing nitrogen molecules lead to the release of electrons. The electrons are captured by CF<sub>3</sub>OOCF<sub>3</sub>, generating the reagent anion, CF<sub>3</sub>O<sup>−</sup>. Potentials of −240 V and −220V (relative to the pinhole and the instrument housing which are held at ground potential) are applied to the stainless steel <sup>210</sup>Po holder and −220V to the lens, respectively, such that only negative ions are transmitted across the flow tube in a transverse direction to the diluted sample flow. Product ions are formed through reactions of neutral analyte molecules with reagent ions as they move across the flow tube. The anions (reagent and product ions) are then pushed towards the pinhole and enter the chamber containing the conical hexapole.

The ion-molecule reactions (with a trace compound R) which can occur are: proton transfer ([R.B.1]), fluoride transfer ([R.B.2]) or clustering with a CF<sub>3</sub>O<sup>−</sup> ion ([R.B.3]) (Crounse et al., 2006; Paulot et al., 2009a)

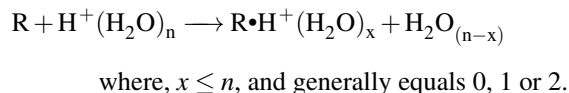


When operating the instrument in negative SMS mode, anions were scanned sequentially for 0.5 seconds from m/z=50 to m/z=275. The acquisition of a full mass spectrum thus requires ~ 2 min. The m/z of the reagent anion and its major clusters with water and hydrogen peroxide (m/z=85 (CF<sub>3</sub>O<sup>−</sup>), m/z=103 (CF<sub>3</sub>O<sup>−</sup>•H<sub>2</sub>O) and m/z=119 (CF<sub>3</sub>•H<sub>2</sub>O<sub>2</sub>)) are omitted from the scans due to their high intensities; these anions are quantified at m/z +1—mostly from the <sup>13</sup>C isotopologues.

### B.1.3 Positive ion mode

In positive ion mode, 400 sccm of N<sub>2</sub> (without CF<sub>3</sub>OOCF<sub>3</sub>) is passed through the ion source. Residual H<sub>2</sub>O in the gas stream reacts with N<sub>2</sub><sup>+</sup> ions (generated from the collisions of the α particles with the bath gas) to form H<sup>+</sup>•(H<sub>2</sub>O)<sub>n</sub> reagent ions in the ion source. The positively charged ions are directed out of the source and across the flow tube by inverting the polarity of the potentials on the ion source and the lens from those

used in negative ion mode. The most abundant positive ions detected by the spectrometer correspond to  $n = 3, 4$ . The pressure ( $\sim 3 \times 10^{-3}$  hPa) inside the conical hexapole limits the transmission of ions with  $m/z < 50$ , so that the  $n = 1$  and 2 water clusters cannot be detected. The ion-molecule reactions which occur in positive ion mode are:

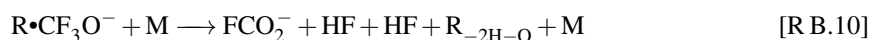
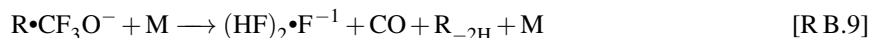
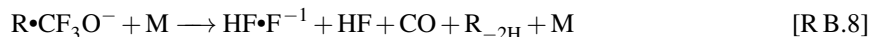
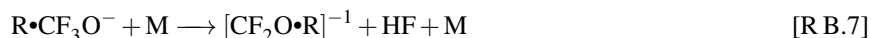
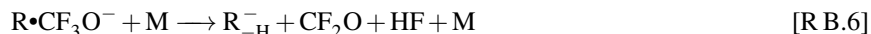


When operating the instrument in positive SMS mode, ions are scanned sequentially for 0.5 seconds from  $m/z=30$  to  $m/z=235$ . The full mass spectrum requires approximately 1 min and 40s. Ions with  $m/z=55$  ( $H^+ \cdot (H_2O)_3$ ),  $m/z=73$  ( $H^+ \cdot (H_2O)_4$ ) are omitted due to their high intensities.

#### B.1.4 Negative ion MSMS mode

The ion generation for the negative ion MSMS mode is identical to the negative ion SMS mode. The main difference of MSMS mode as compared to the SMS mode is the addition of a small flow of  $N_2$  into the Q2 quadrupole such that the pressure inside Q2 reaches approximately  $2.5 \times 10^{-3}$  hPa. To increase the signal-to-noise ratio in MSMS mode, the resolution of Q3 is set to a full-width half-maximum of approximately 1.5 amu. While this does give fairly broad peaks, the chance of distinct fragment ions (excluding isotopic pairs, e.g.,  $^{12}C$  and  $^{13}C$ ) occurring at adjacent masses (and thus being indistinguishable at this resolution) is small.

In many cases, the formation of the daughter ions induced by collisions of the parent ion (e.g.,  $R \cdot CF_3O^-$ ) with the bath gas (M) can be explained through the following CID channels:



The distribution across the possible CID channels ([R B.4]–[R B.10]) for a given parent ion,  $\text{R}\cdot\text{CF}_3\text{O}^-$ , varies greatly depending upon the nature of R (acidity, fluoride affinity, dipole moment, etc.). This distribution can also be modified by changing the average collision energy in Q2, i.e., changing the kinetic energy (velocity) of the ion upon entering Q2. In this work, the ion energies (velocities) are tuned to be quite low (slow) to prevent CID from occurring in the conical hexapole. As a result, it is not possible to alter the collision energies in Q2 significantly without scattering most of the ions onto undetectable trajectories. For a given parent ion  $m/z$ , the collisional energy in Q2 was the same across all experiments, and was adjusted as a function of the parent ion mass in order to place the parent ion (and latter the fragment ions) on detectable trajectories, namely those moving through Q2.

## B.2 Theoretical method: formation of $\beta$ and $\delta$ -IEPOX

All stationary points in reactions R2a and R2b and the analogue  $\beta$ 1-ISOPOOH reaction have been optimized with the B3LYP/6-31G(d) method. The transition state (TS) between the alkyl radical and the epoxide has a single imaginary frequency at  $729\text{ cm}^{-1}$ ,  $689\text{ cm}^{-1}$  and  $676\text{ cm}^{-1}$  for the  $\beta$ 1-TS,  $\beta$ 4-TS, and  $\delta$ 4-TS, respectively (Wavefunction Inc., 2008). As expected, the imaginary mode is a vibration along the OO bond. Intrinsic Reaction Coordinate (IRC) calculations were done in both the forward and backward direction (Frisch, 2004). We let the IRC calculation run 20 steps (each 0.01 a.u. along the reaction path) in each direction, which was sufficient to connect the TS to the optimized structures. For example, for the  $\beta$ 1-channel, the 20 steps in backward reaction led to a structure very close to the optimized alkyl radical. The



OO distance in the final IRC step is only 0.02 Å longer than the OO distance in the optimized structure. The final structure in the forward direction has the HO group loosely attached and the oxirane is not completely formed. The COC angle is 58° in the last step and is 62° in the optimized  $\beta$ -IEPOX. The CO distance is 1.62 Å whereas it is 1.44 Å in  $\beta$ -IEPOX. We also located a product complex with the HO radical hydrogen bound to the expoxide oxygen atom. With the amount of excess energy available this complex is unlikely to form and is of little importance for the reaction. Similar results are obtained for the  $\beta$ 4- and  $\delta$ 4-channel.

We have calculated B3LYP single-point energies with the correlation consistent polarized triple zeta (cc-pVTZ) basis set on the B3LYP/6-31G(d) optimized structures and have also optimized each structure with the B3LYP/cc-pVTZ method. The B3LYP/cc-pVTZ and B3LYP/6-31G(d) structures are similar. The B3LYP/cc-pVTZ optimized geometries of the TS have a single imaginary frequency at a slightly lower frequency of 704 cm<sup>-1</sup>, 658 cm<sup>-1</sup> and 651 cm<sup>-1</sup> for the  $\beta$ 1-TS,  $\beta$ 4-TS, and  $\beta$ 4-TS, respectively, in good agreement with the B3LYP/6-31G(d) results. The B3LYP/cc-pVTZ optimized geometries are shown in Figs. 3.5, B.3 and B.4, and the B3LYP relative energies are given in Tables B.4, B.6 and B.7. For all three reactions, the B3LYP/cc-pVTZ optimized relative energies are very close to the B3LYP/cc-pVTZ single point relative energies on the 6-31G(d) structure, and within 2 kcal/mol of the B3LYP/6-31G(d) energies.

To corroborate the B3LYP results we have calculated, for the four B3LYP/cc-pVTZ optimized stationary points on the  $\beta$ 4-ISOPPOOH to  $\beta$ -IEPOX reaction, single point energies with second-order perturbation Møller-Plesset (MP2) and the recently developed explicitly correlated coupled cluster (CCSD(T)-F12) methods, as implemented in MOLPRO 2008.1 (Tew et al., 2007; Werner et al., 2008). We have used the VDZ-F12 orbital basis sets of Peterson et al. that have been specifically optimized for use with explicitly correlated F12 methods (Petersen et al., 2008). The VDZ-F12 basis sets are of similar size to the aug-cc-pVDZ basis set. Density fitting approximations (Martin et al., 2006; Werner et al., 2007) were used in all explicitly correlated calculations using the VDZ/JKFIT and the AVDZ/MP2FIT auxiliary basis sets of Weigend et al. (Weigend et al., 2002; Weigend, 2002). We have used the resolution of the identity (RI) auxiliary basis sets of Yousaf et al. for all RI approximations (Yousaf and Peterson, 2008). In the MP2 calculations we have used the cc-pVTZ and aug-cc-pVTZ basis sets. We found that the unrestricted MP2 (UMP2) calculation on  $\beta$ 4-TS, led to a large spin contamination ( $S^2 = 1.27$  with UMP2/aug-cc-pVTZ) which is unreasonable, and hence the UMP2 results are not included. Instead we have used the restricted open (ROMP2) for the two radicals and RMP2 for the  $\beta$ 4-ISOPPOOH to  $\beta$ -IEPOX structures.

The calculated relative MP2 and CCSD(T) energies are given in Table B.5. These higher-level correlated results for the  $\beta$ 4-ISOPPOOH reaction corroborate the B3LYP results. The noticeable difference between the

B3LYP and correlated results is in the barrier between the alkyl radical and the TS, which is about 10 kcal/mol with B3LYP and CCSD(T)-F12 and about 3–5 kcal/mol with the RMP2 method. The explicitly correlated F12 method with the VDZ-F12 basis set is known to give near basis set limit CCSD(T) results (Tew et al., 2007), and is as such considered to approach chemical accuracy (Lane and Kjaergaard, 2007; Vöhringer-Martinez et al., 2007). These higher-level calculations corroborate the B3LYP result, that the reaction to form the epoxide is energetically favorable and proceeds through a small barrier.

### B.3 Possible interferences from isomers of IEPOX

We have shown in the previous section that the identification of ISOPOOH and IEPOX was supported by CIMS-CID, via their unique fragmentation pattern. Other observations confirm our attribution.

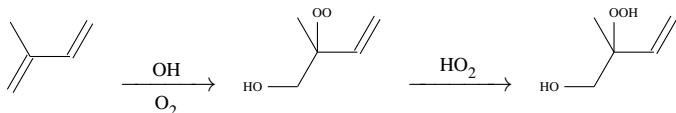
From the ratio of  $m/z=204$  to  $m/z=203$  (largely a measure of the  $^{13}\text{C}$  content of the ion), we find that both the first- and second-generation MW118 compounds have five carbons, consistent with IEPOX formation.

Because of the high yield, the candidate isomers need to be formed from ISOPOOH via a mechanism which incorporates one  $^{18}\text{OH}$  while releasing one  $^{16}\text{OH}$ . The reaction of OH with ISOPOOH will proceed almost exclusively by addition of OH to the remaining double bond. The measured lifetime of ISOPOOH is completely consistent with this understanding. In a previous section, we showed using quantum mechanical calculations that, following the addition of the OH, the energetic barrier to formation of IEPOX lies significantly below the OH+ISOPOOH entrance channel energy. This implies that the lifetime of the highly excited alkylradical  $\text{HO}\cdot\text{ISOPOOH}$  will be very short before fragmentation to the epoxide and OH. To form a peroxy radical ( $\text{RO}_2$ ), many nanoseconds will be required, as only 1 in 5 collisions will be with  $\text{O}_2$  and few of these will be reactive. Consistent with the lack of formation of the  $\text{RO}_2$  following the OH addition to ISOPOOH, we do not observe any dihydroxydihydroperoxide. The  $^{18}\text{OH}$  experiments further confirm that the second-generation product results from the addition of a second OH radical and, by mass balance, loss of OH. This can be seen in Fig. 3.4 where the 205 signal (one  $^{18}\text{O}$ ) is converted mostly to a second-generation product with two  $^{18}\text{OH}$  ( $m/z=207$ ). Again, these observations are consistent with the formation of IEPOX. The isomers of IEPOX, which have been previously proposed based on iSOA speciation (Surratt et al., 2006; Wang et al., 2005), cannot explain our observations (Table B.8). However, they may have resulted from IEPOX heterogeneous chemistry (Wang et al., 2005).

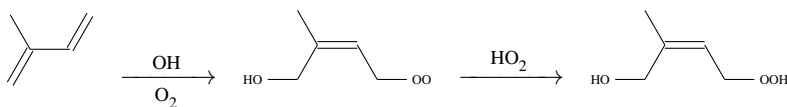
## B.4 Additional mechanisms

### B.4.1 Addition of OH on isoprene second double bond

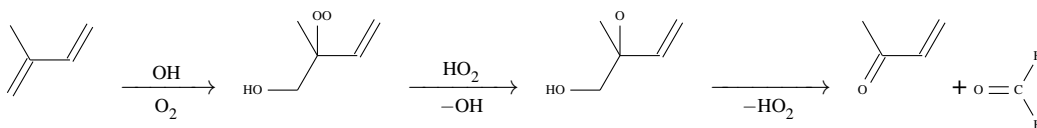
In the main body of the manuscript, we have described the addition of OH onto the double bond which does not carry the methyl group. Addition also occurs on the other double bond and yields  $\beta$ 1 – ISOPOOH ([R B.11]),  $\delta$ 1 – ISOPOOH ([R B.12]) and MVK ([R B.13]).



[R B.11]



[R B.12]



[R B.13]

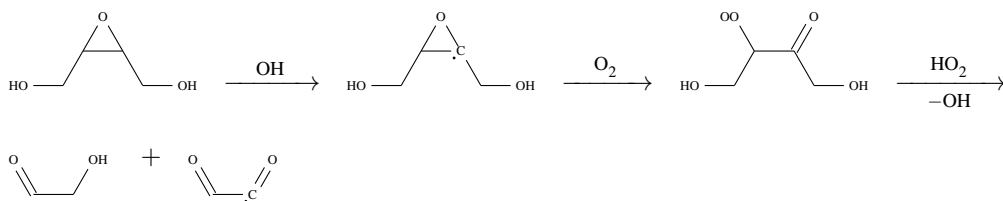
Given the yield of IEPOX,  $\delta$ 1-ISOPOOH produced by ([R B.12]) is likely to lead, at least partly, to  $\delta$ 1-IEPOX. This would suggest that OH can add substantially on the side of the double bond bearing the methyl group ( $\sim 50\%$ ). Addition of OH on carbons 2 and 3 of isoprene is less than 10% and was not considered in this study (Fan and Zhang, 2004).

### B.4.2 Fate of IEPOX

We investigated this reaction using synthesized BEPOX reacting with labeled  $^{18}\text{OH}$ . It appears that the reaction of IEPOX with OH occurs mostly by abstraction of the H  $\alpha$  to the alcohol followed by the opening of the oxirane C-O bond.

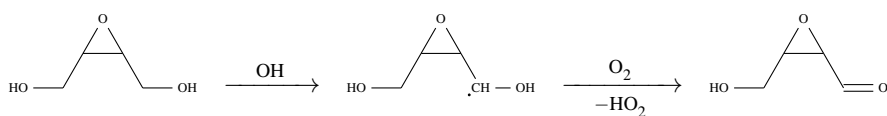
Five different channels were considered:

- abstraction of the epoxidic H



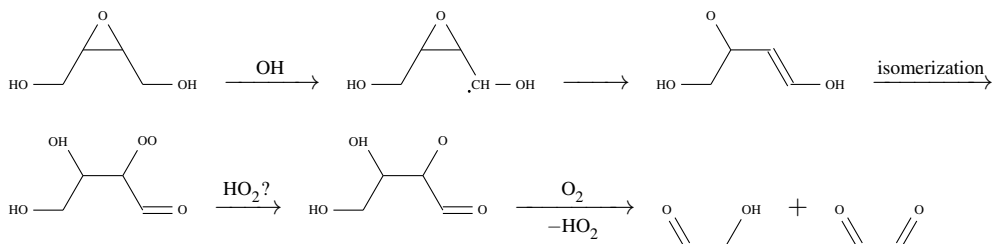
[R B.14]

- abstraction of the H  $\alpha$  of the alcohol followed by reaction with  $O_2$



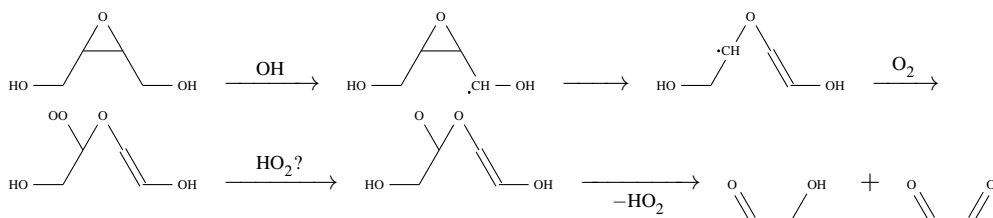
[R B.15]

- Abstraction of the H  $\alpha$  of the alcohol followed by opening of C-O bond of the oxirane



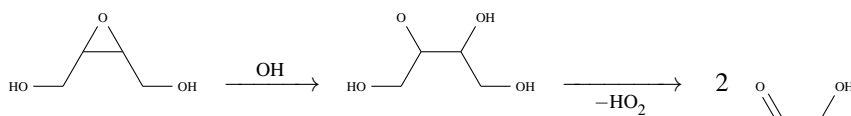
[R B.16]

- Abstraction of the H  $\alpha$  of the alcohol followed by opening of C-C bond of the oxirane. The isomerization follows the mechanism proposed by Dibble (2004a,b).



[R B.17]

- Addition of OH to the oxirane



[R B.18]

The only mechanism yielding singly labeled glycolaldehyde is [R B.18]. Very little signal is recorded at this mass suggesting that OH is not incorporated into the oxirane. This is also consistent with the absence of dilabeled hydroxyacetone and glycolaldehyde in the isoprene +  $^{18}\text{OH}$  experiments.

The signal recorded at  $m/z=187$  corresponding to the product of [R B.15] also represents a minor contribution to the total signal. This is consistent with the unlabeled isoprene experiment where little signal is recorded at  $m/z=201$ , the analog of  $m/z=187$  in the isoprene system.

[R B.14] (Meleshevich, 1970), [R B.16] and [R B.17] all yield non-labeled glycolaldehyde and are difficult to distinguish directly because of the BEPOX symmetry. However, data from isoprene +  $^{18}\text{OH}$  experiment suggest high yields of both singly-labeled hydroxyacetone and glycolaldehyde from IEPOX photoxidation. This suggests that the analogue of [R B.14] for isoprene is not the main oxidation channel, as no glycolaldehyde can result from this channel. Furthermore if [R B.14] is an important decomposition pathway, dilabeled glycolaldehyde from  $\delta 4$ -IEPOX would be formed. However, dilabeled glycolaldehyde is not observed. [R B.16] and [R B.17] are mostly indistinguishable and further studies are required to investigate these mechanisms in more detail. It is suggested here that the reaction of IEPOX with OH occurs mostly by abstraction of the H  $\alpha$  to the alcohol followed by the opening of the oxirane C-O bond ([R B.17]). The signal recorded at  $m/z=91$  in PTR-MS mode may be associated with the formation of the enol, 3 hydroxy-2-propenal.

Furthermore the analogue of [R B.16] applied to the IEPOX seems thermodynamically unfavorable as it requires a rearrangement, which involves the formation of a primary radical from a secondary radical.  $\delta 1$ -IEPOX cannot undergo [R B.17] and its fate remains uncertain. For simplicity we have assumed in our kinetic model and in the proposed GEOS-CHEM mechanism that  $\delta 1$  - IEPOX shares the fate of  $\delta 4$  - IEPOX, yielding hydroxyacetone.

## B.5 Kinetic mechanism

In our simulations of the laboratory experiments, we used a simplified chemical scheme focusing on the first few hours. The different isotopes for each species are explicitly treated but we neglect any kinetic isotope effect on the reaction rate constants or the yields of the reactions.

Cross reactions of peroxy radicals are treated using a class approach (Madronich and Calvert, 1990; Jenkin et al., 1997; Saunders et al., 2003). This approach was modified to account for the possibility of homomolecular biradical cross-reactions. The reaction of a peroxy radical ( $\text{RO}_2$ ) with a class of peroxy radical  $\text{CLO}_2$  is defined as:

$$\frac{d[\text{RO}_2]}{dt} = -k_{\text{CO}_2}^{\text{RO}_2}[\text{RO}_2][\text{CLO}_2] \left( 1 + \frac{[\text{RO}_2]}{[\text{CLO}_2]} \delta(\text{RO}_2, \text{CLO}_2) \right)$$

where  $\delta(x,y)$  is the Dirac function. A simplified scheme is used to treat the products of the  $\text{RO}_2+\text{RO}_2$  channel. This approximation is justified as the experiment was designed to limit the role of these reactions.

Peroxy radicals formed by the reaction of OH with isoprene were divided into two classes:  $\beta$  (70%) and  $\delta$  peroxy radicals (30%). Addition of OH on the internal carbons are neglected as they account for less than 10% of the carbon (Crutzen et al., 2000).

The expected product of the alkoxy channel for the  $\delta$  channels (isomer of 1-hydroxy-4-oxo-2-methylbut-2-ene, similar to the mechanism depicted in Fig. 3.1c) is not observed in large yields. Therefore we assume that the alkoxy channel is only occurring for the  $\beta$  peroxy radicals, consistent with the formation of MVK and MACR. The fraction of  $\beta$  peroxy radicals that yield OH while reacting with  $\text{HO}_2$  (Fig. 3.1c) is  $\sim 12\%$ . The ratio between the yields of MVK and MACR is assumed to be equal to the one derived under high  $\text{NO}_x$  conditions.

In addition to the  $^{16}\text{OH}$  regenerated from the VOC photooxidation, an additional conversion of  $^{18}\text{OH}$  to  $^{16}\text{OH}$  of  $\sim 7\text{s}^{-1}$  takes place in our experiments. A minor fraction of this conversion can be attributed to the reaction of OH with water (13%) (Dubey et al., 1997). Experiments at reduced oxygen concentration suggest that the reaction of OH with  $\text{O}_2$  could account for the bulk of this conversion ( $k \sim 1.3 \times 10^{-18} \text{ cm}^3 \text{ molec}^{-1} \text{ s}^{-1}$ ) (Greenblatt and Howard, 1989). For the conditions of this experiment, the production of  $^{18}\text{OH}$  from hydrogen peroxide photolysis,  $\sim 2.2 \times 10^8 \text{ s}^{-1} ([\text{H}_2\text{O}_2]=2 \text{ ppmv})$  largely exceeds the conversion of  $^{18}\text{OH}$  to  $^{16}\text{OH}$ .

Uncertainties regarding the fate of IEPOX as described in the previous section have little effect on our conclusions since channels [R B.16] and [R B.17] share the same products.

Comparison between modeled and measured ISOPOOH and IEPOX are shown in Figs. B.5 (Experiment 1, see Table B.1) and B.6 (Experiment 3). For Experiment 2, modeled  $^{16}\text{OH}$  is about  $4.5 \times 10^5 \text{ molec cm}^{-3}$ ,  $^{18}\text{OH}$   $1.8 \times 10^6 \text{ molec cm}^{-3}$ ,  $\text{H}^{16}\text{O}^{16}\text{O}$   $2 \times 10^9 \text{ molec cm}^{-3}$ ,  $\text{H}^{16}\text{O}^{18}\text{O}$   $1.1 \times 10^8 \text{ molec cm}^{-3}$  and  $\text{H}^{18}\text{O}^{18}\text{O}$   $2.8 \times 10^9 \text{ molec cm}^{-3}$ .

## B.6 GEOS-Chem

GEOS-CHEM v8.01.04 (<http://www-as.harvard.edu/chemistry/trop/geos/>) driven by assimilated meteorological observations from the Goddard Earth Observing System (GEOS-4) of the NASA Global Modeling and Assimilation Office (GMAO) (Bey et al., 2001) is used to assess the global impact of the isoprene chemistry described herein. The model is run with a spatial resolution of  $4^\circ$  latitude and  $5^\circ$  longitude and 30 vertical levels (22 in the troposphere).

Isoprene emissions are taken from the Global Emission Inventory Activity (GEIA) inventory (Guenther et al., 1995). The default chemical mechanism is updated to incorporate recently proposed modification to the high  $\text{NO}_x$  chemistry (Paulot et al., 2009a) as well as the low- $\text{NO}_x$  regime derived in this study (Table B.9). Dry deposition for IEPOX and ISOPOOH is modeled using  $\text{H}_2\text{O}_2$ , while hydroxymethylhydroperoxide (HMHP) parameters are used to model their wet deposition.

A model spin-up of 15 months is done before the results are retained. The results presented in this study are for northern hemisphere summer 2002 and northern hemisphere winter 2001. Isoprene emissions from GEIA are scaled in GEOS-CHEM so that the flux of isoprene to the atmosphere is  $\sim 342 \text{ TgC/yr}$ . This yields a yearly IEPOX formation of  $\sim 65 \text{ TgC/yr}$ . Estimates of isoprene emissions range from 250–750  $\text{TgC/yr}$ . Assuming that IEPOX formation scales with isoprene emissions, this leads to our global estimate of yearly production of IEPOX:  $95 \pm 45 \text{ TgC/yr}$  (167  $\text{Tg/yr}$ ).

The formation of IEPOX from isoprene is predicted to be asymmetric with a larger yield in the southern hemisphere (Fig. B.7). More than 60% of IEPOX is formed in the tropics ( $-15^\circ$ – $+15^\circ$ ) reflecting the influence of anthropogenic activities on the chemistry of isoprene.

## B.7 Field measurements

### B.7.1 TC4

The NASA Tropical Composition, Cloud and Climate Coupling (TC4) mission was designed to investigate the atmospheric structure, properties, and processes in the tropical troposphere. This mission, based out of San Jose, Costa Rica, was conducted during July and August 2007 and consisted of coordinated flights between several NASA aircraft including the DC-8, ER-2, and WB-57. Two Caltech CIMS instruments (single quadrupole instrument and the Varian tandem-MS instrument) were deployed on the DC8.

Low-level legs were flown over the Columbian jungle during several flights. During these legs large signals at  $m/z=203$  were observed with the single quadrupole instrument. Quantification of ISOPOOH and IEPOX is not possible due to uncertainties regarding the ion transmission efficiency for the quadrupole at these high masses as well as the inability of the single quadrupole to separate these mass analogues. The tandem-MS did not monitor  $m/z=203$  during this experiment.

### B.7.2 ARCTAS

The primary scientific focus of the 2008 summer NASA Arctic Research of the Composition of the Troposphere from Aircraft and Satellites (ARCTAS) mission was to study boreal forest fire emissions. ARCTAS was a NASA contribution within the greater Third International Polar Year effort (POLARCAT). The NASA DC-8 aircraft was based in Cold Lake, Alberta during the summer phase of ARCTAS, with nine total flights: two transit flights between Cold Lake and Southern California, four local flights from Cold Lake, two flights between Cold Lake and Thule, Greenland, and one local flight from Thule. More information about the ARCTAS mission, including details of the DC-8 instrument payload and an overview of the mission scientific objectives, is available at <http://www.espo.nasa.gov/arctas/>.

Two Caltech-CIMS instruments were flown aboard the DC-8 during ARCTAS: the single quadrupole (Crounse et al., 2006) and the triple quadrupole (identical to the instrument in the chamber). The triple quadrupole was operated exclusively in CID-MSMS mode while in flight. Both flight instruments monitored  $m/z=203$ , though the tandem MS did so for only five of the nine flights.

A subset of the  $m/z=203$  daughters ( $m/z=63$ ,  $m/z=85$ ,  $m/z=137$ ,  $m/z=203$ ) were measured by the tandem MS for the last five flights of summer ARCTAS. By assuming that the only source of  $m/z=203$  is ISOPOOH and IEPOX, we can infer ISOPOOH and IEPOX respective signals from the flight data. As discussed



in the text, ISOPOOH•CF<sub>3</sub>O<sup>-</sup> was determined to be the source of m/z=63 daughter ion in the chamber experiments. The m/z=183 daughter ion, used in the chamber study as the fingerprint for IEPOX, was not measured during flight. Signal potentially attributable to IEPOX was determined for the flight data by removing the ISOPOOH contribution to the m/z=137 daughter ion signal, using the relationship between the m203 daughters derived from an OH + isoprene chamber experiment where the aircraft tandem MS instrument monitored all relevant m203 daughter masses:

$$(m/z = 203 \rightarrow 137) = (1.49 \pm 0.03) \times (m/z = 203 \rightarrow 63) + (1.43 \pm 0.03) \times (m/z = 203 \rightarrow 183)$$

where the coefficients and 2 $\sigma$  uncertainties (of the fit) are obtained from a multivariate linear regression.

Both tandem MS instruments sampled from the same chamber during this calibration experiment. By determining the IEPOX contribution to the m/z = 203  $\rightarrow$  137 ion signal in terms of the m/z = 203  $\rightarrow$  183 ion signal and also determining the scaling factor between the m/z = 203  $\rightarrow$  183 ion signals of the two instruments, the IEPOX sensitivity used for the chamber experiments can be applied to the ARCTAS data to obtain in situ IEPOX mixing ratios. Determination of in situ ISOPOOH mixing ratios required only obtaining the scaling factor between the m/z = 203  $\rightarrow$  63 ion signals of the two instruments before applying the ISOPOOH sensitivity used for the chamber experiments.

The possibility of mass interferences at m/z=203 in situ precludes the definitive attribution of the m/z=203 signal, in its entirety, to ISOPOOH and IEPOX. One known interferent at m/z=203 was identified from data not yet published from a chamber study of the OH oxidation of 2-Methyl-3-Buten-2-ol (MBO). The MBO oxidation product at m/z=203 yields no daughter ion at m/z=63 but does yield a daughter ion mass at m/z=137. Consequently, the presence of MBO oxidation products may influence the calculated ARCTAS IEPOX mixing ratios, but not the ARCTAS ISOPOOH mixing ratios. We currently know of no mass interferences for the m/z=63 daughter ion of m/z=203. In recognition of the potential for interferences, however, the ARCTAS data for ISOPOOH and IEPOX will be hereafter referred to as ISOPOOH<sub>flt</sub> and IEPOX<sub>flt</sub>, respectively, to distinguish the in situ data from the chamber data.

Both ISOPOOH<sub>flt</sub> and IEPOX<sub>flt</sub> were observed during four of the last five ARCTAS flights, as shown in Fig. B.8. All of the ISOPOOH<sub>flt</sub> and most of the IEPOX<sub>flt</sub> were detected below 1.5 km above ground level (Fig. B.9). The highest mixing ratios of both ISOPOOH<sub>flt</sub> and IEPOX<sub>flt</sub> during the mission, 1.2 ppbv and 3.4 ppbv, respectively, were encountered while flying 0.7 km above ground level at 40.7319°

N, 122.0492° W. Signal for ISOPOOH<sub>flt</sub> was always accompanied by IEPOX<sub>flt</sub> signal, but IEPOX<sub>flt</sub> was observed without concurrent ISOPOOH<sub>flt</sub> signal, consistent with IEPOX having a significantly longer lifetime than ISOPOOH.

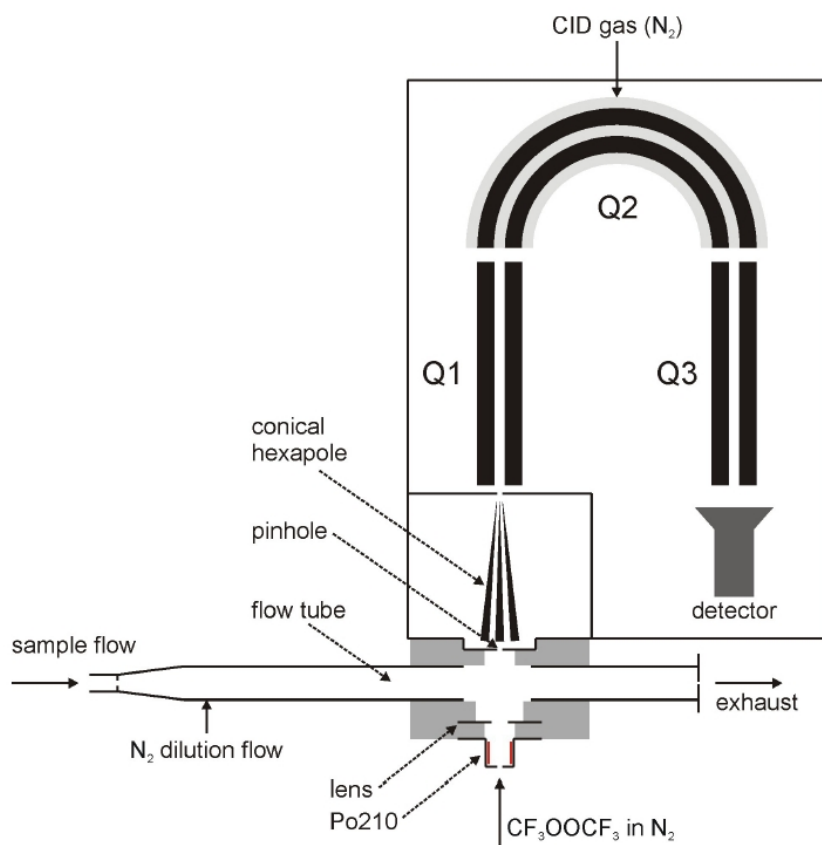


Figure B.1: Schematic diagram of the Caltech Chemical Ionization Mass Spectrometer (CIMS)

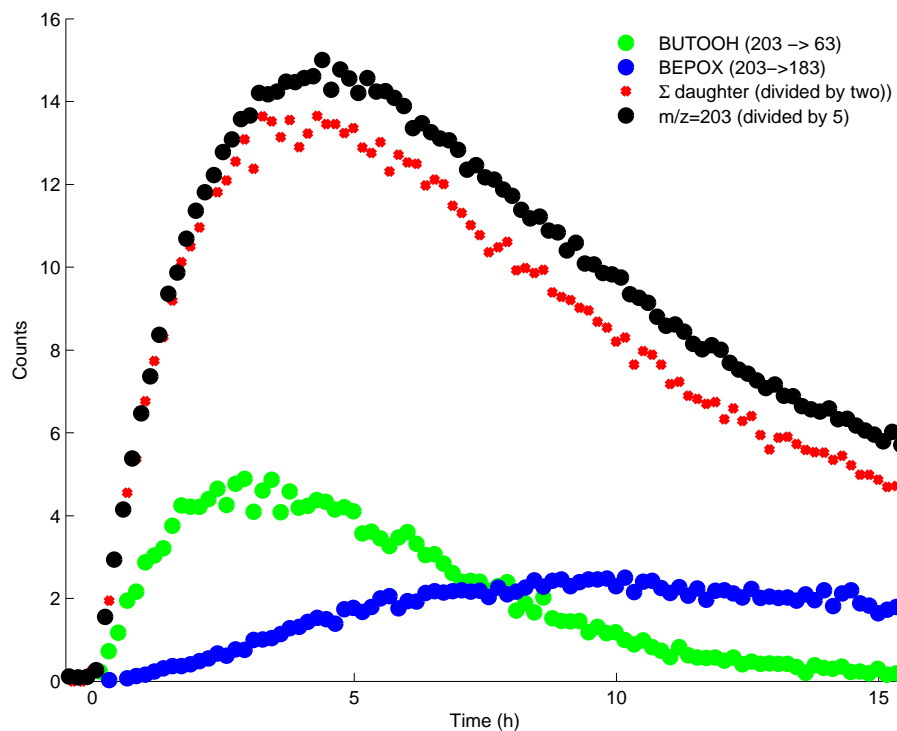


Figure B.2: Following the time when the photolysis of  $\text{H}_2\text{O}_2$  (initially 1 ppmv) begins ( $t = 0$ ), we observe the formation of BUTOOH and then BEPOX together detected at  $m/z=189$  (black). Tandem mass spectroscopy provides for separation of the  $m/z=189$  signal: BUTOOH (green) is observed as the  $m/z=63$  daughter while BEPOX (blue) is observed as the  $m/z=169$  daughter. The sum of the measurable daughters of  $m/z=189$  (red) correctly captures the profile of the parent signal.

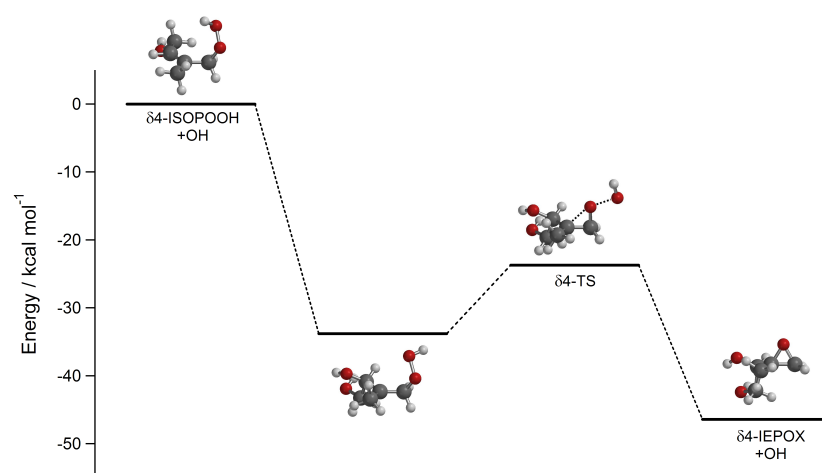


Figure B.3: Relative energies of the B3LYP/cc-pVTZ optimized geometries for the formation of  $\delta 4$ -IEPOX from  $\delta 4$ -ISOPPOOH

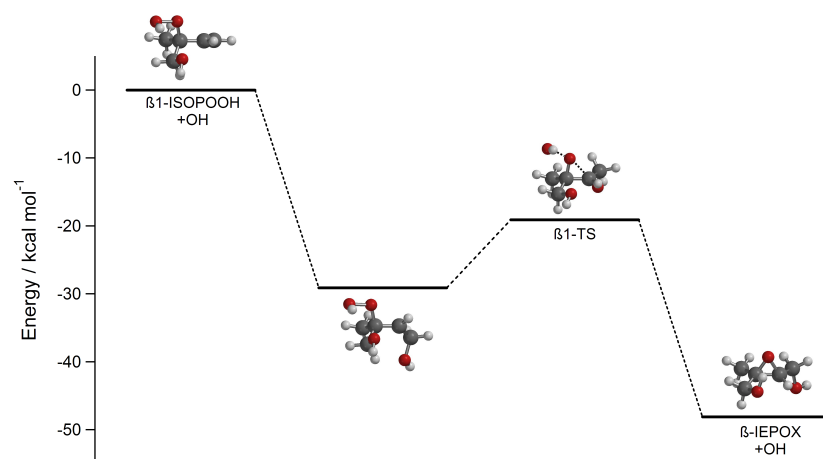


Figure B.4: Relative energies of the B3LYP/cc-pVTZ optimized geometries for the formation of  $\beta$ -IEPOX from  $\beta$ 1-ISOPPOOH

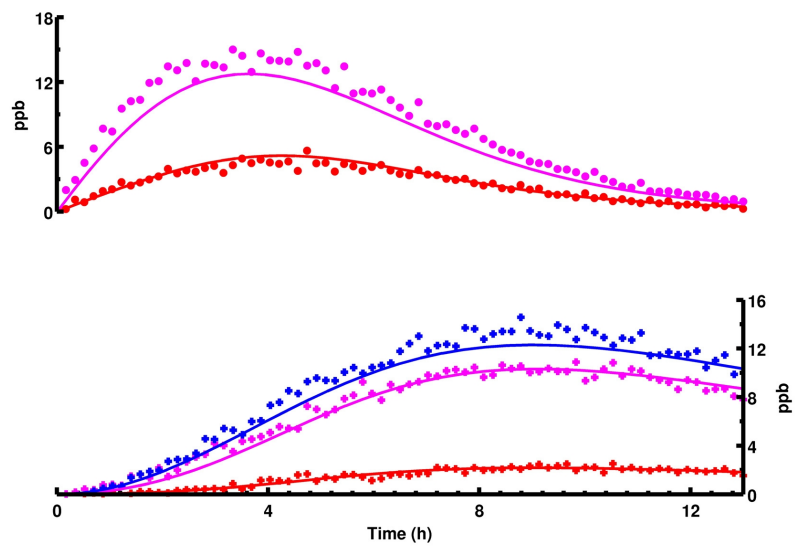


Figure B.5: Same as Fig. 3.4 for Experiment 1

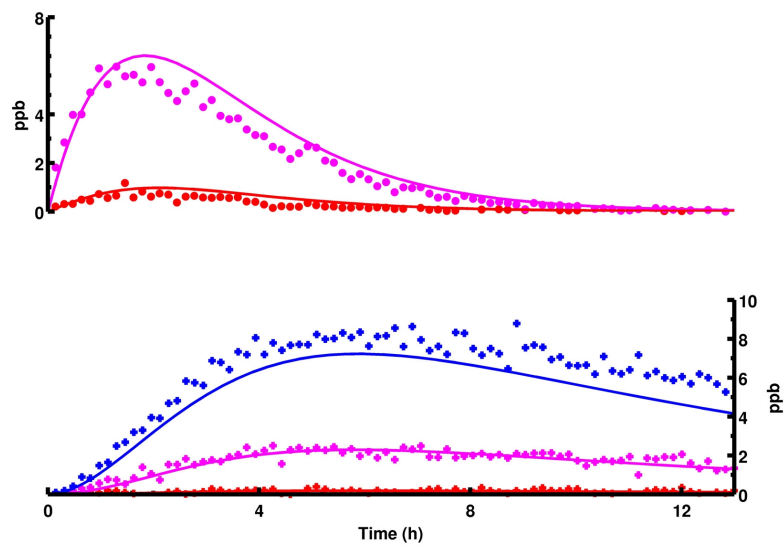


Figure B.6: Same as Fig. 3.4 for Experiment 3



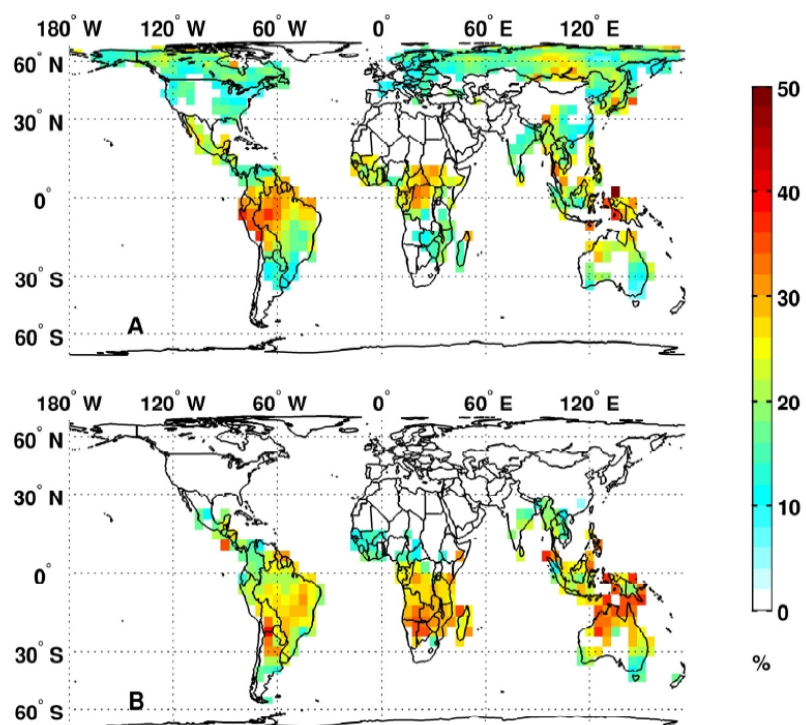


Figure B.7: Modeled yield of IEPOX from the reaction of isoprene + OH in the planetary boundary layer. Grid cells where isoprene mixing ratio is lower than 50 pptv are not shown.

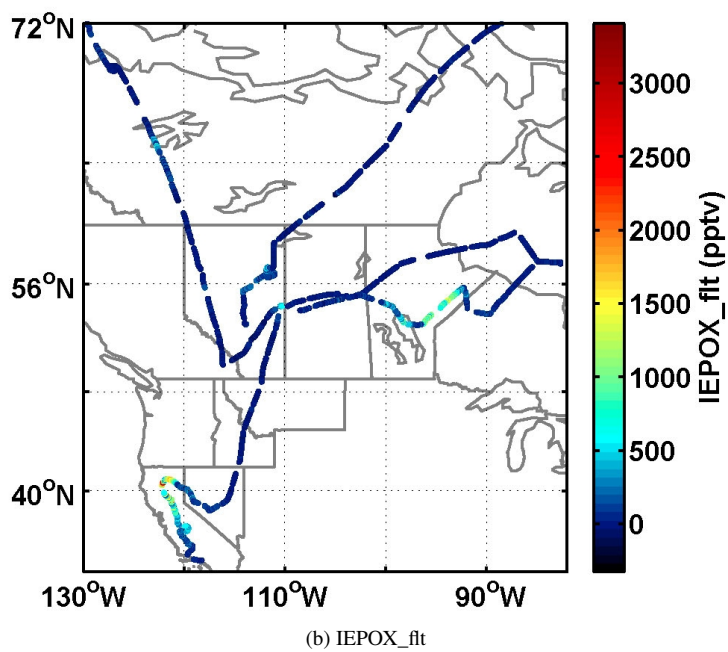
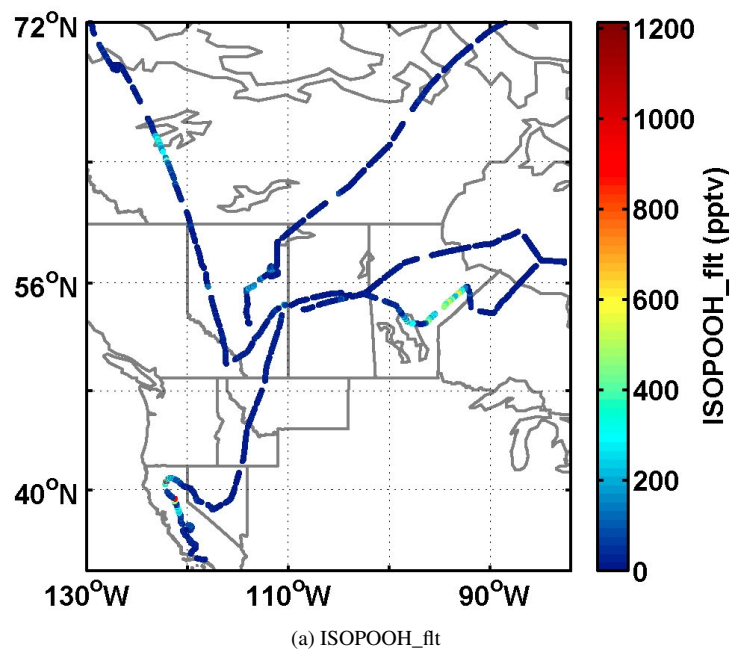


Figure B.8: Flight tracks for 2008 summer ARCTAS flights on July 5th, 8th, 10th, and 12th indicating the location of data and the mixing ratio for ISOPOOH\_fit and IEPOX\_fit

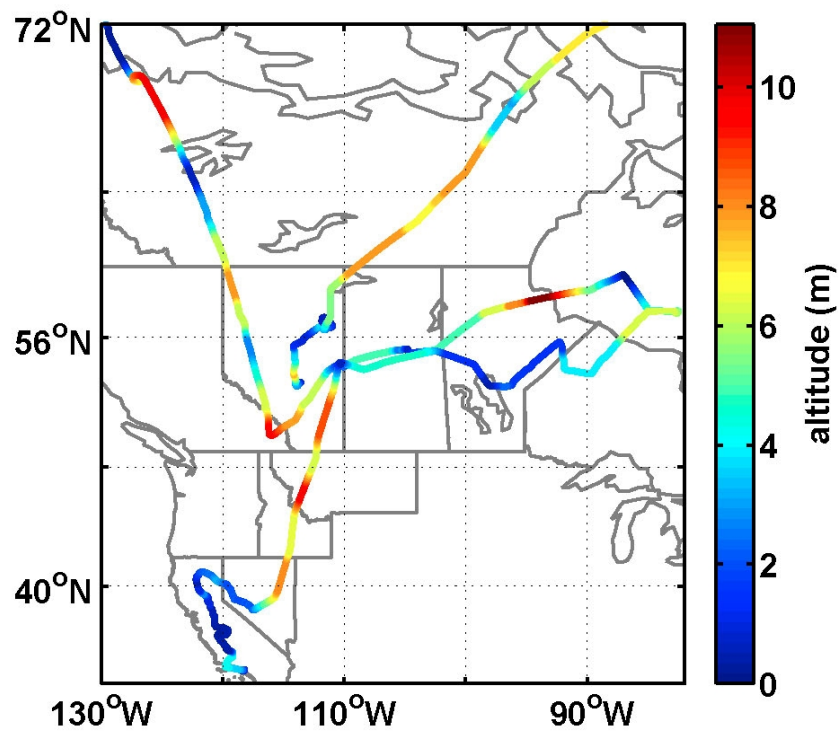


Figure B.9: Flight tracks for 2008 summer ARCTAS flights on July 5th, 8th, 10th, and 12th with color indicating the altitude of the DC-8 aircraft

Table B.1: Initial conditions (in ppbv)

Experiment	Isoprene	$\text{H}^{18}\text{O}^{18}\text{OH}$	$\text{H}^{18}\text{O}^{16}\text{OH}$	$\text{H}^{16}\text{O}^{16}\text{OH}$	$\text{NO}_x$
Exp 1	70	1700	57.2	3.5	1.3
Exp 2	23.5	1750	58	3.76	0.77
Exp 3	20.9	2860	94	5.9	0.1

Table B.2: Theoretical weighted average dipole moments ( $\mu$ ) and polarizabilities ( $\alpha$ ) for conformers with abundance greater than 1%. *Cis* and *trans* refer to the position of the CH<sub>2</sub>OH group with respect to the plane of the oxirane.

Compound	$\mu$ (D)	$\alpha(\text{\AA}^3)$
$\beta$ -IEPOX ( <i>cis</i> )	2.47	8.98
$\beta$ -IEPOX ( <i>trans</i> )	1.00	9.01
$\delta$ 1-IEPOX	2.39	9.98
$\delta$ 4-IEPOX	2.30	8.93
$\beta$ 1-ISOPPOOH	2.19	9.44
$\beta$ 4-ISOPPOOH	2.20	9.44
$\delta$ 1-ISOPPOOH	2.85	9.63
$\delta$ 4-ISOPPOOH	3.34	9.66
BEPOX ( <i>cis</i> )	2.71	7.52
BEPOX ( <i>trans</i> )	0.55	7.47
(2Z) - but-2-ene-1,4-diol	2.93	7.28
but-3-ene-1,2-diol	2.29	7.21
2-methylbut-3-ene-1,2-diol	2.01	8.79
3-methylbut-3-ene-1,2-diol	2.30	8.76
(2Z)-2-methylbut-2-ene-1,4-diol	2.98	8.98

Table B.3: Comparison of the experimental and theoretical calibration for three representative compounds

	Theoretical calibration (normalized counts/pptv)	Experimental calibration (normalized counts/pptv)
BEPOX ( <i>cis</i> )	$2.0 \times 10^{-4}$	$2.0 \times 10^{-4}$
Hydroxyacetone	$2.7 \times 10^{-4}$	$2.6 \times 10^{-4}$
Glycolaldehyde	$2.2 \times 10^{-4}$	$2.3 \times 10^{-4}$

Table B.4: Calculated relative energies (kcal/mol) of the stationary points in the  $\beta$ 4- ISOPOOH to  $\beta$ -IEPOX (reaction (3.2a) and Fig. 3.5)

	B3LYP/6-31G(d)	B3LYP/cc-pVTZ// B3LYP/6-31G(d)	B3LYP/cc-pVTZ
$\beta$ 4-ISOPOOH	0	0	0
Alkyl radical	-32.9	-30.4	-30.6
$\beta$ 4-TS	-21.1	-19.7	-20.0
$\beta$ 4-IEPOX	-47.8	-47.4	-47.4

Table B.5: Calculated relative energies (kcal/mol) of the stationary points in the  $\beta$ 4- ISOPOOH to  $\beta$ -IEPOX (reaction (3.2a) and Fig. 3.5). All single point energies on the B3LYP/cc-pVTZ optimized geometries

	RMP2/ cc-pVTZ	RMP2/ aug-cc-pVTZ	MP2-F12b/ VDZ-F12	CCSD(T)-F12b/ VDZ-F12
$\beta$ 4-ISOPOOH	0	0	0	0
Alkyl radical	-33.6	-34.1	-34.8	-30.9
$\beta$ 4-TS	-28.7	-31.3	-31.8	-18.2
$\beta$ 4-IEPOX	-54.1	-54.6	-55.5	-50.9



Table B.6: Calculated relative energies (kcal/mol) of the stationary points in the  $\delta 4$ - ISOPOOH to  $\delta$ -IEPOX (reaction (3.2b) and Fig. B.3)

	B3LYP/6-31G(d)	B3LYP/cc-pVTZ// B3LYP/6-31G(d)	B3LYP/cc-pVTZ
$\delta 4$ -ISOPOOH	0	0	0
Alkyl radical	-37.4	-33.9	-33.8
$\delta 4$ -TS	-25.9	-23.7	-23.7
$\delta 4$ -IEPOX	-48.1	-46.5	-46.4

Table B.7: Calculated relative energies (kcal/mol) of the stationary points in the  $\beta$ 1- ISOPOOH to  $\beta$ -IEPOX (reaction (3.2a) analog and Fig. B.4)

	B3LYP/6-31G(d)	B3LYP/cc-pVTZ// B3LYP/6-31G(d)	B3LYP/cc-pVTZ
$\beta$ 1-ISOPOOH	0	0	0
Alkyl radical	-31.8	-29.1	-29.1
$\beta$ 1-TS	-20.6	-19.0	-19.1
$\beta$ -IEPOX	-48.8	-48.2	-48.1

Table B.8: Isomers of IEPOX previously observed in the aerosol phase

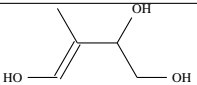
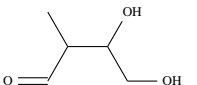
Possible isomer	Example	Incompatibility with the measurements
Alkene triol		Alkene triol formation has been reported in the aerosol phase . Proposed formation schemes involve enol/ketone equilibrium with dihydroxycarbonyl (Surratt et al., 2006) or acid catalyzed rearrangement of dihydroxyepoxide (Wang et al., 2005). In both mechanisms, formation of alkene triols requires a solvent. The proposed mechanisms cannot take place in the gas-phase. Furthermore, such a compound features a double bond and thus is not consistent with the observed lifetime of the second generation product.
Dihydroxycarbonyl		Formation of isobaric dihydroxycarbonyl has previously been proposed through a keto/enol mechanism with the previous isomer (Surratt et al., 2006). CIMS has been shown to be sensitive to this class of compounds (Paulot et al., 2009a). CID of hydroxyacetone and glycolaldehyde standards show a loss of $\text{CF}_3\text{O}^-$ ( $m/z=85$ ) exclusively with no measurable loss of HF (20 a.m.u.) or $\text{FCO}_2^-$ (fragment at $m/z=63$ ). Therefore they cannot account for the formation of daughter $m/z=183$ which is specific to IEPOX.

Table B.9: Low NO<sub>x</sub> mechanism for the photooxidation of isoprene

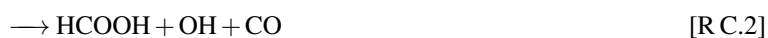
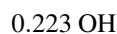
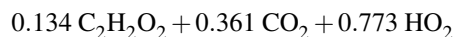
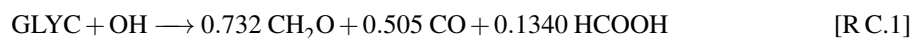
					$A (\times 10^{11})$ $\text{cm}^3 \text{molec}^{-1} \text{s}^{-1}$	$-E_a/R$ K
ISOP	+	OH	→	ISOPOO	2.7	390
ISOPOO	+	HO <sub>2</sub>	→	0.880 ISOPOOH + 0.120 OH + 0.047 MACR 0.073 MVK + 0.120 HO <sub>2</sub> + 0.120 CH <sub>2</sub> O	0.074	700
ISOPOOH	+	OH	→	IEPOX + OH	1.9	390
IEPOX	+	OH	→	0.700 ISOPOO + 0.300 HC5 + 0.300 OH	1.9	390
IEPOX	+	OH	→	IEPOXOO	5.78	-400
IEPOXOO	+	HO <sub>2</sub>	→	0.725 HAC + 0.275 GLYC + 0.275 GLYX 0.275 MGLY + 1.125 OH + 0.825 HO <sub>2</sub> 0.200 CO <sub>2</sub> + 0.375 CH <sub>2</sub> O + 0.074 HCOOH + 0.251 CO	0.074 0.074	700 700

## Appendix C

# Importance of secondary sources in the atmospheric budgets of formic and acetic acids

### C.1 Yield of formic and acetic acids from the oxidation of glycolaldehyde and hydroxyacetone by OH

The photooxidation of glycolaldehyde yields FA (Butkovskaya et al., 2006a). The yield of FA decreases while the yield of  $\text{CH}_2\text{O}$  increases as temperature increases. This is likely related to the channel  $\text{CO} + \text{HCOOH} + \text{OH}$  ([R C.1]) since the increased production of FA is accompanied by an increased production of OH. To simplify the representation of this reaction, we divide the oxidation of glycolaldehyde by OH into two different pathways



The branching ratio between the pathways ([R C.1]) and ([R C.2]) is calculated using the measured yield of  $\text{CH}_2\text{O}$  and  $\text{HCOOH}$  at different temperatures:  $Y_1 = 1 - 5.01 \times 10^{-6} \times \exp(\frac{2612}{T})$ .

FA and AA are also formed in the photooxidation of hydroxyacetone (Butkovskaya et al., 2006b). The yields of FA and AA are obtained by assuming  $Y_{\text{FA}} = Y_{\text{AA}}$  and  $Y_{\text{FA}} + Y_{\text{AA}} + Y_{\text{C}_3\text{H}_4\text{O}_2} = 1$  which yields

$$\beta(T) = Y_{\text{FA}} + Y_{\text{AA}} = 2.63 \times 10^{-3} \times \exp(1206/T) \quad (\text{C.1})$$

## C.2 Retrieval of FA by ground FTS

### C.2.1 Method

For all stations but Thule and La Réunion, FA is retrieved from spectra using GFIT (Wunch et al., 2010). For Thule (Hannigan et al., 2009) and La Réunion (Senten et al., 2008), FA is retrieved using SFIT2 (Rinsland et al., 1998). Both retrieval methods consist of a “forward model”, which computes an atmospheric transmittance spectrum for a prescribed set of conditions, and an “inverse method” which compares each measured spectrum with the calculation, and decides how best to modify the a priori profile to achieve a better match. GFIT scales the a priori profile via a non-linear least-squares spectral fitting algorithm. SFIT2 enables the retrieval of a vertical profile by the use of the optimal estimation method (Rodgers, 2000). However, in the case of FA, the degrees of freedom of the signal are close to one, such that the essential result is the total column, as for GFIT.

The a priori altitude, pressure, temperature and specific humidity profiles used in GFIT and SFIT2 are from NCEP/NCAR analysis product (Kalnay et al., 1996) with the exception of the cruises in the Atlantic Ocean. The window used to retrieve FA is centered at  $1106.32 \text{ cm}^{-1}$  with a width of  $6.75 \text{ cm}^{-1}$ . For La Réunion, a smaller window ( $1102.75 - 1106.4 \text{ cm}^{-1}$ ) is used to avoid the strong water band at  $1106.7 \text{ cm}^{-1}$ .

Interfering gases are  $\text{H}_2\text{O}$ ,  $\text{O}_3$ ,  $\text{HDO}$ ,  $\text{CH}_4$ ,  $\text{NH}_3$ ,  $\text{CCl}_2\text{F}_2$  and  $\text{CHClF}_2$  (+  $\text{H}_2^{18}\text{O}$ ,  $\text{H}_2^{17}\text{O}$ ,  $^{16}\text{O}^{16}\text{O}^{18}\text{O}$  for La Réunion). For La Réunion, the profile of  $\text{H}_2\text{O}$ ,  $\text{O}_3$ ,  $\text{HDO}$ ,  $\text{CCl}_2\text{F}_2$  and  $\text{CHClF}_2$  is first retrieved using dedicated windows for each target molecule. Their profiles are then used to retrieve FA.

The FA retrieval is especially sensitive to the  $\text{H}_2\text{O}$  and  $\text{O}_3$  profiles. We find that small modifications of the water spectroscopy in the FA window reduces the residuals. These modifications are:

- increase in the pressure shift from  $-0.0175$  to  $-0.0210 \text{ cm}^{-1}/\text{atm}$
- increase in the width from  $0.061$  to  $0.062 \text{ cm}^{-1}/\text{atm}$
- increase in the temperature dependence of the width from  $0.29$  to  $0.45$ .

These modifications were applied in the retrieval at Barcroft, Bremen, Paramaribo and Wollongong as well as for the cruises.

For the cruises, we use measured H<sub>2</sub>O and O<sub>3</sub> vertical profiles over the ship by balloon-borne radio and ozone sonde.

For Paramaribo, the O<sub>3</sub> profile is inferred from Shadoz measurements at the Paramaribo station (Thompson et al., 2003) combined with an ACE-FTS climatology.

For Thule, H<sub>2</sub>O is retrieved by scaling H<sub>2</sub>O a priori profile. O<sub>3</sub> and HCOOH are retrieved simultaneously.

For Wollongong, O<sub>3</sub> profiles are derived from monthly mean HALOE data (Russell et al., 1993).

## C.2.2 Error analysis

### C.2.2.1 Error in the spectroscopy

The FA Q branch line intensity has an uncertainty of  $\sim 7\%$  (Vander Auwera et al., 2007) which translates into a  $\sim 7\%$  error in the retrieved FA total column. Fig. C.1 illustrates the dependence of the retrieved FA at Paramaribo on the window used to retrieve FA (Table C.1). The choice of the spectral microwindow used to retrieve FA could result in a systematic bias in the FA total column as large as  $\sim \pm 2.7 \times 10^{15}$  molec/cm<sup>2</sup>.

### C.2.2.2 Error in FA profile

Fig. C.2 illustrates the effect of the a priori FA vertical profile (Fig. C.3) on the retrieved FA total column at Paramaribo. FA retrieval at Barcroft, Bremen, Paramaribo, Thule and Wollongong as well as the Atlantic cruises use the FA vertical profile from the ATMOS mission as a priori. This profile assumes most FA is located in the boundary layer, i.e., that FA total column is driven by local sources. In contrast, the FA a priori vertical profile used in La Réunion (from PEM-tropics A (Hoell et al., 1999) and ACE-FTS (González Abad et al., 2009)) assumes that most FA peaks in the free troposphere, i.e., that FA total column is driven by transport. At Paramaribo, the modeled FA vertical profile shows evidence of both transport and local sources. The choice of a priori profile results in an uncertainty of  $\sim 17\%$  in the retrieved FA profile.

The overall uncertainty is thus  $\sim 19\%$  with a systematic bias up to  $\pm 2.7 \times 10^{15}$  molec/cm<sup>2</sup>.

Table C.1: Windows used to retrieve FA

	Center ( $\text{cm}^{-1}$ )	Width ( $\text{cm}^{-1}$ )	Interfering Chemical Species
P	1090.00	13.00	O <sub>3</sub> H <sub>2</sub> O HDO CCl <sub>2</sub> F <sub>2</sub> CHClF <sub>2</sub> CH <sub>4</sub> NH <sub>3</sub> CO <sub>2</sub> CH <sub>3</sub> OH CCl <sub>3</sub> F
Ps	1091.50	10.50	O <sub>3</sub> H <sub>2</sub> O HDO CCl <sub>2</sub> F <sub>2</sub> CHClF <sub>2</sub> CH <sub>4</sub> NH <sub>3</sub> CO <sub>2</sub> CH <sub>3</sub> OH CCl <sub>3</sub> F
Q	1106.32	6.75	O <sub>3</sub> H <sub>2</sub> O HDO CCl <sub>2</sub> F <sub>2</sub> CHClF <sub>2</sub> CH <sub>4</sub> NH <sub>3</sub>
Qs	1104.60	3.65	O <sub>3</sub> H <sub>2</sub> O HDO CCl <sub>2</sub> F <sub>2</sub> CHClF <sub>2</sub> CH <sub>4</sub> NH <sub>3</sub>
R	1221.00	12.00	O <sub>3</sub> H <sub>2</sub> O HDO CCl <sub>2</sub> F <sub>2</sub> CHClF <sub>2</sub> CH <sub>4</sub> NH <sub>3</sub> N <sub>2</sub> O
Rs	1119.00	8.00	O <sub>3</sub> H <sub>2</sub> O HDO CCl <sub>2</sub> F <sub>2</sub> CHClF <sub>2</sub> CH <sub>4</sub> NH <sub>3</sub> N <sub>2</sub> O



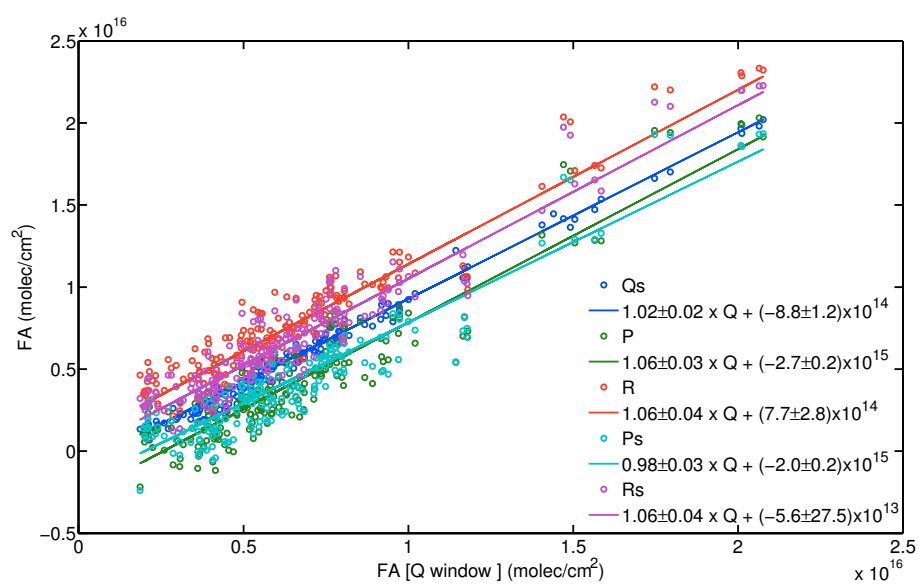


Figure C.1: Influence of the window on the retrieved FA total column at Paramaribo

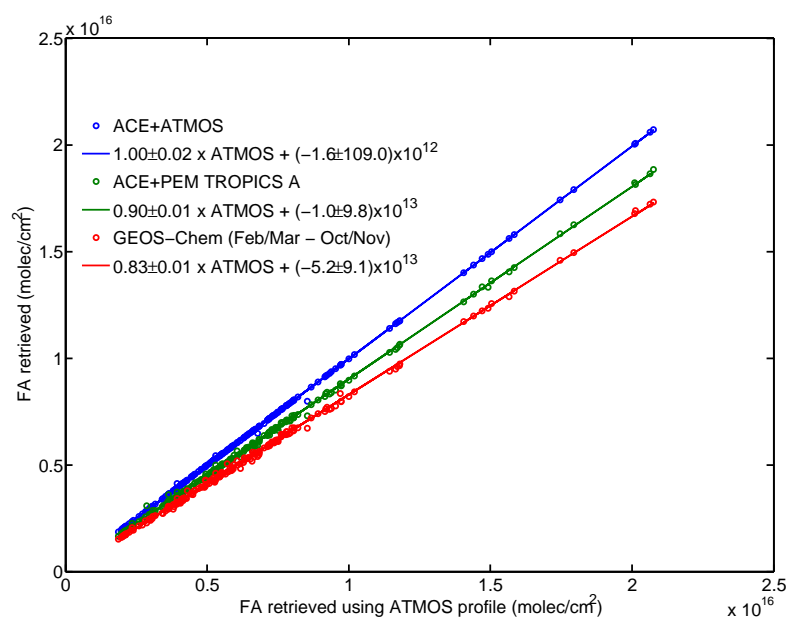


Figure C.2: Influence of FA a priori vertical profile on the retrieved FA total column at Paramaribo

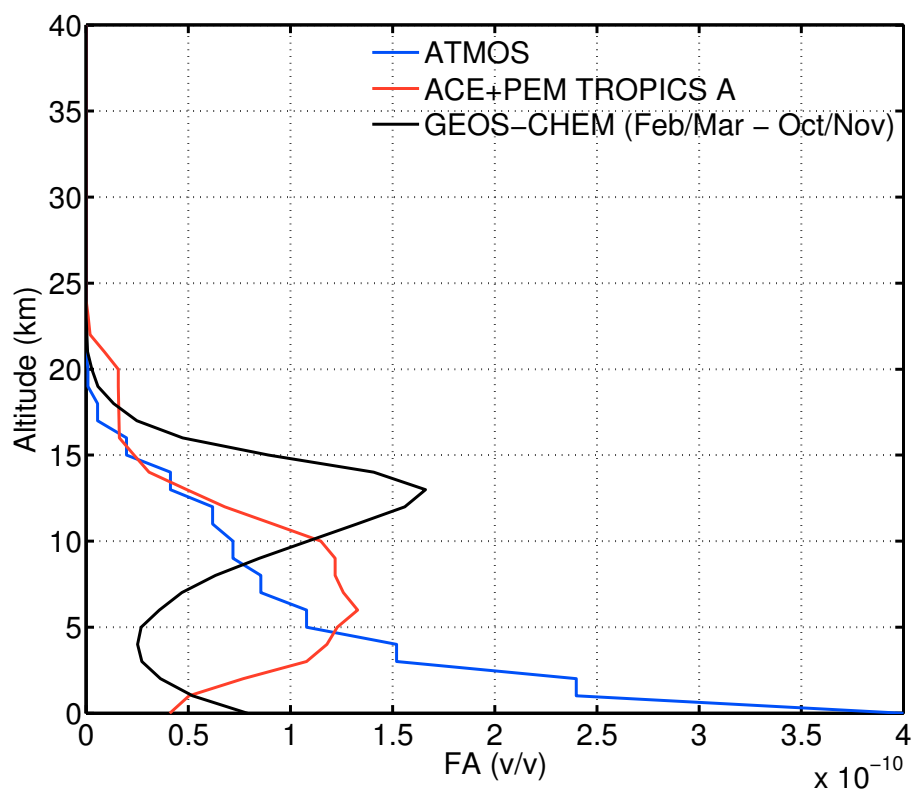


Figure C.3: A priori vertical profiles of FA used to retrieve FA total column

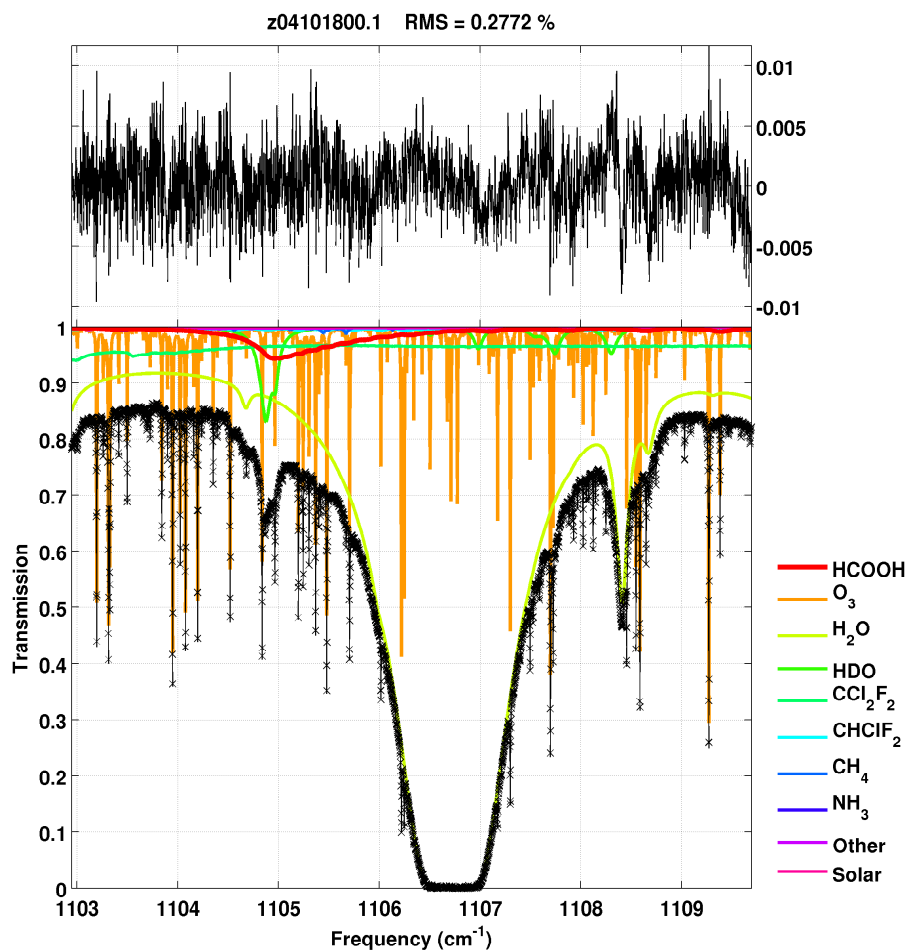


Figure C.4: An example of FA retrieval at Paramaribo using GFIT using the Q window. Top panel represents the fit residuals (computed–measured spectrum). Bottom panel represents the computed spectrum (black line), measured spectrum (black crosses), as well as the contribution of the different gases in the window used to retrieve FA. The weakness of FA absorption and the strong interference of H<sub>2</sub>O in the region make the retrieval of FA challenging. For this spectrum, the retrieved FA total column is  $1.02 \times 10^{16}$  molec/cm<sup>2</sup> ( $\pm 19\% \pm 2.7 \times 10^{15}$  molec/cm<sup>2</sup>).

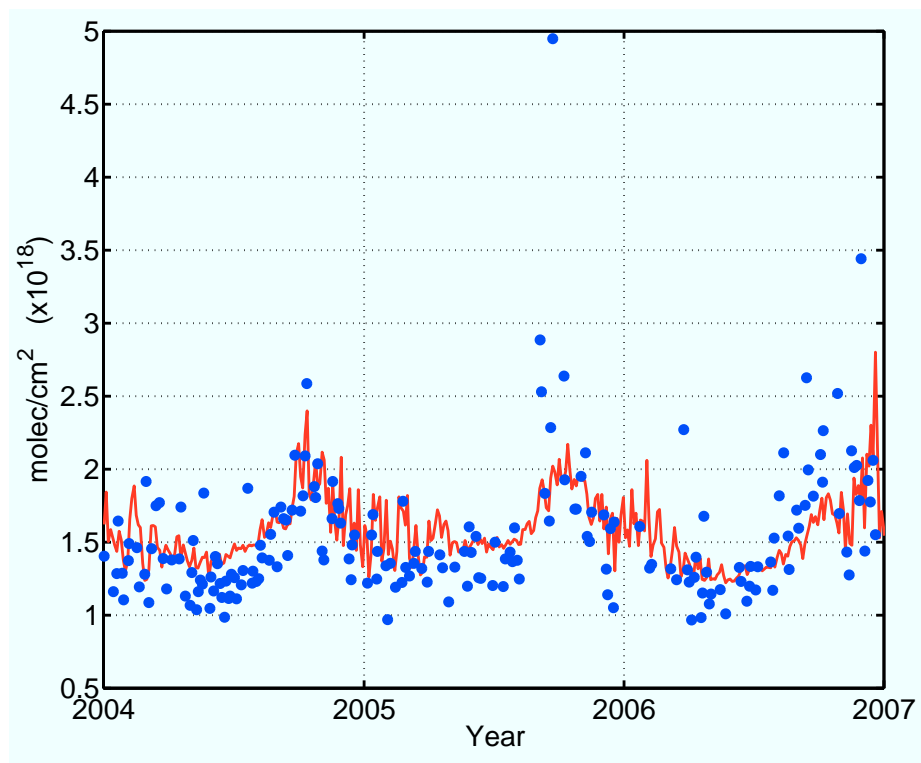


Figure C.5: Same as Fig. 3a for CO (Wollongong). Note the anomalously high CO at the end of 2007, reflecting intense biomass burning in the region.

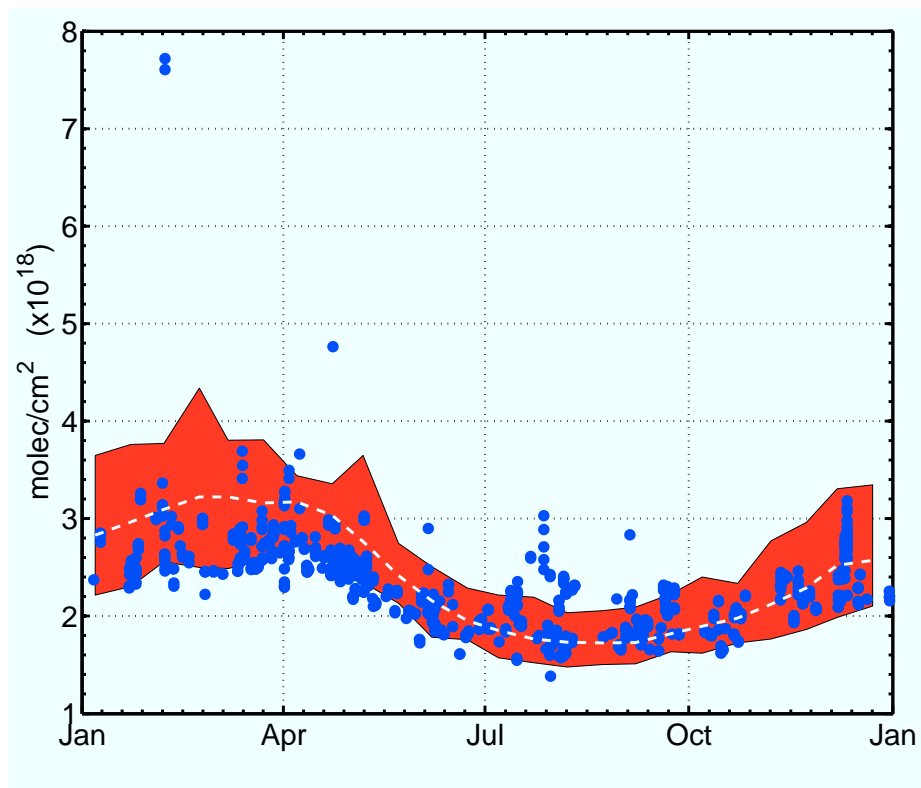


Figure C.6: Same as Fig. 4.4c for CO at Bremen

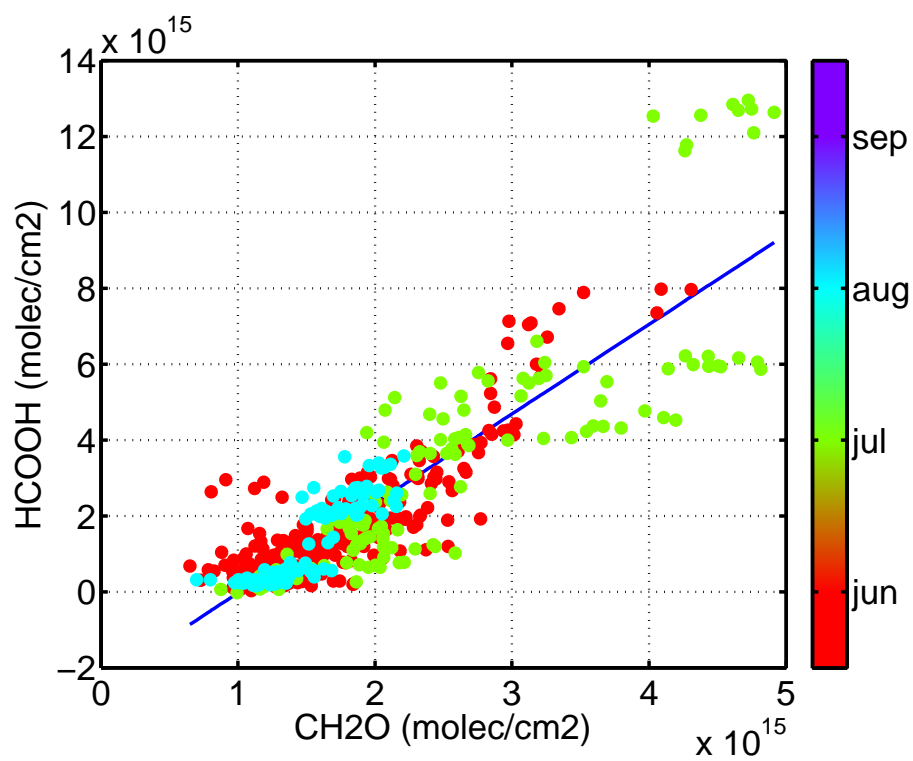


Figure C.7: Relationship between FA and CH<sub>2</sub>O at Barcroft ( $FA \simeq 2.3 \times CH_2O$ ,  $R^2 = 0.77$ )

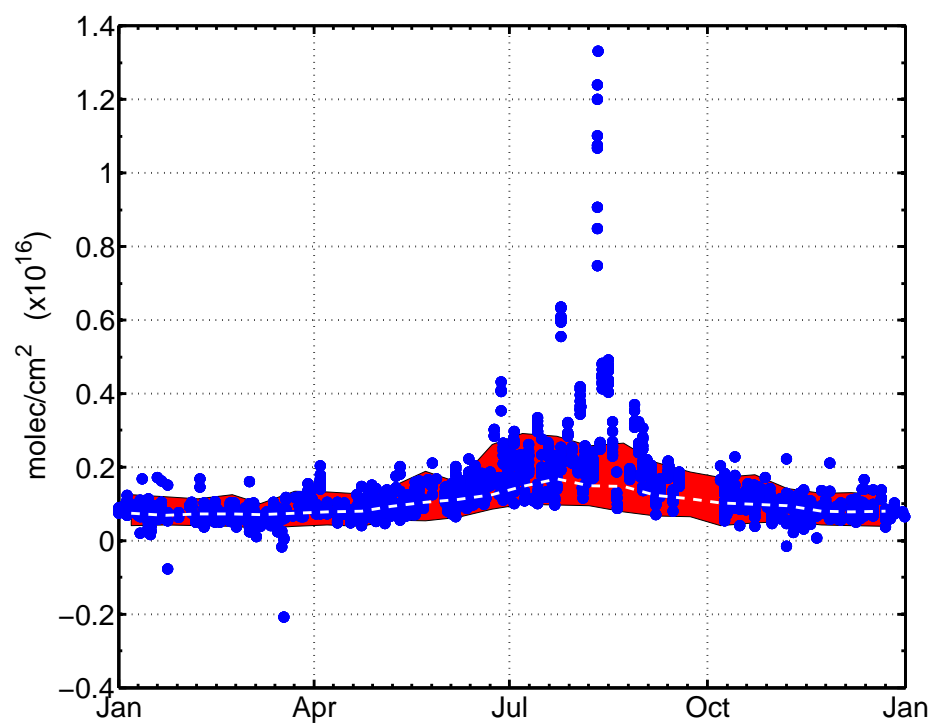


Figure C.8: Same as Fig. 4.4c for  $\text{CH}_2\text{O}$  at Barcroft



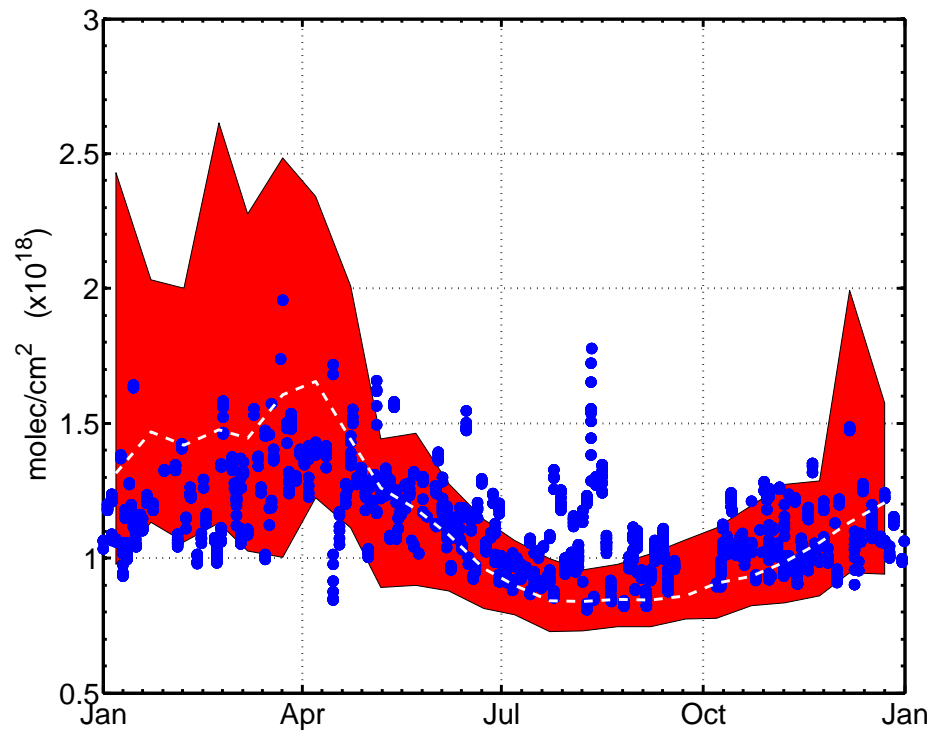


Figure C.9: Same as Fig. 4.4c for CO at Barcroft

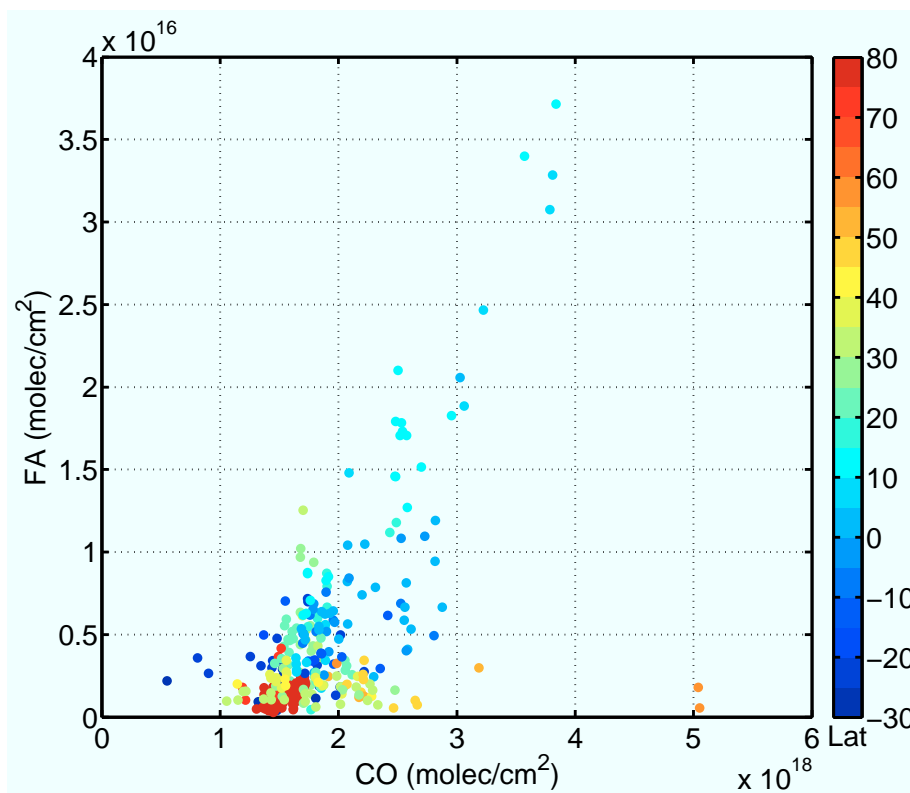


Figure C.10: Relationship between CO and FA total columns (molec/cm<sup>2</sup>) measured during cruises in the Atlantic Ocean

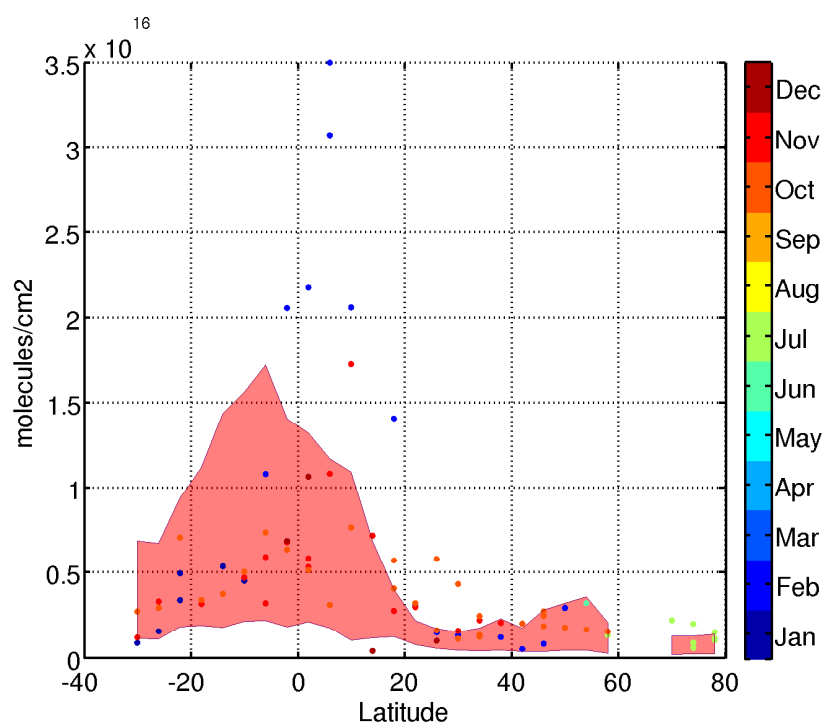


Figure C.11: Effect of a diffuse source of FA associated with aerosol aging on FA total column over the Atlantic (scenario R3). Color code same as Fig. 4.5

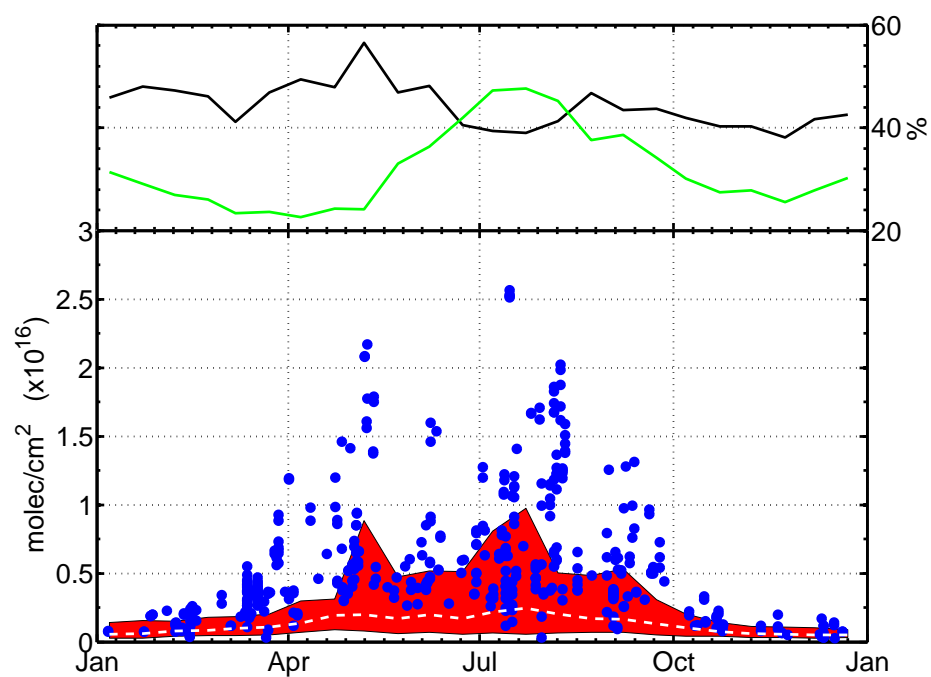


Figure C.12: Effect of a diffuse source of FA associated with aerosol aging on FA total column over Bremen. Color code same as Fig. 4.4b

Table C.2: Regional and global burden for FA (in %)

	Tropics (24°S – 24°N)	Mid latitudes (24°N – 76°N)	Polar regions (76°N – 90°N)	Global
Biomass burning	1.4	0.7	1.3	1.2
Biofuel	0.2	0.1	0.5	0.2
Terrestrial vegetation	2.6	2.4	2.4	2.4
Soil	2.0	1.1	3.3	2.0
Anthropogenic (Fossil fuel + Cattle)	0.6	0.3	7.0	1.7
Photooxidation (biogenic)	82.5	82.7	64.2	79.2
Photooxidation (Anthropogenic + Biomass)	10.7	12.7	21.3	13.3
Overall	58.9	22.4	17.8	10.7 Gmol

Table C.3: Regional and global burden for AA (in %)

	Tropics (24°S – 24°N)	Mid latitudes (76°S – 24°S)	(76°N – 24°N)	(90°S – 76°S)	Polar regions (76°N – 90°N)	Global
Biomass burning	12.3	6.0	8.2	3.7	6.7	10.2
Biofuel	3.6	1.5	12.1	0.7	9.7	4.7
Terrestrial vegetation	2.4	2.4	2.2	1.0	1.1	2.4
Soil	2.6	1.4	2.6	0.7	0.7	2.3
Anthropogenic	0.7	0.4	9.3	0.2	4.7	2.2
(Fossil fuel + Cattle)						
Photooxidation	77.2	86.5	64.2	91.1	74.4	76.9
(biogenic)						
Photooxidation	1.2	1.6	1.4	2.6	2.7	1.3
(Anthropogenic +Biomass)						
Overall	61.4	20.2	17.7	0.2	0.5	9.1 Gmol

Table C.4: Photochemical sources of FA and AA implemented in the GEOS-Chem chemical mechanisms. HC5: hydroxymethylbutenal (from isoprene), ISOP: isoprene, IEPOX: dihydroxyepoxide from isoprene photooxidation,  $\delta$  – ISOPN: organic nitrates from isoprene (1,4 and 4,1 additions), MACR: methacrolein, MBO: methylbutenol, MONX: lumped monoterpenes, MVK: methylvinylketone, PRPE: propene +  $\geq 4$ C alkene

PRPE + O <sub>3</sub>	→	0.148FA + 0.096AA	Assume 3:2 relationship between [CH <sub>3</sub> CHOO]* + HCHO channel and CH <sub>3</sub> CHO + [CH <sub>2</sub> OO]* channel Carter (2010)
ISOP + O <sub>3</sub>	→	0.204FA	Derived from Aschmann et al. (1996); Grosjean et al. (1993)
MVK + O <sub>3</sub>	→	0.352FA	Derived from Aschmann et al. (1996); Grosjean et al. (1993)
MACR + O <sub>3</sub>	→	0.326FA	Assumed to be similar to isoprene
HC <sub>5</sub> + O <sub>3</sub>	→	0.200FA	Carter (2010)
C <sub>2</sub> H <sub>4</sub> + O <sub>3</sub>	→	0.370FA	cf. Main text
MONX + O <sub>3</sub>	→	0.075FA + 0.080AA	Carrasco et al. (2007)
MBO + O <sub>3</sub>	→	0.300FA	Atkinson et al. (2006)
CH <sub>3</sub> C(O)O <sub>2</sub> + HO <sub>2</sub>	→	0.150AA	From the alcohol+carbonyl channel Lightfoot et al. (1992)
CH <sub>3</sub> C(O)O <sub>2</sub> + RO <sub>2</sub>	→	0.110AA	Hatakeyama et al. (1986)
C <sub>2</sub> H <sub>2</sub> + OH	→	0.4FA	Butkovskaya et al. (2006a)
GLYC + OH	→	$\alpha_1(T)FA + \alpha_2(T)AA$	Reactions ([R C.1]) and ([R C.2])
HAC + OH	→	$\beta(T)(FA + AA)$	Butkovskaya et al. (2006b)
IEPOX + OH + NO/HO <sub>2</sub>	→	0.074 FA	Reaction (C.1)
ISOPN $\delta^+$ OH + NO	→	0.310FA	Paulot et al. (2009b)
MACRN + OH + NO	→	0.08AA + 0.07FA	Paulot et al. (2009a)
MVKN + OH	→	0.650FA	Paulot et al. (2009a)

## Appendix D

# Impact of the isoprene photochemical cascade on tropical ozone

### D.1 Rate constant adjoint

The adjoint of the chemistry has been implemented in GEOS-Chem by Henze et al. (2007). Minor modifications are required to obtain the needed adjoint sensitivities for isoprene chemistry.

- Rate constant adjoint

$$\begin{aligned} Rate &= Rate \times SF && \text{forward} \\ \tilde{SF} &= \tilde{SF} + Rate \times \tilde{Rate} && \text{adjoint} \end{aligned}$$

- Isoprene nitrate (Recycling) adjoint

$$\begin{aligned} Rate_1 &= Rate \times Y \times SF && \text{forward} \\ Rate_2 &= Rate \times (1 - Y) \times SF && \text{forward} \\ \tilde{SF} &= \tilde{SF} + Y \times Rate \times (\tilde{Rate}_1 - \tilde{Rate}_2) && \text{adjoint} \end{aligned}$$



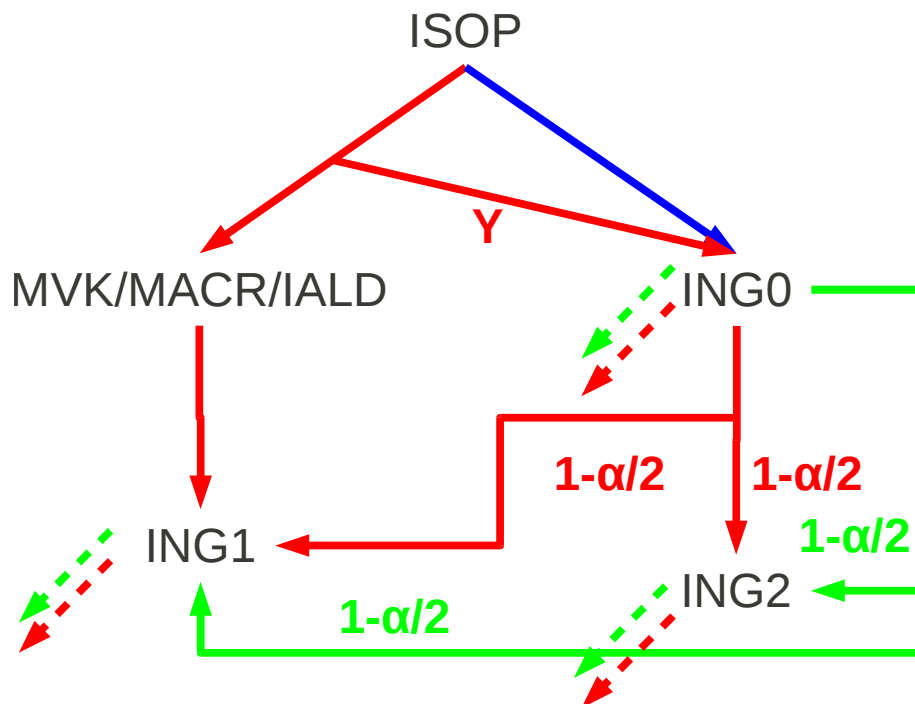


Figure D.1: Schematic representation of the isoprene nitrate photochemical cascade. Red arrows designate reaction with OH/NO, green arrows designate reaction with ozone and blue arrows represent NO<sub>3</sub> chemistry. Dashed arrows represent O<sub>x</sub> release. Y is the isoprene nitrate yield (ING<sub>0</sub>) and  $\alpha$  the fraction of NO<sub>x</sub> released in ING<sub>0</sub> oxidation by OH and ozone. MVK, MACR and IALD designate major second-generation products of isoprene oxidations under high NO<sub>x</sub> conditions.

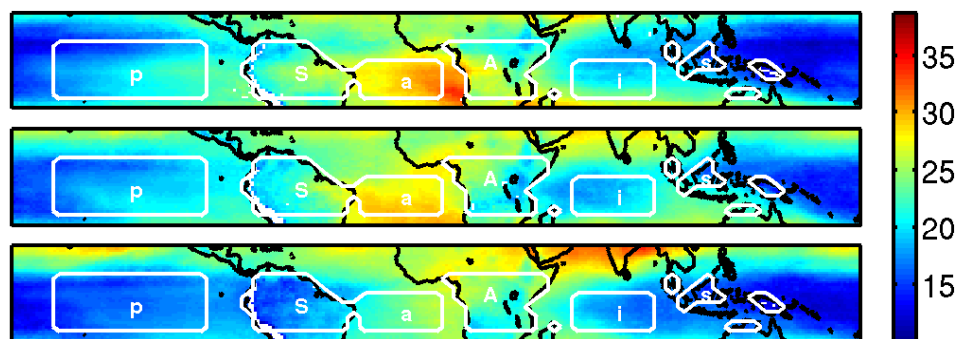


Figure D.2: OMI/MLS tropospheric total column ozone (Ziemke et al., 2006) in Dobson units. The different geographical regions used in the adjoint simulations are denoted by white contours. The tropical region extends from  $15^{\circ}\text{S}$  to  $7^{\circ}\text{N}$ . Top panel: June 2006–October 2006, middle panel: November 2006–February 2007, bottom panel: March 2007–May 2007

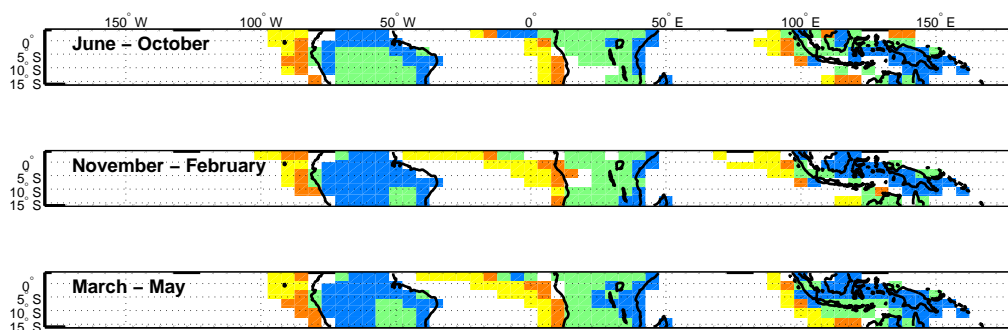


Figure D.3: K-means clustering analysis of the factors controlling  $\mathcal{D}_{\text{ING}}$  reveals important regional and seasonal differences. During periods of large biomass burning, the influence of the recycling /production and losses of secondary nitrate  $\text{ING}_1$  and  $\text{ING}_2$  is reinforced relative to the isoprene nitrate yield (blue cluster), as the formation of  $\text{ING}_0$  has a small effect on the budget of  $\text{NO}_x$ . Conversely in regions where the ratio of isoprene to  $\text{NO}_x$  is high (South America (B, C) and eastern South East Asia), a large fraction of  $\text{NO}_x$  is segregated in  $\text{ING}_0$ . This depresses OH and ozone formation, diminishing the fraction of  $\text{ING}_0$  oxidized locally. In these regions, the impact of isoprene nitrate chemistry on the local  $\text{NO}_x$  budget is primarily controlled by the yield of  $\text{ING}_0$ . The long range effect of isoprene nitrate chemistry on  $\text{NO}_y$  is solely controlled by  $\text{ING}_2$  (orange). The analysis was restricted to regions where  $\mathcal{D}_{\text{ING}}$  accounts for more than 5% of the total production/loss of  $\text{NO}_x$ .

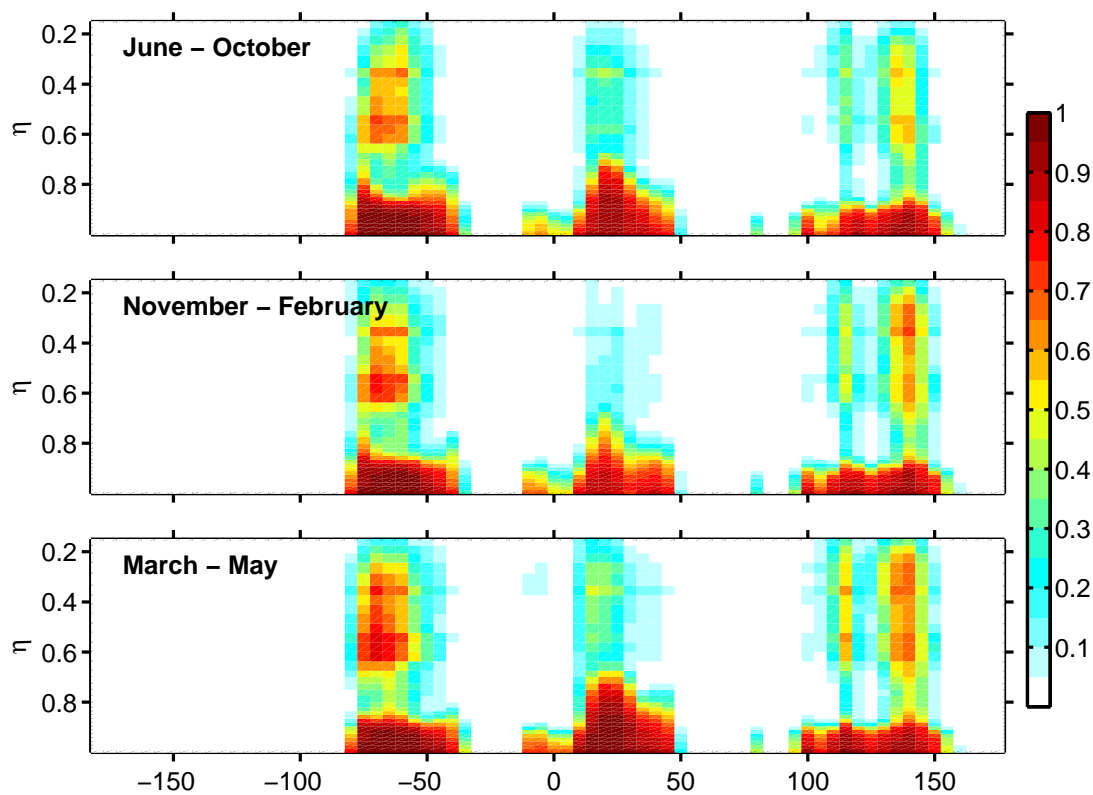


Figure D.4: Isoprene contributes significantly to the loss of OH even at high altitude. The color code indicates the ratio between the loss of OH through isoprene + OH and the loss of OH by isoprene and CO. A: June 2006–October 2006, B: November 2006–February 2007, C: March 2007–May 2007

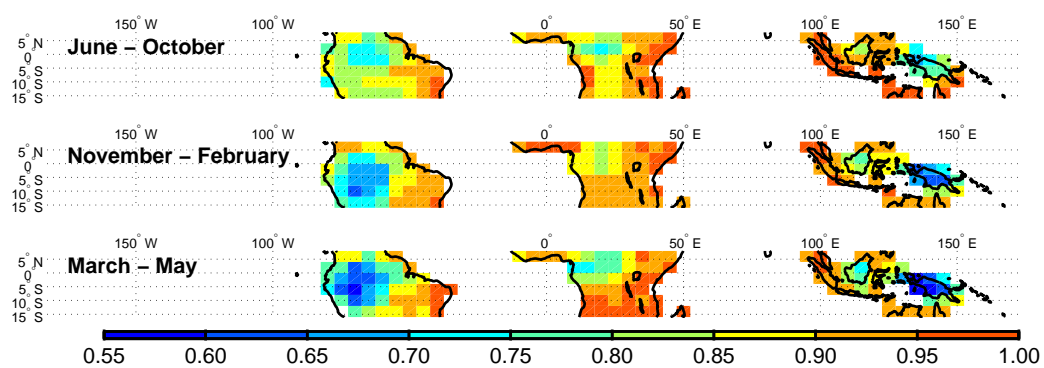


Figure D.5: Fraction of isoprene oxidized below 800 mbar

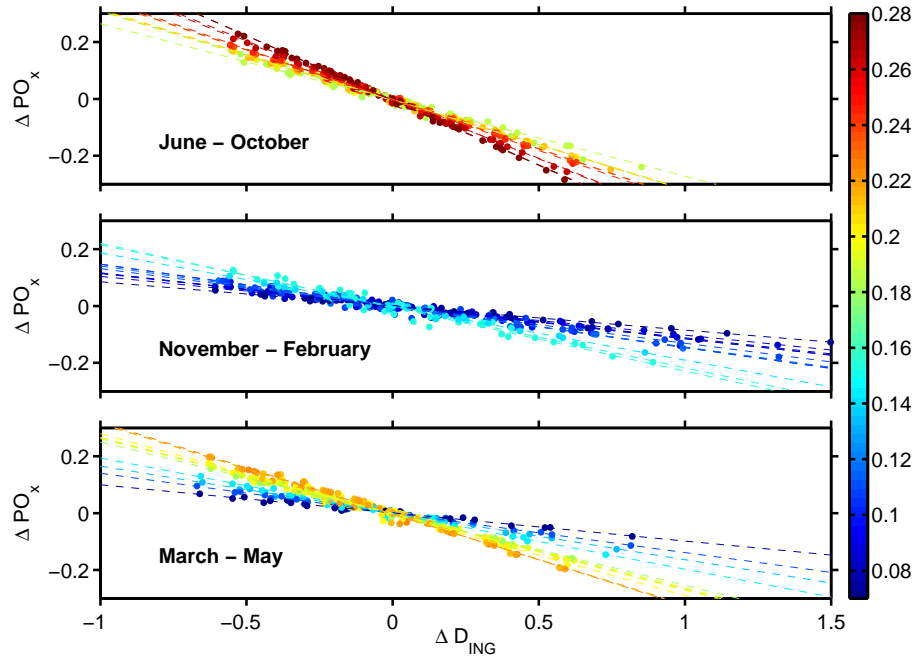


Figure D.6: Seasonal variations of the relationship between  $\mathcal{D}_{\text{ING}}$  and  $P_{\text{O}_x}$  over South America (A), Africa (B) and South East Asia (C) resulting from different representation of ING chemistry. Variations in  $\mathcal{D}_{\text{ING}}$  and  $P_{\text{O}_x}$  are normalized to the reference simulation ( $Y = 10\%$ ,  $\alpha = 50\%$  and default deposition). The linear fit for each month is indicated by a dashed line. The color code indicates the ratio between  $\mathcal{D}_{\text{ING}}$  and  $\mathcal{L}_{\text{NO}_x}$  in the reference run for each month.

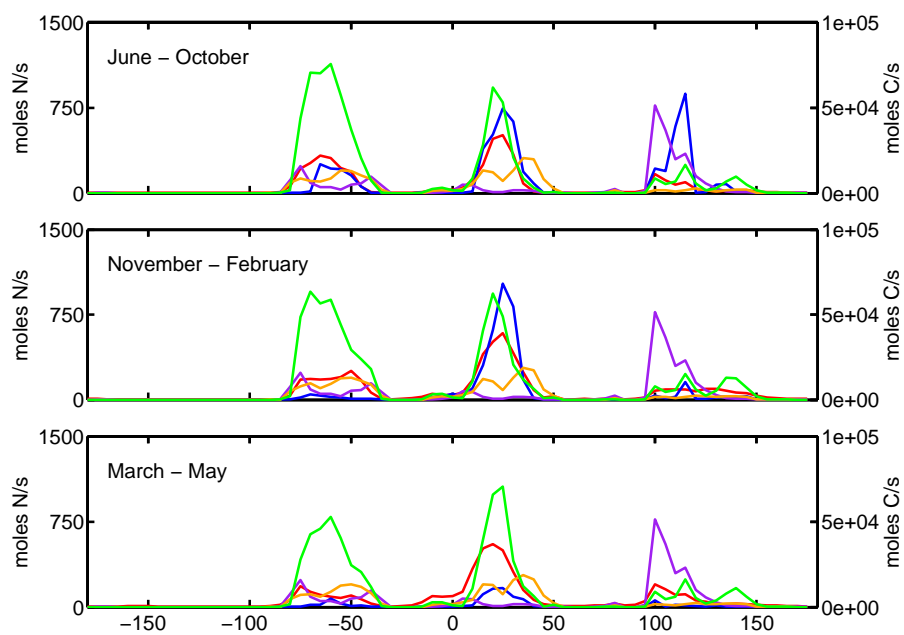


Figure D.7: Seasonal emissions of isoprene (green), lightning NO<sub>x</sub> (red), biomass burning NO<sub>x</sub> (blue, ×0.5), anthropogenic NO<sub>x</sub> (violet), soil NO<sub>x</sub> (orange).

Table D.1: Notations

$\frac{R_y}{R_x} \mathcal{S}_X^Y$	normalized sensitivity of mean tropospheric Y over the region $R_y$ to changes in X over the region $R_x$ . For photochemical processes, unless otherwise noted, $R_y$ extends from the surface to the free troposphere. $\frac{R_y}{R_x} \mathcal{S}_X^Y$ is expressed in %.
a	Atlantic ( $R_x, R_y$ )
A	Africa ( $R_x, R_y$ )
i	Indian ( $R_x, R_y$ )
p	Pacific ( $R_x, R_y$ )
s	South America ( $R_x, R_y$ )
S	Southeast Asia ( $R_x, R_y$ )
t	Tropics ( $R_x, R_y$ )
w	World ( $R_x, R_y$ )
$\mathcal{D}_{\text{ING}}$	net effect of ING chemistry on the $\text{NO}_x$ budget
$\mathcal{L}_{\text{NO}_x}$	Loss of $\text{NO}_x$ (account for the role of PAN and ING as $\text{NO}_x$ reservoirs)
$\mathcal{P}_X$	Photochemical production of X
$E_{\text{bb}}(\text{NO}_x)$	$\text{NO}_x$ emissions from biomass burning
$E_{\text{li}}(\text{NO}_x)$	$\text{NO}_x$ emissions from lightning
$E(\text{ISOP})$	Isoprene emissions
Y	Isoprene nitrate yield
$\alpha$	$\text{NO}_x$ recycling from $\text{ING}_0$ photooxidation



# Bibliography

- A. M. Aghedo, M. G. Schultz, and S. Rast. The influence of African air pollution on regional and global tropospheric ozone. *Atmos. Chem. Phys.*, 2007, 7(5):1193–1212. doi: 10.5194/acp-7-1193-2007.
- S. K. Akagi, R. J. Yokelson, C. Wiedinmyer, M. J. Alvarado, J. S. Reid, T. Karl, J. D. Crounse, and P. O. Wennberg. Emission factors for open and domestic biomass burning for use in atmospheric models. *Atmos. Chem. Phys. Discuss.*, 2010, 10(11):27523–27602. doi: 10.5194/acpd-10-27523-2010.
- H. A. Al-Hosney, S. Carlos-Cuellar, J. Baltrusaitis, and V. H. Grassian. Heterogeneous uptake and reactivity of formic acid on calcium carbonate particles: a Knudsen cell reactor, FTIR and SEM study. *Phys. Chem. Chem. Phys.*, 2005, 7:3587–3595. doi: 10.1039/b510112c.
- A. Altshuller. Review: Natural volatile organic substances and their effect on air quality in the united states. *Atmospheric Environment (1967)*, 1983, 17(11):2131–2165. doi: DOI:10.1016/0004-6981(83)90211-1.
- C. Amelynck, N. Schoon, and E. Arijis. Gas phase reactions of  $\text{CF}_3\text{O}^-$  and  $\text{CF}_3\text{O-H}_2\text{O}$  with nitric, formic, and acetic acid. *Int. J. Mass spectrom.*, 2000, 203(1-3):165–175. doi: 10.1016/S1387-3806(00)00321-3.
- C. H. Anderson, J. E. Dibb, R. J. Griffin, G. S. Hagler, and M. H. Bergin. Atmospheric water-soluble organic carbon measurements at summit, greenland. *Atmos. Environ.*, 2008, 42(22):5612–5621. doi: 10.1016/j.atmosenv.2008.03.006.
- M. O. Andreae. The Biosphere: Pilot or Passenger on Spaceship Earth. *Contributions to Global Change Research*, 2001, pages 59–66. doi: 10.1038/nchembio.2007.5.
- M. O. Andreae and P. Merlet. Emission of trace gases and aerosols from biomass burning. *Global Biogeochem. Cycles*, 2001, 15(4):955–966. doi: 10.1029/2000GB001382.
- M. O. Andreae, T. W. Andreae, R. W. Talbot, and R. C. Harriss. Formic and acetic acid over the central Amazon region, Brazil. I-Dry season. *J. Geophys. Res.*, 1988, 93:1616–1624. doi: 10.1029/JD093iD02p01616.

- M. O. Andreae, D. Rosenfeld, P. Artaxo, A. A. Costa, G. P. Frank, K. M. Longo, and M. A. F. Silva-Dias. Smoking Rain Clouds over the Amazon. *Science*, 2004, 303(5662):1337–1342. doi: 10.1126/science.1092779.
- M. O. Andreae and P. J. Crutzen. Atmospheric Aerosols: Biogeochemical Sources and Role in Atmospheric Chemistry. *Science*, 1997, 276(5315):1052–1058. doi: 10.1126/science.276.5315.1052.
- A. J. Apponi, J. J. Hoy, D. T. Halfen, L. M. Ziurys, , and M. A. Brewster. Hydroxyacetone ( $\text{CH}_3\text{COCH}_2\text{OH}$ ): A Combined Microwave and Millimeter-Wave Laboratory Study and Associated Astronomical Search. *Astrophys. J.*, 2006, 652(2):1787–1795.
- A. T. Archibald, M. R. McGillen, C. A. Taatjes, C. J. Percival, and D. E. Shallcross. Atmospheric transformation of enols: A potential secondary source of carboxylic acids in the urban troposphere. *Geophys. Res. Lett.*, 2007, 34:L21801. doi: 10.1029/2007GL031032.
- J. Arey, S. M. Aschmann, E. S. C. Kwok, and R. Atkinson. Alkyl Nitrate, Hydroxyalkyl Nitrate, and Hydroxycarbonyl Formation from the  $\text{NO}_x$ -Air Photooxidations of  $\text{C}_5$ - $\text{C}_8$  n-Alkanes. *J. Phys. Chem. A*, 2001, 105(6):1020–1027. doi: 10.1021/jp003292z.
- D. W. Arlander, D. R. Cronn, J. C. Farmer, F. A. Menzia, and H. H. Westberg. Gaseous oxygenated hydrocarbons in the remote marine troposphere. *J. Geophys. Res.*, 1990, 95:16391–16403. doi: 10.1029/JD095iD10p16391.
- S. R. Arnold, D. V. Spracklen, J. Williams, N. Yassaa, J. Sciare, B. Bonsang, V. Gros, I. Peeken, A. C. Lewis, S. Alvain, and C. Moulin. Evaluation of the global oceanic isoprene source and its impacts on marine organic carbon aerosol. *Atmos. Chem. Phys.*, 2009, 9(4):1253–1262. doi: 10.5194/acp-9-1253-2009.
- S. M. Aschmann, J. Arey, and R. Atkinson. OH radical formation from the gas-phase reactions of  $\text{O}_3$  with methacrolein and methyl vinyl ketone. *Atmos. Environ.*, 1996, 30(17):2939 – 2943. doi: 10.1016/1352-2310(96)00013-1.
- R. Atkinson. Atmospheric reactions of alkoxy and  $\beta$ -hydroxyalkoxy radicals. *Int. J. Chem. Kinet.*, 1997, a. doi: 10.1002/(SICI)1097-4601(1997)29:2<99::AID-KIN3>3.0.CO;2-F.
- R. Atkinson. Gas-Phase Tropospheric Chemistry of Volatile Organic Compounds: 1. Alkanes and Alkenes. *J. Phys. Chem. Ref. Data*, 1997, b. doi: 10.1063/1.556012.

- R. Atkinson, S. M. Aschmann, E. C. Tuazon, J. Arey, and B. Zielinska. Formation of 3-Methylfuran from the gas-phase reaction of OH radicals with isoprene and the rate constant for its reaction with the OH radical. *Int. J. Chem. Kinet.*, 1989, 21(7):593–604. doi: 10.1002/kin.550210709.
- R. Atkinson, D. L. Baulch, R. A. Cox, J. N. Crowley, R. F. Hampson, R. G. Hynes, M. E. Jenkin, M. J. Rossi, J. Troe, and I. Subcommittee. Evaluated kinetic and photochemical data for atmospheric chemistry: Volume II – gas phase reactions of organic species. *Atmos. Chem. Phys.*, 2006, 6(11):3625–4055. doi: 10.5194/acp-6-3625-200.
- R. Atkinson, J. Arey, and S. M. Aschmann. Atmospheric chemistry of alkanes: Review and recent developments. *Atmos. Environ.*, 2008, 42(23):5859–5871. doi: 10.1016/j.atmosenv.2007.08.040.
- E. D. Baboukas, M. Kanakidou, and N. Mihalopoulos. Carboxylic acids in gas and particulate phase above the Atlantic Ocean. *J. Geophys. Res.*, 2000, 105:14459–14472. doi: 10.1029/1999JD900977.
- J. Baker, J. Arey, and R. Atkinson. Formation and reaction of hydroxycarbonyls from the reaction of OH radicals with 1,3-butadiene and isoprene. *Environ. Sci. Technol.*, 2005, 39(11):4091–4099. doi: 10.1021/es047930t.
- M. P. Barkley, P. I. Palmer, U. Kuhn, J. Kesselmeier, K. Chance, T. P. Kurosu, R. V. Martin, D. Helmig, and A. Guenther. Net ecosystem fluxes of isoprene over tropical South America inferred from Global Ozone Monitoring Experiment (GOME) observations of HCHO columns. *J. Geophys. Res.*, 2008, 113(D20). doi: 10.1029/2008JD009863.
- J. Bechara, A. Borbon, C. Jambert, A. Colomb, and P. E. Perros. Evidence of the impact of deep convection on reactive Volatile Organic Compounds in the upper tropical troposphere during the AMMA experiment in West Africa. *Atmos. Chem. Phys.*, 2010, 10(21):10321–10334. doi: 10.5194/acp-10-10321-2010.
- E. R. Bell, F. F. Rust, and W. E. Vaughan. Decompositions of Di-*t*-alkyl Peroxides. IV. Decomposition of Pure Liquid Peroxide. *JACS*, 1950, 72(1):337–338.
- C. M. Benkovitz, M. T. Scholtz, J. Pacyna, L. Tarrasón, J. Dignon, E. C. Voldner, P. A. Spiro, J. A. Logan, and T. E. Graedel. Global gridded inventories of anthropogenic emissions of sulfur and nitrogen. *J. Geophys. Res.*, 1996, 101:29239–29254. doi: 10.1029/96JD00126.
- P. F. Bernath, C. T. McElroy, M. C. Abrams, C. D. Boone, M. Butler, C. Camy-Peyret, M. Carleer, C. Clerbaux, P. Coheur, R. Colin, P. DeCola, M. DeMazière, J. R. Drummond, D. Dufour, W. F. J. Evans,

- H. Fast, D. Fussen, K. Gilbert, D. E. Jennings, E. J. Llewellyn, R. P. Lowe, E. Mahieu, J. C. McConnell, M. McHugh, S. D. McLeod, R. Michaud, C. Midwinter, R. Nassar, F. Nichituu, C. Nowlan, C. P. Rinsland, Y. J. Rochon, N. Rowlands, K. Semeniuk, P. Simon, R. Skelton, J. J. Sloan, M. Soucy, K. Strong, P. Tremblay, D. Turnbull, K. A. Walker, I. Walkty, D. A. Wardle, V. Wehrle, R. Zander, and J. Zou. Atmospheric Chemistry Experiment (ACE): Mission overview. *Geophys. Res. Lett.*, 2005, 32(L15S01):L15S01. doi: 10.1029/2005GL022386.
- H. L. Bethel, R. Atkinson, and J. Arey. Kinetics and products of the reactions of selected diols with the OH radical. *Int. J. Chem. Kinet.*, 2001, 33(5):310–316.
- I. Bey, D. J. Jacob, R. M. Yantosca, J. A. Logan, B. D. Field, A. M. Fiore, Q. Li, H. Y. Liu, L. J. Mickley, and M. G. Schultz. Global modeling of tropospheric chemistry with assimilated meteorology – Model description and evaluation. *J. Geophys. Res.*, 2001, 106(23):23073–23095. doi: 10.1029/2001JD000807.
- A. Bierbach, I. Barnes, and K. H. Becker. Product and kinetic study of the OH-initiated gas-phase oxidation of furan, 2-methylfuran and furanaldehydes at  $\simeq 300$  K. *Atmos. Environ.*, 1995, 29(19):2651–2660.
- A. F. Bouwman and K. W. V. D. Hoek. Scenarios of animal waste production and fertilizer use and associated ammonia emission for the developing countries. *Atmos. Environ.*, 1997, 31(24):4095–4102. doi: 10.1016/S1352-2310(97)00288-4.
- K. W. Bowman, D. B. A. Jones, J. A. Logan, H. Worden, F. Boersma, R. Chang, S. Kulawik, G. Osterman, P. Hamer, and J. Worden. The zonal structure of tropical O<sub>3</sub> and CO as observed by the Tropospheric Emission Spectrometer in November 2004 – Part 2: Impact of surface emissions on O<sub>3</sub> and its precursors. *Atmos. Chem. Phys.*, 2009, 9(11):3563–3582. doi: 10.5194/acp-9-3563-2009.
- A. A. Boyd, P.-M. Flaud, N. Daugey, and R. Lesclaux. Rate Constants for RO<sub>2</sub> + HO<sub>2</sub> Reactions Measured under a Large Excess of HO<sub>2</sub>. *J. Phys. Chem. A*, 2003, 107(6):818–821. doi: 10.1021/jp026581r.
- W. J. Broadgate, P. S. Liss, and S. A. Penkett. Seasonal emissions of isoprene and other reactive hydrocarbon gases from the ocean. *Geophys. Res. Lett.*, 1997, 24(21):2675–2678. doi: 10.1029/97GL02736.
- S. S. Brown, J. A. deGouw, C. Warneke, T. B. Ryerson, W. P. Dubé, E. Atlas, R. J. Weber, R. E. Peltier, J. A. Neuman, J. M. Roberts, A. Swanson, F. Flocke, S. A. McKeen, J. Brioude, R. Sommariva, M. Trainer, F. C. Fehsenfeld, and A. R. Ravishankara. Nocturnal isoprene oxidation over the Northeast United States

- in summer and its impact on reactive nitrogen partitioning and secondary organic aerosol. *Atmos. Chem. Phys.*, 2009, 9(9):3027–3042.
- N. I. Butkovskaya, A. Kukui, N. Pouvesle, and G. Le Bras. Rate constant and mechanism of the reaction of OH radicals with acetic acid in the temperature range of 229–300 K. *J. Phys. Chem. A*, 2004, 108(34): 7021–7026. doi: 10.1021/jp048444v.
- N. I. Butkovskaya, N. Pouvesle, A. Kukui, and G. L. Bras. Mechanism of the OH-initiated oxidation of glycolaldehyde over the temperature range 233–296 K. *J. Phys. Chem. A*, 2006, a. doi: 10.1021/jp064993k.
- N. I. Butkovskaya, N. Pouvesle, A. Kukui, Y. Mu, and G. Le Bras. Mechanism of the OH-initiated oxidation of hydroxyacetone over the temperature Range 236–298 K. *J. Phys. Chem. A*, 2006, b. doi: 10.1021/jp056345r.
- T. M. Butler, D. Taraborrelli, C. Brühl, H. Fischer, H. Harder, M. Martinez, J. Williams, M. G. Lawrence, and J. Lelieveld. Improved simulation of isoprene oxidation chemistry with the echam5/messy chemistry-climate model: lessons from the gabriel airborne field campaign. *Atmos. Chem. Phys.*, 2008, 8(16): 4529–4546.
- M. Cameron, V. Sivakumaran, T. J. Dillon, and J. N. Crowley. Reaction between OH and CH<sub>3</sub>CHO Part 1. Primary product yields of CH<sub>3</sub> (296 K), CH<sub>3</sub>CO (296 K), and H (237–296 K). *Phys. Chem. Chem. Phys.*, 2002, 4(15):3628–3638.
- G. Capes, B. Johnson, G. McFiggans, P. I. Williams, J. Haywood, and H. Coe. Aging of biomass burning aerosols over West Africa: Aircraft measurements of chemical composition, microphysical properties, and emission ratios. *J. Geophys. Res. Atmos.*, 2008, 113:D00C15. doi: 10.1029/2008JD009845.
- M. Capouet, J. Peeters, B. Nozière, and J.-F. Müller. Alpha-pinene oxidation by oh: simulations of laboratory experiments. *Atmos. Chem. Phys.*, 2004, 4(9/10):2285–2311. doi: 10.5194/acp-4-2285-2004.
- S. Carlos-Cuellar, P. Li, A. P. Christensen, B. J. Krueger, C. Burrichter, and V. H. Grassian. Heterogeneous uptake kinetics of volatile organic compounds on oxide surfaces using a Knudsen cell reactor: Adsorption of acetic acid, formaldehyde, and methanol on  $\alpha$ -Fe<sub>2</sub>O<sub>3</sub>,  $\alpha$ -Al<sub>2</sub>O<sub>3</sub>, and SiO<sub>2</sub>. *J. Phys. Chem. A*, 2003, 107(21):4250–4261. doi: 10.1021/jp0267609.

- A. G. Carlton, B. J. Turpin, H. J. Lim, K. E. Altieri, and S. Seitzinger. Link between isoprene and secondary organic aerosol (SOA): Pyruvic acid oxidation yields low volatility organic acids in clouds. *Geophys. Res. Lett.*, 2006, 33(6):L06822.
- N. Carrasco, J. Doussin, M. O'Connor, J. Wenger, B. Picquet-Varrault, R. Durand-Jolibois, and P. Carlier. Simulation chamber studies of the atmospheric oxidation of 2-methyl-3-buten-2-ol: Reaction with hydroxyl radicals and ozone under a variety of conditions. *J. Atmos. Chem.*, 2007, 56(1):33–55. doi: 10.1007/s10874-006-9041-y.
- N. Carrasco, J.-F. Doussin, B. Picquet-Varrault, and P. Carlier. Tropospheric degradation of 2-hydroxy-2-methylpropanal, a photo-oxidation product of 2-methyl-3-buten-2-ol: Kinetic and mechanistic study of its photolysis and its reaction with oh radicals. *Atmos. Environ.*, 2006, 40(11):2011 – 2019. doi: 10.1016/j.atmosenv.2005.11.042.
- W. P. L. Carter. Condensed atmospheric photooxidation mechanisms for isoprene. *Atmos. Environ.*, 1996, 30(24):4275–4290.
- W. P. L. Carter and R. Atkinson. Alkyl nitrate formation from the atmospheric photooxidation of alkanes; a revised estimation method. *J. Atmos. Chem.*, 1989, 8(2):165–173.
- W. P. L. Carter and R. Atkinson. Development and evaluation of a detailed mechanism for the atmospheric reactions of isoprene and NO<sub>x</sub>. *Int. J. Chem. Kinet.*, 1996, 28(7):497–530.
- W. P. Carter. Development of a condensed saprc-07 chemical mechanism. *Atmos. Environ.*, 2010, 44(40): 5336–5345. doi: 10.1016/j.atmosenv.2010.01.024.
- W. L. Chameides. The photochemistry of a remote marine stratiform cloud. *J. Geophys. Res.*, 1984, 89: 4739–4755. doi: 10.1029/JD089iD03p04739.
- W. L. Chameides, R. W. Lindsay, J. Richardson, and C. S. Kiang. The role of biogenic hydrocarbons in urban photochemical smog: Atlanta as a case study. *Science*, 1988, 241(4872):1473. doi: 10.1126/science.3420404.
- S. Chandra, J. R. Ziemke, P. K. Bhartia, and R. V. Martin. Tropical tropospheric ozone: Implications for dynamics and biomass burning. *J. Geophys. Res. Atmos.*, 2002, 107:4188. doi: 10.1029/2001JD000447.

- S. Chandra, J. Ziemke, and R. Martin. Tropospheric ozone at tropical and middle latitudes derived from TOMS/MLS residual: Comparison with a global model. *J. Geophys. Res.*, 2003, 108(9):4291. doi: 10.1029/2002JD002912.
- A. Chebbi and P. Carlier. Carboxylic acids in the troposphere, occurrence, sources, and sinks: A review. *Atmos. Environ.*, 1996, 30(24):4233–4249. doi: 10.1016/1352-2310(96)00102-1.
- X. Chen, D. Hulbert, and P. B. Shepson. Measurement of the organic nitrate yield from OH reaction with isoprene. *J. Geophys. Res.*, 1998, 103(D19):25563–25568. doi: 10.1029/98JD01483.
- T. J. Christian, B. Kleiss, R. J. Yokelson, R. Holzinger, P. J. Crutzen, W. M. Hao, B. H. Saharjo, and D. E. Ward. Comprehensive laboratory measurements of biomass-burning emissions: 1. Emissions from Indonesian, African, and other fuels. *J. Geophys. Res.*, 2003, 108(D23):4719. doi: 10.1029/2003JD003704.
- B. Chuong and P. S. Stevens. Measurements of the kinetics of the OH-initiated oxidation of isoprene. *J. Geophys. Res.*, 2002, 107. doi: {10.1029/2001JD000865}.
- B. Chuong and P. S. Stevens. Measurements of the kinetics of the OH-initiated oxidation of methyl vinyl ketone and methacrolein. *Int. J. Chem. Kinet.*, 2004, 36(1):12–25.
- M. Claeys, B. Graham, G. Vas, W. Wang, R. Vermeylen, V. Pashynska, J. Cafmeyer, P. Guyon, M. O. Andreae, P. Artaxo, et al. Formation of Secondary Organic Aerosols Through Photooxidation of Isoprene. *Science*, 2004, 303(5661):1173–1176.
- C. Clerbaux, A. Boynard, L. Clarisse, M. George, J. Hadji-Lazaro, H. Herbin, D. Hurtmans, M. Pommier, A. Razavi, S. Turquety, C. Wespes, and P.-F. Coheur. Monitoring of atmospheric composition using the thermal infrarediasi/metop sounder. *Atmos. Chem. Phys.*, 2009, 9(16):6041–6054. doi: 10.5194/acp-9-6041-2009.
- W. J. Collins, D. S. Stevenson, C. E. Johnson, and R. G. Derwent. Role of convection in determining the budget of odd hydrogen in the upper troposphere. *J. Geophys. Res.*, 1999, 104:26927–26942. doi: 10.1029/1999JD900143.
- A. Colomb, J. Williams, J. Crowley, V. Gros, R. Hofmann, G. Salisbury, T. Klüpfel, R. Kormann, A. Stickler, C. Forster, et al. Airborne measurements of trace organic species in the upper troposphere over Europe: the impact of deep convection. *Environ. Chem.*, 2006, 3(4):244–259. doi: 10.1071/EN06020.

- A. P. Cox, A. H. Brittain, and D. J. Finnigan. Microwave spectrum, structure, dipole moment and quadrupole coupling constants of cis and trans nitrous acids. *Trans. Faraday Soc.*, 1971, 67:2179–2194.
- D. Creasey, D. Heard, and J. Lee. OH and HO<sub>2</sub> measurements in a forested region of north-western Greece. *Atmos. Environ.*, 2001, 35:4713–4724. doi: 10.1016/S1352-2310(01)00090-5.
- J. D. Crounse, K. A. McKinney, A. J. Kwan, and P. O. Wennberg. Measurement of gas-phase hydroperoxides by chemical ionization mass spectrometry. *Anal. Chem.*, 2006, 78(19):6726–6732. doi: 10.1021/ac0604235.
- J. N. Crowley, M. Ammann, R. A. Cox, R. G. Hynes, M. E. Jenkin, A. Mellouki, M. J. Rossi, J. Troe, and T. J. Wallington. Evaluated kinetic and photochemical data for atmospheric chemistry: Volume V – heterogeneous reactions on solid substrates. *Atmos. Chem. Phys.*, 2010, 10(18):9059–9223. doi: 10.5194/acp-10-9059-2010.
- P. J. Crutzen and P. H. Zimmermann. The changing photochemistry of the troposphere. *Tellus B*, 1991, 43(4):136–151. doi: 10.1034/j.1600-0889.1991.t01-1-00012.x.
- P. Crutzen and J. Lelieveld. Human Impacts on Atmospheric Chemistry. *Annual Reviews in Earth and Planetary Sciences*, 2001, 29(1):17–45. doi: 10.1146/annurev.earth.29.1.17.
- P. Crutzen, J. Williams, U. Pöschl, P. Hoor, H. Fischer, C. Warneke, R. Holzinger, A. Hansel, W. Lindinger, B. Scheeren, et al. High spatial and temporal resolution measurements of primary organics and their oxidation products over the tropical forests of Surinam. *Atmos. Environ.*, 2000, 34(8):1161–1165.
- G. da Silva. Carboxylic acid catalyzed keto-enol tautomerizations in the gas phase. *Angew. Chem.*, 2010, 49:7523–7525. doi: 10.1002/anie.201003530.
- V. Damian, A. Sandu, M. Damian, F. Potra, and G. R. Carmichael. The kinetic preprocessor KPP-a software environment for solving chemical kinetics. *Comput. Chem. Eng.*, 2002, 26(11):1567 – 1579. doi: 10.1016/S0098-1354(02)00128-X.
- E. Davidson. Pulses of nitric oxide and nitrous oxide flux following wetting of dry soil: An assessment of probable sources and importance relative to annual fluxes. *Ecological Bulletins*, 1992, pages 149–155.
- J. A. de Gouw and C. Warneke. Measurements of volatile organic compounds in the Earth's atmosphere using proton-transfer-reaction mass spectrometry. *Mass Spectrom. Rev.*, 2007, 26(2):223–257. doi: 10.1002/mas.20119.



- J. A. de Gouw, A. M. Middlebrook, C. Warneke, P. D. Goldan, W. C. Kuster, J. M. Roberts, F. C. Fehsenfeld, D. R. Worsnop, M. R. Canagaratna, A. A. P. Pszenny, W. C. Keene, M. Marchewka, S. B. Bertman, and T. S. Bates. Budget of organic carbon in a polluted atmosphere: Results from the New England Air Quality Study in 2002. *J. Geophys. Res. Atmos.*, 2005, 110(D9):16305. doi: 10.1029/2004JD005623.
- J. A. de Gouw, C. Warneke, A. Stohl, A. G. Wollny, C. A. Brock, O. R. Cooper, J. S. Holloway, M. Trainer, F. C. Fehsenfeld, E. L. Atlas, S. G. Donnelly, V. Stroud, and A. Lueb. Volatile organic compounds composition of merged and aged forest fire plumes from Alaska and western Canada. *J. Geophys. Res. Atmos.*, 2006, 111:10303. doi: 10.1029/2005JD006175.
- P. F. DeCarlo, E. J. Dunlea, J. R. Kimmel, A. C. Aiken, D. Sueper, J. Crounse, P. O. Wennberg, L. Emons, Y. Shinozuka, A. Clarke, J. Zhou, J. Tomlinson, D. R. Collins, D. Knapp, A. J. Weinheimer, D. D. Montzka, T. Campos, and J. L. Jimenez. Fast airborne aerosol size and chemistry measurements above Mexico City and Central Mexico during the MILAGRO campaign. *Atmos. Chem. Phys.*, 2008, 8(14): 4027–4048. doi: 10.5194/acp-8-4027-2008.
- J. E. Dibb and M. Arsenault. Shouldn't snowpacks be sources of monocarboxylic acids? *Atmos. Environ.*, 2002, 36(15-16):2513–2522. doi: 10.1016/S1352-2310(02)00131-0.
- T. S. Dibble. Intramolecular hydrogen bonding and double H-atom transfer in peroxy and alkoxy radicals from isoprene. *J. Phys. Chem. A*, 2004, a. doi: 10.1021/jp0306702.
- T. S. Dibble. Prompt chemistry of alkenoxy radical products of the double H-atom transfer of alkoxy radicals from isoprene. *J. Phys. Chem. A*, 2004, b. doi: 10.1021/jp0312161.
- T. S. Dibble. Computations on the  $\tilde{A}-\tilde{X}$  transition of isoprene-OH-O<sub>2</sub> peroxy radicals. *J. Comput. Chem.*, 2005, 26(8):836–845.
- T. S. Dibble. Isomerization of oh-isoprene adducts and hydroxyalkoxy isoprene radicals. *J. Phys. Chem. A*, 2002, 106(28):6643–6650. doi: 10.1021/jp025682m.
- T. Dibble. Cyclization of 1, 4-hydroxycarbonyls is not a homogenous gas phase process. *Chem. Phys. Lett.*, 2007, 447(1-3):5–9.
- T. J. Dillon and J. N. Crowley. Direct detection of oh formation in the reactions of ho<sub>2</sub> with ch<sub>3</sub>c(o)o<sub>2</sub> and other substituted peroxy radicals. *Atmos. Chem. Phys.*, 2008, 8(16):4877–4889.

- T. J. Dillon, A. Horowitz, D. Hölscher, J. N. Crowley, L. Vereecken, J. Peeters, and S. Matter. Reaction of HO with hydroxyacetone ( $\text{HOCH}_2\text{C}(\text{O})\text{CH}_3$ ): rate coefficients (233–363 K) and mechanism. *Phys. Chem. Chem. Phys.*, 2006, 8:236–246. doi: 10.1039/b513056e.
- B. Dimitriadis. The role of natural organics in photochemical air pollution: issues and research needs. *J. Air Pollut. Control Assoc. (United States)*, 1981, 31(3).
- R. M. Doherty, D. S. Stevenson, W. J. Collins, and M. G. Sanderson. Influence of convective transport on tropospheric ozone and its precursors in a chemistry-climate model. *Atmos. Chem. Phys.*, 2005, 5(12): 3205–3218. doi: 10.5194/acp-5-3205-2005.
- M. K. Dubey, R. Mohrschladt, N. M. Donahue, and J. G. Anderson. Isotope specific kinetics of hydroxyl radical (oh) with water ( $\text{h}_2\text{o}$ ): Testing models of reactivity and atmospheric fractionation. *J. Phys. Chem. A*, 1997, 101(8):1494–1500. doi: 10.1021/jp962332p.
- R. A. Duce, J. LaRoche, K. Altieri, K. R. Arrigo, A. R. Baker, D. G. Capone, S. Cornell, F. Dentener, J. Galloway, R. S. Ganeshram, et al. Impacts of Atmospheric Anthropogenic Nitrogen on the Open Ocean. *Science*, 2008, 320(5878):893. doi: 10.1126/science.1150369.
- B. N. Duncan, J. A. Logan, I. Bey, I. A. Megretskaya, R. M. Yantosca, P. C. Novelli, N. B. Jones, and C. P. Rinsland. Global budget of CO, 1988-1997: Source estimates and validation with a global model. *J. Geophys. Res. Atmos.*, 2007, 112:22301. doi: 10.1029/2007JD008459.
- E. J. Dunlea, P. F. DeCarlo, A. C. Aiken, J. R. Kimmel, R. E. Peltier, R. J. Weber, J. Tomlinson, D. R. Collins, Y. Shinozuka, C. S. McNaughton, S. G. Howell, A. D. Clarke, L. K. Emmons, E. C. Apel, G. G. Pfister, A. van Donkelaar, R. V. Martin, D. B. Millet, C. L. Heald, and J. L. Jimenez. Evolution of Asian aerosols during transpacific transport in INTEX-B. *Atmos. Chem. Phys.*, 2009, 9(19):7257–7287. doi: 10.5194/acp-9-7257-2009.
- D. P. Edwards, L. K. Emmons, J. C. Gille, A. Chu, J. Attié, L. Giglio, S. W. Wood, J. Haywood, M. N. Deeter, S. T. Massie, D. C. Ziskin, and J. R. Drummond. Satellite-observed pollution from Southern Hemisphere biomass burning. *J. Geophys. Res. Atmos.*, 2006, 111:D14312. doi: 10.1029/2005JD006655.
- A. Eichler, S. Brütisch, S. Olivier, T. Papina, and M. Schwikowski. A 750 year ice core record of past biogenic emissions from Siberian boreal forests. *Geophys. Res. Lett.*, 2009, 36:18813. doi: 10.1029/2009GL038807.

- T. L. Eliason, S. Aloisio, D. J. Donaldson, D. J. Cziczo, and V. Vaida. Processing of unsaturated organic acid films and aerosols by ozone. *Atmos. Environ.*, 2003, 37(16):2207–2219. doi: 10.1016/S1352-2310(03)00149-3.
- T. L. Eliason, J. B. Gilman, and V. Vaida. Oxidation of organic films relevant to atmospheric aerosols. *Atmos. Environ.*, 2004, 38(9):1367–1378. doi: 10.1016/j.atmosenv.2003.11.025.
- G. Enders, R. Dlugi, R. Steinbrecher, B. Clement, R. Daiber, J. Eijk, S. Gäb, M. Haziza, G. Helas, U. Herrmann, M. Kessel, J. Kesselmeier, D. Kotzias, K. Kourtidis, H.-H. Kurth, R. McMillen, G. Roeder, W. Schürmann, U. Teichmann, and L. Torres. Biosphere/Atmosphere interactions: Integrated research in a European coniferous forest ecosystem. *Atmos. Environ.*, 1992, 26(1):171–189. doi: 10.1016/0960-1686(92)90269-Q.
- T. D. Fairlie, D. J. Jacob, and R. J. Park. The impact of transpacific transport of mineral dust in the united states. *Atmos. Environ.*, 2007, 41(6):1251 – 1266. doi: 10.1016/j.atmosenv.2006.09.048.
- A. H. Falkovich, G. Schkolnik, E. Ganor, and Y. Rudich. Adsorption of organic compounds pertinent to urban environments onto mineral dust particles. *J. Geophys. Res. Atmos.*, 2004, 109:D02208. doi: 10.1029/2003JD003919.
- J. Fan and R. Zhang. Atmospheric Oxidation Mechanism of Isoprene. *Environ. Chem.*, 2004, 1(3):140–149.
- F. C. Fehsenfeld, G. Ancellet, T. S. Bates, A. H. Goldstein, R. M. Hardesty, R. Honrath, K. S. Law, A. C. Lewis, R. Leaitch, S. McKeen, J. Meagher, D. D. Parrish, A. A. P. Pszenny, P. B. Russell, H. Schlager, J. Seinfeld, R. Talbot, and R. Zbinden. International Consortium for Atmospheric Research on Transport and Transformation (ICARTT): North America to Europe – Overview of the 2004 summer field study. *J. Geophys. Res. Atmos.*, 2006, 111(36):D23S01. doi: 10.1029/2006JD007829.
- A. M. Fiore, L. W. Horowitz, D. W. Purves, H. L. II, M. J. Evans, Y. Wang, Q. Li, and R. M. Yantosca. Evaluating the contribution of changes in isoprene emissions to surface ozone trends over the eastern United States. *J. Geophys. Res.*, 2005, 110:D12303. doi: {10.1029/2004JD005485}.
- M. Francisco-Marquez, J. R. Alvarez-Idaboy, A. Galano, and A. Vivier-Bunge. A Possible Mechanism for Furan Formation in the Tropospheric Oxidation of Dienes. *Environ. Sci. Technol.*, 2005, 39(22):8797–8802.

- M. Frisch. 2004. Gaussian 03, revision c. 02.
- K. D. Froyd, S. M. Murphy, D. M. Murphy, J. A. de Gouw, N. C. Eddingsaas, and P. O. Wennberg. Contribution of isoprene-derived organosulfates to free tropospheric aerosol mass. *Proc. Natl. Acad. Sci.*, 2010, 107(50):21360–21365. doi: 10.1073/pnas.1012561107.
- T. Fu, D. J. Jacob, F. Wittrock, J. P. Burrows, M. Vrekoussis, and D. K. Henze. Global budgets of atmospheric glyoxal and methylglyoxal, and implications for formation of secondary organic aerosols. *J. Geophys. Res. Atmos.*, 2008, 113:D15303. doi: 10.1029/2007JD009505.
- J. D. Fuentes, M. Lerdau, R. Atkinson, D. Baldocchi, J. W. Bottenheim, P. Ciccioli, B. Lamb, C. Geron, L. Gu, A. Guenther, et al. Biogenic hydrocarbons in the atmospheric boundary layer: a review. *Bull. Am. Meteorol. Soc.*, 2000, 81(7):1537–1575.
- K. Fuhrer and M. Legrand. Continental biogenic species in the Greenland Ice Core Project ice core: Tracing back the biomass history of the North American continent. *J. Geophys. Res.*, 1997, 102:26735–26746. doi: 10.1029/97JC01299.
- A. Galano, J. Alvarez-Idaboy, M. Ruiz-Santoyo, and A. Vivier-Bunge. Rate coefficient and mechanism of the gas phase OH hydrogen abstraction reaction from formic acid: A quantum mechanical approach. *J. Phys. Chem. A*, 2002, 106(41):9520–9528. doi: 10.1021/jp020297i.
- J. N. Galloway, G. E. Likens, W. C. Keene, and J. M. Miller. The composition of precipitation in remote areas of the world. *J. Geophys. Res.*, 1982, 87(C11):8771–8786. doi: 10.1029/JC087iC11p08771.
- S. Gao, D. Hegg, P. Hobbs, T. Kirchstetter, B. Magi, and M. Sadilek. Water-soluble organic components in aerosols associated with savanna fires in southern Africa: Identification, evolution, and distribution. *J. Geophys. Res.*, 2003, 108:8491. doi: 10.1029/2002JD002324.
- S. Gao, N. Ng, M. Keywood, V. Varuthangkul, R. Bahreini, A. Nenes, J. He, K. Yoo, J. Beauchamp, R. Hodyss, et al. Particle phase acidity and oligomer formation in secondary organic aerosol. *Environ. Sci. Technol.*, 2004, 38(24):6582–6589.
- I. J. George, J. Slowik, and J. P. D. Abbatt. Chemical aging of ambient organic aerosol from heterogeneous reaction with hydroxyl radicals. *Geophys. Res. Lett.*, 2008, 35:13811. doi: 10.1029/2008GL033884.

- P. Giacomelli, K. Ford, C. Espada, and P. B. Shepson. Comparison of the measured and simulated isoprene nitrate distributions above a forest canopy. *J. Geophys. Res.*, 2005, 110:D01304. doi: 10.1029/2004JD005123.
- R. Giering and T. Kaminski. Recipes for adjoint code construction. *ACM Transactions on Mathematical Software (TOMS)*, 1998, 24(4):437–474.
- L. Giglio, J. T. Randerson, G. R. van der Werf, P. S. Kasibhatla, G. J. Collatz, D. C. Morton, and R. S. DeFries. Assessing variability and long-term trends in burned area by merging multiple satellite fire products. *Biogeosciences*, 2010, 7(3):1171–1186. doi: 10.5194/bg-7-1171-2010.
- M. Glasius, S. Wessel, C. S. Christensen, J. K. Jacobsen, H. E. Jørgensen, K. C. Klitgaard, L. Petersen, J. K. Rasmussen, T. Stroyer Hansen, C. Lohse, E. Boaretto, and H. J. Sources to formic acid studied by carbon isotopic analysis and air mass characterization. *Atmos. Environ.*, 2000, 34(15):2471–2479. doi: 10.1016/S1352-2310(99)00416-1.
- M. Glasius, C. Boel, N. Bruun, L. M. Easa, P. Hornung, H. S. Klausen, K. C. Klitgaard, C. Lindeskov, C. K. Møller, H. Nissen, A. P. F. Petersen, S. Kleefeld, E. Boaretto, T. S. Hansen, J. Heinemeier, and C. Lohse. Relative contribution of biogenic and anthropogenic sources to formic and acetic acids in the atmospheric boundary layer. *J. Geophys. Res.*, 2001, 106:7415–7426. doi: 10.1029/2000JD900676.
- A. H. Goldstein and I. E. Galbally. Known and unexplored organic constituents in the Earth’s atmosphere. *Environ. Sci. Technol.*, 2007, 41(5):1515–1521. doi: 10.1021/es072476p.
- A. H. Goldstein, C. D. Koven, C. L. Heald, and I. Y. Fung. Biogenic carbon and anthropogenic pollutants combine to form a cooling haze over the southeastern United States. *Proc. Natl. Acad. Sci.*, 2009, 106(22):8835–8840. doi: 10.1073/pnas.0904128106.
- G. González Abad, P. F. Bernath, C. D. Boone, S. D. McLeod, G. L. Manney, and G. C. Toon. Global distribution of upper tropospheric formic acid from the ace-fts. *Atmos. Chem. Phys.*, 2009, 9(20):8039–8047. doi: 10.5194/acp-9-8039-2009.
- J. G. Goode, R. J. Yokelson, D. E. Ward, R. A. Susott, R. E. Babbitt, M. A. Davies, and W. M. Hao. Measurements of excess O<sub>3</sub>, CO<sub>2</sub>, CH<sub>4</sub>, C<sub>2</sub>H<sub>4</sub>, C<sub>2</sub>H<sub>2</sub>, HCN, NO, NH<sub>3</sub>, HCOOH, CH<sub>3</sub>COOH, HCHO, and CH<sub>3</sub>OH in 1997 Alaskan biomass burning plumes by airborne Fourier transform infrared spectroscopy (AFTIR). *J. Geophys. Res.*, 2000, 105(D17):22147–22166. doi: 10.1029/2000JD900287.

- T. E. Graedel and T. Eisner. Atmospheric formic acid from formicine ants: a preliminary assessment. *Tellus Series B Chemical and Physical Meteorology B*, 1988, 40:335–339. doi: 10.1111/j.1600-0889.1988.tb00107.x.
- G. D. Greenblatt and C. J. Howard. Oxygen atom exchange in the interaction of hydroxyl-(18oh) with several small molecules. *J. Phys. Chem.*, 1989, 93(3):1035–1042. doi: 10.1021/j100340a006.
- E. Greenwald, S. North, Y. Georgievskii, and S. Klippenstein. A two transition state model for radical-molecule reactions: Applications to isomeric branching in the oh-isoprene reaction. *J. Phys. Chem. A*, 2007, 111(25):5582–5592.
- D. Grosjean, E. L. Williams, and E. Grosjean. Atmospheric chemistry of isoprene and of its carbonyl products. *Environ. Sci. Technol.*, 1993, 27(5):830–840. doi: 10.1021/es00042a004.
- J. W. Grossenbacher, T. Couch, P. B. Shepson, T. Thornberry, M. Witmer-Rich, M. A. Carroll, I. Faloon, D. Tan, W. Brune, K. Ostling, and S. Bertman. Measurements of isoprene nitrates above a forest canopy. *J. Geophys. Res.*, 2001, 106:24429–24438. doi: 10.1029/2001JD900029.
- J. W. Grossenbacher, D. J. Barket, Jr., P. B. Shepson, M. A. Carroll, K. Olszyna, and E. Apel. A comparison of isoprene nitrate concentrations at two forest-impacted sites. *J. Geophys. Res. Atmos.*, 2004, 109: D11311. doi: 10.1029/2003JD003966.
- M. Grutter, N. Glatthor, G. P. Stiller, H. Fischer, U. Grabowski, M. Höpfner, S. Kellmann, A. Linden, and T. von Clarmann. Global distribution and variability of formic acid as observed by MIPAS-ENVISAT. *J. Geophys. Res. Atmos.*, 2010, 115:10303. doi: 10.1029/2009JD012980.
- C. L. Gu, C. M. Rynard, D. G. Hendry, and T. Mill. Hydroxide radical oxidation of isoprene. *Environ. Sci. Technol.*, 1985, 19(2):151–155.
- A. Guenther, C. N. Hewitt, D. Erickson, R. Fall, C. Geron, T. Graedel, P. Harley, L. Klinger, M. Lerdau, W. A. McKay, T. Pierce, B. Scholes, R. Steinbrecher, R. Tallamraju, J. Taylor, and P. Zimmerman. A global model of natural volatile organic compound emissions. *J. Geophys. Res.*, 1995, 100:8873–8892. doi: 10.1029/94JD02950.
- A. Guenther, C. Geron, T. Pierce, B. Lamb, P. Harley, and F. R. Natural emissions of non-methane volatile organic compounds, carbon monoxide, and oxides of nitrogen from North America. *Atmos. Environ.*, 2000, 34(12-14):2205 – 2230. doi: 10.1016/S1352-2310(99)00465-3.

- A. Guenther, T. Karl, P. Harley, C. Wiedinmyer, P. I. Palmer, and C. Geron. Estimates of global terrestrial isoprene emissions using MEGAN (Model of Emissions of Gases and Aerosols from Nature). *Atmos. Chem. Phys.*, 2006, 6(11):3181–3210. doi: 10.5194/acp-6-3181-2006.
- A. J. Haagen-Smit. Chemistry and Physiology of Los Angeles Smog. *Ind. Eng. Chem.*, 1952, 44(6):1342–1346. doi: 10.1021/ie50510a045.
- J. W. Hannigan, M. T. Coffey, and A. Goldman. Semiautonomous FTS Observation System for Remote Sensing of Stratospheric and Tropospheric Gases. *J. Atmos. Oceanic Technol.*, 2009, 26:1814–1828. doi: 10.1175/2009JTECHA1230.1.
- A. Hansel, A. Jordan, R. Holzinger, P. Prazeller, W. Vogel, and W. Lindinger. Proton transfer reaction mass spectrometry: on-line trace gas analysis at the ppb level. *Int. J. Mass Spectrom. Ion Processes*, 1995, 149-150:609 – 619. doi: 10.1016/0168-1176(95)04294-U.
- P. Harley, V. Fridd-Stroud, J. Greenberg, A. Guenther, and P. Vasconcellos. Emission of 2-methyl-3-buten-2-ol by pines – A potentially large natural source of reactive carbon to the atmosphere. *J. Geophys. Res.*, 1998, 103(D19):25479–25486. doi: 10.1029/98JD00820.
- P. Harley, P. Vasconcellos, L. Vierling, C. C. Pinheiro, J. Greenberg, A. Guenther, L. Klinger, S. S. Almeida, D. Neill, T. Baker, et al. Variation in potential for isoprene emissions among Neotropical forest sites. *Global Change Biol.*, 2004, 10(5):630–650.
- P. C. Harley, R. K. Monson, and M. T. Lerdau. Ecological and evolutionary aspects of isoprene emission from plants. *Oecologia*, 1999, 118(2):109–123. doi: 10.1007/s004420050709.
- A. S. Hasson, G. S. Tyndall, and J. J. Orlando. A product yield study of the reaction of HO<sub>2</sub> radicals with ethyl peroxy (C<sub>2</sub>H<sub>5</sub>O<sub>2</sub>), acetyl peroxy (CH<sub>3</sub> C(O)O<sub>2</sub>), and acetonyl peroxy (CH<sub>3</sub>C(O)CH<sub>2</sub>O<sub>2</sub>) radicals. *J. Phys. Chem. A*, 2004, 108(28):5979–5989. doi: 10.1021/jp048873t.
- S. Hatakeyama, N. Washida, and H. Akimoto. Rate constants and mechanisms for the reaction of hydroxyl (OH) radicals with acetylene, propyne, and 2-butyne in air at 297±2 K. *J. Phys. Chem.*, 1986, 90(1): 173–178. doi: 10.1021/j100273a039.
- C. D. Hatch, R. V. Gough, and M. A. Tolbert. Heterogeneous uptake of the C<sub>1</sub> to C<sub>4</sub> organic acids on a swelling clay mineral. *Atmos. Chem. Phys.*, 2007, 7(16):4445–4458.

- C. L. Heald, J. H. Kroll, J. L. Jimenez, K. S. Docherty, P. F. DeCarlo, A. C. Aiken, Q. Chen, S. T. Martin, D. K. Farmer, and P. Artaxo. A simplified description of the evolution of organic aerosol composition in the atmosphere. *Geophys. Res. Lett.*, 2010, 37:8803. doi: 10.1029/2010GL042737.
- D. K. Henze and J. H. Seinfeld. Global secondary organic aerosol from isoprene oxidation. *Geophys. Res. Lett.*, 2006, 33:L09812. doi: 10.1029/2006GL025976.
- D. K. Henze, A. Hakami, and J. H. Seinfeld. Development of the adjoint of GEOS-Chem. *Atmos. Chem. Phys.*, 2007, 7(9):2413–2433. doi: 10.5194/acp-7-2413-2007.
- D. K. Henze, J. H. Seinfeld, and D. T. Shindell. Inverse modeling and mapping US air quality influences of inorganic PM<sub>2.5</sub> precursor emissions using the adjoint of GEOS-Chem. *Atmos. Chem. Phys.*, 2009, 9(16): 5877–5903. doi: 10.5194/acp-9-5877-2009.
- I. Hermans, J. F. Müller, T. L. Nguyen, P. Jacobs, and J. Peeters. Kinetics of-Hydroxy-alkylperoxyl Radicals in Oxidation Processes. HO<sub>2</sub> Initiated Oxidation of Ketones/Aldehydes near the Tropopause. *J. Phys. Chem. A*, 2005, 109(19):4303–4311.
- S. C. Herndon, M. S. Zahniser, D. D. Nelson, J. Shorter, J. B. McManus, R. Jiménez, C. Warneke, and J. A. de Gouw. Airborne measurements of HCHO and HCOOH during the New England Air Quality Study 2004 using a pulsed quantum cascade laser spectrometer. *J. Geophys. Res. Atmos.*, 2007, 112:D10S03. doi: 10.1029/2006JD007600.
- C. N. Hewitt, A. R. MacKenzie, P. Di Carlo, C. F. Di Marco, J. R. Dorsey, M. Evans, D. Fowler, M. W. Gallagher, J. R. Hopkins, C. E. Jones, B. Langford, J. D. Lee, A. C. Lewis, S. F. Lim, J. McQuaid, P. Misztal, S. J. Moller, P. S. Monks, E. Nemitz, D. E. Oram, S. M. Owen, G. J. Phillips, T. A. M. Pugh, J. A. Pyle, C. E. Reeves, J. Ryder, J. Siong, U. Skiba, and D. J. Stewart. Nitrogen management is essential to prevent tropical oil palm plantations from causing ground-level ozone pollution. *Proc. Natl. Acad. Sci.*, 2009, 106(44):18447–18451. doi: 10.1073/pnas.0907541106.
- J. M. Hoell, D. D. Davis, D. J. Jacob, M. O. Rodgers, R. E. Newell, H. E. Fuelberg, R. J. McNeal, J. L. Raper, and R. J. Bendura. Pacific Exploratory Mission in the tropical Pacific: PEM-Tropics A, August-September 1996. *J. Geophys. Res.*, 1999, 104:5567–5584. doi: 10.1029/1998JD100074.
- L. W. Horowitz, J. Liang, G. M. Gardner, and D. J. Jacob. Export of reactive nitrogen from North America



- during summertime – Sensitivity to hydrocarbon chemistry. *J. Geophys. Res.*, 1998, 103(D11):13451–13476.
- L. W. Horowitz, A. M. Fiore, G. P. Milly, R. C. Cohen, A. Perring, P. J. Wooldridge, P. G. Hess, L. K. Emmons, and J. Lamarque. Observational constraints on the chemistry of isoprene nitrates over the eastern United States. *J. Geophys. Res.*, 2007, 112(D12):12. doi: 10.1029/2006JD007747.
- S. Houweling, F. Dentener, and J. Lelieveld. The impact of nonmethane hydrocarbon compounds on tropospheric photochemistry. *J. Geophys. Res.*, 1998, 103:10673–10696. doi: 10.1029/97JD03582.
- Y. W. Huang, T. J. Dransfield, J. D. Miller, R. D. Rojas, X. G. Castillo, and J. G. Anderson. Experimental Study of the Kinetics of the Reaction of Acetic Acid with Hydroxyl Radicals from 255 to 355 K. *J. Phys. Chem. A*, 2009, 113(2):423–430. doi: 10.1021/jp808627w.
- L. G. Huey, P. W. Villalta, E. J. Dunlea, D. R. Hanson, and C. J. Howard. Reactions of  $\text{CF}_3\text{O}^-$  with atmospheric trace gases. *J. Phys. Chem.*, 1996, 100(1):190–194.
- A. Ito, S. Sillman, and J. E. Penner. Effects of additional nonmethane volatile organic compounds, organic nitrates, and direct emissions of oxygenated organic species on global tropospheric chemistry. *J. Geophys. Res.*, 2007, 112:D06309. doi: 10.1029/2005JD006556.
- D. J. Jacob. Chemistry of OH in remote clouds and its role in the production of formic acid and peroxy-monosulfate. *J. Geophys. Res.*, 1986, 91:9807–9826. doi: 10.1029/JD091iD09p09807.
- D. J. Jacob and D. A. Winner. Effect of climate change on air quality. *Atmos. Environ.*, 2009, 43(1):51 – 63. doi: 10.1016/j.atmosenv.2008.09.051.
- D. J. Jacob and S. C. Wofsy. Photochemistry of biogenic emissions over the Amazon forest. *J. Geophys. Res.*, 1988, 93:1477–1486. doi: 10.1029/JD093iD02p01477.
- D. J. Jacob, B. G. Heikes, S.-M. Fan, J. A. Logan, D. L. Mauzerall, J. D. Bradshaw, H. B. Singh, G. L. Gregory, R. W. Talbot, D. R. Blake, and G. W. Sachse. Origin of ozone and  $\text{NO}_x$  in the tropical troposphere: A photochemical analysis of aircraft observations over the South Atlantic basin. *J. Geophys. Res.*, 1996, 101:24235–24250. doi: 10.1029/96JD00336.
- D. J. Jacob, H. Liu, C. Mari, and R. M. Yantosca. 2000. Harvard wet deposition scheme for GMI.

- L. Jaeglé, D. J. Jacob, W. H. Brune, and P. O. Wennberg. Chemistry of HO<sub>x</sub> radicals in the upper troposphere. *Atmos. Environ.*, 2001, 35(3):469–489. doi: 10.1016/S1352-2310(00)00376-9.
- L. Jaeglé, R. V. Martin, K. Chance, L. Steinberger, T. P. Kurosu, D. J. Jacob, A. I. Modi, V. Yoboue, L. Sigha-Nkamdjou, and C. Galy-Lacaux. Satellite mapping of rain-induced nitric oxide emissions from soils. *J. Geophys. Res.*, 2004, 109. doi: 10.1029/2004JD004787.
- M. E. Jenkin, S. M. Saunders, and M. J. Pilling. The tropospheric degradation of volatile organic compounds: a protocol for mechanism development. *Atmos. Environ.*, 1997, 31(1):81–104.
- M. E. Jenkin, M. D. Hurley, and T. J. Wallington. Investigation of the radical product channel of the CH<sub>3</sub>C(O)O<sub>2</sub> + HO<sub>2</sub> reaction in the gas phase. *Phys. Chem. Chem. Phys.*, 2007, 9(24):3149–3162.
- J. L. Jimenez, M. R. Canagaratna, N. M. Donahue, A. S. H. Prevot, Q. Zhang, J. H. Kroll, P. F. DeCarlo, J. D. Allan, H. Coe, N. L. Ng, A. C. Aiken, K. S. Docherty, I. M. Ulbrich, A. P. Grieshop, A. L. Robinson, J. Duplissy, J. D. Smith, K. R. Wilson, V. A. Lanz, C. Hueglin, Y. L. Sun, J. Tian, A. Laaksonen, T. Raatikainen, J. Rautiainen, P. Vaattovaara, M. Ehn, M. Kulmala, J. M. Tomlinson, D. R. Collins, M. J. Cubison, E. J. Dunlea, J. A. Huffman, T. B. Onasch, M. R. Alfarra, P. I. Williams, K. Bower, Y. Kondo, J. Schneider, F. Drewnick, S. Borrmann, S. Weimer, K. Demerjian, D. Salcedo, L. Cottrell, R. Griffin, A. Takami, T. Miyoshi, S. Hatakeyama, A. Shimono, J. Y. Sun, Y. M. Zhang, K. Dzepina, J. R. Kimmel, D. Sueper, J. T. Jayne, S. C. Herndon, A. M. Trimborn, L. R. Williams, E. C. Wood, A. M. Middlebrook, C. E. Kolb, U. Baltensperger, and D. R. Worsnop. Evolution of Organic Aerosols in the Atmosphere. *Science*, 2009, 326(5959):1525–1529. doi: 10.1126/science.1180353.
- R. D. Johnson III. 2006. NIST Computational Chemistry Comparison and Benchmark Database NIST Standard Reference Database Number 101 Release 14.
- L. Jourdain, H. M. Worden, J. R. Worden, K. Bowman, Q. Li, A. Eldering, S. S. Kulawik, G. Osterman, K. F. Boersma, B. Fisher, C. P. Rinsland, R. Beer, and M. Gunson. Tropospheric vertical distribution of tropical Atlantic ozone observed by TES during the northern African biomass burning season. *Geophys. Res. Lett.*, 2007, 34:L04810. doi: 10.1029/2006GL028284.
- E. Kalnay, M. Kanamitsu, R. Kistler, W. Collins, D. Deaven, L. Gandin, M. Iredell, S. Saha, G. White, J. Woollen, et al. The NCEP/NCAR 40-Year Reanalysis Project. *Bull. Am. Meteorol. Soc.*, 1996, 77(3):437–471.

- M. Karl, H. P. Dorn, F. Holland, R. Koppmann, D. Poppe, L. Rupp, A. Schaub, and A. Wahner. Product study of the reaction of OH radicals with isoprene in the atmosphere simulation chamber SAPHIR. *J. Atmos. Chem.*, 2006, 55(2):167–187.
- M. Karl, A. Guenther, R. Köble, A. Leip, and G. Seufert. A new European plant-specific emission inventory of biogenic volatile organic compounds for use in atmospheric transport models. *Biogeosciences*, 2009, 6(6):1059–1087. doi: 10.5194/bg-6-1059-2009.
- R. Karunanandan, D. Hölscher, T. J. Dillon, A. Horowitz, J. N. Crowley, L. Vereecken, and J. Peeters. Reaction of HO with Glycolaldehyde, HOCH<sub>2</sub>CHO: Rate Coefficients (240–362 K) and Mechanism. *J. Phys. Chem. A*, 2007, 111(5):897–908.
- K. Kawamura, L. Ng, and I. Kaplan. Determination of organic acids (C1–C10) in the atmosphere, motor exhausts, and engine oils. *Environ. Sci. Technol.*, 1985, 19(11):1082–1086. doi: 10.1021/es00141a010.
- W. C. Keene and J. N. Galloway. The biogeochemical cycling of formic and acetic acids through the troposphere - An overview of current understanding. *Tellus Series B Chemical and Physical Meteorology B*, 1988, 40:322–334. doi: 10.1111/j.1600-0889.1988.tb00106.x.
- V. Kerminen, H. Lihavainen, M. Komppula, Y. Viisanen, and M. Kulmala. Direct observational evidence linking atmospheric aerosol formation and cloud droplet activation. *Geophys. Res. Lett.*, 2005, 32(14): L14803. doi: 10.1029/2005GL023130.
- J. Kesselmeier. Exchange of short-chain oxygenated volatile organic compounds (VOCs) between plants and the atmosphere: A compilation of field and laboratory studies. *J. Atmos. Chem.*, 2001, 39(3):219–233. doi: 10.1023/A:1010632302076.
- J. Kesselmeier and M. Staudt. Biogenic Volatile Organic Compounds (VOC): An Overview on Emission, Physiology and Ecology. *J. Atmos. Chem.*, 1999, 33(1):23–88. doi: 10.1023/A:1006127516791.
- J. Kesselmeier, K. Bode, C. Gerlach, and E. Jork. Exchange of atmospheric formic and acetic acids with trees and crop plants under controlled chamber and purified air conditions. *Atmos. Environ.*, 1998, 32(10): 1765–1775. doi: 10.1016/S1352-2310(97)00465-2.
- P. Khare, N. Kumar, K. M. Kumari, and S. S. Srivastava. Atmospheric formic and acetic acids: An overview. *Rev. Geophys.*, 1999, 37:227–248. doi: 10.1029/1998RG900005.

- M. Kopacz, D. J. Jacob, J. A. Fisher, J. A. Logan, L. Zhang, I. A. Megretskaya, R. M. Yantosca, K. Singh, D. K. Henze, J. P. Burrows, M. Buchwitz, I. Khlystova, W. W. McMillan, J. C. Gille, D. P. Edwards, A. Eldering, V. Thouret, and P. Nédélec. Global estimates of CO sources with high resolution by adjoint inversion of multiple satellite datasets (MOPITT, AIRS, SCIAMACHY, TES). *Atmos. Chem. Phys.*, 2010, 10(3):855–876.
- J. H. Kroll, N. L. Ng, S. M. Murphy, R. C. Flagan, and J. H. Seinfeld. Secondary organic aerosol formation from isoprene photooxidation under high-NO<sub>x</sub> conditions. *Geophys. Res. Lett.*, 2005, 32:L18808.
- J. H. Kroll, N. L. Ng, S. M. Murphy, R. C. Flagan, and J. H. Seinfeld. Secondary organic aerosol formation from isoprene photooxidation. *Environ. Sci. Technol.*, 2006, 40(6):1869–1877.
- J. H. Kroll, J. D. Smith, D. L. Che, S. H. Kessler, D. R. Worsnop, and K. R. Wilson. Measurement of fragmentation and functionalization pathways in the heterogeneous oxidation of oxidized organic aerosol. *Phys. Chem. Chem. Phys.*, 2009, 11:8005o. doi: 10.1039/b905289e.
- U. Kuhn, L. Ganzeveld, A. Thielmann, T. Dindorf, G. Schebeske, M. Welling, J. Sciare, G. Roberts, F. X. Meixner, J. Kesselmeier, J. Lelieveld, O. Kolle, P. Ciccioli, J. Lloyd, J. Trentmann, P. Artaxo, and M. O. Andreae. Impact of Manaus City on the Amazon Green Ocean atmosphere: ozone production, precursor sensitivity and aerosol load. *Atmos. Chem. Phys.*, 2010, 10(19):9251–9282. doi: 10.5194/acp-10-9251-2010.
- M. Kurylo and S. Solomon. Network for the detection of stratospheric change: a status and implementation report. 1990, *NASA and NOAA Special Report*.
- A. J. Kwan, J. D. Crounse, A. D. Clarke, Y. Shinozuka, B. E. Anderson, J. H. Crawford, M. A. Avery, C. S. McNaughton, W. H. Brune, H. B. Singh, and P. O. Wennberg. On the flux of oxygenated volatile organic compounds from organic aerosol oxidation. *Geophys. Res. Lett.*, 2006, 33(5):L15815. doi: 10.1029/2006GL026144.
- E. S. C. Kwok and R. Atkinson. Estimation of hydroxyl radical reaction rate constants for gas-phase organic compounds using a structure-reactivity relationship: An update. *Atmos. Environ.*, 1995, 29(14):1685 – 1695. doi: 10.1016/1352-2310(95)00069-B.
- J. R. Lane and H. G. Kjaergaard. Fluorosulfonic acid and chlorosulfonic acid: Possible candidates for

- oh-stretching overtone-induced photodissociation. *J. Phys. Chem. A*, 2007, 111(39):9707–9713. doi: 10.1021/jp074436d.
- B. R. Larsen, D. Di Bella, M. Glasius, R. Winterhalter, N. R. Jensen, and J. Hjorth. Gas-phase OH oxidation of monoterpenes: Gaseous and particulate products. *J. Atmos. Chem.*, 2001, 38(3):231–276. doi: 10.1023/A:1006487530903.
- J. Lathière, D. A. Hauglustaine, A. D. Friend, N. De Noblet-Ducoudré, N. Viovy, and G. A. Folberth. Impact of climate variability and land use changes on global biogenic volatile organic compound emissions. *Atmos. Chem. Phys.*, 2006, 6(8):2129–2146. doi: 10.5194/acp-6-2129-2006.
- A. Lee, A. H. Goldstein, M. D. Keywood, S. Gao, V. Varutbangkul, R. Bahreini, N. L. Ng, R. C. Flagan, and J. H. Seinfeld. Gas-phase products and secondary aerosol yields from the ozonolysis of ten different terpenes. *J. Geophys. Res.*, 2006, 111:D07302. doi: 10.1029/2005JD006437.
- M. Lee, B. G. Heikes, and D. W. O’Sullivan. Hydrogen peroxide and organic hydroperoxide in the troposphere: a review. *Atmos. Environ.*, 2000, 34(21):3475–3494. doi: 10.1016/S1352-2310(99)00432-X.
- S. Lee, D. M. Murphy, D. S. Thomson, and A. M. Middlebrook. Chemical components of single particles measured with Particle Analysis by Laser Mass Spectrometry (PALMS) during the Atlanta SuperSite Project: Focus on organic/sulfate, lead, soot, and mineral particles. *J. Geophys. Res.*, 2002, 107:4003. doi: 10.1029/2000JD000011.
- M. Legrand and M. De Angelis. Light carboxylic acids in Greenland ice: A record of past forest fires and vegetation emissions from the boreal zone. *J. Geophys. Res.*, 1996, 101:4129–4146. doi: 10.1029/95JD03296.
- W. Lei, R. Zhang, W. Sean McGivern, A. Derecskei-Kovacs, and S. North. Theoretical study of isomeric branching in the isoprene–OH reaction: implications to final product yields in isoprene oxidation. *Chem. Phys. Lett.*, 2000, 326(1-2):109–114.
- W. Lei, R. Zhang, W. S. McGivern, A. Derecskei-Kovacs, and S. W. North. Theoretical Study of OH – O<sub>2</sub>-Isoprene Peroxy Radicals. *J. Phys. Chem. A*, 2001, 105(2):471–477.
- J. Lelieveld and P. Crutzen. The role of clouds in tropospheric photochemistry. *J. Atmos. Chem.*, 1991, 12(3):229–267. doi: 10.1007/BF00048075.

- J. Lelieveld, T. M. Butler, J. N. Crowley, T. J. Dillon, H. Fischer, L. Ganzeveld, H. Harder, M. G. Lawrence, M. Martinez, D. Taraborrelli, et al. Atmospheric oxidation capacity sustained by a tropical forest. *Nature*, 2008, 452(7188):737. doi: 0.1038/nature06870.
- M. Lerdau. Ecology. A positive feedback with negative consequences. *Science*, 2007, 316(5822):212 – 213. doi: 10.1126/science.1141486.
- P. D. Lightfoot, R. A. Cox, J. N. Crowley, M. Destriau, G. D. Hayman, M. E. Jenkin, G. K. Moortgat, and F. Zabel. Organic peroxy radicals: Kinetics, spectroscopy and tropospheric chemistry. *Atmos. Environ.*, 1992, 26(10):1805–1961.
- H. Liu, D. J. Jacob, I. Bey, and R. M. Yantosca. Constraints from  $^{210}\text{Pb}$  and  $^7\text{Be}$  on wet deposition and transport in a global three-dimensional chemical tracer model driven by assimilated meteorological fields. *J. Geophys. Res.*, 2001, 106:12109–12128. doi: 10.1029/2000JD900839.
- S. C. Liu, M. Trainer, F. C. Fehsenfeld, D. D. Parrish, E. J. Williams, D. W. Fahey, G. Hübner, and P. C. Murphy. Ozone production in the rural troposphere and the implications for regional and global ozone distributions. *J. Geophys. Res.*, 1987, 92:4191–4207. doi: 10.1029/JD092iD04p04191.
- A. L. Lockwood, P. B. Shepson, M. N. Fiddler, and M. Alaghmand. Isoprene nitrates: preparation, separation, identification, yields, and atmospheric chemistry. *Atmos. Chem. Phys.*, 2010, 10(13):6169–6178. doi: 10.5194/acp-10-6169-2010.
- F. Loreto and V. Velikova. Isoprene produced by leaves protects the photosynthetic apparatus against ozone damage, quenches ozone products, and reduces lipid peroxidation of cellular membranes. *Plant Physiol.*, 2001, 127(4):1781–1787.
- J. MacQueen. Some methods for classification and analysis of multivariate observations. *Proc. Fifth Berkeley Symp. on Math. Statist. and Prob.*, 1967, 1:281–297.
- S. Madronich and J. G. Calvert. Permutation reactions of organic peroxy radicals in the troposphere. *J. Geophys. Res.*, 1990, 95(D5):5697–5715.
- V. Maréchal, M. Pirre, E. D. Rivi re, N. Pouvesle, J. N. Crowley, S. R. Freitas, and K. M. Longo. Modelling the reversible uptake of chemical species in the gas phase by ice particles formed in a convective cloud. *Atmos. Chem. Phys.*, 2010, 10(10):4977–5000. doi: 10.5194/acp-10-4977-2010.

- C. Mari, P. Bechtold, and D. Jacob. Transport and scavenging of soluble gases in a deep convective cloud. *J. Geophys. Res.*, 2000, 105(D17):22255–22268. doi: 10.1029/2000JD900211.
- K. Marstokk and H. Mollendal. Microwave spectra of isotopic glycolaldehydes, substitution structure, intramolecular hydrogen bond and dipole moment. *J. Mol. Struct.*, 1973, 16(2):259–270.
- R. V. Martin, D. J. Jacob, J. A. Logan, J. M. Ziemke, and R. Washington. Detection of a lightning influence on tropical tropospheric ozone. *Geophys. Res. Lett.*, 2000, 27:1639–1642. doi: 10.1029/1999GL011181.
- R. V. Martin, C. E. Sioris, K. Chance, T. B. Ryerson, T. H. Bertram, P. J. Wooldridge, R. C. Cohen, J. A. Neuman, A. Swanson, and F. M. Flocke. Evaluation of space-based constraints on global nitrogen oxide emissions with regional aircraft measurements over and downwind of eastern North America. *J. Geophys. Res.*, 2006, 111. doi: 10.1029/2005JD006680.
- A. A. Maryott and F. Buckley. US National Bureau of Standards Circular No. 537. 1953, *National Bureau of Standards, Washington, DC*.
- F. McLafferty. Tandem mass spectrometry. *Science*, 1981, 214(4518):280–287. doi: 10.1126/science.7280693.
- A. P. Meleshevich. Reactions of epoxy-compounds by a radical mechanism. *Russ. Chem. Rev.*, 1970, 39(3): 213–226.
- R. Méreau, M. T. Rayez, J. C. Rayez, F. Caralp, and R. Lesclaux. Theoretical study on the atmospheric fate of carbonyl radicals: kinetics of decomposition reactions. *Phys. Chem. Chem. Phys.*, 2001, 3(21): 4712–4717.
- L. J. Mickley, D. J. Jacob, and D. Rind. Uncertainty in preindustrial abundance of tropospheric ozone – Implications for radiative forcing calculations. *J. Geophys. Res.*, 2001, 106(D4):3389–3399. doi: 10.1029/2000JD900594.
- D. B. Millet, D. J. Jacob, T. G. Custer, J. A. de Gouw, A. H. Goldstein, T. Karl, H. B. Singh, B. C. Sive, R. W. Talbot, C. Warneke, and J. Williams. New constraints on terrestrial and oceanic sources of atmospheric methanol. *Atmos. Chem. Phys.*, 2008, 8(23):6887–6905. doi: 10.5194/acp-8-6887-2008.
- D. B. Millet, A. Guenther, D. A. Siegel, N. B. Nelson, H. B. Singh, J. A. de Gouw, C. Warneke, J. Williams, G. Eerdekens, V. Sinha, T. Karl, F. Flocke, E. Apel, D. D. Riemer, P. I. Palmer, and M. Barkley. Global

- atmospheric budget of acetaldehyde: 3-d model analysis and constraints from in-situ and satellite observations. *Atmos. Chem. Phys.*, 2010, 10(7):3405–3425.
- E. C. Minerath and M. J. Elrod. Assessing the potential for diol and hydroxy sulfate ester formation from the reaction of epoxides in tropospheric aerosols. *Environ. Sci. Technol.*, 2009, 43(5):1386–1392. doi: 10.1021/es8029076.
- M. J. Molina, A. V. Ivanov, S. Trakhtenberg, and L. T. Molina. Atmospheric evolution of organic aerosol. *Geophys. Res. Lett.*, 2004, 31:22104. doi: 10.1029/2004GL020910.
- A. K. Mollner, S. Valluvadasan, L. Feng, M. K. Sprague, M. Okumura, D. B. Milligan, W. J. Bloss, S. P. Sander, P. T. Martien, R. A. Harley, A. B. McCoy, and W. P. L. Carter. Rate of gas phase association of hydroxyl radical and nitrogen dioxide. *Science*, 2010, 330(6004):646–649. doi: 10.1126/science.1193030.
- W. J. Moxim and H. Levy. A model analysis of the tropical South Atlantic Ocean tropospheric ozone maximum: The interaction of transport and chemistry. *J. Geophys. Res.*, 2000, 105:17393–17416. doi: 10.1029/2000JD900175.
- J. Müller and G. Brasseur. IMAGES: A three-dimensional chemical transport model of the global troposphere. *J. Geophys. Res.*, 1995, 100:16445–16490. doi: 10.1029/94JD03254.
- J. G. Murphy, D. E. Oram, and C. E. Reeves. Measurements of volatile organic compounds over West Africa. *Atmos. Chem. Phys.*, 2010, 10(12):5281–5294. doi: 10.5194/acp-10-5281-2010.
- R. Nassar, J. A. Logan, I. A. Megretskaya, L. T. Murray, L. Zhang, and D. B. A. Jones. Analysis of tropical tropospheric ozone, carbon monoxide, and water vapor during the 2006 El Niño using TES observations and the GEOS-Chem model. *J. Geophys. Res. Atmos.*, 2009, 114:D17304. doi: 10.1029/2009JD011760.
- P. Neeb. Structure-Reactivity Based Estimation of the Rate Constants for Hydroxyl Radical Reactions with Hydrocarbons. *J. Atmos. Chem.*, 2000, 35(3):295–315.
- P. Neeb, F. Sauer, O. Horie, and G. K. Moortgat. Formation of hydroxymethyl hydroperoxide and formic acid in alkene ozonolysis in the presence of water vapour. *Atmos. Environ.*, 1997, 31(10):1417–1423. doi: 10.1016/S1352-2310(96)00322-6.



- N. L. Ng, A. J. Kwan, J. D. Surratt, A. W. H. Chan, P. S. Chhabra, A. Sorooshian, H. O. T. Pye, J. D. Crounse, P. O. Wennberg, R. C. Flagan, and J. H. Seinfeld. Secondary organic aerosol (SOA) formation from reaction of isoprene with nitrate radicals ( $\text{NO}_3$ ). *Atmos. Chem. Phys.*, 2008, 8(14):4117–4140.
- N. M. Ngwabie, G. W. Schade, T. G. Custer, S. Linke, and T. Hinz. Abundances and flux estimates of volatile organic compounds from a dairy cowshed in Germany. *J. Environ. Qual.*, 2008, 37(2):565–573. doi: 10.2134/jeq2006.0417.
- J. M. O’Brien, E. Czuba, D. R. Hastie, J. S. Francisco, and P. B. Shepson. Determination of the hydroxy nitrate yields from the reaction of  $\text{C}_2 - \text{C}_6$  alkenes with OH in the presence of NO. *J. Phys. Chem. A*, 1998, 102(45):8903–8908.
- M. Okumura and S. P. Sander. Gas-phase formation rates of nitric acid and its isomers under urban conditions. 2005, *California Environmental Protection Agency, Air Resources Board*.
- J. J. Orlando and G. S. Tyndall. The atmospheric chemistry of the  $\text{HC(O)CO}$  radical. *Int. J. Chem. Kinet.*, 2001, 33(3):149–156.
- J. J. Orlando, B. Nozière, G. S. Tyndall, G. E. Orzechowska, S. E. Paulson, and Y. Rudich. Product studies of the OH- and ozone-initiated oxidation of some monoterpenes. *J. Geophys. Res.*, 2000, 105:11561–11572. doi: 10.1029/2000JD900005.
- J. J. Orlando, G. S. Tyndall, S. B. Bertman, W. Chen, and J. B. Burkholder. Rate coefficient for the reaction of OH with  $\text{CH}_2 = \text{C}(\text{CH}_3)\text{C}(\text{O})\text{OONO}_2$  (MPAN). *Atmos. Environ.*, 2002, 36(11):1895–1900.
- L. B. Otter, A. Guenther, and J. Greenberg. Seasonal and spatial variations in biogenic hydrocarbon emissions from southern african savannas and woodlands. *Atmos. Environ.*, 2002, 36(26):4265 – 4275. doi: 10.1016/S1352-2310(02)00333-3.
- P. I. Palmer, D. J. Jacob, A. M. Fiore, R. V. Martin, K. Chance, and T. P. Kurosu. Mapping isoprene emissions over North America using formaldehyde column observations from space. *J. Geophys. Res.*, 2003, 108 (D6):4180. doi: 10.1029/2002JD002153.
- X. Pan, J. S. Underwood, J.-H. Xing, S. A. Mang, and S. A. Nizkorodov. Photodegradation of secondary organic aerosol generated from limonene oxidation by ozone studied with chemical ionization mass spectrometry. *Atmos. Chem. Phys.*, 2009, 9(12):3851–3865. doi: 10.5194/acp-9-3851-2009.

- C. Papagni, J. Arey, and R. Atkinson. Rate constants for the gas-phase reactions of OH radicals with a series of unsaturated alcohols. *Int. J. Chem. Kinet.*, 2001, 33(2):142–147.
- J. Park, J. C. Stephens, R. Zhang, and S. W. North. Theoretical Study of the Alkoxy Radicals Derived from Isoprene: Pressure-and Temperature-Dependent Decomposition Rates. *J. Phys. Chem. A*, 2003, 107(33): 6408–6414.
- J. Park, C. G. Jongsma, R. Zhang, and S. W. North. OH/OD Initiated Oxidation of Isoprene in the Presence of O<sub>2</sub> and NO. *J. Phys. Chem. A*, 2004, 108(48):10688–10697.
- J. Park, A. L. Gomez, M. L. Walser, A. Lin, and S. A. Nizkorodov. Ozonolysis and photolysis of alkene-terminated self-assembled monolayers on quartz nanoparticles: implications for photochemical aging of organic aerosol particles. *Phys. Chem. Chem. Phys.*, 2006, 8:2506. doi: 10.1039/b602704k.
- R. J. Park, D. J. Jacob, M. Chin, and R. V. Martin. Sources of carbonaceous aerosols over the United States and implications for natural visibility. *J. Geophys. Res. Atmos.*, 2003, 108:4355. doi: 10.1029/2002JD003190.
- D. D. Parrish, D. T. Allen, T. S. Bates, M. Estes, F. C. Fehsenfeld, G. Feingold, R. Ferrare, R. M. Hardesty, J. F. Meagher, J. W. Nielsen-Gammon, R. B. Pierce, T. B. Ryerson, J. H. Seinfeld, and E. J. Williams. Overview of the Second Texas Air Quality Study (TexAQS II) and the Gulf of Mexico Atmospheric Composition and Climate Study (GoMACCS). *J. Geophys. Res. Atmos.*, 2009, 114:D00F13. doi: 10.1029/2009JD011842.
- A. K. Patchen, M. J. Pennino, A. C. Kiep, and M. J. Elrod. Direct kinetics study of the product-forming channels of the reaction of isoprene-derived hydroxypetroxy radicals with NO. *Int. J. Chem. Kinet.*, 2007, 39(6):353.
- C. Paton-Walsh, N. B. Jones, S. R. Wilson, V. Haverd, A. Meier, D. W. T. Griffith, and C. P. Rinsland. Measurements of trace gas emissions from Australian forest fires and correlations with coincident measurements of aerosol optical depth. *J. Geophys. Res. Atmos.*, 2005, 110:24305. doi: 10.1029/2005JD006202.
- F. Paulot, J. D. Crounse, H. G. Kjaergaard, J. H. Kroll, J. H. Seinfeld, and P. O. Wennberg. Isoprene photooxidation: new insights into the production of acids and organic nitrates. *Atmos. Chem. Phys.*, 2009, a. doi: 10.5194/acp-9-1479-2009.

- F. Paulot, J. D. Crounse, H. G. Kjaergaard, A. Kurten, J. M. St. Clair, J. H. Seinfeld, and P. O. Wennberg. Unexpected Epoxide Formation in the Gas-Phase Photooxidation of Isoprene. *Science*, 2009, b. doi: 10.1126/science.1172910.
- S. E. Paulson and J. H. Seinfeld. Development and evaluation of a photooxidation mechanism for isoprene. *J. Geophys. Res.*, 1992, 97:20.
- S. E. Paulson, R. C. Flagan, and J. H. Seinfeld. Atmospheric photooxidation of isoprene. I: The hydroxyl radical and ground state atomic oxygen reactions. *Int. J. Chem. Kinet.*, 1992, 24(1):79–101.
- J. Peeters, L. Vereecken, and G. Fantechi. The detailed mechanism of the OH-initiated atmospheric oxidation of  $\alpha$ -pinene: a theoretical study. *Phys. Chem. Chem. Phys.*, 2001, 3(24):5489–5504. doi: 10.1039/b106555f.
- J. Peeters, G. Fantechi, and L. Vereecken. A Generalized Structure-Activity Relationship for the Decomposition of (Substituted) Alkoxy Radicals. *J. Atmos. Chem.*, 2004, 48(1):59–80.
- J. Peeters, T. Nguyen, and L. Vereecken. HO<sub>x</sub> radical regeneration in the oxidation of isoprene. *Phys. Chem. Chem. Phys.*, 2009, 11(28):5935–5939. doi: 10.1039/b908511d.
- J. Peeters and J.-F. Muller. Ho<sub>x</sub> radical regeneration in isoprene oxidation via peroxy radical isomerisations. ii: experimental evidence and global impact. *Phys. Chem. Chem. Phys.*, 2010, 12:14227–14235. doi: 10.1039/C0CP00811G.
- A. E. Perring, T. H. Bertram, P. J. Wooldridge, A. Fried, B. G. Heikes, J. Dibb, J. D. Crounse, P. O. Wennberg, N. J. Blake, D. R. Blake, W. H. Brune, H. B. Singh, and R. C. Cohen. Airborne observations of total RONO<sub>2</sub>: new constraints on the yield and lifetime of isoprene nitrates. *Atmos. Chem. Phys.*, 2009, 9(4): 1451–1463. doi: 10.5194/acp-9-1451-2009.
- W. Peters, M. C. Krol, J. P. F. Fortuin, H. M. Kelder, A. M. Thompson, C. R. Becker, J. Lelieveld, and P. J. Crutzen. Tropospheric ozone over a tropical Atlantic station in the Northern Hemisphere: Paramaribo, Surinam (6° N, 55° W). *Tellus Series B Chemical and Physical Meteorology B*, 2004, 56:21–34. doi: 10.1111/j.1600-0889.2004.00083.x.
- A. K. Petersen, T. Warneke, M. G. Lawrence, J. Notholt, and O. Schrems. First ground-based FTIR observations of the seasonal variation of carbon monoxide in the tropics. *Geophys. Res. Lett.*, 2008, 35:3813. doi: 10.1029/2007GL031393.

- G. G. Pfister, L. K. Emmons, P. G. Hess, J. F. Lamarque, J. J. Orlando, S. Walters, A. Guenther, P. I. Palmer, and P. J. Lawrence. Contribution of isoprene to chemical budgets: A model tracer study with the NCAR CTM MOZART-4. *J. Geophys. Res.*, 2008, 113. doi: 10.1029/2007JD008948.
- S. Pinceloup, G. Laverdet, F. Maguin, J.-F. Doussin, P. Carlier, and G. Le Bras. Laboratory investigation of the photooxidation of formaldehyde combining FTIR analysis of stable species and HO<sub>2</sub> detection by the chemical amplifier technique. *J. Photochem. Photobiol., A*, 2003, 157(2-3):275 – 281. doi: 10.1016/S1010-6030(03)00066-2.
- N. Poisson, M. Kanakidou, and P. J. Crutzen. Impact of Non-Methane Hydrocarbons on Tropospheric Chemistry and the Oxidizing Power of the Global Troposphere: 3-Dimensional Modelling Results. *J. Atmos. Chem.*, 2000, 36(2):157–230. doi: 10.1023/A:1006300616544.
- M. J. Prather and D. J. Jacob. A persistent imbalance in HO<sub>x</sub> and NO<sub>x</sub> photochemistry of the upper troposphere driven by deep tropical convection. *Geophys. Res. Lett.*, 1997, 24:3189–3192. doi: 10.1029/97GL03027.
- C. Price, J. Penner, and M. Prather. NO<sub>x</sub> from lightning 1. Global distribution based on lightning physics. *J. Geophys. Res.*, 1997, 102:5929–5942. doi: 10.1029/96JD03504.
- A. Prince, P. Kleiber, V. Grassian, and M. Young. Reactive uptake of acetic acid on calcite and nitric acid reacted calcite aerosol in an environmental reaction chamber. *Phys. Chem. Chem. Phys.*, 2008, 10(1): 142–152. doi: 10.1039/b712915g.
- J. T. Randerson, G. R. van der Werf, L. Giglio, G. J. Collatz, and P. S. Kasibhatla. Global fire emissions database, version 2 (gfv2). Technical report, Oak Ridge National Laboratory Distributed Active Archive Center,
- A. Razavi, F. Karagulian, L. Clarisse, D. Hurtmans, P. F. Coheur, C. Clerbaux, J. F. Müller, and T. Stavrakou. Global distributions of methanol and formic acid retrieved for the first time from theiasi/metop thermal infrared sounder. *Atmos. Chem. Phys.*, 2011, 11(2):857–872. doi: 10.5194/acp-11-857-2011.
- C. E. Reeves and S. A. Penkett. Measurements of peroxides and what they tell us. *Chem. Rev.*, 2003, 103 (12):5199–5218. doi: 10.1021/cr0205053.

- X. Ren, J. R. Olson, J. Crawford, W. H. Brune, J. Mao, R. B. Long, Z. Chen, G. Chen, M. A. Avery, G. W. Sachse, et al. HO<sub>x</sub> chemistry during INTEx-A 2004: Observation, model calculation, and comparison with previous studies. *J. Geophys. Res.*, 2008, 113(D5):5310. doi: 10.1029/2007JD009166.
- C. P. Rinsland, N. B. Jones, B. J. Connor, J. A. Logan, N. S. Pougatchev, A. Goldman, F. J. Murcray, T. M. Stephen, A. S. Pine, R. Zander, E. Mahieu, and P. Demoulin. Northern and southern hemisphere ground-based infrared spectroscopic measurements of tropospheric carbon monoxide and ethane. *J. Geophys. Res.*, 1998, 103:28197–28218. doi: 10.1029/98JD02515.
- C. P. Rinsland, C. D. Boone, P. F. Bernath, E. Mahieu, R. Zander, G. Dufour, C. Clerbaux, S. Turquety, L. Chiou, J. C. Mc-Connell, L. Neary, and J. W. Kaminski. First space-based observations of formic acid (HCOOH): Atmospheric Chemistry Experiment austral spring 2004 and 2005 Southern Hemisphere tropical-mid-latitude upper tropospheric measurements. *Geophys. Res. Lett.*, 2006, 33:L23804. doi: 10.1029/2006GL027128.
- C. P. Rinsland, G. Dufour, C. D. Boone, P. F. Bernath, L. Chiou, P.-F. Coheur, S. Turquety, and C. Clerbaux. Satellite boreal measurements over Alaska and Canada during June-July 2004: Simultaneous measurements of upper tropospheric CO, C<sub>2</sub>H<sub>6</sub>, HCN, CH<sub>3</sub>Cl, CH<sub>4</sub>, C<sub>2</sub>H<sub>2</sub>, CH<sub>3</sub>OH, HCOOH, OCS, and SF<sub>6</sub> mixing ratios. *Global Biogeochem. Cycles*, 2007, 21:B3008. doi: 10.1029/2006GB002795.
- G. O. Roberts, A. Gelman, and W. R. Gilks. Weak Convergence and Optimal Scaling of Random Walk Metropolis Algorithms. *The Annals of Applied Probability*, 1997, 7(1):110–120.
- J. M. Roberts and R. W. Fajer. UV absorption cross sections of organic nitrates of potential atmospheric importance and estimation of atmospheric lifetimes. *Environ. Sci. Technol.*, 1989, 23(8):945–951. doi: 10.1021/es00066a003.
- A. L. Robinson, N. M. Donahue, M. K. Shrivastava, E. A. Weitkamp, A. M. Sage, A. P. Grieshop, T. E. Lane, J. R. Pierce, and S. N. Pandis. Rethinking Organic Aerosols: Semivolatile Emissions and Photochemical Aging. *Science*, 2007, 315(5816):1259. doi: 10.1126/science.1133061.
- C. Rodgers. Inverse methods for atmospheric sounding: Theory and practice. *World Scientific – Atmospheric, Ocean and Planetary Physics*, 2000, 2.
- G. Roelofs and J. Lelieveld. Distribution and budget of O<sub>3</sub> in the troposphere calculated with a chemistry general circulation model. *J. Geophys. Res.*, 1995, 100:20983–20998. doi: 10.1029/95JD02326.

- G. Roelofs and J. Lelieveld. Tropospheric ozone simulation with a chemistry-general circulation model: Influence of higher hydrocarbon chemistry. *J. Geophys. Res.*, 2000, 105:22697–22712. doi: 10.1029/2000JD900316.
- T. N. Rosenstiel, M. J. Potosnak, K. L. Griffin, R. Fall, and R. K. Monson. Increased CO<sub>2</sub> uncouples growth from isoprene emission in an agriforest ecosystem. *Nature*, 2003, 421(6920):256–259. doi: 10.1038/nature01312.
- L. S. Rothman, I. E. Gordon, A. Barbe, D. C. Benner, P. F. Bernath, M. Birk, V. Boudon, L. R. Brown, A. Campargue, J.-P. Champion, K. Chance, L. H. Coudert, V. Dana, V. M. Devi, S. Fally, J.-M. Flaud, R. R. Gamache, A. Goldman, D. Jacquemart, I. Kleiner, N. Lacome, W. J. Lafferty, J.-Y. Mandin, S. T. Massie, S. N. Mikhailenko, C. E. Miller, N. Moazzen-Ahmadi, O. V. Naumenko, A. V. Nikitin, J. Orphal, V. I. Perevalov, A. Perrin, A. Predoi-Cross, C. P. Rinsland, M. Rotger, M. Simeckov, M. A. H. Smith, K. Sung, S. A. Tashkun, J. Tennyson, R. A. Toth, A. C. Vandaele, and J. V. Auwera. The hitran 2008 molecular spectroscopic database. *J. Quant. Spectrosc. Radiat. Transfer*, 2009, 110(9-10):533–572. doi: 10.1016/j.jqsrt.2009.02.013.
- L. Ruppert and K. H. Becker. A product study of the OH radical-initiated oxidation of isoprene: formation of C<sub>5</sub>-unsaturated diols. *Atmos. Environ.*, 2000, 34(10):1529 – 1542. doi: 10.1016/S1352-2310(99)00408-2.
- J. M. Russell, III, L. L. Gordley, J. H. Park, S. R. Drayson, W. D. Hesketh, R. J. Cicerone, A. F. Tuck, J. E. Frederick, J. E. Harries, and P. J. Crutzen. The Halogen Occultation Experiment. *J. Geophys. Res.*, 1993, 98:10777–10797. doi: 10.1029/93JD00799.
- L. M. Russell, S. F. Maria, and S. C. B. Myneni. Mapping organic coatings on atmospheric particles. *Geophys. Res. Lett.*, 2002, 29(16):1779. doi: 10.1029/2002GL014874.
- G. A. Sanadze. Biogenic isoprene (a review). *Russ. J. Plant Physiol.*, 2004, 51:729–741.
- R. Sander. Compilation of Henry’s Law Constants for Inorganic and Organic Species of Potential Importance in Environmental Chemistry (Version 3).
- S. Sander. *Chemical Kinetics and Photochemical Data for Use in Atmospheric Studies Evaluation Number 15*.

- M. G. Sanderson, C. D. Jones, W. J. Collins, C. E. Johnson, and R. G. Derwent. Effect of Climate Change on Isoprene Emissions and Surface Ozone Levels. *Geophys. Res. Lett.*, 2003, 30(18):180000–1. doi: 10.1029/2003GL017642.
- A. Sandu and R. Sander. Technical note: Simulating chemical systems in Fortran90 and Matlab with the Kinetic PreProcessor KPP-2.1. *Atmos. Chem. Phys.*, 2006, 6(1):187–195. doi: 10.5194/acp-6-187-2006.
- E. Sanhueza and M. O. Andreae. Emission of formic and acetic acids from tropical savanna soils. *Geophys. Res. Lett.*, 1991, 18:1707–1710. doi: 10.1029/91GL01565.
- E. Sanhueza, L. Figueroa, and M. Santana. Atmospheric formic and acetic acids in venezuela. *Atmos. Environ.*, 1996, 30(10-11):1861–1873. doi: 10.1016/1352-2310(95)00383-5.
- S. M. Saunders, M. E. Jenkin, R. G. Derwent, and M. J. Pilling. Protocol for the development of the Master Chemical Mechanism, MCM v3 (Part A): tropospheric degradation of non-aromatic volatile organic compounds. *Atmos. Chem. Phys.*, 2003, 3(1):161–180. doi: 10.5194/acp-3-161-2003.
- B. Sauvage, R. V. Martin, A. van Donkelaar, X. Liu, K. Chance, L. Jaeglé, P. I. Palmer, S. Wu, and T.-M. Fu. Remote sensed and in situ constraints on processes affecting tropical tropospheric ozone. *Atmos. Chem. Phys.*, 2007, a.
- B. Sauvage, R. V. Martin, A. Van Donkelaar, and J. R. Ziemke. Quantification of the factors controlling tropical tropospheric ozone and the South Atlantic maximum. *J. Geophys. Res.*, 2007, b. doi: 10.1029/2006JD008008.
- J. H. Seinfeld and S. N. Pandis. Atmospheric chemistry and physics: from air pollution to climate change. 1998, Wiley-Interscience.
- C. Senten, M. De Mazière, B. Dils, C. Hermans, M. Kruglanski, E. Neefs, F. Scolas, A. C. Vandaele, G. Vanhaelewyn, C. Vigouroux, M. Carleer, P. F. Coheur, S. Fally, B. Barret, J. L. Baray, R. Delmas, J. Leveau, J. M. Metzger, E. Mahieu, C. Boone, K. A. Walker, P. F. Bernath, and K. Strong. Technical Note: New ground-based FTIR measurements at Ile de La Réunion: observations, error analysis, and comparisons with independent data. *Atmos. Chem. Phys.*, 2008, 8(13):3483–3508. doi: 10.5194/acp-8-3483-2008.
- D. E. Shallcross and P. S. Monks. New Directions: A role for isoprene in biosphere–climate–chemistry feedbacks. *Atmos. Environ.*, 2000, 34(10):1659–1660.

- T. D. Sharkey and E. L. Singsaas. Why plants emit isoprene. *Nature*, 1995, 374(6525):769–769. doi: 10.1038/374769a0.
- T. D. Sharkey, A. E. Wiberley, and A. R. Donohue. Isoprene Emission from Plants: Why and How. *Annals of Botany*, 2008, 101(1):5–18. doi: 10.1093/aob/mcm240.
- T. D. Sharkey, X. Chen, and S. Yeh. Isoprene increases thermotolerance of fosmidomycin-fed leaves. *Plant Physiol.*, 2001, 125(4):2001–2006. doi: 10.1104/pp.125.4.2001.
- S. Shaw, F. Mitloehner, W. Jackson, E. DePeters, J. Fadel, P. Robinson, R. Holzinger, and A. Goldstein. Volatile organic compound emissions from dairy cows and their waste as measured by proton-transfer-reaction mass spectrometry. *Environ. Sci. Technol*, 2007, 41(4):1310–1316. doi: 10.1021/es061475e.
- S. Sillman, M. A. Carroll, T. Thornberry, B. K. Lamb, H. Westberg, W. H. Brune, I. Faloon, D. Tan, P. B. Shepson, A. L. Sumner, D. R. Hastie, C. M. Mihele, E. C. Apel, D. D. Riemer, and R. G. Zika. Loss of isoprene and sources of nighttime OH radicals at a rural site in the United States: Results from photochemical models. *J. Geophys. Res. Atmos.*, 2002, 107:4043. doi: 10.1029/2001JD000449.
- H. B. Singh, W. H. Brune, J. H. Crawford, F. Flocke, and D. J. Jacob. Chemistry and transport of pollution over the Gulf of Mexico and the Pacific: spring 2006 INTEX-B campaign overview and first results. *Atmos. Chem. Phys.*, 2009, 9(7):2301–2318. doi: 10.5194/acp-9-2301-2009.
- V. Sinha, J. Williams, J. N. Crowley, and J. Lelieveld. The Comparative Reactivity Method – a new tool to measure total OH Reactivity in ambient air. *Atmos. Chem. Phys.*, 2008, 8(8):2213–2227. doi: 10.5194/acp-8-2213-2008.
- R. Sinreich, S. Coburn, B. Dix, and R. Volkamer. Ship-based detection of glyoxal over the remote tropical Pacific Ocean. *Atmos. Chem. Phys.*, 2010, 10(23):11359–11371. doi: 10.5194/acp-10-11359-2010.
- S. Sitch, P. M. Cox, W. J. Collins, and C. Huntingford. Indirect radiative forcing of climate change through ozone effects on the land-carbon sink. *Nature*, 2007, 448(7155):791–794. doi: 10.1038/nature06059.
- G. Sposito. The chemistry of soils. 1989, *Oxford University Press*.
- M. Sprengnether, K. L. Demerjian, N. M. Donahue, and J. G. Anderson. Product analysis of the OH oxidation of isoprene and 1, 3-butadiene in the presence of NO. *J. Geophys. Res.*, 2002, 107(d 15):8–8.



- D. S. Stevenson, F. J. Dentener, M. G. Schultz, K. Ellingsen, T. P. C. van Noije, O. Wild, G. Zeng, M. Amann, C. S. Atherton, N. Bell, D. J. Bergmann, I. Bey, T. Butler, J. Cofala, W. J. Collins, R. G. Derwent, R. M. Doherty, J. Drevet, H. J. Eskes, A. M. Fiore, M. Gauss, D. A. Hauglustaine, L. W. Horowitz, I. S. A. Isaksen, M. C. Krol, J. Lamarque, M. G. Lawrence, V. Montanaro, J. Müller, G. Pitari, M. J. Prather, J. A. Pyle, S. Rast, J. M. Rodriguez, M. G. Sanderson, N. H. Savage, D. T. Shindell, S. E. Strahan, K. Sudo, and S. Szopa. Multimodel ensemble simulations of present-day and near-future tropospheric ozone. *J. Geophys. Res. Atmos.*, 2006, 111:D08301. doi: 10.1029/2005JD006338.
- A. Stickler, H. Fischer, J. Williams, M. de Reus, R. Sander, M. G. Lawrence, J. N. Crowley, and J. Lelieveld. Influence of summertime deep convection on formaldehyde in the middle and upper troposphere over Europe. *J. Geophys. Res. Atmos.*, 2006, 111:D14308. doi: 10.1029/2005JD007001.
- T. Su and W. J. Chesnavich. Parametrization of the ion–polar molecule collision rate constant by trajectory calculations. *J. Chem. Phys.*, 1982, 76:5183.
- W. Sun and M. Saeys. first principles study of the reaction of formic and acetic acids with hydroxyl radicals. *J. Phys. Chem. A*, 2008, 112(30):6918–6928. doi: 10.1021/jp802017q.
- J. D. Surratt, S. M. Murphy, J. H. Kroll, N. L. Ng, L. Hildebrandt, A. Sorooshian, R. Szmigielski, R. Vermeylen, W. Maenhaut, M. Claeys, R. C. Flagan, and J. H. Seinfeld. Chemical composition of secondary organic aerosol formed from the photooxidation of isoprene. *J. Phys. Chem. A*, 2006, 110(31):9665–9690. doi: 10.1021/jp061734m.
- J. D. Surratt, A. W. H. Chan, N. C. Eddingsaas, M. Chan, C. L. Loza, A. J. Kwan, S. P. Hersey, R. C. Flagan, P. O. Wennberg, and J. H. Seinfeld. Reactive intermediates revealed in secondary organic aerosol formation from isoprene. *Proc. Natl. Acad. Sci.*, 2010, 107(15):6640–6645. doi: 10.1073/pnas.0911114107.
- J. D. Surratt, J. H. Kroll, T. E. Kleindienst, E. O. Edney, M. Claeys, A. Sorooshian, N. L. Ng, J. H. Offenberg, M. Lewandowski, M. Jaoui, R. C. Flagan, and J. H. Seinfeld. Evidence for organosulfates in secondary organic aerosol. *Environ. Sci. Technol.*, 2007, 41(2):517–527. doi: 10.1021/es062081q.
- J. D. Surratt, Y. Gómez-González, A. W. H. Chan, R. Vermeylen, M. Shahgholi, T. E. Kleindienst, E. O. Edney, J. H. Offenberg, M. Lewandowski, M. Jaoui, W. Maenhaut, M. Claeys, R. C. Flagan, and J. H. Seinfeld. Organosulfate formation in biogenic secondary organic aerosol. *J. Phys. Chem. A*, 2008, 112(36):8345–8378. doi: 10.1021/jp802310p.

- C. A. Taatjes, N. Hansen, A. McIlroy, J. A. Miller, J. P. Senosiain, S. J. Klippenstein, F. Qi, L. Sheng, Y. Zhang, T. A. Cool, J. Wang, P. R. Westmoreland, M. E. Law, T. Kasper, and K. Kohse-Höinghaus. Enols Are Common Intermediates in Hydrocarbon Oxidation. *Science*, 2005, 308(5730):1887–1889. doi: 10.1126/science.1112532.
- R. W. Talbot, K. M. Beecher, and R. C. Harriss. Atmospheric geochemistry of formic and acetic acids at a mid-latitude temperate site. *J. Geophys. Res.*, 1988, 93(D2):1638–1652. doi: 10.1029/JD093iD02p01638.
- R. W. Talbot, M. O. Andreae, H. Berresheim, D. J. Jacob, and K. M. Beecher. Sources and sinks of formic, acetic, and pyruvic acids over Central Amazonia: 2. Wet Season. *J. Geophys. Res.*, 1990, 95(16):799–16.
- R. W. Talbot, B. W. Mosher, B. G. Heikes, D. J. Jacob, J. W. Munger, B. C. Daube, W. C. Keene, J. R. Maben, and R. S. Artz. Carboxylic acids in the rural continental atmosphere over the eastern United States during the Shenandoah Cloud and Photochemistry Experiment. *J. Geophys. Res.*, 1995, 100(D5): 9335–9344.
- D. Tan, I. Faloon, J. B. Simpas, W. Brune, P. B. Shepson, T. L. Couch, A. L. Sumner, M. A. Carroll, T. Thornberry, E. Apel, D. Riemer, and W. Stockwell. Hox budgets in a deciduous forest: Results from the prophet summer 1998 campaign. *J. Geophys. Res.*, 2001, 106(D20):24407–24427. doi: 10.1029/2001JD900016.
- D. P. Tew, W. Klopper, C. Neiss, and C. Hattig. Quintuple-[small zeta] quality coupled-cluster correlation energies with triple-[small zeta] basis sets. *Phys. Chem. Chem. Phys.*, 2007, 9:1921–1930. doi: 10.1039/B617230J.
- A. M. Thompson, B. G. Doddridge, J. C. Witte, R. D. Hudson, W. T. Luke, J. E. Johnson, B. J. Johnson, S. J. Oltmans, and R. Weller. A tropical Atlantic paradox: Shipboard and satellite views of a tropospheric ozone maximum and wave-one in January-February 1999. *Geophys. Res. Lett.*, 2000, 27:3317–3320. doi: 10.1029/1999GL011273.
- A. Thompson, J. Witte, R. McPeters, S. Oltmans, F. Schmidlin, J. Logan, M. Fujiwara, V. Kirchhoff, F. Posny, G. Coetzee, et al. Southern Hemisphere Additional Ozonesondes (SHADOZ) 1998–2000 tropical ozone climatology: 1. Comparison with Total Ozone Mapping Spectrometer (TOMS) and ground-based measurements. *J. Geophys. Res.*, 2003, 108(D2):8238. doi: 10.1029/2001JD000967.

- J. A. Thornton, P. J. Wooldridge, R. C. Cohen, M. Martinez, H. Harder, W. H. Brune, E. J. Williams, J. M. Roberts, F. C. Fehsenfeld, S. R. Hall, et al. Ozone production rates as a function of  $\text{NO}_x$  abundances and  $\text{HO}_x$  production rates in the Nashville urban plumes. *J. Geophys. Res.*, 2002, 107(D12):4146. doi: 10.1029/2001JD000932.
- E. Tuazon and R. Atkinson. Product study of the gas-phase reaction of methacrolein with the OH radical in the presence of  $\text{NO}_x$ . *Int. J. Chem. Kinet.*, 1990, 22(6):591–602.
- P. Tunved, H.-C. Hansson, V.-M. Kerminen, J. Strom, M. D. Maso, H. Lihavainen, Y. Viisanen, P. P. Aalto, M. Komppula, and M. Kulmala. High Natural Aerosol Loading over Boreal Forests. *Science*, 2006, 312 (5771):261–263. doi: 10.1126/science.1123052.
- S. Turquety, J. A. Logan, D. J. Jacob, R. C. Hudman, F. Y. Leung, C. L. Heald, R. M. Yantosca, S. Wu, L. K. Emmons, D. P. Edwards, and G. W. Sachse. Inventory of boreal fire emissions for North America in 2004: Importance of peat burning and pyroconvective injection. *J. Geophys. Res. Atmos.*, 2007, 112: D12S03. doi: 10.1029/2006JD007281.
- C. R. Usher, A. E. Michel, and V. H. Grassian. Reactions on mineral dust. *Chem. Rev.*, 2003, 103(12): 4883–4940. doi: 10.1021/cr020657y.
- M. Val Martin, J. A. Logan, R. A. Kahn, F.-Y. Leung, D. L. Nelson, and D. J. Diner. Smoke injection heights from fires in North America: analysis of 5 years of satellite observations. *Atmos. Chem. Phys.*, 2010, 10 (4):1491–1510. doi: 10.5194/acp-10-1491-2010.
- R. Van Dingenen, F. J. Dentener, F. Raes, M. C. Krol, L. Emberson, and J. Cofala. The global impact of ozone on agricultural crop yields under current and future air quality legislation. *Atmos. Environ.*, 2009, 43(3):604 – 618. doi: 10.1016/j.atmosenv.2008.10.033.
- A. van Donkelaar, R. V. Martin, R. J. Park, C. L. Heald, T. M. Fu, H. Liao, and A. Guenther. Model evidence for a significant source of secondary organic aerosol from isoprene. *Atmos. Environ.*, 2007, 41 (6):1267–1274.
- J. Vander Auwera, K. Didriche, A. Perrin, and F. Keller. Absolute line intensities for formic acid and dissociation constant of the dimer. *J. Chem. Phys.*, 2007, 126(12):124311–124320. doi: 10.1063/1.2712439.

- V. Velazco, J. Notholt, T. Warneke, M. Lawrence, H. Bremer, J. Drummond, A. Schulz, J. Krieg, and O. Schrems. Latitude and altitude variability of carbon monoxide in the Atlantic detected from ship-borne Fourier transform spectrometry, model, and satellite data. *J. Geophys. Res. Atmos.*, 2005, 110: 9306. doi: 10.1029/2004JD005351.
- B. Veyret, R. Lesclaux, M. T. Rayez, J. C. Rayez, R. A. Cox, and G. K. Moortgat. Kinetics and mechanism of the photo-oxidation of formaldehyde. 1. Flash photolysis study. *J. Phys. Chem.*, 1989, 93(6):2368–2374.
- C. Vigouroux, F. Hendrick, T. Stavrou, B. Dils, I. De Smedt, C. Hermans, A. Merlaud, F. Scolas, C. Senten, G. Vanhaelewyn, S. Fally, M. Carleer, J.-M. Metzger, J.-F. Müller, M. Van Roozendaal, and M. De Mazière. Ground-based FTIR and MAX-DOAS observations of formaldehyde at Réunion Island and comparisons with satellite and model data. *Atmos. Chem. Phys.*, 2009, 9(24):9523–9544. doi: 10.5194/acp-9-9523-2009.
- A. Vlasenko, I. J. George, and J. P. D. Abbatt. Formation of Volatile Organic Compounds in the Heterogeneous Oxidation of Condensed-Phase Organic Films by Gas-Phase OH. *J. Phys. Chem. A*, 2008, 112(7): 1552–1560. doi: 10.1021/jp0772979.
- E. Vöhringer-Martinez, B. Hansmann, H. Hernandez, J. S. Francisco, J. Troe, and B. Abel. Water Catalysis of a Radical-Molecule Gas-Phase Reaction. *Science*, 2007, 315(5811):497. doi: 10.1126/science.1134494.
- R. Volkamer, F. San Martini, L. T. Molina, D. Salcedo, J. L. Jimenez, and M. J. Molina. A missing sink for gas-phase glyoxal in Mexico City: Formation of secondary organic aerosol. *Geophys. Res. Lett.*, 2007, 34:L19807. doi: 10.1029/2007GL030752.
- R. von Kuhlmann, M. G. Lawrence, P. J. Crutzen, and P. J. Rasch. A model for studies of tropospheric ozone and nonmethane hydrocarbons: Model description and ozone results. *J. Geophys. Res. Atmos.*, 2003, a. doi: 10.1029/2002JD002893.
- R. von Kuhlmann, M. Lawrence, P. Crutzen, and P. Rasch. A model for studies of tropospheric ozone and nonmethane hydrocarbons: Model evaluation of ozone-related species. *J. Geophys. Res.*, 2003, b. doi: 10.1029/2002JD003348.
- R. von Kuhlmann, M. G. Lawrence, U. Pöschl, and P. J. Crutzen. Sensitivities in global scale modeling of isoprene. *Atmos. Chem. Phys.*, 2004, 4(1):1–17. doi: 10.5194/acp-4-1-2004.

- K. J. Wall, C. L. Schiller, and G. W. Harris. Measurements of the HONO photodissociation constant. *J. Atmos. Chem.*, 2006, 55(1):31–54.
- M. L. Walser, J. Park, A. L. Gomez, A. R. Russell, and S. A. Nizkorodov. Photochemical Aging of Secondary Organic Aerosol Particles Generated from the Oxidation of d-Limonene. *J. Phys. Chem. A*, 2007, 111(10): 1907–1913. doi: 10.1021/jp066293l.
- P. Wang, J. Fishman, V. L. Harvey, and M. H. Hitchman. Southern tropical upper tropospheric zonal ozone wave-1 from SAGE II observations (1985-2002). *J. Geophys. Res. Atmos.*, 2006, 111:D08305. doi: 10.1029/2005JD006221.
- W. Wang, I. Kourtchev, B. Graham, J. Cafmeyer, W. Maenhaut, and M. Claeys. Characterization of oxygenated derivatives of isoprene related to 2-methyltetrols in Amazonian aerosols using trimethylsilylation and gas chromatography/ion trap mass spectrometry. *Rapid Commun. Mass Spectrom.*, 2005, 19(10): 1343–1351.
- Y. Wang and D. Jacob. Anthropogenic forcing on tropospheric ozone and OH since preindustrial times. *J. Geophys. Res.*, 1998, 103(D23):31123–31136. doi: 10.1029/1998JD100004.
- Y. Wang, D. J. Jacob, and J. A. Logan. Global simulation of tropospheric O<sub>3</sub>-NO<sub>x</sub>-hydrocarbon chemistry 1. Model formulation. *J. Geophys. Res.*, 1998, 103:10713–10726. doi: 10.1029/98JD00158.
- C. Warneke, R. Holzinger, A. Hansel, A. Jordan, W. Lindinger, U. Pöschl, J. Williams, P. Hoor, H. Fischer, P. Crutzen, et al. Isoprene and Its Oxidation Products Methyl Vinyl Ketone, Methacrolein, and Isoprene Related Peroxides Measured Online over the Tropical Rain Forest of Surinam in March 1998. *J. Atmos. Chem.*, 2001, 38(2):167–185.
- C. Warneke, R. Bahreini, J. Brioude, C. A. Brock, J. A. de Gouw, D. W. Fahey, K. D. Froyd, J. S. Holloway, A. Middlebrook, L. Miller, S. Montzka, D. M. Murphy, J. Peischl, T. B. Ryerson, J. P. Schwarz, J. R. Spackman, and P. Veres. Biomass burning in Siberia and Kazakhstan as an important source for haze over the Alaskan Arctic in April 2008. *Geophys. Res. Lett.*, 2009, 36:2813. doi: 10.1029/2008GL036194.
- Wavefunction Inc. 2006. Spartan'06.
- Wavefunction Inc. 2008. Spartan'08.

- R. J. Weber, A. P. Sullivan, R. E. Peltier, A. Russell, B. Yan, M. Zheng, J. de Gouw, C. Warneke, C. Brock, J. S. Holloway, E. L. Atlas, and E. Edgerton. A study of secondary organic aerosol formation in the anthropogenic-influenced southeastern United States. *J. Geophys. Res. Atmos.*, 2007, 112:13302. doi: 10.1029/2007JD008408.
- F. Weigend. A fully direct RI-HF algorithm: Implementation, optimised auxiliary basis sets, demonstration of accuracy and efficiency. *Phys. Chem. Chem. Phys.*, 2002, 4:4285–4291. doi: 10.1039/b204199p.
- F. Weigend, A. Köhn, and C. Hättig. Efficient use of the correlation consistent basis sets in resolution of the identity MP2 calculations. *J. Chem. Phys.*, 2002, 116:3175–3183. doi: 10.1063/1.1445115.
- P. O. Wennberg, T. F. Hanisco, L. Jaeglé, D. J. Jacob, E. J. Hints, E. J. Lanzendorf, J. G. Anderson, R.-S. Gao, E. R. Keim, S. G. Donnelly, L. A. Negro, D. W. Fahey, S. A. McKeen, R. J. Salawitch, C. R. Webster, R. D. May, R. L. Herman, M. H. Proffitt, J. J. Margitan, E. L. Atlas, S. M. Schauffler, F. Flocke, C. T. McElroy, and T. P. Bui. Hydrogen Radicals, Nitrogen Radicals, and the Production of O<sub>3</sub> in the Upper Troposphere. *Science*, 1998, 279(5347):49–53. doi: 10.1126/science.279.5347.49.
- F. W. Went. Blue Hazes in the Atmosphere. *Nature*, 1960, 187:641–643. doi: 10.1038/187641a0.
- H.-J. Werner, P. J. Knowles, F. R. Manby, M. Schütz, et al. 2008. Molpro, version 2008.1, a package of ab initio programs.
- H.-J. Werner, T. B. Adler, and F. R. Manby. General orbital invariant MP2-F12 theory. *J. Chem. Phys.*, 2007, 126(16). doi: {10.1063/1.2712434}.
- M. . L. Wesely. Parameterization of surface resistances to gaseous dry deposition in regional-scale numerical models. *Atmos. Environ.*, 1989, 23(6):1293–1304. doi: 10.1016/j.atmosenv.2007.10.058.
- C. Wiedinmyer, A. Guenther, P. Harley, N. Hewitt, C. Geron, P. Artaxo, R. Steinbrecher, and R. Rasmussen. *Global Organic Emissions from Vegetation (in Emissions of Atmospheric Trace Compounds)*, volume 18 of *Advances in Global Change Research*.
- C. Wiedinmyer, X. Tie, A. Guenther, R. Neilson, and C. Granier. Future Changes in Biogenic Isoprene Emissions: How Might They Affect Regional and Global Atmospheric Chemistry? *Earth Interact.*, 2006, 10:1–19.
- World Health Organization. 2005. Air quality guidelines global update.

- S. Wu, L. J. Mickley, D. J. Jacob, J. A. Logan, R. M. Yantosca, and D. Rind. Why are there large differences between models in global budgets of tropospheric ozone ? *J. Geophys. Res.*, 2007, 112(D05302). doi: 10.1029/2006JD007801.
- D. Wunch, G. C. Toon, J.-F. L. Blavier, R. Washenfelder, J. Notholt, B. J. Connor, D. W. T. Griffith, V. Sherlock, and P. O. Wennberg. The Total Carbon Column Observing Network (TCCON). *Philos. Trans. R. Soc. London, Ser. A*, 2010, Accepted.
- R. Yevich and J. Logan. An assessment of biofuel use and burning of agricultural waste in the developing world. *Global Biogeochem. Cycles*, 2003, 17(4):1095. doi: 10.1029/2002GB001952.
- J. J. Yienger and H. Levy. Empirical model of global soil-biogenic NO<sub>x</sub> emissions. *J. Geophys. Res.*, 1995, 100:11447–11464. doi: 10.1029/95JD00370.
- R. J. Yokelson, I. T. Bertschi, T. J. Christian, P. V. Hobbs, D. E. Ward, and W. M. Hao. Trace gas measurements in nascent, aged, and cloud-processed smoke from African savanna fires by airborne Fourier transform infrared spectroscopy (AFTIR). *J. Geophys. Res.*, 2003, 108(D13):8478. doi: 10.1029/2002JD002322.
- R. J. Yokelson, J. D. Crounse, P. F. DeCarlo, T. Karl, S. Urbanski, E. Atlas, T. Campos, Y. Shinozuka, V. Kapustin, A. D. Clarke, A. Weinheimer, D. J. Knapp, D. D. Montzka, J. Holloway, P. Weibring, F. Flocke, W. Zheng, D. Toohey, P. O. Wennberg, C. Wiedinmyer, L. Mauldin, A. Fried, D. Richter, J. Walega, J. L. Jimenez, K. Adachi, P. R. Buseck, S. R. Hall, and R. Shetter. Emissions from biomass burning in the Yucatan. *Atmos. Chem. Phys.*, 2009, 9(15):5785–5812. doi: 10.5194/acp-9-5785-2009.
- D. York, N. M. Evensen, M. L. Martínez, and J. D. B. Delgado. Unified equations for the slope, intercept, and standard errors of the best straight line. *Am. J. Phys.*, 2004, 72(3):367–375. doi: 10.1119/1.1632486.
- K. E. Yousaf and K. A. Peterson. Optimized auxiliary basis sets for explicitly correlated methods. *J. Chem. Phys.*, 2008, 129(18):184108. doi: 10.1063/1.3009271.
- R. Zander, P. Duchatelet, E. Mahieu, P. Demoulin, G. Roland, C. Servais, J. V. Auwera, A. Perrin, C. P. Rinsland, and P. J. Crutzen. Formic acid above the Jungfrauoch during 1985-2007: observed variability, seasonality, but no long-term background evolution. *Atmos. Chem. Phys.*, 2010, 10(20):10047–10065. doi: 10.5194/acp-10-10047-2010.

- C. S. Zender, H. Bian, and D. Newman. Mineral Dust Entrainment and Deposition (DEAD) model: Description and 1990s dust climatology. *J. Geophys. Res. Atmos.*, 2003, 108:4416. doi: 10.1029/2002JD002775.
- L. Zhang, D. J. Jacob, X. Liu, J. A. Logan, K. Chance, A. Eldering, and B. R. Bojkov. Intercomparison methods for satellite measurements of atmospheric composition: application to tropospheric ozone from TES and OMI. *Atmos. Chem. Phys.*, 2010, 10(10):4725–4739. doi: 10.5194/acp-10-4725-2010.
- T. Zhu, I. Barnes, and K. H. Becker. Relative-rate study of the gas-phase reaction of hydroxy radicals with difunctional organic nitrates at 298 K and atmospheric pressure. *J. Atmos. Chem.*, 1991, 13:301–311.
- J. R. Ziemke and S. Chandra. Seasonal and interannual variabilities in tropical tropospheric ozone. *J. Geophys. Res.*, 1999, 104:21425–21442. doi: 10.1029/1999JD900277.
- J. R. Ziemke, S. Chandra, B. N. Duncan, L. Froidevaux, P. K. Bhartia, P. F. Levelt, and J. W. Waters. Tropospheric ozone determined from Aura OMI and MLS: Evaluation of measurements and comparison with the Global Modeling Initiative’s Chemical Transport Model. *J. Geophys. Res. Atmos.*, 2006, 111: D19303. doi: 10.1029/2006JD007089.
- J. R. Ziemke, S. Chandra, B. N. Duncan, M. R. Schoeberl, O. Torres, M. R. Damon, and P. K. Bhartia. Recent biomass burning in the tropics and related changes in tropospheric ozone. *Geophys. Res. Lett.*, 2009, 36(15):L15819. doi: 10.1029/2009GL039303.
- P. Zimmerman, R. Chatfield, J. Fishman, P. Crutzen, and P. Hanst. Estimates on the production of CO and H<sub>2</sub> from the oxidation of hydrocarbon emissions from vegetation. *Geophys. Res. Lett.*, 1978, 5(8):679–682. doi: 10.1029/GL005i008p00679.